

AN ABSTRACT OF THE DISSERTATION OF

Andrew E. Smith for the degree of Doctor of Philosophy in Chemistry presented on June 10, 2010.

Title: Functional Transition Metal Oxides: Structure-property Relationships

Abstract approved: _____

M. A. Subramanian

Transition metal oxides are an important class of materials for the wide variety of optical, electrical, dielectric, magnetic, and thermal properties observed. Their unique structure-property relationships allow for property tuning and often provide insight into the fundamentals of chemistry. The work in this thesis was focused on the design, synthesis and physical property characterization of novel materials with applications in mind. In particular, magneto-electric multiferroics and spintronics are a promising technology for applications in many areas of electronics where either the magnetic or electric properties can be manipulated with electric or magnetic fields respectively.

$\text{La}_2\text{MnRhO}_6$ thin films were found to exhibit a change in the defect structure, surface morphology, and magnetic properties for films grown at different oxygen pressures revealing the importance of deposition methods. Bulk ceramic of La_2MRhO_6 ($\text{M} = \text{Cr}, \text{Mn}, \text{Fe}, \text{Co}, \text{Ni}$ and Cu) were characterized and all were found to be orthorhombic p-type semiconductors. Unique magnetism was found for $\text{M} = \text{Fe}$ and Cr with both showing magnetic hysteresis at 5K. The Cu analogue is likely to be in a $2+/3+$ oxidation state, and showed a favorable power factor up to ~ 575 K. $\text{LaCo}_{1-x}\text{Rh}_x\text{O}_3$ compositions were found

to exhibit an interesting lattice crossover at $x = 0.5$. Strong evidence for at least some conversion of $\text{Rh}^{3+}/\text{Co}^{3+}$ to $\text{Rh}^{4+}/\text{Co}^{2+}$ is found in both structural and electrical transport data. A thermoelectric figure-of-merit (ZT) of about 0.075 has been achieved for $\text{LaCo}_{0.5}\text{Rh}_{0.5}\text{O}_3$ at 775 K

YMnO_3 is a well known magneto-electric material, and in our study, we have prepared complete or nearly complete solid solutions with YInO_3 , YAlO_3 , and $\text{YCu}_{0.5}\text{Ti}_{0.5}\text{O}_3$ systems in order to better understand the structure-property relationships. Our results indicate exciting optical properties as a wide range of blue was observed in the YInO_3 solid solution, the intensity of which was critically dependent on the apical bond distances and the crystal field splitting. The YInO_3 and $\text{YCu}_{0.5}\text{Ti}_{0.5}\text{O}_3$ systems showed magnetic and magneto-electric suppression for increasing values as expected, but the field dependent capacitance for YInO_3 showed a unique improvement and sign swap indicating a strong magneto-electric coupling. We determined the YAlO_3 structure to have been improperly reported based on bond valence calculations. Our investigation into the YAlO_3 - YMnO_3 system is underway, however we believe a carbonate group exists within the basal plane resulting in a chemical formula such as $\text{YAl}_{1-x}\text{Mn}_x\text{O}_{3-y}(\text{CO}_3)_y$.

For the high-k dielectric $\text{CaCu}_{3-x}\text{Mn}_x\text{Ti}_{4-y}\text{Fe}_y\text{O}_{12}$ and $\text{CaCu}_3\text{Ti}_4\text{O}_{12-x}\text{F}_x$, the limits of x , y were determined. A structural study on ceramic samples determined single phase materials, and dielectric measurements showed improvement of properties for fluorinated samples with the dielectric loss lowered while maintaining a high dielectric constant. It is likely that F may be concentrating on important planar defect sites. A colossal decrease in the dielectric constant was observed for Mn-Fe co-doped samples and provides insight into dual site occupations of dopants.

©Copyright by Andrew E. Smith
June 10, 2010
All Rights Reserved

Functional Transition Metal Oxides: Structure-property Relationships

by

Andrew E. Smith

A DISSERTATION

submitted to

Oregon State University

in partial fulfillment of
the requirements for the
degree of

Doctor of Philosophy

Presented June 10, 2010
Commencement June 2011

Doctor of Philosophy dissertation of Andrew E. Smith presented on June 10, 2010.

APPROVED:

Major Professor, representing Chemistry

Chair of the Department of Chemistry

Dean of the Graduate School

I understand that my dissertation will become part of the permanent collection of Oregon State University libraries. My signature below authorizes release of my dissertation to any reader upon request.

Andrew E. Smith, Author

ACKNOWLEDGEMENTS

My time at Oregon State University has been an amazing and life changing experience and the success of this tenure is due to the guidance, support and friendship of many individuals without which it would have been impossible. I am indebted to each and every one of them.

It is with the utmost sincerity, gratitude and appreciation that I acknowledge my advisor and friend, Dr. Mas Subramanian. I had the distinct honor of being Mas's first graduate student, and as such I was able to experience everything for the first time with him. It was an amazing experience. Mas was and still is interminably dedicated to my success and has always guided me with respect, integrity, honesty, generosity, patience, and humor. His profound knowledge, constant engagement, and joviality created a fostering environment which allowed me to think openly and creatively. Without his unique guidance and friendship I would have never been able to accomplish as much as I did. I am forever grateful and I will certainly miss him when I leave.

I am also very grateful to Dr. Arthur Sleight who has been a great source of information and perspective. His dedication and unending knowledge in structure-property relationships has given great insight into much of this work. He has contributed to every chapter in this thesis. I am extremely grateful for his help and honesty, and am extremely lucky to have had the chance to work with such a remarkable scientist.

I also thank Dr. Michael Lerner, Dr. Janet Tate, Dr. Philip Watson, Dr. Kerry McPhail, and Dr. Vincent Remcho for serving as my graduate committee. Dr. Lerner, Dr. Tate and Dr. Watson have been great teachers and role models, and have been great sources of information. In addition, I would also like to thank Dr. Vincent Remcho for

sitting on my committee on such late notices. His enthusiasm is inspiring. Thank you for your support.

There are a number of people in different groups to whom I owe a great deal of thanks for their enthusiastic support, help, and friendship. First, I must thank my group members under Dr. Mas Subramanian; Hiroshi Mizoguchi, Moumita Ghosh, Jun Li, Krishnendu Biswas, James Eilertsen, Alvin Gatimu, Sean Muir, Theeranun 'June' Siritanon, and Peng Jiang. Thank you for helping make our group a fun and enjoyable one. Another thanks to Alvin and Peng for help with compositional assessments and proofreading, and to Dr. Jun Li for many helpful discussions. In addition, thanks to Dr. Keszler and his research group, Dr. Lerner and his research group, and Dr. Tate and her research group for collaborations and sharing of facilities. Dr. Lev Zakharov has also of great help in single crystal refinements. And, of course, thank you to all of my friends and peers in the chemistry department including the OSU department of chemistry staff; Linda, Joey, Kristi, Cindy, Rene, Mary, Tim, Dan, Ted, Luanne, Paula, and Talley. You have been great friends and have helped me with all my questions, problems, and snide remarks. Your good nature and consistent support has been a blessing.

With love and appreciation I also thank my wife Allison, and family; Tom, Dory, Brent, Jessica, Tyler, Lauren, Dom, Brittany, Stephanie, Jacob, Pat, Joe, Andrew and Eric. Their love and encouragement has allowed me to seek out my dreams and aspirations no matter how big or small. Your support has been invaluable.

CONTRIBUTION OF AUTHORS

I would like to acknowledge the many people who have contributed to this work in one way or another. I appreciate your hard work and support no matter how big or how small. Without your contributions, this work would certainly be lacking. Dr. Mas Subramanian and Dr. Arthur Sleight have contributed significantly to every chapter in this thesis.

Chapter 3: Dr. Art Ramirez provided magnetic data for some rhodium based perovskites before we obtained our PPMS at OSU. This was my first introduction to magnetism. Dr. Wilfred Prellier and Dr. W.C. Sheets at CRISMAT in Caen, France assisted with thin film deposition and measurements of $\text{La}_2\text{RhMnO}_6$. Dr. Jun Li performed GSAS refinements and gave much insight on the solid solution $\text{LaCo}_{1-x}\text{Rh}_x\text{O}_3$.

Chapter 4: For the $\text{YIn}_{1-x}\text{Mn}_x\text{O}_3$ solid solution, Dr. Gavin Lawes and Dr. Ambesh Dixit at Wayne State University have provided great support in magneto capacitance measurements. In addition, Dr. Lev Zakharov and Dr. Hiroshi Mizoguchi assisted in the structural refinements and in discussion of the optical measurements, and Dr. Kris Delaney and Dr. Nicola Spaldin contributed theoretical calculations. Dr. Jun Li has contributed structural refinements in the $\text{YAl}_{1-x}\text{Mn}_x\text{O}_3$ solid solution and YAlO_3 structural analysis.

Chapter 5: For the fluorine doped CCTO samples, Tom Calvarese at DuPont has assisted in some dielectric measurements, and in fluorine fusion analysis. Dr. Alain Wattieux in Bordeaux has provided Fe-Mossbauer measurements of Fe/Mn doped CCTO.

Chapter 6: Dr. Bernard Reveau, Dr. Valerie Pralong, and Dr. Antoine Maignan at CRISMAT, in coordination with the IGERT program through the University of Oregon, were gracious enough to provide support for two separate visits to CRISMAT in Caen, France to work on synthesis and characterization of bronze materials.

Throughout this work, several funding agencies have contributed significant financial support making it possible to synthesize these new materials and perform measurements on them. Support has been provided by grants from the National Science Foundation (DMR 0804167), Air Force Research Laboratory (FA8650-05-1-5041), NSF-IGERT through the University of Oregon, and NETL's on-going research on development of materials for energy applications under the RDS Contract DE-AC26-04NT41817.

TABLE OF CONTENTS

	<u>Page</u>
1 Introduction.....	1
1.1 Transition Metal Oxides	1
1.1.1 Practical Applications	2
1.2 Electronic Properties	3
1.3 Dielectric Properties.....	6
1.3.1 Dielectric Constant and Loss	7
1.3.2 High κ Materials	10
1.4 Thermoelectric Properties	11
1.5 Magnetic Properties	16
1.5.1 Fundamentals of Magnetism.....	16
1.5.2 Magnetic Ordering	17
1.5.3 Magnetic Exchange.....	21
1.5.4 Multiferroics	23
1.6 References.....	25
2 Experimental Methods of Analysis.....	29
2.1 X-Ray Diffraction: MiniFlex II Diffractometer.....	30
2.2 Dielectric: NorECs ProboStat and LCR Meters	33
2.3 Quantum Design Physical Property Measurement System	34
2.3.1 Magnetometry	35
2.3.2 Magnetocapacitance.....	37
2.3.3 DC Electrical Resistivity.....	39
2.4 Seebeck and Resistivity: ZEM-3 Thermoanalyzer	40
2.5 Optical Measurements	42
2.6 Thermogravimetric Analysis (TGA).....	44

TABLE OF CONTENTS (Continued)

	<u>Page</u>
2.7	References.....44
3	Structure and Physical Properties of Rhodium Based Perovskite oxides46
3.1	Abstract.....46
3.2	Introduction.....49
3.3	Effect of Oxygen Concentration on the Structure and Magneto-Electric Properties of $\text{LaRh}_{1/2}\text{Mn}_{1/2}\text{O}_3$ Thin Films52
3.3.1	Introduction.....52
3.3.2	Thin Film Deposition.....55
3.3.3	Results and Discussion58
3.3.4	Conclusion69
3.4	Electrical and Magnetic Properties of New Rhodium Perovskites: La_2MRhO_6 , M = Cr, Fe, Cu71
3.4.1	Introduction.....71
3.4.2	Results.....72
3.4.3	Discussion77
3.4.4	Conclusion80
3.4.5	Experimental81
3.5	Lattice Crossover and Mixed Valency in the $\text{LaCo}_{1-x}\text{Rh}_x\text{O}_3$ Solid Solution ...83
3.5.1	Introduction.....83
3.5.2	Results and Discussion85
3.5.2.1	Structural Properties.....85
3.5.2.2	Electrical Properties94
3.5.2.3	Magnetic Properties97
3.5.3	Effect of Sr on the thermoelectric performance of $\text{LaCo}_{1-x}\text{Rh}_x\text{O}_3$99
3.5.4	Conclusion101
3.5.5	Experimental102
3.6	References.....103

TABLE OF CONTENTS (Continued)

	<u>Page</u>
4 Effect of Cation Substitution on the Structure, Magnetic, and Electrical Properties of Hexagonal YMnO ₃ Based Oxides	110
4.1 Abstract	110
4.2 Introduction	113
4.3 Effects of Indium Substitution in YMnO ₃ Ceramics	120
4.3.1 Suppression of Multiferroic Order in Hexagonal YMn _{1-x} In _x O ₃ Ceramics	121
4.3.1.1 Introduction	121
4.3.1.2 Results and Discussion	123
4.3.2 Mn ³⁺ in Trigonal Bipyramidal Coordination: A New Blue Chromophore	133
4.3.2.1 Introduction	133
4.3.2.2 Results and Discussion	134
4.3.3 Conclusion	144
4.3.4 Experimental	145
4.4 Synthesis and Magnetic Properties of aYMnO ₃ - YCu _{0.5} Ti _{0.5} O ₃ Solid Solution	148
4.4.1 Introduction	148
4.4.2 Results and Discussion	150
4.4.3 Conclusion	161
4.4.4 Experimental	162
4.5 Structural Investigation of Hexagonal YAlO ₃ and Related Compositions	163
4.5.1 Introduction	163
4.5.2 Results and Discussion	164
4.5.3 Conclusion	171
4.5.4 Experimental	172
4.6 References	173

TABLE OF CONTENTS (Continued)

	<u>Page</u>
5 Tuning the Dielectric Properties of $\text{CaCu}_3\text{Ti}_4\text{O}_{12}$ Through Compositional Control	178
5.1 Abstract	178
5.2 Introduction	179
5.3 Substitutional Variations in the High- κ Dielectric $\text{CaCu}_3\text{Ti}_4\text{O}_{12}$	184
5.3.1 An Anion Substitution Route to Low Loss $\text{CaCu}_3\text{Ti}_4\text{O}_{12}$	184
5.3.1.1 Introduction	184
5.3.1.2 Results and Discussion	185
5.3.1.3 Conclusion	190
5.3.1.4 Experimental	190
5.3.2 Colossal Drop in the Colossal Dielectric $\text{CaCu}_3\text{Ti}_4\text{O}_{12}$	192
5.3.2.1 Introduction	192
5.3.2.2 Results and Discussion	192
5.3.2.3 Conclusion	200
5.3.2.4 Experimental	201
5.4 References	202
6 Miscellaneous Oxide Systems	204
6.1 Introduction	204
6.2 Transition Metal Bronzes Based on $\beta\text{-TiO}_2$	204
6.3 Perovskite Lanthanide Iridates	209
6.4 References	216
General Conclusions and Future Work	217
Bibliography	220

LIST OF FIGURES

<u>Figure</u>	<u>Page</u>
1.1 Generalized electronic band structure of transition metal oxides with metallic or semiconducting/insulating behavior. It should be noted that generally the band gap in semiconductors is much smaller than that of insulators	3
1.2 Generalized temperature dependence of the electronic conductivity for metals, semiconductors, and insulators.	5
1.3 Parallel plate capacitor with dielectric (sky blue) between plates. A is the area of the dielectric, and d is the thickness of the dielectric. The + and – symbols indicate charges that have migrated across the sample.....	7
1.4 Illustration of the Seebeck effect of two different materials. Adapted from Tritt et al. [20]	12
1.5 Illustration of the Peltier effect between two different materials. Adapted from Tritt et al. [20]	13
1.6 Relationships between the ZT, thermal conductivity (κ), electrical conductivity (σ) and Seebeck coefficient (α) for insulators, semiconductors and metals [22]....	15
1.7 Magnetic classifications for various types of magnetic interactions. Column one indicates the class type and corresponding spin orientation, while the remaining columns specify information regarding temperature dependence of the susceptibility or inverse susceptibility. Adapted from J.P. Jakybovics [29].	20
1.8 Degree of overlap for d-orbitals with oxygen 2 <i>P</i> orbitals	22
1.9 Schematic representation of the GK rules with a ferromagnetic interaction between one metal cation with a half-filled <i>d</i> orbital and the adjacent metal cation with an empty <i>d</i> orbital through an intervening oxygen ion in a 180° superexchange interaction.....	22
1.10 Giant magnetoresistance effect found in Fe-Cr layers (A.Fert et al).	24
2.1 Rigaku MiniFlex II diffractometer (a) and the inner workings with x-ray tube, sample platform and detector labeled (b)	30
2.2 Bragg’s Law reflection showing a generalized geometric relationship for an incident and diffracted beam.....	31

LIST OF FIGURES (Continued)

<u>Figure</u>	<u>Page</u>
2.3 NorECs Probostat dielectric set-up used in high temperature capacitance measurements.....	33
2.4 Quantum Design Physical Property Measurement System set up for ACMS measurements.....	35
2.5 Representation of the ACMS coil set and tube assemblage (left), expanded view with labels of the ACMS coil set detection unit (center), and mounted ‘as prepared’ sample (right). ACMS coil set illustrations taken and modified from Quantum Design application notes [5].	36
2.6 Representative views of the dielectric probe used in measuring the the capacitance of samples within the PPMS. The probe head and BNC connections (a), sample holder attachment console (b), and sample holder (c), are shown.....	38
2.7 PPMS resistivity puck with a bar sample connected to position 1 using the four probe contact technique. Notice the labeled voltage and current contacts	40
2.8 ZEM Thermoanalyzer (a) and mounted sample in the thermal chamber (b).....	41
2.9 Illustration of an integrating sphere (a) and a fiber optic system (b) used in diffuse reflectance measurements (inset is an illustration of the end of a fiber optic cable). A standard sample of BaSO ₄ can be seen, (b) bottom right	43
3.1 Common representations of the ABO ₃ perovskite structure as (a) A-cation, green spheres, centered with BO ₆ octahedra, B-blue and O-red, on cell corners, and (right) BO ₆ octahedra centered with A cations on corners.....	50
3.2 A XRD θ -2 θ scan curve of a typical LRMO film grown on LAO substrate. The substrate (00 l) are marked in the figures. The inset shows a rocking curve recorded around the 001 reflection of the film	56
3.3 A plot of the out-of-plane c -axis lattice parameter of LRMO thin films grown on STO and LAO substrates as a function of the oxygen background pressure during growth	57
3.4 SEM images of LRMO films grown at a) 300 mTorr and b) 800 mTorr along with three-dimensional AFM images showing the surface of LRMO films deposited on LAO at c) 300 mTorr and d) 800 mTorr oxygen background pressure. The scan size is 500 nm by 500 nm.....	59

LIST OF FIGURES (Continued)

<u>Figure</u>	<u>Page</u>
3.5 A plot of the temperature dependence of the ZFC and FC responses of LRMO films grown under different oxygen background pressures of (a) 100 mTorr, (b) 300 mTorr, (c) 600 mTorr, and (d) 800 mTorr.	61
3.6 M(H) hysteresis loops for LRMO films grown under different oxygen pressures on LAO substrates measured at 10 K. The inset displays the M(T) curve recorded with 1 T. Magnetic field is applied parallel to the [100] direction of the substrate	63
3.7 A plot of the resistivity of LRMO films as a function of temperature. The inset displays the $\log \rho$ as a function of inverse temperature (Arrhenius plot)	67
3.8 A plot of the temperature dependence of the real part of the dielectric response (ϵ) measured at certain frequencies for a 100 nm thick LRMO film grown on a 50 nm thick layer of LaNiO_3 deposited on (001)-oriented LAO. The inset shows a plot of the dielectric loss as a function of temperature for the same selected frequencies.	67
3.9 A plot of the dielectric loss as a function of temperature measured at certain frequencies	69
3.10 Electrical conductivity of La_2MRhO_6 pellets for M = Co, Ni, Cu (a) and M = Cr, Mn, Fe (b). Note the difference in scale for (a) and (b).....	73
3.11 Electrical resistivity and Seebeck coefficient for $\text{La}_2\text{CuRhO}_6$	74
3.12 Power factor calculated for $\text{La}_2\text{CuRhO}_6$ from 300 - 575 K	74
3.13 Magnetic susceptibility (left) and inverse magnetic susceptibility (right) for field cooled (FC, red) and zero field cooled (ZFC, black) for $\text{La}_2\text{CuRhO}_6$ from 5 – 320 K under an applied field of 0.5 Tesla.....	75
3.14 Magnetic susceptibility (left) and inverse magnetic susceptibility (right) for field cooled (FC, red) and zero field cooled (ZFC, black) for $\text{La}_2\text{FeRhO}_6$ from 5 – 320 K under an applied field of 0.5 Tesla.....	76
3.15 Magnetic susceptibility (left) and inverse magnetic susceptibility (right) for field cooled (FC, red) and zero field cooled (ZFC, black) for $\text{La}_2\text{CrRhO}_6$ from 5 – 320 K under an applied field of 0.5 Tesla.....	76
3.16 La_2MRhO_6 unit cell volumes vs. M^{3+} radii	78

LIST OF FIGURES (Continued)

<u>Figure</u>	<u>Page</u>
3.17 Hysteresis loop for $\text{La}_2\text{FeRhO}_6$ obtained at 5 K	79
3.18 Hysteresis loop for $\text{La}_2\text{CrRhO}_6$ obtained at 5 K	80
3.19 XRD patterns of $\text{LaCo}_{1-x}\text{Rh}_x\text{O}_3$ (open circles) and calculated data (solid line) by Rietveld refinement. Allowed Bragg reflections are shown as vertical lines for both structural variations.....	85
3.20 Rietveld refinement of $\text{LaCo}_{1-x}\text{Rh}_x\text{O}_3$ ($x = 0.5$) with orthorhombic structure. Observed data are shown as open circles, calculated data as the solid line, allowed Bragg reflections as vertical lines, and difference curve ($I_o - I_c$) at the bottom	86
3.21 Cell parameters as a function of Rh concentration for solid solutions $\text{LaCo}_{1-x}\text{Rh}_x\text{O}_3$. Straight lines are drawn to guide the eyes. (a) Cell edge b of the orthorhombic phase was divided by $\sqrt{2}$; (b) Cell volume V of the rhombohedral phase was normalized ($\times 2$), based on Z , to match the orthorhombic cell volume.	86
3.22 Cell edges and tolerance factor t calculated by SPuDS (a), and observed and predicted tilt angles calculated by Tubers and SPuDS, respectively (b).	90
3.23 Composition dependence of lattice strain $[2(a^2 + b^2 + c^2 - ab - bc - ca)/3a_0^2]^{1/2}$ caused by orthorhombic distortion.....	91
3.24 Bond distances vs. x in $\text{LaCo}_{1-x}\text{Rh}_x\text{O}_3$	92
3.25 Bond angles vs. x in $\text{LaCo}_{1-x}\text{Rh}_x\text{O}_3$	93
3.26 Temperature dependence of the Seebeck coefficient (a) and electrical resistivity (b) for $\text{LaCo}_{1-x}\text{Rh}_x\text{O}_3$	95
3.27 Temperature dependence of the thermal conductivity (a) and dimensionless figure-of-merit ZT (b) for $\text{LaCo}_{1-x}\text{Rh}_x\text{O}_3$	96
3.28 Temperature dependence of the Seebeck coefficient (a) and electrical resistivity (b) for $\text{La}_{1-y}\text{Sr}_y\text{Co}_{1-x}\text{Rh}_x\text{O}_3$	98
3.29 Temperature dependence of the Seebeck coefficient (a) and electrical resistivity (b) for $\text{La}_{1-y}\text{Sr}_y\text{Co}_{1-x}\text{Rh}_x\text{O}_3$	100

LIST OF FIGURES (Continued)

<u>Figure</u>	<u>Page</u>
3.30 Temperature dependence of the thermal conductivity (a) and dimensionless figure-of-merit ZT (b) for $\text{La}_{1-y}\text{Sr}_y\text{Co}_{1-x}\text{Rh}_x\text{O}_3$	101
4.1 Interrelationships of the properties of multiferroics for ferromagnetism, ferroelectricity, and ferroelasticity. Adapted from N.A. Spaldin et al [2]	113
4.2 Orthorhombic structure for RMnO_3 oxides where $\text{R} = \text{La} - \text{Dy}$. Green spheres are R^{3+} cations, Red spheres are oxygen cations, and Mn occupies the center of the octahedra, light grey.....	115
4.3 Representation of the asymmetric hexagonal YMnO_3 structure with unique atoms labeled. Note the displaced Y1 and Y2 atoms and the unique coordination of Mn^{3+} in rotationally distorted MnO_5 polyhedra.	116
4.4 M-site substitutional effects on YMnO_3 structure. Dark cyan is observed hexagonal structure, orange is coexisting hexagonal and perovskite structures, yellow is perovskite structure, and yellow/hash marks are perovskite and impurities. Gray bars are unreported compositions or incomplete analysis. *Cu-Mo co substitution is a 3:1 ratio [8,17-26].....	119
4.5 Normalized powder x-ray diffraction patterns for the full solid solution in $\text{YIn}_{1-x}\text{Mn}_x\text{O}_3$. YMnO_3 and YInO_3 parent compounds are on bottom and top respectively	123
4.6 Unit cell dimensions and c/a ratio for the $\text{YIn}_{1-x}\text{Mn}_x\text{O}_3$ solid solution. It is clear that the similar basal-plane bond lengths in end members lead to a weak variation of across the solid solution series. The c/a ratio varies strongly due to the large apical bond-length difference for In-O and Mn-O.....	124
4.7 (a) Temperature dependence of the magnetic susceptibility measured at $\mu_0\text{H}=0.5$ T for different $\text{YIn}_{1-x}\text{Mn}_x\text{O}_3$ samples, as indicated. The inset plots the susceptibility less a background correction to more clearly emphasize the magnetic anomalies in the $x=1$ and $x=0.25$ samples. (b) Specific heat, plotted as C/T versus T, for the $\text{YIn}_{1-x}\text{Mn}_x\text{O}_3$ samples, as indicated	125
4.8 Relative change in capacitance for $\text{YIn}_{1-x}\text{Mn}_x\text{O}_3$ samples as labeled. The dielectric anomalies associated with the magnetic ordering transitions are indicated by the dashed arrow.....	128

LIST OF FIGURES (Continued)

<u>Figure</u>	<u>Page</u>
4.9 Magnetic field dependence of the capacitive response for different samples, as indicated. The solid bars on the $x=1$, $x=0.5$, and $x=0.25$ curves provide a visual estimate of the scatter in the data before smoothing. The dashed line on the $x=0.25$ curve shows the fit described in the text.....	129
4.10 Temperature dependence of the magnetocapacitive coupling constant (as described in the text) for the $x=0.5$ and $x=0.25$ $\text{YIn}_{1-x}\text{Mn}_x\text{O}_3$ samples.....	131
4.11 Temperature dependence of the antiferromagnetic ordering transition on x in $\text{YIn}_{1-x}\text{Mn}_x\text{O}_3$. The different symbols represent the transition temperature extracted from different measurements, as indicated. The dashed line shows the curve used to estimate the initial suppression of T_N , as described in the text.	133
4.12 The structures of YMnO_3 (left) and YbFe_2O_4 (right) as blue trigonal bipyramids (Mn or Fe), grey Y or Yb and cyan O atoms. The YMnO_3 structure consists of layers of corner-shared MnO_5 trigonal bipyramids. The YbFe_2O_4 structure is similar, but has a double-layer of corner-shared trigonal bipyramids that edge share between the layers. Schematic energy levels for the spin up Mn^{3+} 3d orbitals in trigonal bipyramidal coordination are shown. We note that transitions from e' to a' are formally dipole allowed in this symmetry	135
4.13 Unit cell dimensions and c/a ratio for the $\text{YIn}_{1-x}\text{Mn}_x\text{O}_3$ solid solution. It is clear that the similar basal-plane bond lengths in end members lead to a weak variation of across the solid solution series. The c/a ratio varies strongly due to the large apical bond-length difference for In-O and Mn-O.....	137
4.14 Colors of pellets and powders at selected compositions. The intense blue color appears at our lowest concentration of Mn doping in YMnO_3 . With increasing Mn composition, the color darkens until eventually YMnO_3 is found to be black.	137
4.15 Diffuse reflectance spectra for the $\text{YIn}_{1-x}\text{Mn}_x\text{O}_3$ solid solution. Strong absorption in the red-green spectral region, combined with a relatively weak absorption in the blue region, is responsible for the observed intense blue color. With increasing Mn composition, the first absorption peak broadens and the second onset lowers in energy, such that YMnO_3 absorbs almost equally throughout the visible region (see text).....	138
4.16 Structural variation for substitutions in $\text{YMn}_{1-x}\text{M}_x\text{O}_3$	149

LIST OF FIGURES (Continued)

<u>Figure</u>	<u>Page</u>
4.17 X-ray diffraction patterns for $\text{YMn}_{1-x}(\text{Cu}_{0.5}\text{Ti}_{0.5})_x\text{O}_3$. End members are at the bottom ($\text{YCu}_{0.5}\text{Ti}_{0.5}\text{O}_3$) and top (YMnO_3).	151
4.18 Local coordination environment and energy level diagrams from Mn^{3+} in the perovskite (LaMnO_3 - left) and hexagonal (YMnO_3 - right) structures.....	152
4.19 Unit cell dimensions (bottom) and c/a ratio (top) for $\text{YMn}_{1-x}(\text{Cu}_{0.5}\text{Ti}_{0.5})_x\text{O}_3$	153
4.20 Inverse magnetic susceptibility (a) and magnetic susceptibility (b) for $\text{YMn}_{1-x}(\text{Cu}_{0.5}\text{Ti}_{0.5})_x\text{O}_3$. Magnetic anomalies are labeled by arrows (a-inset)	154
4.21 Temperature dependence of the relative capacitance for $\text{YMn}_{1-x}(\text{Cu}_{0.5}\text{Ti}_{0.5})_x\text{O}_3$ with arrows indicating the magnetic ordering temperature.....	157
4.22 Compositional dependence of the antiferromagnetic ordering temperature and Curie-Weiss temperature (bottom) and calculated and observed magnetic moments (top) for $\text{YMn}_{1-x}(\text{Cu}_{0.5}\text{Ti}_{0.5})_x\text{O}_3$	158
4.23 Substitutional allowances in hexagonal $\text{YCu}_{0.5}\text{Ti}_{0.5}\text{O}_3$	159
4.24 Diffuse reflectance spectra for the $\text{Y}(\text{Cu}_{0.5}\text{Ti}_{0.5})_{1-x}\text{Al}_x\text{O}_3$ for $x \leq 0.5$	160
4.25 Centric YAlO_3 (left) and non-centric YMnO_3 (right).....	163
4.26 Powder x-ray diffraction patterns for YAlO_3 . Arrows indicate the impurity phase $\text{Y}_4\text{Al}_2\text{O}_9$	165
4.27 Thermal Gravimetric Analysis of YAlO_3 from a dehydrated citrate gel	166
4.28 IR-spectra of YAlO_3 and BaCO_3 as reference	168
4.29 Powder x-ray diffraction patterns for $\text{YAl}_{1-x}\text{Mn}_x\text{O}_3$ in $x = 0.1$ intervals	169
4.30 Unit cell dimensions (bottom) and c/a ratio (top) for $\text{YAl}_{1-x}\text{Mn}_x\text{O}_3$	170
5.1 Structural illustration of cubic perovskite BaTiO_3 with arrows indicating Ti^{4+} offset within corner shared octahedra upon decreasing temperature. Red spheres are oxygen, and the Green central sphere is barium	180
5.2 Dielectric constant as a function of temperature for BaTiO_3 . Structures are inset at the proper temperature ranges. Adapted from W.J. Merz [5]	181

LIST OF FIGURES (Continued)

<u>Figure</u>	<u>Page</u>
5.3 Transformation of AMO_3 cubic perovskite (left) to the A-site ordered perovskite (center), and the distorted pseudo-cubic perovskite $\text{CaCu}_3\text{Ti}_4\text{O}_{12}$ (right). The $\text{CaCu}_3\text{Ti}_4\text{O}_{12}$ cubic unit cell with TiO_6 yellow octahedra, calcium body center (12 CN), red, and copper square planar coordination, dark blue. Oxygen anions are turquoise.....	182
5.4 Structure of the cubic pseudo-perovskite ($\text{Im}\bar{3}$) $\text{CaCu}_3\text{Ti}_4\text{O}_{12}$ with TiO_6 octahedra, Cu in square planar coordination (small black spheres) about O (small light grey spheres) and Ca at the origin and cube center (medium size grey spheres)	184
5.5 Room temperature XRD powder patterns for $\text{CaCu}_3\text{Ti}_4\text{O}_{12-x}\text{F}_x$ samples where $x = 0-0.8$. The inset in the upper left corner is an expanded view of the shift in (222) peak around $2\theta\ 42.5^\circ$. Shoulders in the peaks are due to $\text{CuK}\alpha_2$ radiation	186
5.6 Lattice parameter expansion as a result of fluorine substitution for oxygen, and the valence reduction of $\text{Cu}^{2+} \rightarrow \text{Cu}^{1+}$	187
5.7 Result of fluorine substitution on the dielectric constant (κ) and dielectric loss (loss tangent, $\tan \delta$) for pure and F-doped $\text{CaCu}_3\text{Ti}_4\text{O}_{12-x}\text{F}_x$ where $x = 0-1.2$ at 25°C at a frequency of 100 kHz.....	187
5.8 Temperature dependence of the dielectric constant (κ) for pure and F-doped $\text{CaCu}_3\text{Ti}_4\text{O}_{12-x}\text{F}_x$ at a frequency of 100 kHz	189
5.9 Temperature dependence of the dielectric loss (loss tangent, $\tan \delta$) for pure and F-doped $\text{CaCu}_3\text{Ti}_4\text{O}_{12-x}\text{F}_x$ at a frequency of 100 kHz	189
5.10 Room temperature powder x-ray diffraction patterns for $\text{CaCu}_3\text{Ti}_4\text{O}_{12-x}\text{F}_x$ samples where $x = 0-0.5, 1$	193
5.11 Lattice parameter expansion as a result of Mn and Fe co-substitution for Cu and Ti respectively	195
5.12 Mossbauer analysis of the nominal composition $\text{CaCu}_{2.5}\text{Mn}_{0.5}\text{Ti}_{3.5}\text{Fe}_{0.5}\text{O}_{12}$	195
5.13 Temperature dependence of the dielectric constant (κ), top, and the dielectric loss (loss tangent, $\tan \delta$) for $\text{CaCu}_{3-x}\text{Mn}_x\text{Ti}_{4-x}\text{Fe}_x\text{O}_{12}$ at a frequency of 1 MHz	196

LIST OF FIGURES (Continued)

<u>Figure</u>	<u>Page</u>
5.14 Magnetic susceptibility versus temperature of $\text{CaCu}_{3-x}\text{Mn}_x\text{Ti}_{4-x}\text{Fe}_x\text{O}_{12}$ for $x = 0$, and $0.1-0.5$ measured at 1 Tesla. Inset: inverse susceptibility of the aforementioned compositions	198
5.15 Mossbauer analysis of the nominal composition $\text{LaCu}_3\text{Ti}_3\text{FeO}_{12}$	199
6.1 Monoclinic C_2/m bronze structure of Na_xTiO_2 . The structure contains a zig-zag row of double octahedra, two distinct octahedral sites (one with 4 edges shared, blue, and 5 edges shared, green), and a closely related perovskite unit. This representation shows a full occupation of the Na site, yellow spheres. In reality, there would be a disordered partial occupation.	206
6.2 Powder diffraction patterns for $\text{Ln}_2\text{NiIrO}_6$ where $\text{Ln} = \text{La}, \text{Pr}, \text{Nd}, \text{Sm}$ (a) and monoclinic structure along the y-axis with Ni and Ir ordered in octahedral centers, and Ln as green spheres	210
6.3 Magnetic susceptibility and inverse magnetic susceptibility for ZFC (blue) and FC (red) measurements on (a) $\text{La}_2\text{NiIrO}_6$, and (b) $\text{Pr}_2\text{NiIrO}_6$	213
6.4 Magnetic susceptibility and inverse magnetic susceptibility for ZFC (blue) and FC (red) measurements on (a) $\text{Nd}_2\text{NiIrO}_6$, and (b) $\text{Sm}_2\text{NiIrO}_6$	214

LIST OF TABLES

<u>Table</u>	<u>Page</u>
3.1 Expected superexchange interactions for ordered LRMO films.....	64
3.2 Cell dimensions and heating parameters.....	72
3.3 Details of electrical measurements at 300 K.....	73
3.4 Summary of magnetic measurements at 0.5 Tesla at 5 - 320 K.	77
3.5 Structural parameters for $\text{LaCo}_{1-x}\text{Rh}_x\text{O}_3$ ($0.0 \leq x \leq 1.0$) system. The atomic positions of Co/Rh are at (0,0,0) and (0,0,1/2) in rhombohedral and orthorhombic structures, respectively	88
3.6 Bond distances (\AA) and angles ($^\circ$) for orthorhombic $\text{LaCo}_{1-x}\text{Rh}_x\text{O}_3$ where $0.2 \leq x \leq 1.0$	88
4.1 Bond lengths (\AA) for $\text{YIn}_{0.37}\text{Mn}_{0.63}\text{O}_3$	140
4.2 Atomic coordinates and equivalent isotropic displacement parameters ($\text{\AA}^2 \times 10^3$). $U(\text{eq})$ is defined as one third of the trace of the orthogonalized U^{ij} tensor.....	141
4.3 Crystal data and structure refinement for $\text{YIn}_{0.37}\text{Mn}_{0.63}\text{O}_3$ at 173 K	141
4.4 Results for Curie-Weiss analysis of magnetic susceptibility	155
5.1 Fluorine content of selected samples.	186
5.2 Magnetic data calculated from paramagnetic region, $T > 150 \text{ K}$	198
6.1 Crystallographic data and unit cell parameters from single crystal analysis of $\text{NaCu}_3\text{Ti}_4\text{O}_{12}$ melt. The refined values yielded a formula of $\text{Na}_{0.8}\text{Cu}_{0.4}\text{Cu}_{3.6}\text{O}_8$	207
6.2 Cell dimensions based on monoclin C_2/m space group, dielectric properties and color for $\text{Na}_{0.86}\text{M}_{0.43}\text{Ti}_{3.57}\text{O}_8$	207
6.3 Summary of magnetic measurements for $\text{Na}_{0.86}\text{M}_{0.43}\text{Ti}_{3.57}\text{O}_8$ measured at 1.0 Tesla from 5 - 300 K.....	208
6.4 Unit cell dimensions	211

LIST OF TABLES (Continued)

<u>Table</u>	<u>Page</u>
6.5 Expected super-exchange interactions for ordered $\text{Ln}_2\text{NiIrO}_6$	211
6.6 Summary of ZFC and FC magnetic measurements at 0.5 Tesla at 5 - 320 K	215

To my wife ALLISON:

Your love and support has provided a fruitful
environment for me to grow beyond what I am.
For your patience, understanding, love, friendship
and devotion, you have allowed me to succeed
in some way everyday.

Thank you.

This thesis is dedicated to

Dr. Mas Subramanian

Your passion and enthusiasm
for chemistry is an inspiration.

Thank you for everything!

Functional Transition Metal Oxides: Structure-property Relationships

Chapter 1

Introduction

1.1 Transition Metal Oxides

Transition metal oxides, (TMOs), have a rich history as the “go to” materials for electronic devices. It is not just the stability that makes these materials suitable for many applications, but the wide range of electronic properties (insulators, ferroelectrics, semiconductors, metals, and superconductors) [1], magnetic properties (paramagnetism, ferro/ferrimagnetism, antiferromagnetism, and diamagnetism), and the cross coupling of electric and magnetic properties (magneto-capacitance, magneto-resistance, and multiferroics in general) of these materials that are often found [1,2]. These properties can be tailored to specific applications by subtle distortions of the coordination environments, or changes in composition. This is certainly the case for TMOs having a perovskite or hexagonal structure [3]. The simple, complex perovskite and the hexagonal structure can accommodate many transition, alkali, alkali earth, and lanthanide metals, including some post transition elements. In this work, attempts are made to design property-specific materials by compositional and structural control. Specifically, $\text{CaCu}_3\text{Ti}_4\text{O}_{12}$, $\text{La}_2\text{RhMnO}_6$, and YMnO_3 are used as parent materials in the search for new high-k dielectrics, magnetism, and multiferroics respectively. Our

goal is to discuss in detail the synthesis, structure, and characterization of these ‘tuned’ materials.

The next few sections are designed to give a very brief introduction to the basics necessary for later discussion. This may be trivial in some cases, but exposure to these concepts is warranted. The electronic, dielectric thermoelectric, and magnetic properties will be discussed, and the perovskite structure will be introduced.

1.1.1 Practical Applications

Transition metal oxides have a rich history in furnishing the potential for promising applications in state of the art fields. Because of the variety of properties observed in these materials, TMOs fulfill roles that make our everyday lives a little more enjoyable. Fields of study including high-k dielectrics, optical, magnetic and electric field sensors, non-volatile storage, and multiferroics are progressing current electronics into a new generation of devices and consumer based products. For the current generation of handheld device users, this is most apparent in the size, memory capacity, and capabilities of electronics such as cellular phones, PDAs, iPods, and external hard drives. TMOs are also present in catalytic converters, regenerative breaking, and solar energies, and are being studied in thermoelectrics, and negative thermal expansion for spacecraft and oral composites for tooth repair [2]. This thesis is devoted to better understanding the synthesis and physical properties of transition metal oxides for a variety of potential applications.

1.2 Electronic Properties

The solid state chemist generally takes a middle ground between physicists and engineers regarding the way properties of ceramic materials are approached. For instance, a physicist may consider the quantitative understanding of ionic/electronic behavior of a material, while an engineer may consider the material as having a specific electronic value and character as a component based on electrical measurements. The role of a solid state chemist is thus one that considers both the applications in which the material will be used while being able to understand the effects of structure, composition, and eventual setting relating to electrical behavior. With a basic understanding of structure-property relationships, the electron transport properties of a TMO (electrical conductivity, thermal conductivity, and thermopower) can be predicted and manipulated to some degree.

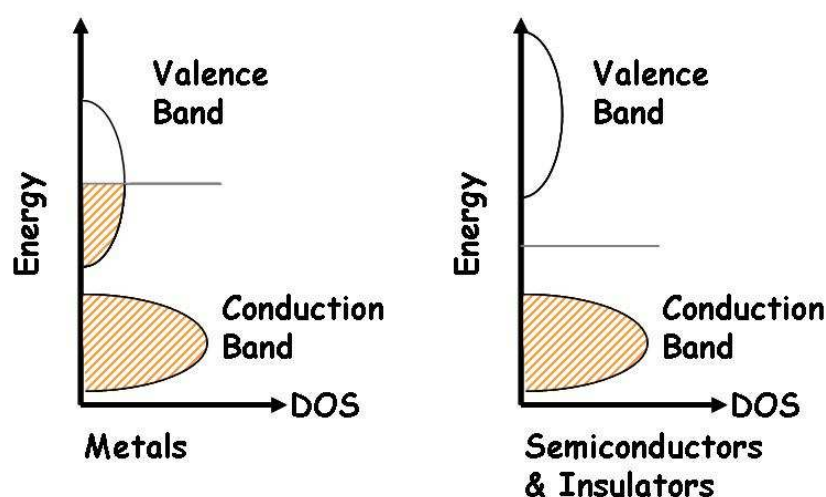


Figure 1.1 Generalized electronic band structure of transition metal oxides with metallic or semiconducting/insulating behavior. It should be noted that generally the band gap in semiconductors is much smaller than that of insulators.

The electrical properties of a solid are generally classified based on the magnitude of conduction or resistance. Whether a metal, semiconductor or insulator, only electronic conduction subsists. The magnitude of the conduction is thus strongly correlated to the number of electrons available for participation and is therefore dictated by the arrangement and occupation of electronic states and levels (i.e. electron band structure, Fig 1.1) and the atomic interactions. Insulators tend to be ionic or strongly covalent, and thus the valence electrons are tightly bound to the atom (high electron localization). Semiconductors, however, are predominately covalent and have valence electrons that are weakly bound to the atoms, thus they are free to move upon some thermal excitation.

In the ideal model of a solid at absolute zero, a metal will have an overlap of the conduction band and valence band, or the occupation of electrons in a band with states above and adjacent available for excitation. Semiconductors and insulators do not have this overlap, rather a forbidden 'band gap' where in a pure material there are no allowed states for an electron to occupy. In semiconductors, this gap is generally less than 2 eV, whereas insulators have a band gap greater than 2 eV.

With this understanding the effect of temperature on these classifications is thus easier to understand. Metallic solids will conduct down to the lowest attainable temperature, and become less conducting upon increasing temperature due to lattice vibrations which cause barriers for the movement of carriers. Insulators and semiconductors will become more conducting upon increasing temperatures (Fig 1.2) due to thermal excitations of electrons into the empty conduction band. Because

semiconductors generally have smaller band gaps than insulator, the increase in conductivity will generally be larger and faster than in insulators [4, 5].

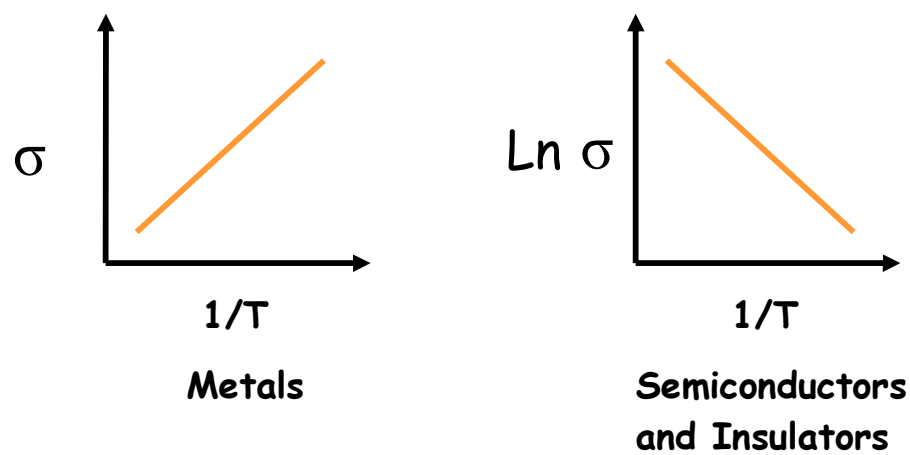


Figure 1.2 Generalized temperature dependence of the electronic conductivity for metals, semiconductors, and insulators.

An Arrhenius plot ($\ln \sigma$ vs. $1/T$) is often used to show the temperature dependence of the conductivity or resistivity of a material. The well known relation is

$$\sigma = \sigma_0 \exp \frac{E_a}{k_B T}$$

where σ_0 is a constant and E_a is the activation energy of the conductivity, k_B is

Boltzman's constant ($8.617 \times 10^{-5} \text{ eV/K}$), and T is the temperature. Taking the log of both sides of the

$$\text{Ln } \sigma = \text{Ln } \sigma_o + \frac{Ea}{k_B} \frac{1}{T}$$

equation gives a linear relationship in which case the activation energy can be calculated from the slope of a plot of $\text{Ln } \sigma$ vs. $1/T$.

1.3 Dielectric Properties

Dielectric materials have a rich history in electronics industries regardless of application. Some applications include: printed circuit boards, substrates, electronic and microwave components, sensor windows, microwave absorbers, wireless communications, cellular base stations, radio links, separators, wideband networks and especially capacitors [6].

The electronic properties of insulators are often measured differently than metals and semiconductors. Dielectric constant and loss measurements are the most common methods for evaluating a dielectric due to the ease of analysis. In addition, physical characteristics, structure of the elements, and the density of the solid can be derived from the measured dielectric constant, capacitance, and loss information

As previously mentioned, dielectric materials are insulators. In dielectrics, or nonmetallic solids, charges do not have a propensity to move easily and thus the formation of ‘charge islands’ is possible (in Latin, the word *insula* is defined as ‘island’ and is the origin of the word insulator) [7]. The most common use of a dielectric material is in that of a capacitor. A capacitor is an insulating material that is, in effect, sandwiched between two conducting plates. When an electric field is

applied, the charges that were once pinned are forced to migrate towards the opposite charge that has accumulated at the conducting electrode. This is referred to as polarization and occurs due the external electric field that distorts the electron clouds, which in turn generates an opposing electric field that affects the macroscopic field inside and outside the dielectric [5].

1.3.1 Dielectric Constant and Loss

The measure of a dielectric, or the ability of the dielectric material to store a charge relative to a vacuum, is quantified by the dielectric constant and loss. In a parallel plate capacitor (dielectric material between two plates) the capacitance of a material is directly related to the quantity of charge stored in either plate. As a voltage is applied across the capacitor, the plates become oppositely charged (one positive,

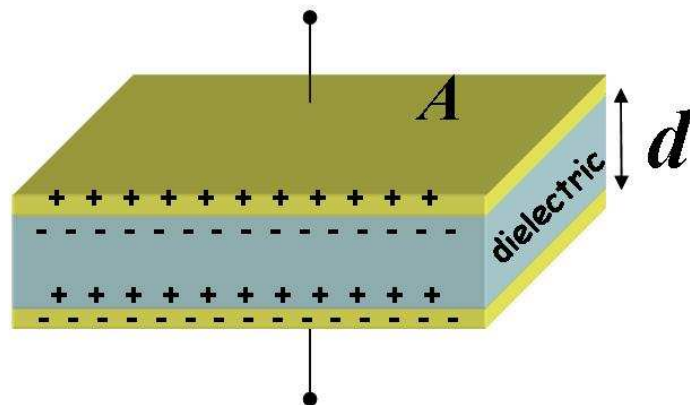


Figure 1.3 Parallel plate capacitor with dielectric (sky blue) between plates. A is the area of the dielectric, and d is the thickness of the dielectric. The $+$ and $-$ symbols indicate charges that have migrated across the sample.

one negative) with the electric field in the direction of positive to negative flow, Fig

1.3. The capacitance C is thus a charge Q per voltage V ,

$$C = \frac{Q}{V}$$

For a dielectric material between the plates with a relative permittivity ϵ_r and plate area A , the capacity for a plate spacing d would be,

$$C = \epsilon_0 \epsilon_r \frac{A}{d}$$

And therefore,

$$\epsilon_r = \frac{C}{C_0} = \frac{\epsilon}{\epsilon_0}$$

where ϵ_0 is a universal constant known as the permittivity of free space with a value of 8.854×10^{-12} F/m, ϵ is the permittivity of the dielectric material, and C_0 the capacitance of vacuum. The ratio of ϵ / ϵ_0 is a value greater than unity and reflects the increase in charge storing capacity due to the inserted material. This value is referred to as the relative permittivity ϵ_r , or the dielectric constant κ .

$$\kappa = \frac{Cd}{\epsilon_0 A}$$

Many factors can affect the dielectric constant, but the most common factors are temperature, frequency, bonding, crystal structure, and defects [4, 5]. Changes due to temperature variations can give important details about the crystal structure, and the type of dielectric character present. This will be discussed in detail later.

The magnitude of the dielectric constant depends on the degree to which a material polarizes, or the amount of charge displacement that occurs. Therefore, a material with

a low dielectric constant such as dry air, $\epsilon_r \approx 1$ at 1 kHz, is unable to maintain a charge displacement. Some materials with a moderate dielectric constant include polymers, porcelain, paper, Teflon, and dry wood. Transition metal oxides, however, tend to have higher dielectric constants (BaTiO_3 $\epsilon_r = 10^3$ at 100 Hz) [4-6, 8].

The dielectric constant alone does not determine the overall ‘goodness’ of a dielectric material. In most cases the dielectric loss (loss tangent) may be the determining factor. In a perfect dielectric, current leads the voltage by 90° when an alternating current is passed through the material. In this case, the molecules in the material are able instantaneously align and stay in phase with the changing field. However, most dielectrics are unable to stay in phase with the changing field and thus experience a phase lag. When a phase lag occurs electrical energy is lost (or absorbed by the material) in the form of heat. Thus, the phase lag changes the angle of leading current by δ . The dielectric loss is also referred to as $\tan \delta$.

In addition, the power loss is often used as a measure of efficiency in a dielectric. It can be quantified as:

$$\text{Power loss} = \pi f V_0^2 \epsilon_r \tan \delta$$

where f is the frequency, V_0 the maximum value of the voltage, and the product $\epsilon_r \cdot \tan \delta$ is the loss factor. The loss factor therefore illustrates the usefulness of a material as a dielectric.

Under certain conditions all dielectrics will experience dielectric breakdown. This occurs when the applied electric field exceeds a critical value causing electrons to migrate into the conduction band. The dielectric strength is therefore the maximum

applied voltage the material can withstand before breakdown occurs. For use as a capacitor, a good dielectric material should comprise of a high dielectric constant, low dielectric loss, and a high dielectric strength. The effect of temperature on these qualities should also be minimal [4-6].

1.3.2 High κ Materials

In the last 20-30 years the material most frequently used as an insulator in gate dielectrics and energy storage capacitors has been SiO_2 , $\epsilon_r = 3.9$. As the modernization of electronics continues to shrink the size of devices, certain components must also be reduced. This reduction in size presents new issues regarding performance and properties. In gate dielectrics, the SiO_2 film has been reduced to nearly 2nm. Further reduction in film thickness results in increased leakage currents due to direct tunneling. In order to continue decreasing the film thickness, the dielectric constant must be enhanced. Therefore, high- κ dielectrics are a suitable replacement and are the focus of not only thin films, but also memory storage capacitors such as FeRAM (ferroelectric random access memory).

Materials exhibiting a dielectric constant greater than ~ 8 are generally considered to be high- κ dielectrics. However, for storage capacitors the dielectric constant should be far greater, $\epsilon_r > 1000$. Most high dielectric constants are found in ferroelectric materials and are the result of a spontaneous polarization associated with a structural phase transition. Perovskites, especially perovskite titanates, tend to make up a large portion of these materials, and tend to have higher dielectric constants in general. The

perovskite BaTiO_3 is the most widely known example. Ferroelectrics, including relaxor behavior, despite having high dielectric constants, present problems regarding stability due to their strong dependence on temperature and frequency.

In 2000, Subramanian and coworkers measured the dielectric properties of the pseudo perovskite material $\text{CaCu}_3\text{Ti}_4\text{O}_{12}$ (CCTO) and found it to have a dielectric constant of about 10,000 at 100 kHz that was nearly independent of temperature in the range of 150 to 600 K [9]. Due to the impressive dielectric properties, considerable interest in CCTO materials has resulted in a plethora of research on them [10-17], and makes it one of the frontrunners for use in a multitude of applications in microelectronics. To date there are over 500 published articles on CCTO and similar materials [18].

1.4 Thermoelectric Properties

Heightened interest in thermoelectrics has been driven by the demand to reduce fossil fuels dependence and improve alternative energy technologies [19]. At present, several areas of alternative energy exist with the most recognizable being geothermal, solar, wind, and hydroelectric. While these areas continue to improve, new research has developed additional sources for renewable energy. One of these potential sources is thermoelectrics. Thermoelectric devices incorporate materials in which a thermal gradient can generate electricity. Applications of such thermoelectrics may include industrial waste heat recovery in automobile exhaust, geothermal, or solar heat (steam generators, photovoltaics), and in electronics where complimentary metal oxide

semiconductors (CMOS) computer processors have the potential to increase processing speeds by up to 200% [20]. Therefore, thermoelectrics have the potential to recoup a vast amount of energy in current industrial processes, and can additionally be applied to modern devices and machinery [19-21].

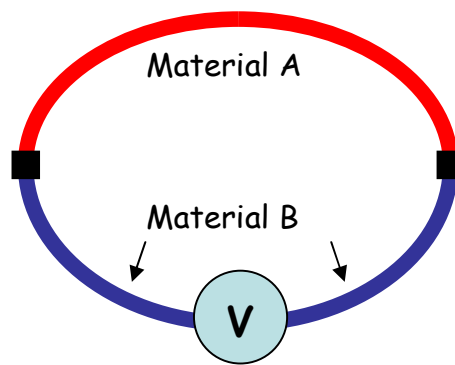


Figure 1.4 Illustration of the Seebeck effect of two different materials. Adapted from Tritt et al. [20].

A fundamental discussion of thermoelectric materials should start with an introduction to the Seebeck effect and the Peltier effect. The Seebeck effect was discovered in the early 1800's when it was found that a thermal gradient across the junctions of two dissimilar materials created a voltage that was proportional to the thermal gradient, Fig 1.4. Thus, the Seebeck coefficient (α), or thermopower, is the ratio of a voltage generated for a temperature difference, $\alpha = \Delta V / \Delta T$, and is an intrinsic property of the material. This is the basis for power generation in thermoelectric devices. Metals tend to have relatively low Seebeck coefficients, a few $\mu\text{V/K}$, whereas semiconductors and insulators can have Seebeck coefficients of several hundreds $\mu\text{V/K}$. Additional information can be extracted from the Seebeck

coefficient including the type of charge carrier. For a positive Seebeck coefficient, holes are considered the dominant carrier and are labeled as p-type. For a negative Seebeck coefficient, electrons are considered the dominant carriers, and are labeled as n-type. Different applications require the use of one type instead of the other. A common application of the Seebeck phenomena is in thermocouples to measure precise temperatures [21]. Generally, two conductors of known thermal characteristics are used to make thermocouples. The temperature difference between the two materials can then be determined from previously calibrated voltages.

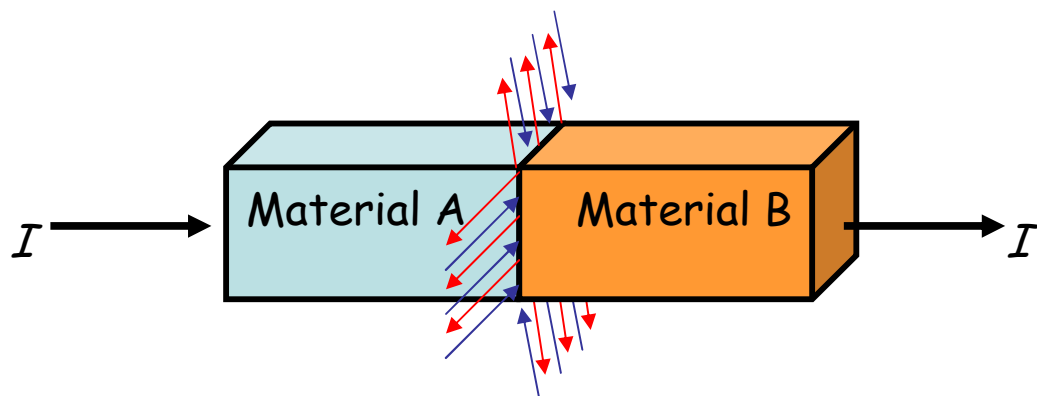


Figure 1.5 Illustration of the Peltier effect between two different materials. Adapted from Tritt et al.[20].

Not long after the Seebeck effect was discovered, the Peltier effect was reported. Peltier described the observation that for an applied electrical current at the junction of two dissimilar materials, heat was either liberated or absorbed depending on the direction of current flow Fig 1.5. The Peltier effect is the basis for electronic refrigeration. The Peltier and Seebeck effects are interrelated as defined by the Peltier coefficient, Π ;

$$\Pi = \alpha T$$

The rate to which heat is liberated or absorbed at the junction, Q_P is thus a function of the current through the junction, Seebeck coefficient of the material and temperature;

$$Q_P = \Pi I = \alpha T I$$

The Seebeck coefficient alone, however, does not fully describe the potential or efficiency of the material as a thermoelectric. Instead, the potential of the material is determined by a dimensionless figure of merit denoted ZT ,

$$ZT = \frac{\alpha^2 \sigma T}{\kappa} = \frac{\alpha^2 T}{\rho \kappa}$$

Where, α is the Seebeck coefficient, σ is the electrical conductivity, ρ is the electrical resistivity, and κ is the total thermal conductivity ($\kappa = \kappa_E + \kappa_L$; electronic and lattice contributions respectively). Thus, the ZT of a material may be increased for higher Seebeck coefficients and conductivities, and lower thermal conductivity. A significant issue to deal with is that each of these terms are interrelated. Generally higher conductivities are followed by lower Seebeck coefficients and higher electronic contributions to the thermal conductivity. It is thus easy to recognize that a good

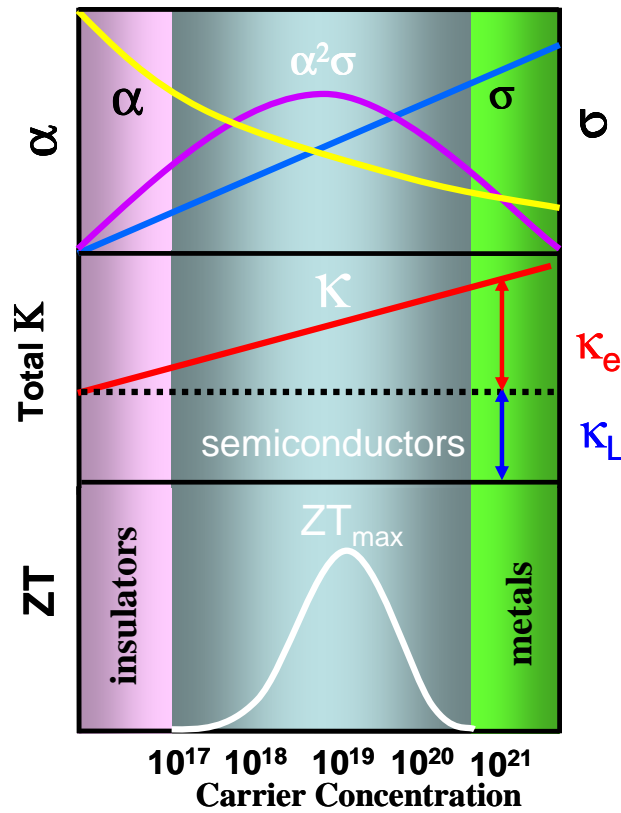


Figure 1.6 Relationships between the ZT, thermal conductivity (κ), electrical conductivity (σ) and Seebeck coefficient (α) for insulators, semiconductors and metals [22].

thermoelectric should have the properties of both metals and insulators, and are most commonly found as semiconductors, Fig 1.6. Current technologies require a $ZT > 1$ for the efficiencies and power conversion to be worthwhile [23]. However, these values are traditionally difficult to reach for many different types of materials, especially oxides [24].

1.5 Magnetic Properties

Magnetism is a phenomenon that has been known for hundreds of years. However the underlying principals have eluded researchers until recently. Iron and the mineral lodestone (magnetite or Fe_3O_4) are arguably the most well known examples of magnetic materials. In fact, Cleopatra was once said to have worn a lodestone around her head in order to prevent herself from normal aging, and Pliny the Elder (a Greek philosopher) had written of hills that attracted iron. These accounts are some of the first recognitions of magnetic phenomena, but many attribute the first true use of magnetism by the Chinese in primitive compasses where a splinter of lodestone floating on water was found to always point in a single direction, North [25].

Today, it is known that many of our luxuries are comprised of magnetic materials. This includes computer memories, TV's, medical equipments, generators, transformers, etc. Many of these inventions are recent ones and are such due to the complex and subtle nature of the phenomena; even today there is still a large effort to understand and discover novel materials with novel magnetic properties. Indeed, the many oxidation states of the transition metals make them suitable for research in magnetic oxide materials and will thus be the focus of this discussion.

1.5.1 Fundamentals of Magnetism

The magnetic properties of a magnetic material are largely dependent upon the materials interaction with an external applied field. The magnetic induction, or field

strength within the sample, is a function of the applied magnetic field (H) and the intensity of the magnetization (I),

$$B = H + 4\pi I$$

where I/H is the magnetic moment per unit volume and is referred to as the volume susceptibility (χ), an extrinsic property. Thus, permeability (μ) is defined as

$$\mu = \frac{B}{H} = 1 + 4\pi \frac{I}{H} = 1 + 4\pi\chi$$

In order to discuss the intrinsic magnetic properties of a magnetic material, the molar susceptibility, χ_m (units of μ_B), is used,

$$\chi_m = \chi \frac{Fw}{\rho}$$

where Fw is the formula weight and ρ is the density. In most cases, materials can be assigned to a specific group based on the behavior of the susceptibility as a function of temperature [26-28]

1.5.2 Magnetic Ordering

Generally speaking, magnetism is due to the magnetic moments associated with individual electrons with regards to spin and orbit. The pauli exclusion principle along with Hund's rule states that no two electrons can have the same quantum numbers (ie principle, azimuthal, magnetic and spin projection). So, for a specific orbital, there can only be two electrons, and when filled, only one electron may exist in the spin up or spin down orientation. When all of the electrons in orbitals are paired, the atom is

said to be diamagnetic. When placed in a magnetic field, the material shows a repulsive force, and because of this resistance towards the field, it shows a small and negative magnetization. Many ceramic materials that don't contain a transition metal or lanthanide are commonly found to be diamagnetic

When there are unpaired electrons, an atom is said to be paramagnetic. In the absence of a magnetic field, the magnetic moments point in random directions (Fig 1.7, column 1), and all of the moments cancel each other. However, the presence of a magnetic field causes some of the magnetic moments to align preferentially in the applied field direction, and thus enhances the magnetic flux density. This produces a net magnetic magnetization and results in a small and positive magnetic susceptibility. It should be noted that for paramagnetism, there is no reciprocal interaction between adjacent unpaired electrons. Because diamagnetic and paramagnetic materials show no net magnetization in the absence of a magnetic field, they are considered non-magnetic.

For some materials, the magnetic moments of distinct atoms or ions may be strongly correlated. Even in the absence of an applied field the moments spontaneously align parallel to one another in regions called domains. For a ferromagnetic material, the exchange interaction causes the electron spins to align in the same direction (Fig 1.7), but for an antiferromagnetic material spins align opposite one another, or an antiparallel.

The characteristic behavior of the magnetic susceptibility as a function of temperature can also be seen in Figure 1.7. Ferromagnetic and antiferromagnetic

materials exhibit a spontaneous alignment of spins at a certain critical temperature at which point the magnetic susceptibility shows a transition. At temperatures above this transition, the material is commonly paramagnetic. Because paramagnetic materials have weakly correlated electrons, they obey the Curie-Weiss law;

$$\chi_m = \frac{C}{(T + \theta)}$$

where C is the Curie constant and θ is the Weiss constant. When the Curie-Weiss law is obeyed, a plot of the inverse susceptibility as a function of temperature yields a straight line, and from this plot, the Curie constant (slope) and Weiss constant (x-intercept) can be extracted. This is necessary because valuable information regarding the majority interactions present in the material can be deduced. The magnitude of the moment can be determined by the Curie constant for a spin only approximation as

$$\mu = \sqrt{\frac{3kC}{N_A}} = 2.84 \sqrt{C} \mu_B$$

Where k is Boltzman's constant, N_A is Avagadro's Number, and μ_B is the Bohr magneton. The sign of the Weiss constant is an indication of the short range interactions between adjacent atoms. For adjacent atoms with independent spins (paramagnetism) the Weiss constant is zero. A negative Weiss constant indicates antiparallel spin alignment (antiferromagnetic), and a positive Weiss constant indicated parallel spin alignment (ferromagnetism). Figure 1.7 is a representation of


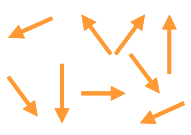
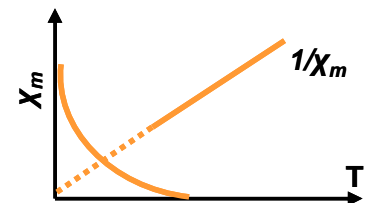
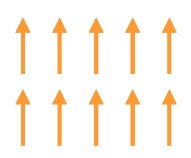
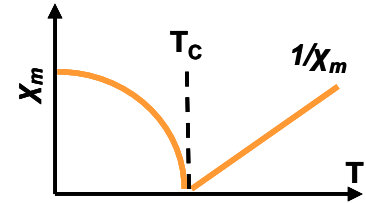
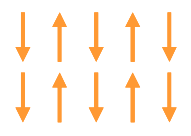
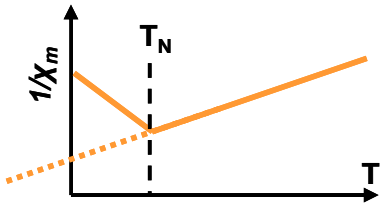
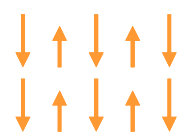
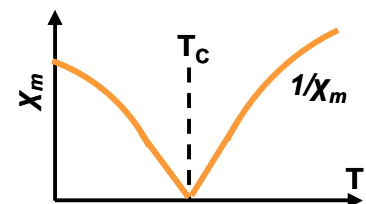
Classification & orientation of magnetic moments	Critical temperature	Magnitude of χ_m	Temperature dependence of χ_m
Diamagnetic	None	-10^{-6} to -10^{-5}	
Paramagnetic 	None	10^{-5} to 10^{-3}	
Ferromagnetic 	T_c Curie Temp. $\chi_m = C/(T - \theta)$	Large below T_c	
Anti - Ferromagnetic 	T_N Neel Temp. $\chi_m = C/(T \pm \theta)$	10^{-5} to 10^{-3}	
Ferrimagnetic 	T_c Curie Temp. $\chi_m \approx C/(T - \theta)$	Large below T_c	

Figure 1.7 Magnetic classifications for various types of magnetic interactions. Column one indicates the class type and corresponding spin orientation, while the remaining columns specify information regarding temperature dependence of the susceptibility or inverse susceptibility. Adapted from J.P. Jakybovics, J.P [29].

these types of behavior. Additional interactions may result in complex magnetic behaviors which do not follow these trends; spin-glass, superparamagnet, and ferrimagnetism to name a few [26-28].

1.5.3 Magnetic exchange

Magnetism in solids is quite complex, more so than in isolated systems due to the many possible interactions between atomic moments. As such, several types of exchange mechanisms have been realized to explain observations. When distances between atoms are small and there is significant overlap of orbitals, direct exchange is present. This exchange coupling is strong for smaller distances, but weakens rapidly as interatomic distances increase. Indirect exchange can occur when atomic moments couple over distances greater than atom-atom distances. Generally this occurs through an intermediary non-magnetic ion such as an anion in superexchange (notably in insulators), or through itinerant electrons in RKKY interactions (notably in metals).

Superexchange in oxides occurs through nonmagnetic oxygen anions, the strength of which depends on the distances between ions and the degree of overlap of the cation and anion orbitals, Figure 1.8. The most straightforward example is for rock salt or the ideal perovskite structure. In these structures, there is a 180 degree M-O-M angle in which magnetic moments on either side of the oxygen anion couple, usually anti-parallel. Due to the amount of overlap for Figure 1.9 shows the symmetry relationships for a ferromagnetic M-O-M interaction. Here the electron transfer, or partial covalence, is shown between the oxygen $p\sigma$ orbital and the metal e_g orbital of

principal overlap. The shaded d orbital of the second metal cation in (b) is a t_{2g} orbital, and the intra-atomic interaction between electrons in different orbitals of this second

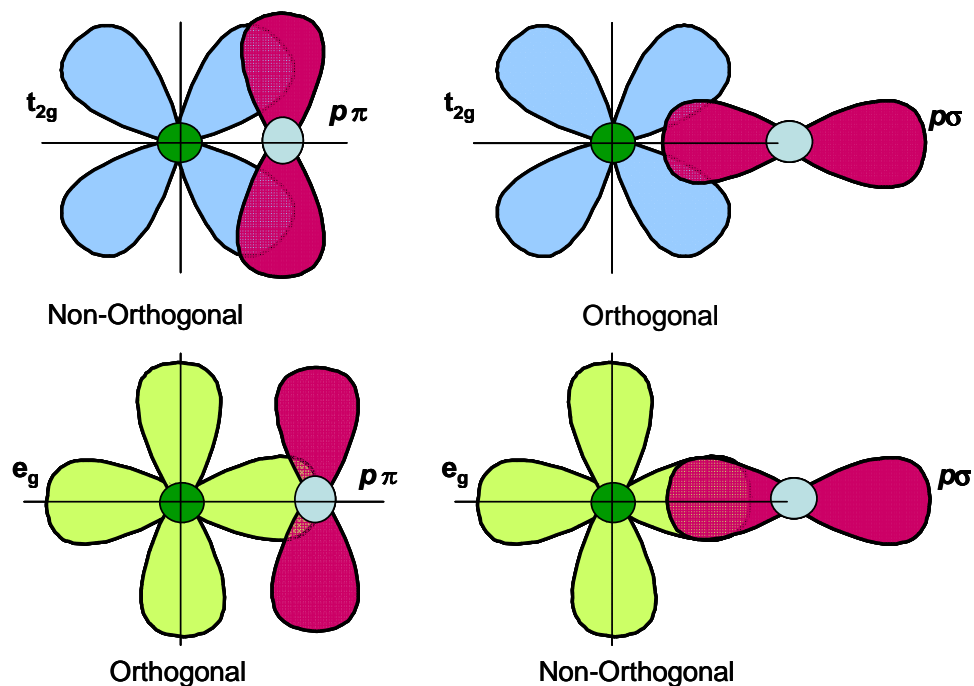


Figure 1.8 Degree of overlap for d -orbitals with oxygen $2P$ orbitals

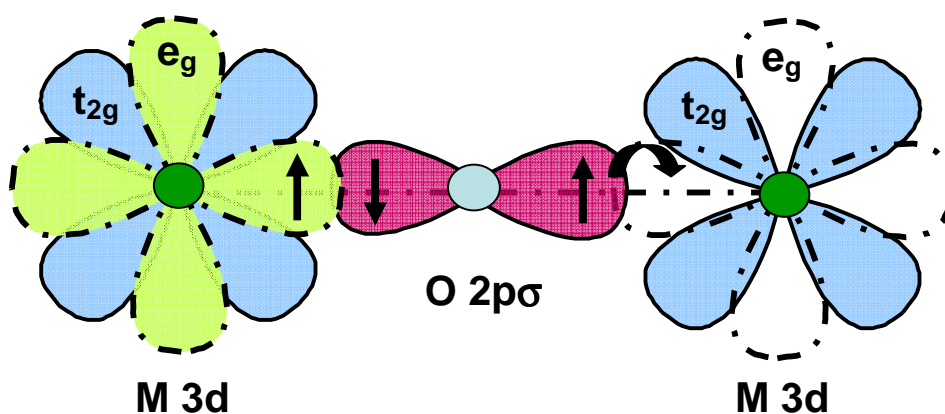


Figure 1.9 Schematic representation of the GK rules with a ferromagnetic interaction between one metal cation with a half-filled d orbital and the adjacent metal cation with an empty d orbital through an intervening oxygen ion in a 180° superexchange interaction.

metal cation would lead to a lower energy if the occupied t_{2g} orbital also has a spin-up electron.

Competing interactions (ferromagnetic or antiferromagnetic) between two magnetic cations and an intervening anion can be evaluated using the Goodenough-Kanamori (GK) rules [27, 30-32]. Their assessment of 180° M-O-M superexchange interactions concluded that the cation-anion orbital overlap is greater for the cation e_g orbitals than the cation t_{2g} orbitals due to covalency of the σ bonds [27]. Thus, the interactions between the e_g orbitals are stronger and tend to dominate the magnetic behavior. Based on these rules, it is generally understood that ferromagnetism is observed in oxides where interactions occur between empty or filled e_g orbitals and half filled e_g orbitals. Examples of this include $Ni^{2+} - O - Mn^{4+}$ or $Cr^{3+} - O - Fe^{3+}$. There are still unresolved observations for M-O-M interactions involving a 3d M-O-M 4d/5d. This will be of discussion in later chapters.

1.5.3 Multiferroics

For the information storage industry, magnetism has been utilized in several components of the traditional computer hard drive. These magnetic materials have a storied history and can be seen in some of the earliest computers where magnetoresistance was exploited to read data which was stored in magnetic domains. Miniaturized handheld memory devices and the exponential growth of storage capacity as a function of size are now staples of the information storage industry.

Despite modernization, current devices continue to utilize this mature field of study. Novel theories contend to capitalize on not only the charge (+ or -) of the electron, but also the spin (up or down), the result of which would be faster hard drive processing speeds (ie reading and writing of data) which translates to a larger storage capability for a given size. These devices are thus known as ‘spintronics’.

Spintronics in theory utilize multiferroism, a term referring to a material in which at least two of the properties, Ferromagnetism (FM), Ferroelectricity (FE), or Ferroelasticity (FElas) occur in the same phase. For coupling between the two order parameters FM and FE, also referred to as magnetoelectric multiferroics, a magnetic field can be used to induce an electric polarization or vice versa. It has become a hot topic for many industries with widespread potential applications raging from multiple state memory elements and ‘spintronics’, to current controlled magnetic valves and magnetic field sensors.

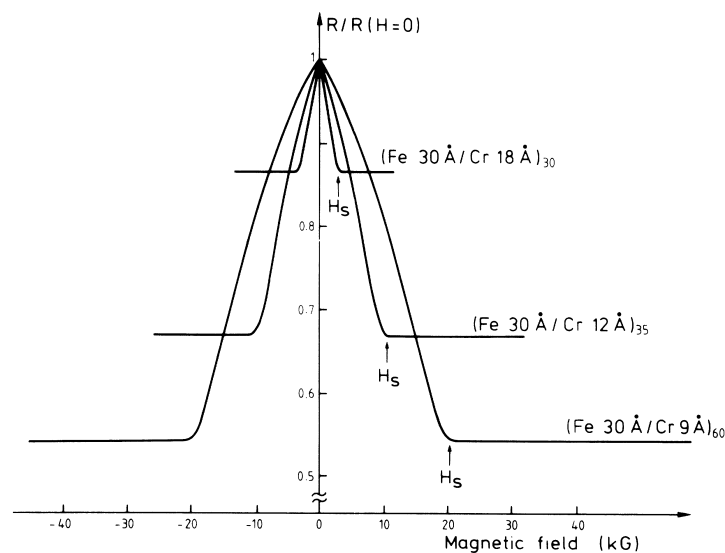


Figure 1.10 Giant magnetoresistance effect found in Fe-Cr layers (Baibich et al).

The discovery of GMR, giant magnetoresistance, in 1988 ushered in the spintronic era [34, 35]. GMR is an effect in which a magnetic material or magnetic composite (consisting of magnetic and non magnetic layers) experiences a large change in the electrical resistance as a function of varying applied magnetic fields, Figure 1.10 [36]. These materials were utilized by researchers at IBM in the read heads of hard drives. The result was a dramatic increase in the storage capacity. Current hard drives use spin valves, a similar design utilizing composite layers to switch magnetic layers by low applied fields, and thus causing large changes in the resistance.

The ordered double perovskite $\text{La}_2\text{Ni}^{2+}\text{Mn}^{4+}\text{O}_6$ was found to be a ferromagnetic and semiconducting at $T_c = 275$ K, the importance of which being the near room temperature transition [37-39]. This material has since become the foundation for the exploration of other semiconducting ferromagnets including $\text{La}_2\text{RhMnO}_6$ which has a $T_c = 150$ K [40]. Despite the lower Curie temperature, there is still much to learn about 3d and 4d or 5d transition metal double perovskites [40-42]. The focus of later chapters will be on the design and investigations of similar materials, including non perovskite type oxides for magnetodielectrics. This topic will be specifically discussed later.

1.6 References

1. J.B. Goodenough. *Prog. Solid State Chem.*, 5 (1971) 145
2. C.N.R. Rao, B. Reveau. *Transition Metal Oxides: Structure, Properties, and synthesis of Ceramic Oxides*, 2nd ed.; John Wiley & Sons: New York, 1998

3. J. B. Goodenough and J. M. Longo *Landolt-Bornstein, Group III, Vol. 4: Magnetic and Other Properties of Oxides and Related Compounds*, Springer-Verlag, New York (1970) p. 126
4. A.R. West. *Basic Solid State Chemistry*, 2nd ed.; John Wiley & Sons: New York, 1999
5. W. D. Kingery, H. K. Bowen, D. R. Uhlmann. *Introduction to Ceramics*, 2nd ed.; John Wiley & Sons: New York, 1976
6. R.C. Buchanan. *Ceramic Materials for Electronics: Processing, Properties, and Applications*, Marcel Dekker, Inc.: New York, 1986
7. G. Ellert. *The Physics Hypertextbook: Dielectrics*. N.p., Jan. 2010. Web. 23 Mar. 2010.
8. B. Jaffe, W.R. Cook, Jr., H. Jaffe. *Piezoelectric Ceramics*. Academic Press: New York, 1971
9. M.A. Subramanian, D. Li, N. Duan, B.A. Reisner, A.W. Sleight. *J. Solid State Chem.*, 151 (2000) 323
10. G. Chiodelli, V. Massarottie, D. Capsoni, M. Bini, C.B. Azzoni, M.C. Mozzati, P. Lupotto. *Solid State Commun.*, 132 (2004) 241
11. T.B. Adams, D.C. Sinclair, A.R. West, *Adv. Mater.*, 14 (18) (2002) 1321
12. A.P. Ramirez, M.A. Subramanian, M. Gardel, G. Blumberg, D. Li, T. Vogt, S.M. Shapiro. *Solid State Commun.*, 115 (2000) 217
13. C.C. Homes, T. Vogt, S.M. Shapiro, S. Wakimoto, A.P. Ramirez. *Science*, 293 (2001) 673
14. M.A. Subramanian, A.W. Sleight. *Solid State Sci.*, 4, 347 (2002)
15. L. Feng, X. Tang, Y. Yan, X. Chen, Z. Jiao, G. Cao, *Phys. Status Solidi Rapid Res. Lett.*, 203 (4) (2006) 22
16. R.K. Grubbs, E.L. Venturini, P.G. Clem, J.J. Richardson, B.A. Tuttle, G.A. Samara, *Phys. Rev. B* 72 (2005) 1
17. S.W. Choi, S.H. Hong, Y.M. Kim, *J. Am. Ceram. Soc.*, 90 (2007) 4009
18. SciFinder: Scholar. *Am. Chem. Soc.*, Web. 23 Mar. 2010

19. T.M. Tritt, M.A. Subramanian, *Mat. Res. Soc. Bul.*, 31 (2006) 188
20. T.M. Tritt. *Thermoelectric Materials: Principles, Structure, Properties, and Applications*. Encyclopedia of Materials: Science and Technology (2002) 1-11
21. S.O. Kasap, *Thermoelectric Effects in Metals: Thermocouples*. An e-booklet (1997-2001)
22. M.A. Subramanian, *personal communication*, November 2009
23. G.D. Mahan, J.O. Sofo, *Proc. Natl. Acad. Sci.* 19 (1996) 7436
24. T. He, J. Chen, T.G. Calvarese, M.A. Subramanian, *Solid State Sci.*, 8 (2006) 467
25. D.C. Mattis. *The Theory of Magnetism Made Simple*. World Scientific Publishing Co.: New York, 2006
26. P.W. Selwood. *Magnetochemistry*; Interscience Publishers, Inc.: New York, 1943
27. J.B. Goodenough. *Magnetism and the Chemical Bond*; John Wiley & Sons: New York, 1963
28. M.M. Schieber, *Experimental Magnetochemistry: Nonmetallic Magnetic Materials*; Interscience Publishers, John Wiley & Sons: New York, 1967
29. J.P. Jakubovics. *Magnetism and Magnetic Materials*, Institute of Metals: London, 1987
30. P.W. Anderson. *Phys. Rev.*, 79, 350 (1950)
31. J.B. Goodenough, A.L. Loeb. *Phys. Rev.*, 98 (1955) 391; J.B. Goodenough. *ibid.* 100 (1955) 564
32. J. Kanamori. *J. Phys. Chem. Solids*, 10 (1959) 87
33. G.E. Bacon. *Neutron Scattering in Chemistry*; Butterworths Inc.: Boston, 1977
34. R. Schad, C.D. Potter, P. Belien, G. Verbanck, V.V. Moschchalkov, Y. Bruynseraede. *Appl. Phys. Lett.*, 64 (1994) 3500
35. M.N. Baibich, J.M. Broto, A. Fert, F. Nguyen Van Dau, F. Petroff, P. Eitenne, G. Creuzet, A. Friederich, J. Chazelas. *Phys. Rev. Lett.*, 61 (1988) 2472

- 36. G. Binasch, P. Grunberg, F. Saurenbach, W. Zinn. *Phys. Rev. B*, 39 (1989) 4828
- 37. A. Wold, R.J. Arnott, J. B. Goodenough. *J. Appl. Phys.*, 29 (1958) 387
- 38. J.B. Goodenough, A. Wold, R.J. Arnott, N. Menyuk. *Phys. Rev.*, 124 (1961) 373
- 39. N.Y. Vasanthacharya, P. Ganguly, J.B. Goodenough, C.N.R. Rao. *J. Phys. C: Solid State Phys.*, 17 (1984) 2745
- 40. C. Schinzer, *J. Phys. Chem. Solids.*, 61 (2000) 1543.
- 41. G. Demazeau, B. Siberchicot, S.F. Matar, C. Gayet, A. Largeteau, *J. Appl. Phys.*, 75 (1994) 4617.
- 42. A.V. Powell, J.G. Gore, P.D. Battle, *J. Alloys Compd.*, 201 (1993) 73

Chapter 2

Experimental Methods of Analysis

For nearly all sciences and technologies, instrumental methods of analysis have been the primary means for acquiring useful and reliable information. The timeliness and quality of research done today is the result of the improved capabilities of instrumentation, specifically automations, resolution, simultaneous detections, lower limits of detection, and higher sensitivities [1]. Because scientists in every field of research base critical findings and important decisions on the acquired data, it is an obligation of the user to obtain a fundamental understanding of the instrumentation and applications in order to confidently apply their findings. It is for this reason that I feel a discussion of the instrumentation and methodology therein is necessary. This chapter serves as an introduction to the instrumentation and methodology used for characterization in this thesis.

Most solid state bulk inorganic chemists would agree that x-ray diffraction is an absolute necessity in their toy chest of instrumentation. However, since there is no single technique that can comprehensively characterize a sample, a series of analyses are often combined to provide a complete assessment. Generally most consider diffraction and spectroscopy as a main tool, but combine these with thermal analysis and physical property measurements to reinforce findings and fully characterize a material.

2.1 X-Ray Diffraction: MiniFlex II diffractometer

One of the most important tools for characterization in this thesis was X-ray powder diffraction. As in most chemistries concerning solids, a complete characterization requires an understanding of the materials crystal structure (unit cell parameters, atomic positions, etc.), impurities or defects (and quantity/location), size and shape of crystallites, and compositional inhomogeneities, if any. As mentioned earlier, several methods of analysis may need to be performed to obtain all of this information. X-ray diffraction, however, can offer a critical start in answering initial questions regarding structure.

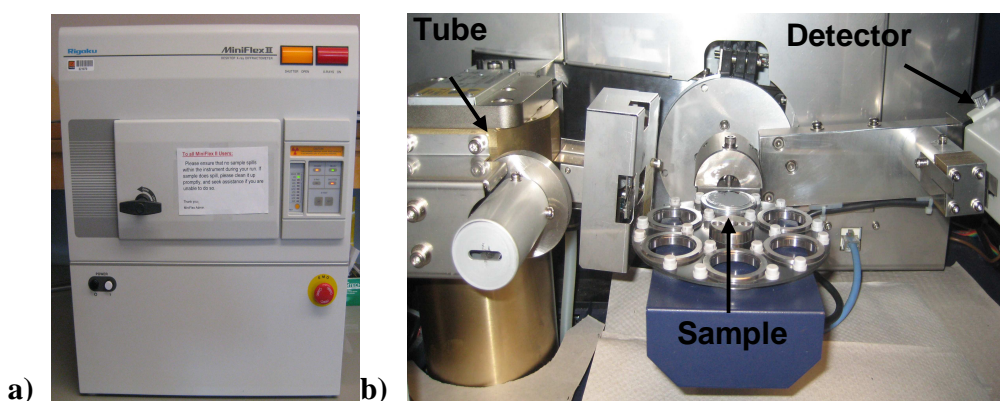


Figure 2.1 Rigaku MiniFlex II diffractometer (a) and the inner workings with x-ray tube, sample platform and detector labeled (b).

Nearly all of the diffraction patterns collected in this thesis were done so using the Rigaku MiniFlex II bench top diffractometer, Figure 2.1a and b. A beam of electrons is accelerated from a heated tungsten filament toward an anode through a large voltage ($V > 10\text{kV}$) and is directed toward a Copper metal target on the anode. X-rays are

generated from the striking incident electrons which ionize some of the Cu 1s electrons. The outer orbitals release an electron to occupy the 1s vacancy, and energy is given off from the transition as x-radiation which have a characteristic x-ray spectrum [2]. The x-rays are directed out a Be window toward the sample to be measured. Often times a Ni filter is used to absorb Kbeta peaks which are undesirable, however this instrument uses a graphite monochromator which has the same function. The MiniFlex II operates at fixed tube voltage of 30 kV and a fixed tube output current of 15 mA [3].

The characteristic $\text{CuK}\alpha$ ($\lambda = 1.5406 \text{ \AA}$) radiation is diffracted off the sample as shown in Figure 2.2 which shows the ideal behavior for the incident beam and the

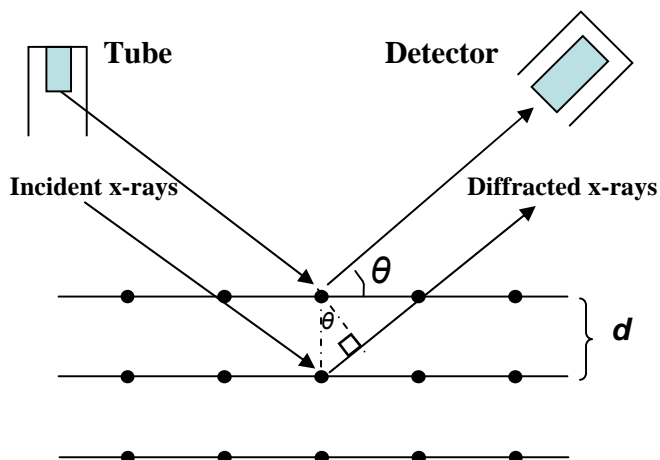


Figure 2.2 Bragg's Law reflection showing a generalized geometric relationship for an incident and diffracted beam.

geometric relationships. Bragg's law states that diffraction can occur whenever

$$n\lambda = 2 d \sin \theta$$

is satisfied. This is generally performed for powder diffraction by varying theta, θ , and fixing the wavelength, λ . In general, n (an integer) is the order of reflection, λ is the wavelength of the incident X-rays (1.54\AA for Cu $k\alpha$), d is the interplanar spacing and θ is the angle of incidence. The powder consists of small crystallites, or an assemblage of small crystallites, and the orientation is random such that some of these crystallites will diffract from the 111 plane, and others from the 110 plane for example. As a whole, all planes will be represented. Because Bragg's law has stringent conditions for a given crystal, the structural attributes of the material will diffract from characteristic planes giving unique intensities for specific 2θ values [2, 4].

The measurement conditions and sample preparation, however can greatly affect the intensity and shape of such peaks. If θ and λ are known, the d -spacing or distance between diffracting lattice planes, d , can be calculated. From these values, it is possible to calculate the lattice parameters and angles for the crystal structure. Likewise, if the lattice parameters and angles are known for a crystal system, it is possible to calculate where the characteristic diffraction lines should be present along 2θ . These relationships for this analysis are priceless when it comes to learning about the crystal systems of materials and in comparing theoretical to observed patterns. With an understanding of the structure, the physical properties can also be rationalized, and thus it is easy to realize the importance of this technique.

The Miniflex II (Figure 2.1a) utilizes either a 6-sample changer which rotates the sample during the measurement, or a single sample holder without rotation. Generally, the 6-sample changer is used for most fast scan measurements (scans where the 2θ

variation is $>2^\circ/\text{min}$) when phase identification is the only objective. However, for analysis of unit cell parameters and structural refinements, a slow scan is necessary. This means that the 2θ increment is small and is varied slowly allowing the intensity to reach its maximum, and the d-spacing to be more accurately determined. This affects the not only the peak shape which relates to the crystallite size and lattice strain, but also unit cell parameters which are dependant on d-spacing and 2θ position.

2.2 Dielectric: NorECs Probostat and LCR Meters

PPMS. Capacitance and loss tangent measurements were taken on HP 4275A and HP 4284 LCR meters using most often using a NorECs ProboStat setup. In order to form a parallel plate capacitor, electrodes were formed on the surfaces of the samples using a silver paint (in n-butyl acetate or terpinol). The Ag paint is cured at $\sim 90^\circ\text{C}$ for several hours. High temperature measurements require a higher

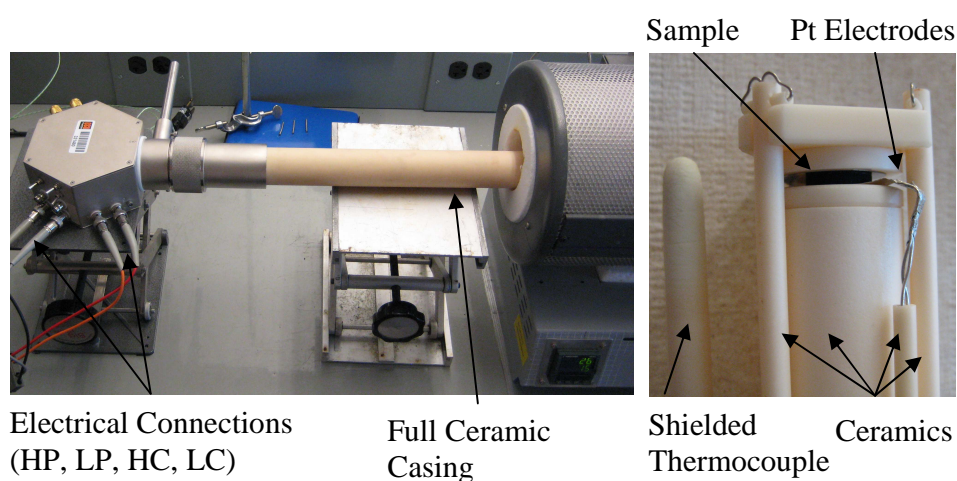


Figure 2.3 NorECs Probostat dielectric set-up used in high temperature capacitance measurements.

annealing temperature, generally within $\sim 100^\circ\text{C}$ of the final measurement temperature.

Before measurements, an open (air) and short (copper pellet) correction was performed to normalize the instrument to the approximate thickness of the samples.

Capacitance measurements were performed with a NorECs Probostat at fixed frequencies of 1, 10, 100, 500, 1000 kHz using the HP 4284 LCR meter, and frequencies from 1MHz -13 MHz were measured on the HP 4275A LCR meter. As needed, linear frequency sweeps were performed as well. The NorECs Probostat was used in the majority of high temperature capacitance measurements. Figure 2.3 shows the set up used.

2.3 Quantum Design Physical Property Measurement System

The Physical Property Measurement System (PPMS) is a versatile instrument built by Quantum Design, Figure 2.4. It operates on a multi system platform that allows for several measurements to be made (AC transport, DC resistivity, AC & DC magnetism), in a wide range of temperatures, with simple adjustments to the unit itself. Liquid helium is used as the cooling agent which allows temperature dependent measurements to be made from room temperature to ~ 3 K. The PPMS at Oregon State University is equipped with an EverCool liquid helium recycling system, which essentially allows the instrument to self replenish liquid helium lost during system venting and regular measurements by use of a condensing unit and external helium gas. This eliminates the need for regular liquid helium transfers.

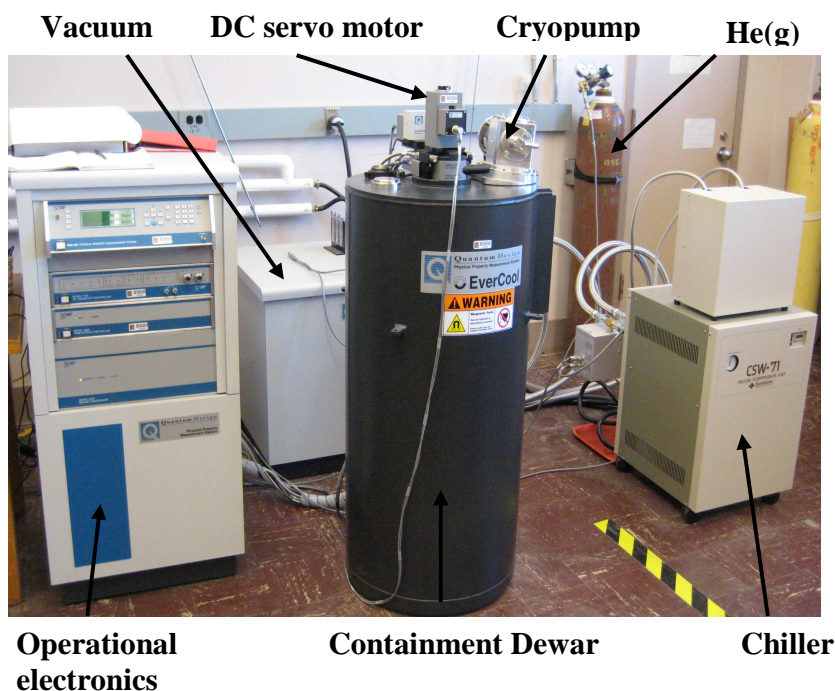


Figure 2.4 Quantum Design Physical Property Measurement System set up for ACMS measurements.

2.3.1 Magnetometry

The AC/DC Magnetometry System (ACMS) is an attachment of the PPMS which allows for AC susceptibility and DC magnetization. Most of the magnetic measurements performed in this thesis utilize a technique for DC measurements known as extraction magnetometry. The ACMS coil set, Figure 2.5, is inserted into the main dewar chamber, connected to the instrument via a 12-pin connector at the base of the sample chamber. The sample, loaded in a polycarbonate straw is vibrated vertically through the coil set by the DC servo motor. Sample preparation is an important aspect of the measurement process as the sample should not be

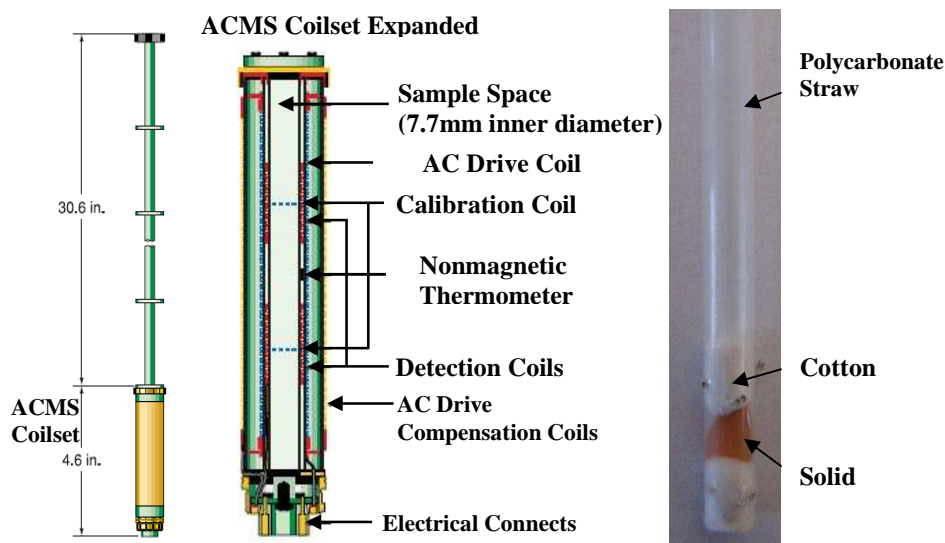


Figure 2.5 Representation of the ACMS coil set and tube assemblage (left), expanded view with labels of the ACMS coil set detection unit (center), and mounted ‘as prepared’ sample (right). ACMS coil set illustrations taken and modified from Quantum Design application notes [5]

allowed to move freely in the straw as it can affect the sample centering if the sample does not move according to the DC servo motor. Thus, the sample can be measured as a sintered mass or as a tightly packed powder. An applied field induces a magnetization in the sample that is detected by the ACMS coil set as an induced voltage. The amplitude of the voltage signal is thus related to the magnetic moment and the speed of vertical movement for a given extraction. Although automated, an important aspect of the measurement is the speed in which an extraction is made. A faster speed for an extraction generally results in enhanced signal strength and thus directly relates to the measurement accuracy. Equally important then is the samples location with respect to the detection coils. Thus, it is necessary to locate the sample using a single point DC extraction. This allows the instrument to correct for the

sample displacement when the DC servo motor is engaged. If the sample has not been centered, the operator runs the risk of inaccurate magnetization measurements. Generally the AC excitation location is more accurate as there is better resolution, but it is recommended to locate the sample using the method employed for actual measurements [5].

For DC magnetization measurements, an applied field is necessary. The PPMS at Oregon State University utilizes a superconducting magnet capable of magnetic fields as high as 7 Tesla, however an applied field of 0.1 – 1 Tesla is generally sufficient for temperature dependent measurements. It should be noted that if attempting to determine the effective moment, Curie constant and transition temperatures through the Curie-Weiss relationship, a sufficient temperature range above any transition temperature is required. This temperature range would be well into the paramagnetic region. Thus, it is necessary to have some insight into the potential magnetic interactions present for a sample, and may require several measurement runs to resolve temperature discrepancies.

2.3.2 Magnetocapacitance

A portion of this thesis is based on an interest in multiferroics and magnetodielectrics, thus involving the study of the interplay between electric and magnetic order parameters. The probe used, Figure 2.6, was designed and built at DuPont, and is used in coordination with a commercial PPMS. The probe is set up to measure 2 samples

simultaneously, but in most cases measurements were done on a single sample, Figure 2.6 c shows 2 samples. The coaxial wires are connected to copper posts soldered into

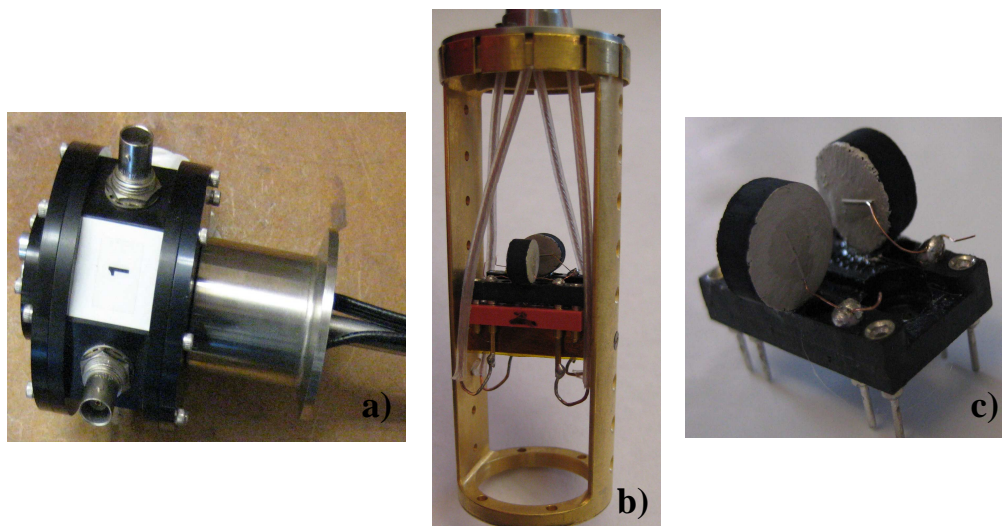


Figure 2.6 Representative views of the dielectric probe used in measuring the the capacitance of samples within the PPMS. The probe head and BNC connections (a), sample holder attachment console (b), and sample holder (c), are shown.

a stationary 14-pin IC socket. A removeable IC socket is used to make sample loading more efficient. Copper wires are connected to the electroded surfaces of the sample with addition Ag paint, and the sample is glued to the IC socket (pins in this area are removed from the IC socket). The wires are soldered to pins of the IC socket where pressure contact connections are made to the stationary IC socket. The probe, which is connected to an HP 4194A impedance analyzer, is inserted into the PPMS sample chamber. The PPMS is used for the temperature and magnetic field control, and the LCR meter is used to measure the dielectric properties. Generally, measurements are performed while warming through the magnetic ordering temperature. The data is normalized and assessed as a change in the capacitance in reference to a specific

temperature, usually well above the magnetic ordering temperature. A second measurement of field dependent capacitance is measured well below the magnetic ordering temperature. The magnetic field is varied while measuring the capacitance. The field variations effect of a magnetocapacitor would be an increase or decrease in capacitance. These values are generally normalized to the capacitance at 0 field for at a specific temperature.

2.3.3 DC Electrical Resistivity

Electrical transport is a very useful bulk physical property to measure in coordination with other analytical analysis as it is very sensitive to variations from structural distortions, bond angles and magnetic/structural transitions. This can give unique insight into the mechanisms present in various samples, especially when comparing a solid solution.

The PPMS can be easily set up to perform DC resistivity measurements. The resistivity puck shown in Figure 2.7 uses the same 12-pin connector at the base of the sample chamber as that used for a connection to the ACMS coil set mentioned previously. The PPMS resistivity puck is designed to measure four probe resistivity on 3 samples independently. Four probe resistivity is one of two general techniques used for measuring resistivity based on the resistivity of the sample. Normally the four probe technique is employed when the sample resistivity is $\rho < 10 \text{ } \Omega\text{-cm}$. This is necessary as the voltage leads and current leads are separated thus removing the

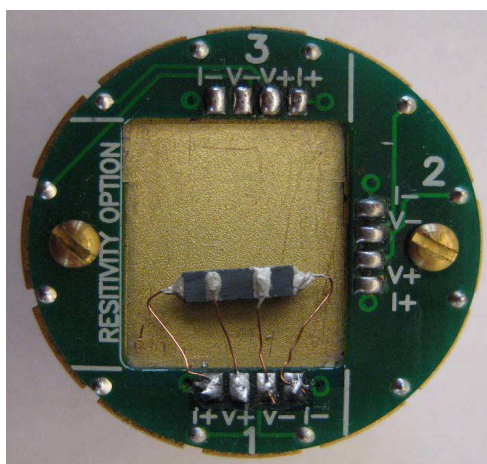


Figure 2.7 PPMS resistivity puck with a bar sample connected to position 1 using the four probe contact technique. Notice the labeled voltage and current contacts.

contribution of the lead wire and contact resistance. Samples with resistivities above $\rho = 10 \text{ } \Omega\text{-cm}$ can be measured by the two probe technique where the contact and lead wire resistance will not have much affect on the total resistivity. For samples measured in the PPMS, the four probe technique is the only option. As shown in Figure 2.7, four contact wires are attached to the sample bar of known dimension by means of silver paste or silver epoxy. When sample are irregularly shaped, or cannot be fashioned into bars, the van der Pauw method can be used in which there are no restrictions on the size or shape of the sample. In this work, however, all samples could be fashioned into bars for analysis.

2.4 Seebeck and Resistivity: ZEM-3 thermoanalyzer

Another important bulk property, especially for thermoelectrics, is the Seebeck coefficient, or thermoelectric power, α . Much like electrical resistivity, the Seebeck

coefficient is largely on the nature charge carriers. Thus, Seebeck measurements are useful in the determination of the majority contribution to the conduction process, where a positive Seebeck coefficient is the result of holes (p-type), and a negative Seebeck coefficient is the result of electrons (n-type). The Seebeck coefficients measured were done so using the ULVAC-RIKO ZEM-3 Thermoanalyzer, Figure 2.8 a and b. Figure 2.8a is a view of the main components consisting of a heater and water cooling unit which is generally flushed by He(g). This thermal chamber surrounds the sample and probe contacts shown in Figure 2.8b. The sample is

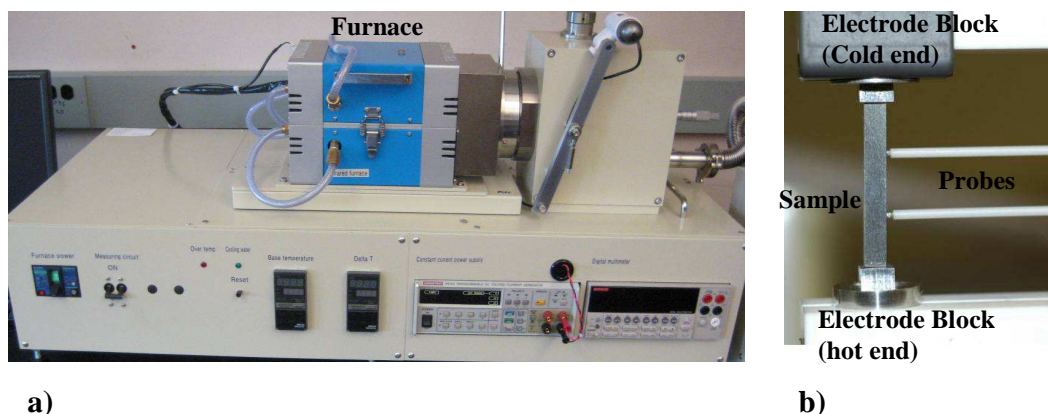


Figure 2.8 ZEM Thermoanalyzer (a) and mounted sample in the thermal chamber (b).

placed on the spring loaded electrode blocks (Ni contacts) which are then tightened against the sample. The electrode blocks are connected to a power supply which is used to generate the thermal gradient across the sample. The Pt probes are brought into contact with sample from the side. The voltage across the sample is measured through the probes (set at a standard distance of 3mm), and the difference in the voltage between the two probes, ΔV , is measured using a digital multi-meter. Point

temperature measurements are made using the two side probes as well. The measured temperature is an average of these two point measurements. Thus, the Seebeck coefficient can be measured as $\Delta V / \Delta T$. The sign of the Seebeck coefficient is determined by the charge flow for the thermal gradient. The cold end is then positive for holes and negative for electrons. An external thermocouple is used to measure the set furnace temperature of the thermal chamber [6]. In addition to Seebeck measurements, the electrical resistivity may also be simultaneously measured by the four probe method using the ZEM-3.

2.5 Optical Measurements

Optical properties of powder samples were measured in Dr. Janet Tate's lab in OSU Physics Department using either a W or Xe light source, or a fiber optic system characterized by diffuse reflectance in the UV-visible region. In the first setup, the diffuse reflectance spectra of powdered samples were collected in the range of 250 – 900 nm using W or Xe lamps, and a grating double monochromator. The spectrometer is calibrated from a He-Ne laser and known Xe source emission lines and position. The diffuse light reflected by the powders was collected with an integrating sphere and detected using a Si diode detector, Figure 2.9 (a) [7]. The data is then normalized to the signal obtained from MgO powder under the same conditions. The Kubelka-Munk function was used to convert reflectance data to a function of absorbance. The plotted absorbance as a function of electron volts, eV, or wavelength, nm, gives a characteristic pattern which is generally dependent on the electron occupation of

orbitals and can provide approximate band gap magnitudes. This can give a great deal of insight into the electronic properties and reinforce electrical resistivity assessments.

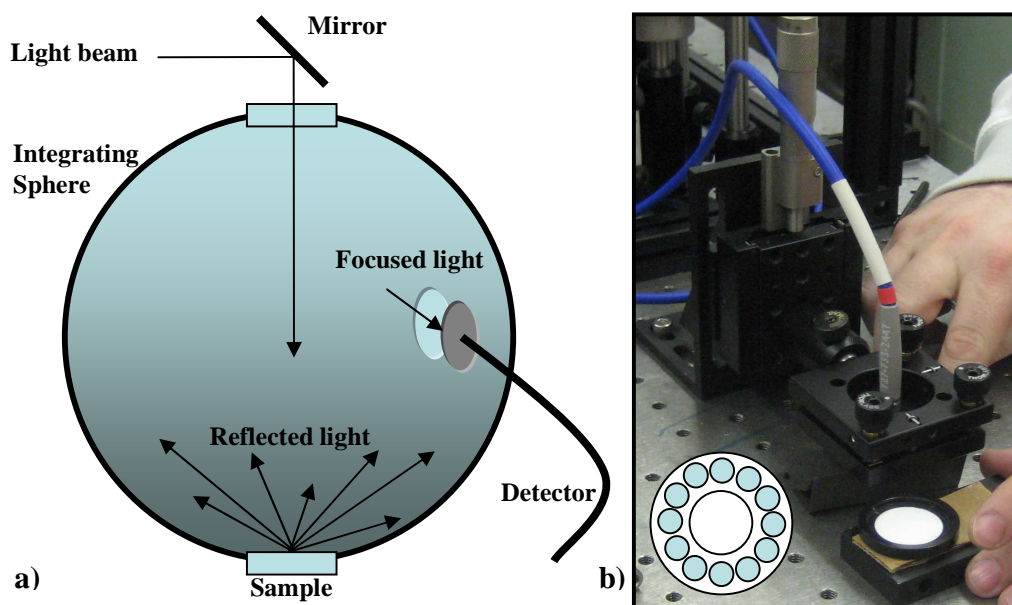


Figure 2.9 Illustration of an integrating sphere (a) and a fiber optic system (b) used in diffuse reflectance measurements (inset is an illustration of the end of a fiber optic cable). A standard sample of BaSO_4 can be seen, (b) bottom right.

In addition to the integrating sphere approach, there is also a common method of diffuse reflectance spectroscopy that utilizes fiber optic technology. In this method, light from a light source is passed through a bifurcated (Y-shaped) optical fiber assembly (Figure 2.9 (b) inset shows the end of such a wire with blue spheres as the light output), onto the sample, and back into the bifurcate optical fiber (Figure 2.9 (b) inset center white circle) where it is taken to a spectrophotometer [8]. MgO or BaSO_4 is often used a light reference and is also used to coat the inside of the integrating spheres. Samples of $\text{YIn}_{1-x}\text{Mn}_x\text{O}_3$ were measured by the first method, and all other

samples were measured by the second method. A test was performed to compare the two methods which proved to be quite similar.

2.6 Thermogravimetric Analysis

Thermogravimetric analysis (TGA) is an analytical tool often used in researching the characteristics of polymers, including degradation temperatures and/or the evaporation of residual or absorbed moisture. It can thus be used in the determination of organic components in inorganic systems such as hydroxyl or carbonate groups as these may be volatile fractions within the sample. The instrument used in this work was a Metler Toledo TGA 850. Generally, a small mass of powder samples (~10-30 mg) are put in a small pre-dried crucible and placed on a platinum pan which is attached to a high precision balance. The sample's mass is constantly weighed as the sample is heated at a standard rate in a selected atmosphere. The resulting data can then be plotted as a weight percent or mass loss versus temperature [2].

2.7 References

1. B. Lamp. "Instrumental Analysis." Truman State University.
http://www2.truman.edu/~blamp/chem322/pdf/chapter%201%20_9-3%20corrections_.pdf. Accessed May 2010.
2. A.R. West. *Basic Solid State Chemistry*, 2nd ed.; John Wiley & Sons: New York, 1999

3. Rigaku Corporation. *X-Ray Diffractometer MiniFlexx II Instruction Manual*, 2nd ed.; Rigaku Corporation, 2006
4. B.D. Cullity, S.R. Stock. *Elements of X-Ray Diffraction*, 3rd ed.; Prentice Hall; New Jersey, 2001.
5. Quantum Design. *Physical Property Measurement System Hardware and Operations Manual*, 2nd Ed.; Quantum Design, 1999
6. ULVAC-RIKO, Inc. *Model ZEM-3 Thermoanalyzer: Power Conversion Efficiency Measuring Instrument Instruction Manual*.
7. R. Kykyneshi. M.S. Thesis, Oregon State University, Corvallis, OR, 2004
8. Ocean Optics, Inc. "We Make A Fiber For That!" Ocean Optics, Inc.
<http://www.oceanoptics.com/Products/opticalfibers.asp>. Accessed May 2010

Chapter 3

Structure and Physical Properties of Rhodium Based Perovskites

3.1 Abstract

Epitaxial $\text{LaRh}_{1/2}\text{Mn}_{1/2}\text{O}_3$ thin films have been grown on (001)-oriented LaAlO_3 and SrTiO_3 substrates using pulsed laser deposition. The optimized thin film samples are semiconducting and ferromagnetic with a Curie temperature close to 100 K, a coercive field of 1200 Oe, and a saturation magnetization of $1.7 \mu_B$ per formula unit. The surface texture, structural, electrical, and magnetic properties of $\text{LaRh}_{1/2}\text{Mn}_{1/2}\text{O}_3$ was examined as a function of the oxygen concentration during deposition. While an elevated oxygen concentration yields thin films with optimal magnetic properties, slightly lower oxygen concentrations result in thin films with improved texture and crystallinity.

The compositions $\text{La}_2\text{FeRhO}_6$, $\text{La}_2\text{CrRhO}_6$, $\text{La}_2\text{CuRhO}_6$ were prepared for the first time, and their electrical and magnetic properties were determined. Known $\text{La}_2\text{MnRhO}_6$, $\text{La}_2\text{CoRhO}_6$, and $\text{La}_2\text{NiRhO}_6$ were also prepared and their properties determined for comparison. All six phases have the orthorhombic perovskite structure. Electrical resistivity measurements as a function of temperature indicate that all phases are semiconducting. Seebeck measurements show that all are p-type conductors. Magnetic measurements indicate generally antiferromagnetic interactions for all compositions, although evidence for weak ferromagnetism is found in the case of $\text{La}_2\text{CrRhO}_6$ and $\text{La}_2\text{FeRhO}_6$. The oxidation state of M appears to be close to 3+ for

Fe and Cr, and a mixture of 2+/3+ for Cu. A favorable combination of electrical conductivity and Seebeck coefficient results in a relatively high thermoelectric power (1.11 W/m-K² at ~575K) factor for La₂CuRhO₆.

The full LaCo_{1-x}Rh_xO₃ solid solution was investigated utilizing structural, electrical transport, magnetic, and thermal conductivity characterization. Strong evidence for at least some conversion of Rh³⁺/Co³⁺ to Rh⁴⁺/Co²⁺ is found in both structural and electrical transport data. The crystal structure is that of a rhombohedrally distorted perovskite over the range $0.0 \leq x \leq 0.1$. The common orthorhombic distortion of the perovskite structure is found over the range $0.2 \leq x \leq 1.0$. A crossover of all three orthorhombic cell edges occurs at $x = 0.5$ giving the appearance of a cubic structure, which actually remains orthorhombic. The octahedra in the orthorhombic structure must be distorted for x values less than 0.5, and the observed distortion suggests orbital ordering for Co²⁺. Electrical resistivity measurements as a function of temperature show semiconducting-like regions for all compositions. There is a steady increase in electrical resistivity as the Rh content increases. Large positive thermopower values are generally obtained above 475 K. With increasing Rh substitution there is a decrease in thermal conductivity, which slowly rises with increasing temperature due to increased electrical conductivity. The electronic part of the thermal conductivity is suppressed significantly upon Rh substitution. A thermoelectric figure-of-merit (ZT) of about 0.075 has been achieved for LaCo_{0.5}Rh_{0.5}O₃ at 775 K, and is expected to reach 0.15 at 1000 K.

Publications based on this chapter:

- 1) Sheets, W.C., Smith, A.E., Subramanian, M.A., Prellier, W., Effect of oxygen concentration on the structural and magnetic properties of $\text{LaRh}_{0.5}\text{Mn}_{0.5}\text{O}_3$ thin films. *Journal of Applied Physics*, 105 (2009) 023915
- 2) Smith, Andrew E., Sleight, Arthur W., Subramanian, M. A., Electrical and magnetic properties of new rhodium perovskites: La_2MRhO_6 , M = Cr, Fe, Cu. *Materials Research Bulletin*, 45 (4) (2010) 460-463
- 3) Li, J., Smith, Andrew E., Kwong, K.-S., Powell, C., Sleight, A. W., Subramanian, M. A. Lattice crossover and mixed valency in the $\text{LaCo}_{1-x}\text{Rh}_x\text{O}_3$ solid solution. *Journal of Solid State Chemistry*, (In press: doi:10.1016/j.jssc.2010.04.021) (2010)
- 4) Kwong, Kyei-Sing, Smith, Andrew E., Subramanian, M. A. The effect of Rh and Sr substitution on the thermoelectric performance of LaCoO_3 . *Materials Research Society Symposium DD: Thermoelectric Materials*, (In press: vol. 1267) (2010)

3.2 Introduction

For most ternary oxides with the composition AMO_3 , the perovskite structure is observed. The structural atomic arrangement was first reported upon the discovery and investigation of the mineral CaTiO_3 in 1839 by Gustav Rose. Rose was a chemist on an expedition in the Ural mountains (Russia) who named the material's structural class after an influential Russian aristocrat, Lev Alexeievitch Perovsky (1792-1856). Thereafter, many materials were found adopting similar crystal structures. The term 'perovskite' was then used to categorize this large class of materials [1-2].

The vast number of compounds in the perovskite class is due to the extreme flexibility of the structure. When both charge and ionic radii are considered, the perovskite structure can accommodate nearly every member of the periodic table (excluding halogens, beryllium, phosphorus, and from atomic number 94 on) [3]. Thus, it's relatively easy to conceive that extensive studies have yielded many interesting and unique properties in perovskite systems. For example, perovskites have been found to exhibit ferroelectric and dielectric (BaTiO_3), colossal dielectric ($\text{CaCu}_3\text{Ti}_4\text{O}_{12}$), piezoelectric ($\text{PbZr}_{1-x}\text{Ti}_x\text{O}_3$), magnetoresistance ($\text{Ln}_{1-x}\text{A}^{2+}_x\text{MnO}_3$), ferromagnetism ($\text{La}_2\text{NiMnO}_6$), fluorescence ($\text{Cr}^{3+}:\text{LaAlO}_3$), superconductivity ($\text{BaPb}_{1-x}\text{Bi}_x\text{O}_3$), and electro optical ($\text{KTa}_{0.65}\text{Nb}_{0.35}\text{O}_3$) behavior [4-9]. In addition, subtle distortions of bonds, bond angles, and coordination environments affect the bond overlap, and band energy levels which also contribute to the unique properties observed.

To help understand later discussion, a short review is warranted. The ideal perovskite structure has the AMX_3 formula, where A and M are cations and X is an anion. Since this work refers mainly to oxides, we will only discuss the AMO_3 and similar formulas. As mentioned previously, the A and B cations can vary greatly which means many cation charges are possible. Several combinations of these charges are observed such as $A = 1+, 2+, 3+$ and $M = 2+, 3+, 4+, 5+$. Generally, the traditional observation of the ideal perovskite lattice is that the A cation is large and in a dodecahedral coordination with oxygen, and the M cation is smaller and in an octahedral coordination with oxygen. The ideal perovskite unit cell is shown in Figure 3.1 with the A cation centered (a) and M cation centered (b). It has a cubic symmetry

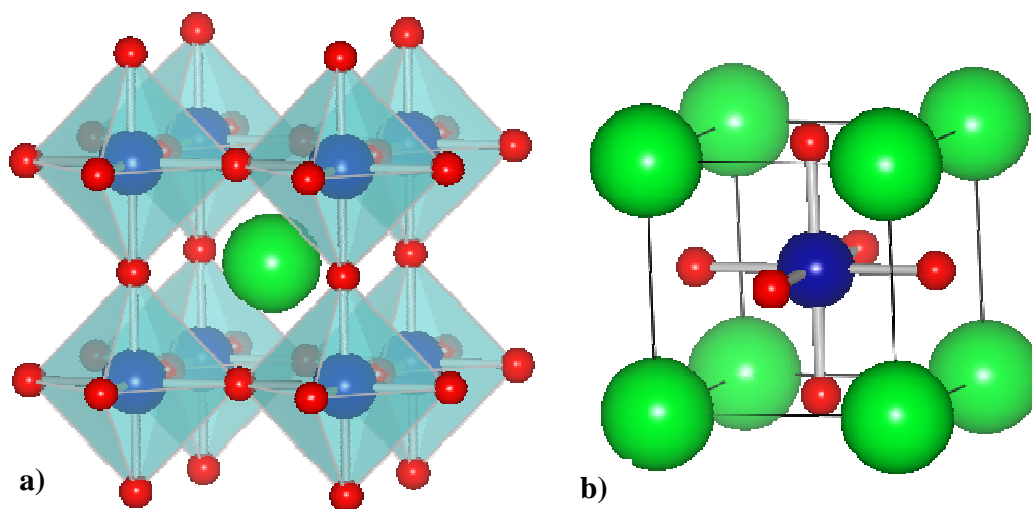


Figure 3.1 Common representations of the AMO_3 perovskite structure as (a) A-cation, green spheres, centered with MO_6 octahedra, M-blue and O-red, on cell corners, and (right) MO_6 octahedra centered with A cations on corners

with space group $pm-3m$. The corner shared MO_6 octahedra have M-O-M bond angles of 180° and O-M-O bond angles of 90° [3, 4, 6].

To address the site size limitations of the perovskite, Goldschmidt defined a tolerance factor, t [10]. The ideal cubic perovskite structure is such that $(r_A + r_O) = \sqrt{2}(r_M + r_O)$, Where r_A , r_M and r_O are the radii of the A cation, M cation, and O anion, respectively. The size requirements for stability of the cubic structure are relatively strict so when a size mismatch occurs between A and M cations, several distortions are possible, such as the tilting of octahedra, or deformity of the octahedra, or cation offset. Thus, for the tolerance factor, $t = (r_A + r_O)/[\sqrt{2}(r_M + r_O)]$ where ideal is unity, or 1, deviations have values that are greater or less than unity. For the most part, the tolerance factor provides an idea of what symmetry may be observed at room temperature and atmospheric pressure, but it is not unambiguous. Several other factors play a large role in determining the structural symmetry such as covalency, lone-pairs, or Jahn-Teller effects, and this is why the cubic pm-3m space group can be observed for tolerance factors of $0.81 \leq t \leq 1.11$ [3].

In general, octahedral rotations occur due to the size of the A cation in a position too large for it. It happens that the A site is generally too large for most of the lanthanides and thus, the most common symmetry of the LnMO_3 class, and the perovskite class in general, is the orthorhombic space group Pnma or Pbnm, (figures will be provided within sections). The materials discussed in this chapter tend towards an orthorhombic symmetry.

3.3 Effect of Oxygen Concentration on the Structure and Magneto-Electric Properties of $\text{LaRh}_{1/2}\text{Mn}_{1/2}\text{O}_3$ Thin Films

3.3.1 Introduction

The mixed M -site perovskites of composition $\text{La}M_{1/2}\text{Mn}_{1/2}\text{O}_3$ have received renewed attention recently owing to their coexisting ferromagnetic and semiconducting/insulating properties [11-25]. Remarkable near room temperature ferromagnetic transition temperatures of 280 and 230 K have been reported for both bulk and thin film samples of $\text{La}_2\text{NiMnO}_6$ (LNMO) [11, 26] and $\text{La}_2\text{CoMnO}_6$ (LCMO) [12, 27] perovskites, respectively. In thin film form, such ferromagnetic semiconductors have potential applications in next-generation spintronic devices, including spin-based transistors and advanced magnetic memory storage elements [28]. The structural and valence orderings of the transition metal cations on the B -site plays a vital role in determining the magnetic properties of the samples. In ordered samples it is expected that the empty e_g orbitals of Mn^{4+} interacts with the half-filled e_g orbitals of M^{2+} ($M = \text{Co}, \text{Ni}$) through a $\sim 180^\circ$ $\text{Mn}^{4+}\text{--O--}M^{2+}$ Goodenough–Kanamori interaction, resulting in a ferromagnetic coupling. A decrease in order on the M -site, however, reduces the magnetic phase transition temperature by increasing the number of antiferromagnetic interactions. The composition of the M -site cations in, $\text{La}M_{1/2}M'_{1/2}\text{O}_3$ perovskites is not limited to third row transition metals, and, indeed, studies of bulk $\text{LaRh}_{1-x}M_x\text{O}_3$ [29-33] and $\text{LaIr}_{1-x}M_x\text{O}_3$ ($M = \text{Mn}, \text{Fe}, \text{or Ni}$) [34, 35] samples have been reported previously.

While high-spin configurations are anticipated for first row ($3d$) transition metals, a low-spin configuration is preferred for second ($4d$) and third row ($5d$) transition metals, owing to the increased splitting energy between the e_g and t_{2g} orbitals. In order to obtain a strong ferromagnetic virtual spin-spin superexchange interaction with heavier transition metal cations, such as Rh^{4+} or Ir^{4+} possessing empty e_g orbitals, a complimentary high-spin first row transition cation with a partially filled e_g orbital is required on the M -site (e.g., Mn^{2+} , Fe^{2+} , or Ni^{2+}). In this letter, we investigate the thin film deposition of $\text{LaRh}_{1/2}\text{Mn}_{1/2}\text{O}_3$ (LRMO) and examine how its structure, morphology, and magnetic properties are altered by adjusting the oxygen background pressure during deposition.

Numerous studies have examined the structural and magnetic properties of $\text{LaM}_{1/2}\text{Mn}_{1/2}\text{O}_3$ samples to understand their local ordering on the M -site sublattice, or lack thereof. In particular, two different types of ordering are possible: the atomic (i.e., rocksalt, random, or a mixture of each) and oxidation state order of the transition metals (i.e., M^{2+}/Mn^{4+} or M^{3+}/Mn^{3+}). Although a degree of mixed valency always can be anticipated, there has been disagreement over the predominant cation oxidation states. For example, three independent neutron diffraction studies report different manganese and nickel oxidation states in LNMO samples. Blasco et al. [36] and Rogado et al. [26] reported the presence of Ni^{2+} and Mn^{4+} cations, whereas Bull et al. [37] conclude that Ni^{3+} and Mn^{3+} are present. More recently, data from electron energy loss spectroscopy measurements, Raman scattering, and X-ray photoelectron spectroscopy indicate Ni^{2+} and Mn^{4+} to be the prevalent oxidation states in LNMO

thin films[34]. However, the authors also observed an increase in charge disproportionation of Ni^{2+} and Mn^{4+} to Ni^{3+} and Mn^{3+} when decreasing the oxygen background pressure during film deposition. Similar to LNMO, an ideal $\text{Rh}^{4+}/\text{Mn}^{2+}$ charge distribution cannot be assumed for LRMO films, owing to the similar stabilities of tetravalent (Rh^{4+}) and trivalent (Rh^{3+}) rhodium oxidation states. Schnizer [33] proposed a $\text{Rh}^{4+}/\text{Mn}^{2+}$ charge distribution because no structural distortion from Mn^{3+} , a $3d^4$ high-spin ion exhibiting a strong Jahn–Teller effect, was evident in the Rietveld refinement. On the other hand, Haque and Kamegashira suggested $\text{Rh}^{3+}/\text{Mn}^{3+}$ valence states since the observed effective magnetic moments derived from the magnetic states of $\text{LaRh}_{1/2}\text{Mn}_{1/2}\text{O}_3$ in the paramagnetic region are near to the spin-only values of this combination.

In terms of the atomic order, the majority of studies conclude that a large amount of local rocksalt ordering occurs on the B-site sublattice, but not across a long-range scale. Indeed, all of the aforementioned neutron diffraction studies of bulk LNMO provide evidence for a locally ordered Ni/Mn atomic arrangement [26, 36, 37]. Refinements of these neutron diffraction studies, however, also suggest the presence of antisite defects (i.e., Ni and Mn atoms are not ordered perfectly) within the ordered *M*-site sublattice, which when accounted for improve the refinement of the data. Data from polarized Raman spectra and measurement of saturation magnetization values near the theoretical maxima in LCMO and LNMO thin films corroborate that a large amount of cation ordering exists in such samples [11, 12, 20, 21]. On a smaller scale, selected area electron diffraction reveals a majority *I*-centered phase coexisting with

domains of a minority *P*-type phase, the latter which is dispersed throughout the *I*-type matrix [17, 24]. The presence of the mirror plane *a* in the *I*-type phase and the numerous orientations observed for the *P*-type nanodomains argues against the complete long-range ordering of the Ni/Mn sublattice. In bulk $\text{LaRh}_{1/2}\text{Mn}_{1/2}\text{O}_3$ samples, no evidence for long-range ordering was observed in Rietveld refinements of x-ray diffraction (XRD) patterns [23]. However, their magnetic properties indicate at least a partially ordered arrangement of the Rh/Mn cations exists, enabling ferromagnetic spin-spin superexchange interactions.

3.3.2 Thin Film Deposition

Although samples of LRMO have been examined in the bulk, thin film samples have not been fabricated or studied. Multiple thin films were grown on both the (001)-oriented LaAlO_3 (LAO) and SrTiO_3 (STO) substrates. Stoichiometric $\text{LaRh}_{1/2}\text{Mn}_{1/2}\text{O}_3$ was employed as a target, which was synthesized by conventional solid state methods. The films were deposited between 650–750°C by the PLD technique using a KrF excimer laser (248 nm, 3 Hz) at different (10–800 mTorr) atmospheres of flowing oxygen under dynamic vacuum. On average, 5000 pulses yielded films with a thickness of 100–150 nm, depending on the oxygen background pressure. The crystalline structure of the thin film samples was examined by XRD using a Seifert 3000P diffractometer ($\text{Cu } K\alpha$, $\lambda \text{ \AA} = 1.5406$). A Philips X'Pert diffractometer was used for the in-plane XRD measurements of the film samples. Figure 1a shows the XRD θ - 2θ pattern for a LRMO film grown on LAO at 720 °C and 300 mTorr oxygen

pressure. The peaks were indexed based on a pseudocubic unit cell and only the peaks corresponding $(00l)$ reflections (where $l = 1, 2, 3, \dots$) were observed, which indicates that the out-of-plane lattice parameters is a multiple of the perovskite subcell parameter ($a_{\text{sub}} \text{ \AA} = 3.93$). The absence of diffraction peaks from secondary phases or randomly orientated grains evidences the preferential orientation of the films. The full widths at half maximum (FWHMs) is 0.072° for the (002) reflection of LRMO (inset of Fig. 3.2), as measured by XRD rocking-curve analysis (ω -scan), and when

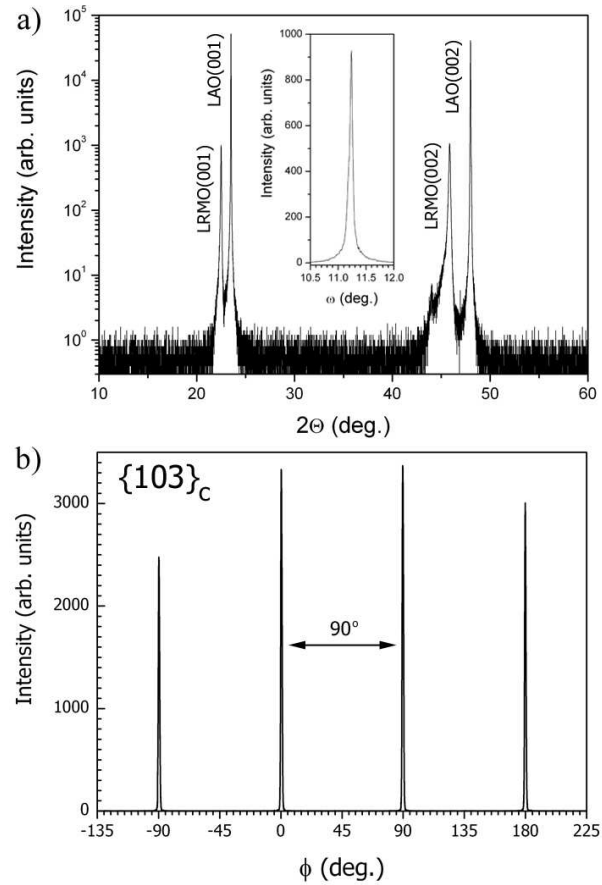


Figure 3.2 XRD θ - 2θ scan curve of a typical LRMO film grown on LAO substrate. The substrate $(00l)$ are marked in the figures. The inset shows a rocking curve recorded around the 001 reflection of the film.

compared to the FWHM of 0.06° measured for the LaAlO_3 substrate evidences the high quality of the thin film sample. The in-plane orientation, as evaluated by the XRD Φ -scan of the LRMO (103) reflection of the cubic subcell [Fig. 3.2 b], shows four peaks separated by 90° revealing the fourfold symmetry and indicating that the LRMO film is epitaxial with respect to the substrate. A large degree of in-plane texture $\text{FWHM}_\Phi = 0.9^\circ$ is observed for the films grown on LAO(001).

The out-of-plane lattice parameter c and defect structure of LRMO films on STO(001) and LAO(001) substrates varies as a function of the oxygen pressure present during deposition. As shown in Fig. 3.3, films deposited at lower oxygen

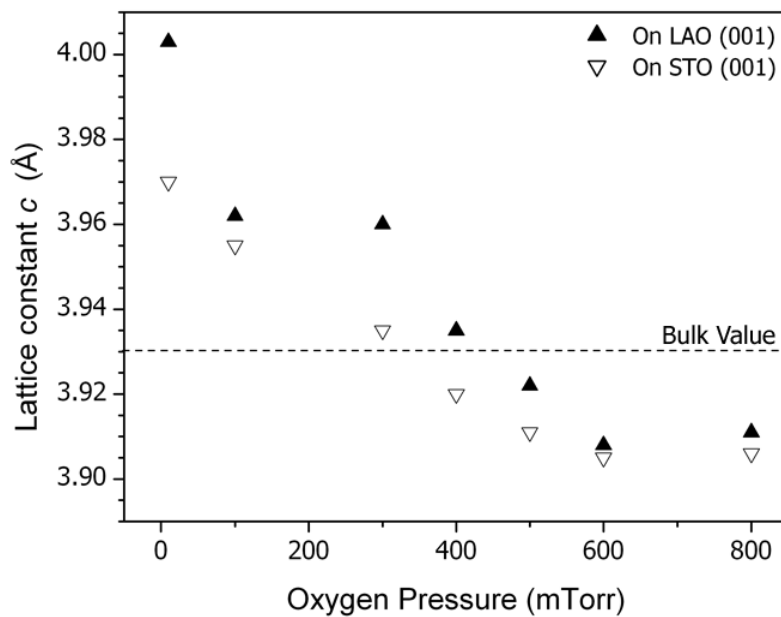


Figure 3.3 A plot of the out-of-plane c -axis lattice parameter of LRMO thin films grown on STO and LAO substrates as a function of the oxygen background pressure during growth.

pressure have an expanded lattice parameter c when compared to the pseudocubic bulk value (3.93 Å), and increasing the oxygen pressure steadily decreases the lattice

parameter c , which eventually becomes less than that of the bulk value. Previous studies of other perovskite thin films have attributed this lattice expansion at lower oxygen pressures to an increase in the defect concentration [22, 24]. Two mechanisms have been proposed to account for such an increase at lower oxygen pressures, (i) oxygen vacancies caused by the lack of oxygen present during deposition and (ii) lattice damage resulting from the increase in flux and energy of species colliding with the surface of the growing film. Studies comparing the growth of LNMO films in 50 mTorr oxygen and a 50 mTorr Ar/O₂ (10/1 ratio) mixture indicate that the latter defect type dominates [24]. The increased out-of-plane lattice parameter c observed in the present study most likely have the same origin—films grown at lower oxygen pressure having a greater defect concentration and lattice disorder owing to the increased surface bombardment by high energy species during growth. As summarized previously, this defect structure is especially important in mixed B -site perovskite films owing to the high degree of lattice order required to optimize their magnetic properties.

3.3.3 Results and Discussion

Scanning electron microscopy (SEM) and atomic force microscopy (AFM) images confirm the successful manipulation of LRMO film microstructure by altering the oxygen pressure during deposition (Fig. 3.4). Two samples were selected based upon either their optimized crystallinity (300 mTorr) or magnetic properties (800 mTorr). As shown in Fig. 3.4 b, SEM images of LRMO films grown at higher oxygen pressure

(800 mTorr) reveal the films are composed of relatively small, discrete grains. A layer of particles, which appear to be clusters of nanoparticles ~ 100 nm in diameter, is clearly visible with a single grain overgrowth. In contrast, at lower oxygen pressures (300 mTorr) the underlying films appear smooth and featureless by SEM (i.e., no observable grains at the maximum magnification).

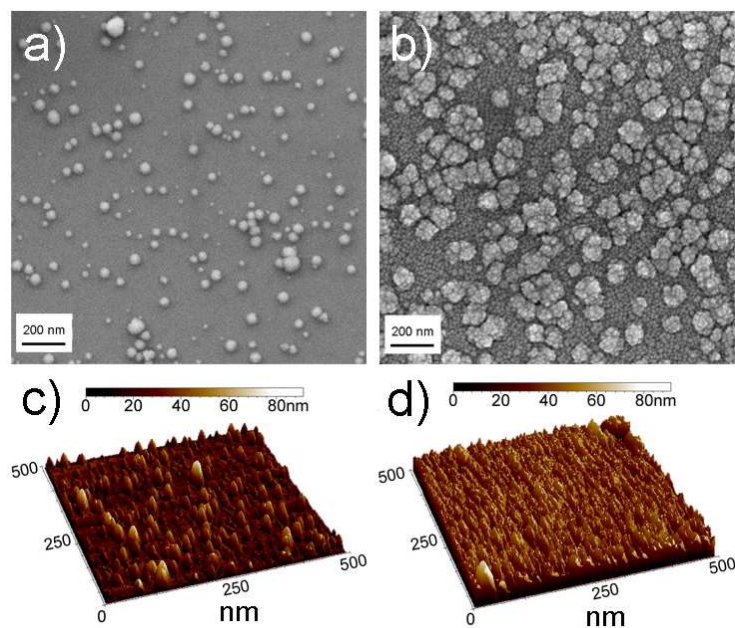


Figure 3.4 SEM images of LRMO films grown at a) 300 mTorr and b) 800 mTorr along with three-dimensional AFM images showing the surface of LRMO films deposited on LAO at c) 300 mTorr and d) 800 mTorr oxygen background pressure. The scan size is 500 nm by 500 nm.

Small particulates remain on the surface (20–50 nm), but they are smaller in diameter and cover less of the film surface [Fig. 3.4 a]. AFM images also reveal a distinct difference in the morphology between these two types of films [Figs. 3.4 c, 3.4 d], although at smaller length scales. In addition to the visible difference in surface morphology, differences exist in the root mean square roughness (R_{rms}) and the

maximum peak-to-valley roughness (R_{pv}) values. Films grown at lower oxygen concentration are smoother (R_{rms} nm) = 10, although as can be observed in the SEM images numerous granules up to 100 nm in height (R_{pv} nm) = 104 are scattered across the surface of the film. At higher oxygen growth pressures, AFM images indicate significant roughening has occurred, although a significant increase in root mean square roughness is not observed (R_{rms} nm) = 12. The granular surface of LRMO thin films grown at 800 mTorr is better evidenced by the enhanced maximum peak-to-valley roughness (R_{pv} nm) = 192 measured for these films.

Measurements of magnetization (M) versus applied magnetic field (H) and temperature (T) were performed on all samples using a superconducting quantum interference device magnetometer. The zero-field cooled (ZFC) and field-cooled (FC) responses for LRMO films deposited under different oxygen pressures was measured under a low applied field of 500 Oe and at a higher applied field of 10 kOe. Figure 3.5 illustrates the ZFC and FC magnetization curves measured at 500 Oe for samples deposited at 100, 300, 600, and 800 mTorr oxygen background pressure. The values of the ferromagnetic Curie temperature (T_C) were estimated from the minimum of the temperature derivative of the magnetization ($\delta M/\delta T$). Two different ferromagnetic Curie temperatures are observed in the series of LRMO films, and the presence, absence, or coexistence of each ferromagnetic phase is dependent on the oxygen background pressure during film growth. Samples deposited at high oxygen pressures mTorr) (≥ 600 display a single magnetic transition with a Curie temperature (T_C) of K ~ 80 , which corresponds well with the T_C value of 72 K reported previously for

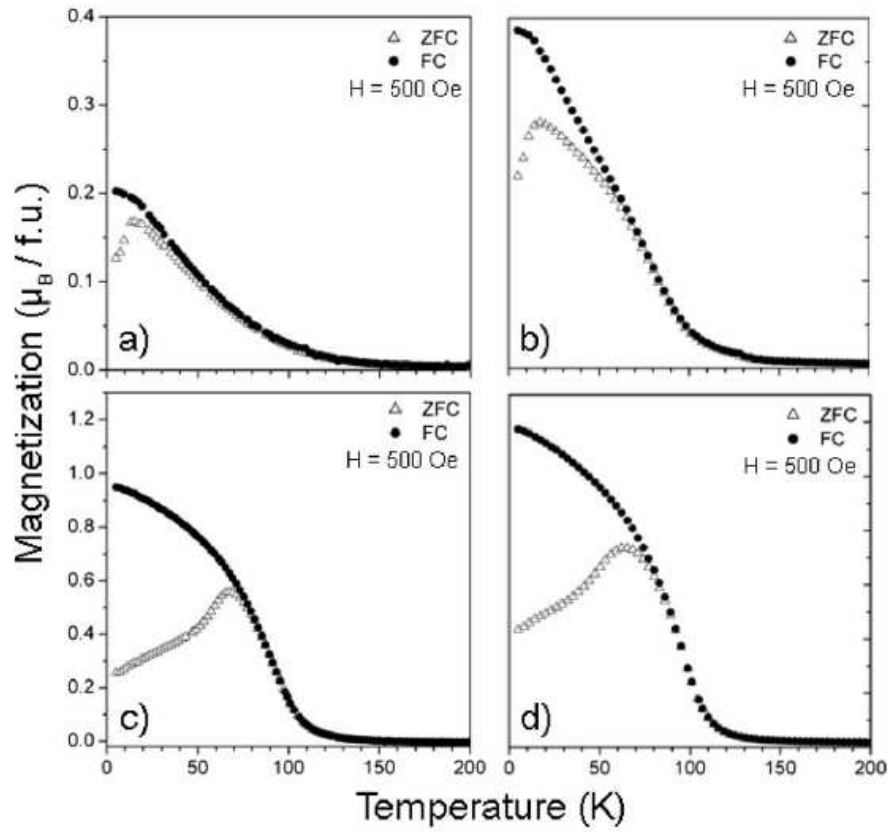


Figure 3.5 A plot of the temperature dependence of the ZFC and FC responses of LRMO films grown under different oxygen background pressures of (a) 100 mTorr, (b) 300 mTorr, (c) 600 mTorr, and (d) 800 mTorr.

polycrystalline LRMO samples [33].

In contrast, films deposited at low oxygen background pressures (\leq mTorr) 100 demonstrate a much lower T_C ferromagnetic phase (T_C K) ~ 30 . Films deposited at intermediate oxygen background pressures [e.g., 300 mTorr in Figure 3.5 b] contain a mixture of the two ferromagnetic phases, evidenced by two different $\delta M/\delta T$ minima—one corresponding to the high T_C ferromagnetic phase (T_C K) ~ 80 and the other with the lower T_C ferromagnetic phase (T_C K) ~ 30 . The presence of two different

ferromagnetic phases also has been observed in LCMO thin film samples, and also depends on the deposition conditions [12]. In particular, the lower T_C ferromagnetic phase in LCMO films is associated with the existence of oxygen vacancies [22]. For all samples, the magnetization in the FC curves increase consistently with decreasing temperature, whereas the ZFC curves demonstrate a cusp shape below the ferromagnetic T_C . These cusps disappear when the magnetic field is increased to 10 kOe [inset of Figure 3.5], which is a characteristic of spin-glass behavior [12]. Application of a stronger magnetic field also increases the T_C of the LRMO film to 104 K as the enhanced field suppresses the contribution from antiferromagnetic interactions [33]. The magnetic hysteresis in-plane loops measured at 10 K for LRMO films grown at certain oxygen background pressures (100, 300, 600, and 800 mTorr) is shown in Fig. 3.6. Both the saturation magnetization and coercive fields increase with rising oxygen background pressure, and the maximum value of saturation magnetization measured at 10 K for a LRMO film deposited at 800 mTorr is $1.7\mu_B/\text{f.u.}$. The loop for this optimized sample shows a well-defined hysteresis with a coercive field approximately equal to 1.2 kOe, and a saturation field close to 5 kOe. The enhancement in the saturation magnetization with increasing background oxygen pressure likely results from an increased number and size of domains with ordering of the M -site cations and a reduction of oxygen vacancies [22, 24]. A similar enhancement in the coercivity can be attributed to the accompanied reduction in magnetic wall domains within the thin film sample.

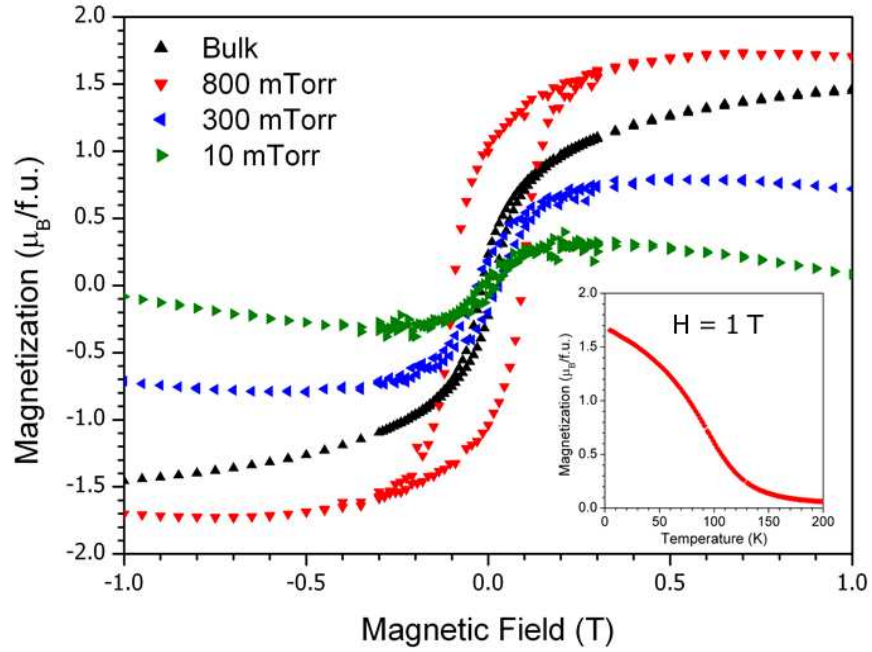


Figure 3.6 M(H) hysteresis loops for LRMO films grown under different oxygen pressures on LAO substrates measured at 10 K. The inset displays the M(T) curve recorded with 1 T. Magnetic field is applied parallel to the [100] direction of the substrate

The magnetic properties of each potential cation combination between the d orbitals of high-spin $\text{Mn}^{2+}(3d^5)$ and low-spin $\text{Rh}^{4+}(4d^5)$ cations, through the oxygen $2p$ orbitals, can be interpreted based on the rules for the sign of spin-spin superexchange interactions [38, 39], and are summarized in Table 3.1. Virtual spin transfer between half-filled to empty orbitals, $\text{Mn}^{2+}(e^2)\text{--O--Rh}^{4+}(e^0)$, along with full to half-filled orbitals, $\text{Mn}^{2+}(t^2)\text{--O--Rh}^{4+}(t^4)$, yield ferromagnetic coupling. In contrast,

Table 3.1 Expected superexchange interactions for ordered LRMO films

<i>M</i>-Cation		<i>M'</i>-Cation		Interaction	Result
$\text{Rh}^{4+}, 4d^5$	(LS)	$\text{Mn}^{2+}, 3d^5$	(HS)		
2 e_g	Empty	2 e_g	Half	σ	FM
1 t_{2g}	Half	1 t_{2g}	Half	π	AFM
2 t_{2g}	Full	2 t_{2g}	Half	π	FM
$\text{Rh}^{4+}, 4d^5$	(LS)	$\text{Rh}^{4+}, 4d^5$	(LS)		
1 t_{2g}	Full	2 e_g	Full	π	AFM
$\text{Mn}^{2+}, 3d^5$	(HS)	$\text{Mn}^{2+}, 3d^5$	(HS)		
2 e_g	Half	2 e_g	Half	σ	AFM
3 t_{2g}	Half	3 t_{2g}	Half	π	AFM

antiferromagnetic coupling results from virtual spin transfer between half-filled to half-filled orbitals, for example, $\text{Mn}^{2+}(e^2)\text{--O--Mn}^{2+}(e^2)$ and $\text{Rh}^{4+}(t^1)\text{--O--Rh}^{4+}(t^1)$. Ferromagnetic interactions are stronger between e orbitals than t orbitals because the overlap of the σ -bonding e electrons is greater and their ΔE is smaller than that of the π -bonding electrons for t orbitals. Therefore, a well ordered LRMO film dominated by σ -bonding $\text{Mn}^{2+}(e^2)\text{--O--Rh}^{4+}(e^0)$ interactions is expected to generate ferromagnetic coupling. An increase in point disorder, however, enhances the number of $\text{Mn}^{2+}(e^2)\text{--O--Mn}^{2+}(e^2)$ and $\text{Rh}^{4+}(t^1)\text{--O--Rh}^{4+}(t^1)$ antiferromagnetic interactions within the sample. In addition, antiphase grain boundaries, where the cation positions are inverted, can also yield a significant number of such antiferromagnetic interactions. Competition between these ferromagnetic and antiferromagnetic interactions in partially B-site disordered samples leads to complex magnetic behavior and most likely produces the observed spin-glass behavior in LRMO films [22]. The alternative high-spin Jahn–

Teller $\text{Mn}^{3+}(3d^4)$ and low-spin $\text{Rh}^{3+}(4d^6)$ cation combination must also be considered. An ordered $\text{Rh}^{3+}/\text{Mn}^{3+}$ interaction generates both σ -bonding $\text{Mn}^{3+}(e^1)\text{--O--Rh}^{3+}(e^0)$ and π -bonding $\text{Mn}^{3+}(t^3)\text{--O--Rh}^{3+}(t^6)$ ferromagnetic interactions. In the case of disorder, however, three-dimensional ferromagnetic vibronic superexchange between Jahn–Teller cations $\text{Mn}^{3+}(e^1)\text{--O--Mn}^{3+}(e^1)$ and diamagnetic $\text{Rh}^{3+}(t^6)\text{--O--Rh}^{3+}(t^6)$ interactions are also possible [40]. Such vibronic superexchange between $\text{Mn}^{3+}(e^1)\text{--O--Mn}^{3+}(e^1)$ provides less stabilization when compared to the ferromagnetic superexchange of $\text{Mn}^{2+}\text{--O--Rh}^{4+}$ cations, and may account for the lower T_C ferromagnetic phase [22]. At the same time, the observation of an additional low temperature maximum in the ac susceptibility of polycrystalline LRMO has been attributed to either (i) competing interactions antiferromagnetic and ferromagnetic interactions between identical and different species of neighboring cations in statistically ordered domains or (ii) ferromagnetic domains coexisting with an important paramagnetic volume fraction [33]. Nonetheless, an increase in oxygen vacancies reduces the number of ferromagnetic interactions from ordered $\text{Mn}^{2+}\text{--O--Rh}^{4+}$ lattices, and possibly explains why the contribution from the higher T_C ferromagnetic phase is diminished significantly in films deposited at lower oxygen background pressure.

The maximum value of saturation magnetization ($1.7\mu_B/\text{f.u.}$) is below the expected spin-only value (μ_{calc}) of $4.36\mu_B/\text{f.u.}$ for $\text{Rh}^{4+}/\text{Mn}^{2+}$ valence states [33] or $4.65\mu_B/\text{f.u.}$ for $\text{Rh}^{3+}/\text{Mn}^{3+}$ valence states [31]. For polycrystalline LRMO samples, using the former spin-only value, the magnetic data indicated the ferromagnetic volume fraction to be $\sim 35\%$, which can be attributed to the fraction of cation ordered domains, and

therefore indicating that the majority of the B-site sublattice remains disordered. A similar calculation comparing the saturation magnetization of the optimized LRMO films at 10 K with the spin-only value yields a slightly enhanced ferromagnetic volume fraction of $\sim 40\%$. Films grown at lower oxygen concentrations possess reduced ferromagnetic volume fractions with the minimum value reaching 7% for a LRMO thin film grown at 10 mTorr oxygen background pressure. These results are consistent with an increase in structural defects, and therefore antiferromagnetic superexchange interactions, in thin films grown at lower oxygen pressure.

The dc-electrical properties of the film samples were measured by a physical property measurement system in four-probe configuration. Figure 3.7 illustrates the resistivity as a function of temperature. As expected, the thin film samples were semiconducting with a high resistivity of $\sim 10^1 \Omega \text{ cm}$ at room temperature, which increases with decreasing temperature until the resistance exceeds the maximum value that can be measured ($R > 10^7 \Omega$) at $K \sim 200$. An Arrhenius plot of the $\log \rho$ versus inverse temperature (inset of Figure 3.7) reveals a linear dependence, indicating semiconductor behavior with a low activation energy of 0.16 eV.

Magnetodielectric responses have been reported previously for ferromagnetic LaMnO_3 polycrystalline and thin film samples [23, 26]. Epitaxial bilayer LRMO/LNO films were grown on (001-oriented LAO substrates to examine the dielectric response of LRMO under various temperatures, frequencies, and magnetic fields. Prior to the deposition of 100 nm thick LRMO film, a bottom electrode of LaNiO_3 (50 nm) was deposited at 700 °C at an oxygen pressure of 100 mTorr.

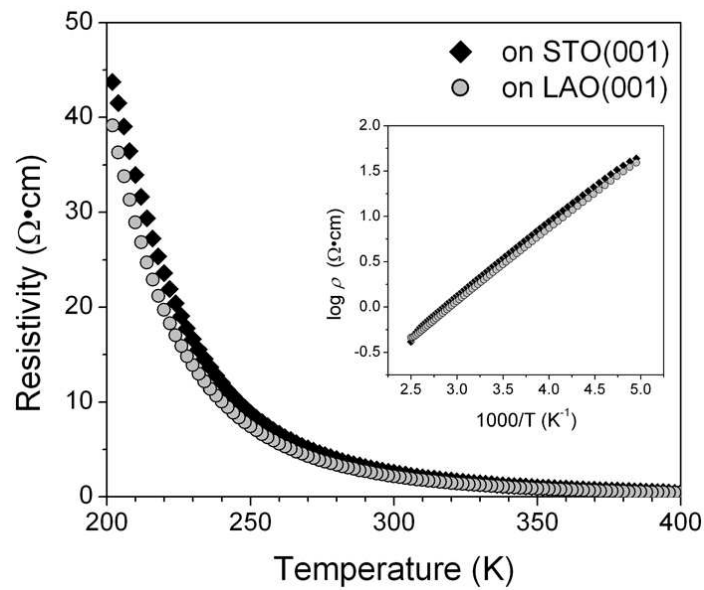


Figure 3.7 A plot of the resistivity of LRMO films as a function of temperature. The inset displays the $\log \rho$ as a function of inverse temperature (Arrhenius plot).

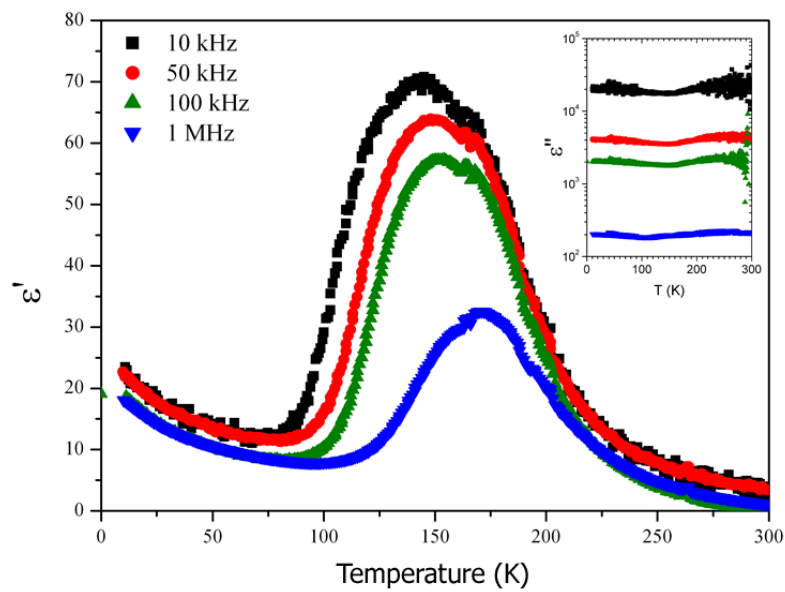


Figure 3.8 A plot of the temperature dependence of the real part of the dielectric response (ϵ') measured at certain frequencies for a 100 nm thick LRMO film grown on a 50 nm thick layer of LaNiO_3 deposited on (001)-oriented LAO. The inset shows a plot of the dielectric loss as a function of temperature for the same selected frequencies.

Square gold pads of $400 \times 400 \mu\text{m}^2$ dimensions (physical mask) were sputtered on top of the LRMO films and the LNO regions unexposed to the LRMO deposition. The fabricated heterostructures were characterized in the metal-insulator-metal configuration to study their dielectric properties. Figure 3.8 shows the temperature dependence of the dielectric permittivity (ϵ) at selected frequencies for a LRMO film deposited with an oxygen back pressure of 800 mTorr. At low temperature the dielectric permittivity at all frequencies remains near 10–20 until ϵ increases to a maximum at temperatures near 150–175 K. Then, the dielectric permittivity decreases to a minimum at higher temperature where values near 1 are reached. There is large frequency dispersion as illustrated by both the decrease in intensity and shift to higher temperatures for the maximum value of the dielectric permittivity with increasing applied frequency. Although the dielectric anomaly occurs near temperatures observed for the magnetic ordering temperature of LRMO, such enhancements in the capacitance of a semiconductor with observable grain boundaries likely are extrinsic [41, 42]. As summarized by Scott [43], Maxwell–Wagner effects can occur at grain boundaries near the magnetic ordering temperature of magnetoresistive materials, and can lead to enhancements of the dielectric constant exceeding 1000%. Indeed, our plot matches closely with the calculated real part of the dielectric constant in a Maxwell–Wagner equivalent circuit reported previously, suggesting such artifacts predominate [43]. As shown in Fig. 3.9, the films are lossy and the dielectric loss remains relatively constant at all temperatures, data which provide further evidence that the observed dielectric anomaly is unrelated to true magnetoelectric coupling. It should also be

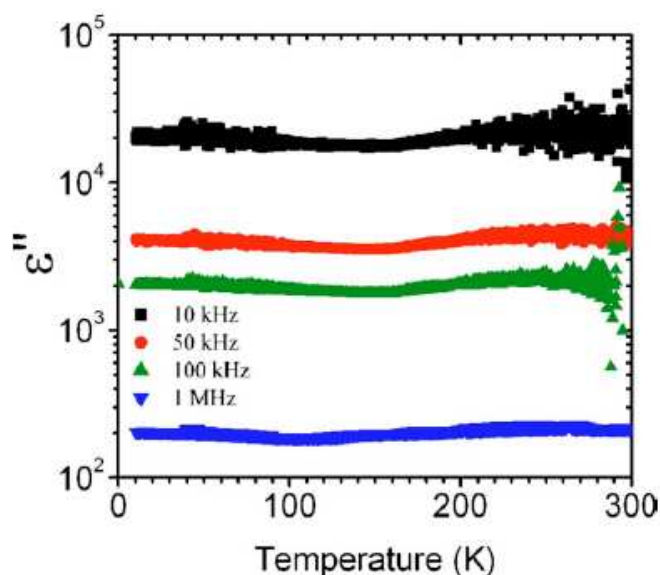


Figure 3.9 A plot of the dielectric loss as a function of temperature measured at certain frequencies.

noted that unlike polycrystalline and thin film samples of the double perovskite LNMO, no significant change in the dielectric permittivity of LRMO films was observed upon the application of magnetic fields up to 10 kOe at a constant frequency (50 kHz).

3.3.4 Conclusion

In conclusion, epitaxial LRMO thin films have been deposited on both (001)-oriented STO and LAO using the pulsed laser deposition technique. A change in the defect structure, surface morphology, and magnetic properties was observed for LRMO films grown at different oxygen pressures. All films are semiconducting and ferromagnetic; however, the Curie temperature, coercive field, and saturation

magnetization of LRMO films are dependent on the oxygen background pressure during deposition. Higher oxygen deposition pressures (> 600 mTorr) yield films with a rougher surface morphology and a reduced defect structure, the latter which improves the local ordering of the M -site cations and enhances the magnetization of the film. Films deposited at lower oxygen pressures display a second low temperature T_C ferromagnetic phase, which may be associated with the alternate $\text{Mn}^{3+}/\text{Rh}^{3+}$ valence state. Such results further demonstrate the critical role oxygen background pressure during film growth plays in controlling the morphology, crystalline structure, and magnetic properties of $\text{LaM}_{1/2}\text{Mn}_{1/2}\text{O}_3$ perovskite films.

3.4 Electrical and Magnetic Properties of New Rhodium Perovskites: La_2MRhO_6 , $\text{M} = \text{Cr, Fe, Cu}$

3.4.1 Introduction

Most semiconducting oxides can be doped n-type or p-type, with n-type doping being much more common. However, Rh^{3+} rhodates have band gaps of about 2.2 eV and both n- and p-type doping are generally possible [44]. Thus, p-type LuRhO_3 has been shown to be effective as a cathode in the photodecomposition of water using sunlight in a cell that produced not only H_2 and O_2 but produced electricity as well [44]. The catalytic activity of LuRhO_3 is important for this cell, and perovskite-type rhodates are generally known as good catalysts [45]. Some p-type rhodates have also been of interest as transparent conductors [46]. With the discovery of good thermoelectric properties for some Co oxides [47-51], the potential of rhodates as thermoelectrics has come under investigation because Rh sits just under Co in the periodic table [47, 50, 52-56]. Some Cu and Rh delafossites have also been investigated as potential thermoelectric candidates [52, 57, 58]. CuRhO_2 with Mg doping was reported to show a $ZT \sim 0.15$ at 1000 K [52]. In addition, the solid solutions $\text{LaNi}_{1-x}\text{Rh}_x\text{O}_3$ and $\text{LaCo}_{1-x}\text{Rh}_x\text{O}_3$ with the perovskite structure have recently been shown to have promise as thermoelectric materials [59, 60]. For $\text{LaNi}_{1-x}\text{Rh}_x\text{O}_3$ ($x = 0-0.3$) a ZT was estimated to be 0.044 at 800 K [69]. The analogous cobalt solid solution ($\text{LaCo}_{1-x}\text{Rh}_x\text{O}_3$), also with an orthorhombic perovskite structure, was reported as a possible route to promising thermoelectrics; its high Seebeck coefficient and

lower resistivity allowed for a ZT reaching 0.075 at 775 K [60]. These findings suggested that other first row transition metal cations should be evaluated in combination with Rh in the perovskite structure. Here we report on the synthesis, magnetic and some thermoelectric properties of several new perovskite rhodates.

3.4.2. Results

Lattice parameters derived from our X-ray diffraction data are provided in Table 3.2. In no case were peaks observed that would indicate ordering of the M and Rh atoms. Plots of $\log \sigma$ vs. $1000/T$ are shown in Figure 3.10. Activation energies derived from these plots are given in Table 3.3. Room temperature electrical resistivity and Seebeck coefficients are also summarized in Table 3.3. The sign of the Seebeck coefficient is always positive, indicating that the dominant carriers are holes in the valence band. The highest electrical conductivity was obtained for M = Ni and Cu. Both electrical resistivity and Seebeck coefficients for $\text{La}_2\text{CuRhO}_6$ are plotted vs. temperature in Figure 3.11. The power factor for $\text{La}_2\text{CuRhO}_6$ is shown in Figure 3.12.

Table 3.2 Cell dimensions and heating parameters

La_2MRhO_6	Cr	Mn	Fe	Co	Ni	Cu
a (Å)	5.552	5.555	5.572	5.529	5.546	5.552
b (Å)	5.565	5.599	5.599	5.538	5.541	5.709
c (Å)	7.851	7.852	7.874	7.822	7.845	7.844
Vol (Å ³)	242.52	244.22	245.64	239.52	241.01	248.6
Final Temp (°C)	1400	1100	1300	1250	1275	1300
Total Heat Time (hrs)	80	60	58	36	60	40
Color	Brown	Black	Brown	Black	Black	Black

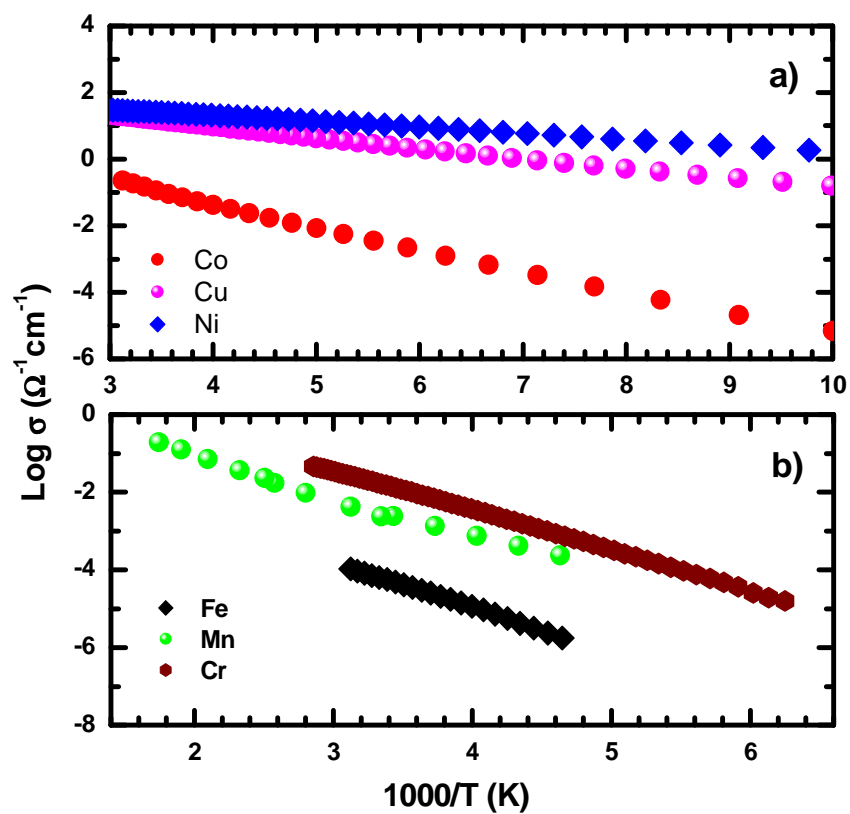


Figure 3.10 Electrical conductivity of La_2MRhO_6 pellets for $M = \text{Co}, \text{Ni}, \text{Cu}$ (a) and $M = \text{Cr}, \text{Mn}, \text{Fe}$ (b). Note the difference in scale for a and b.

Table 3.3 Details of electrical measurements at 300 K

La_2MRhO_6	Cr	Mn*	Fe	Co*	Ni*	Cu
Resistivity ($\Omega\text{-cm}$)	58.6	316.2	15706	5.1	0.0375	0.0563
Seebeck Coeff. ($\mu\text{V/K}$)	643.2	146.3	242.6	418.6	30.1	149.5
Activation Energy (eV)	0.204	0.203	0.218	0.151	0.034	0.068

*Data here was reproduced and is consistent with reported values [59, 60, 65]

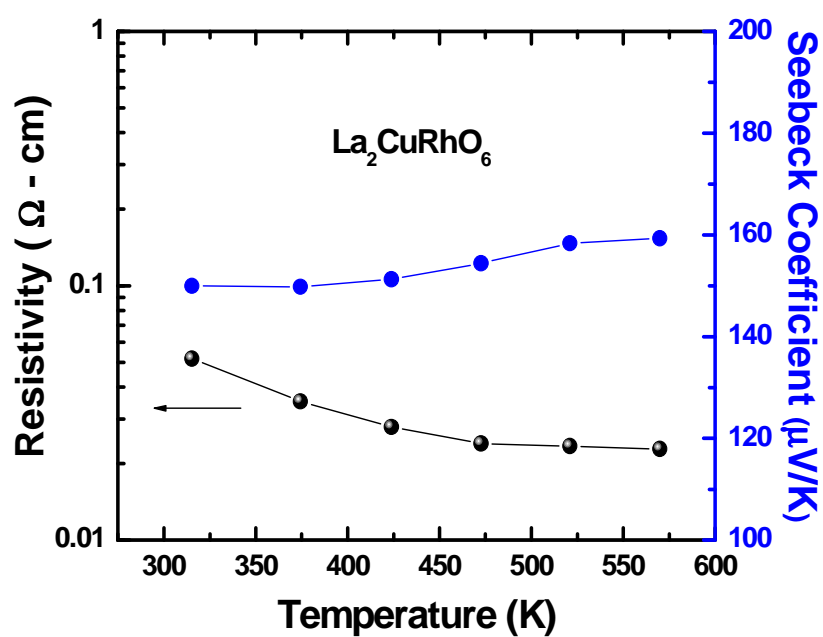


Figure 3.11 Electrical resistivity and Seebeck coefficient for $\text{La}_2\text{CuRhO}_6$ from 300 - 575 K.

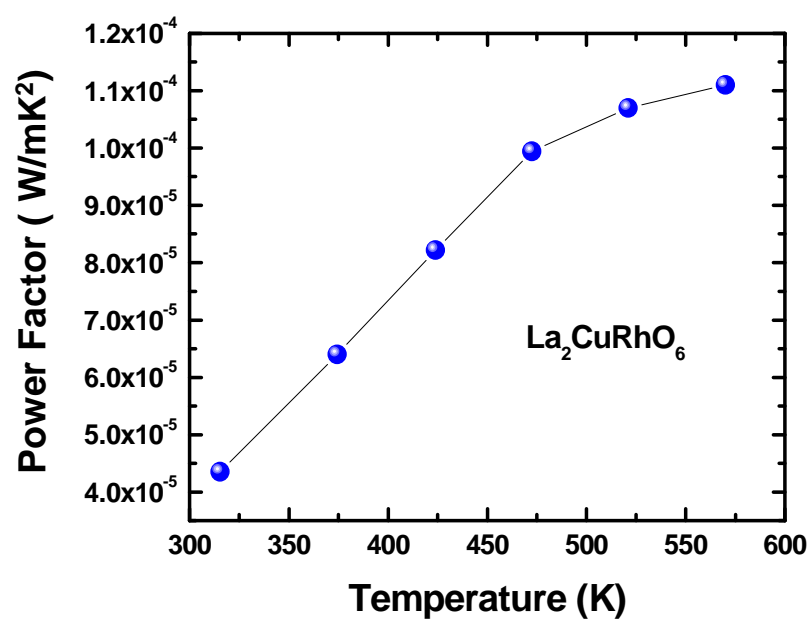


Figure 3.12 Power factor calculated for $\text{La}_2\text{CuRhO}_6$ from 300 - 575 K.

Magnetic susceptibility results for $M = \text{Fe}$, Cu , and Cr are shown in Figures 3.13, 3.14, and 3.15. Table 3.4 summarizes our magnetic measurements for $M = \text{Cr}$, Mn , Fe , Co , Ni , and Cu . Similar measurements have been previously reported for $M = \text{Mn}$, Co , and Ni ; our results are in reasonable agreement with these reports [33, 48, 60-62]. For all M cations studied except $M = \text{Mn}$ and Fe , Θ_w is negative, indicative of dominant antiferromagnetic interactions. The calculated spin-only moments based on the assumption that all the M cations are in +3 oxidation state do not agree with those calculated from Curie-Weiss plots. The discrepancy commonly occurs unless measurements are extended to higher temperatures than we have used, but may also

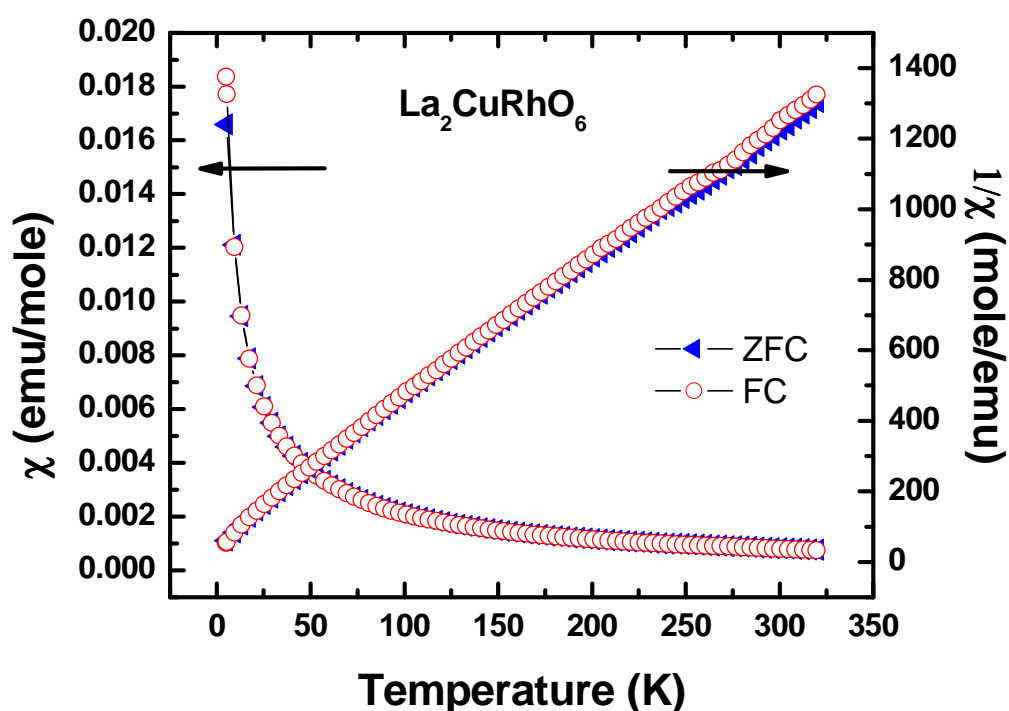


Figure 3.13 Magnetic susceptibility (left) and inverse magnetic susceptibility (right) for field cooled (FC, red) and zero field cooled (ZFC, black) for $\text{La}_2\text{CuRhO}_6$ from 5 – 320 K under an applied field of 0.5 Tesla.

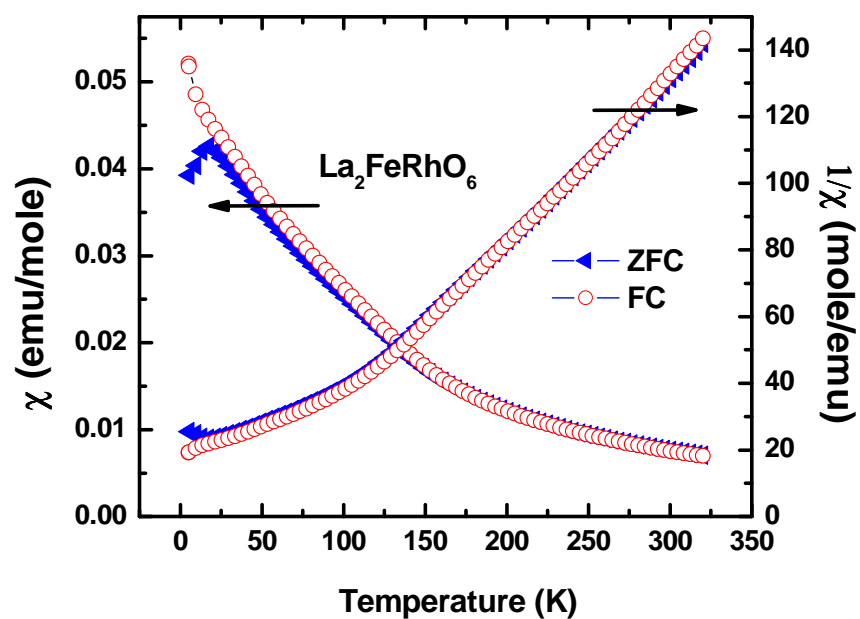


Figure 3.14 Magnetic susceptibility (left) and inverse magnetic susceptibility (right) for field cooled (FC, red) and zero field cooled (ZFC, black) for $\text{La}_2\text{FeRhO}_6$ from 5 – 320 K under an applied field of 0.5 Tesla.

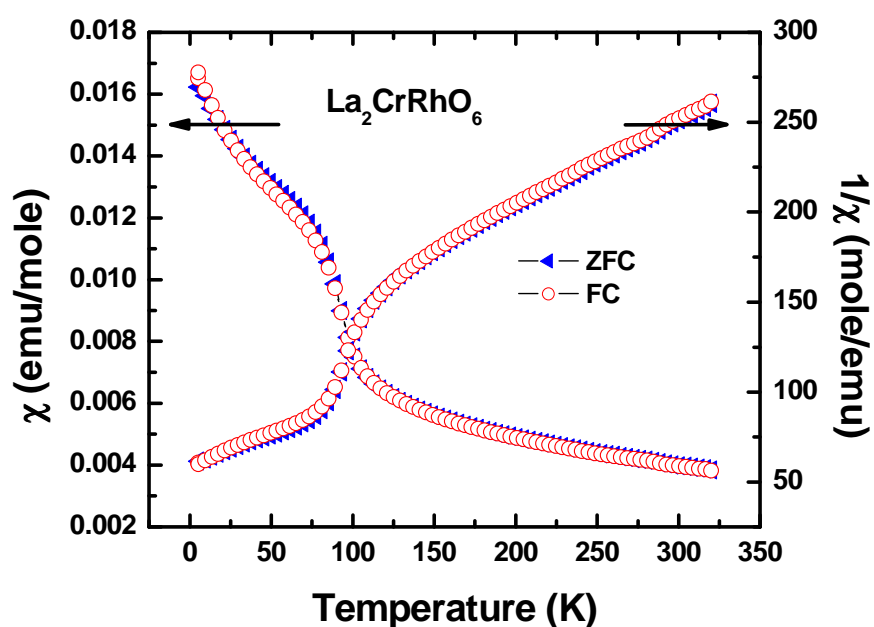


Figure 3.15 Magnetic susceptibility (left) and inverse magnetic susceptibility (right) for field cooled (FC, red) and zero field cooled (ZFC, black) for $\text{La}_2\text{CrRhO}_6$ from 5 – 320 K under an applied field of 0.5 Tesla.

Table 3.4 Summary of magnetic measurements at 0.5 Tesla at 5 - 320 K

La_2MRhO_6	Cr	Mn*	Fe^\dagger	Co*	Ni*	Cu
Θ_w (K)	-241.3	+131.8	+28.0 -91.5	-109.5	-136.2	-32.1
C (emu K/mole)	2.156	4.222	2.057 4.937	1.677	1.038	3.465
$\mu_{\text{calc}} (\text{M}^{2+}\text{Rh}^{4+})$	5.196	6.170	5.196	4.239	3.316	2.447
$\mu_{\text{calc}} (\text{M}^{3+}\text{Rh}^{3+})$	3.873	4.900	5.920	4.900	1.730	2.828
$\mu_{\text{obs}} (\mu_B)$	4.155	5.815	4.059 6.288	3.664	2.884	1.471

*Data here was reproduced and is in relatively good agreement with reported values [33, 48, 60-62]

†Two values are listed here based on two distinct slopes in the $1/\chi$ vs. T plots, upper (150 - 320 K) and lower (50 - 90 K)

indicate mixed valency in some systems. However, the large discrepancy in the case of Cu strongly suggests that the oxidation state of Cu is not +3. Large discrepancies have also been observed in other perovskite systems containing copper [35].

3.4.3. Discussion

No contribution to magnetism is expected for Rh^{3+} in its normal $4d^6$ low-spin configuration, and our magnetic measurements support an oxidation state of 3+ for M and Rh for La_2MRhO_6 compounds with M = Cr, Fe. However, the magnetic moment in the case of Cu suggests a lower oxidation state than 3+ and thus a higher oxidation state for Rh. A similar situation is observed for M = Mn, Co and Ni. Although a magnetic moment might be expected from $4d^5 \text{Rh}^{4+}$, in fact little or no moment is typically found for Rh^{4+} in oxides [63]. For $\text{La}_2\text{CoRhO}_6$, the observed low magnetic moment may be due to an intermediate spin arrangement ($S = 1$) and is probably

similar to the magnetic behavior observed in LaCoO_3 [48, 64]. A plot of M^{3+} cation radii vs. cell volume (Fig. 3.16) for La_2MRhO_6 compounds also points to a lower oxidation state for Cu. A $\text{Cu}^{2+}/\text{Rh}^{4+}$ combination is expected to give a larger cell volume than a $\text{Cu}^{3+}/\text{Rh}^{3+}$ combination because Cu^{2+} is much larger than Cu^{3+} , but Rh^{4+} is only slightly smaller than Rh^{3+} [65]. The high electrical conductivity of $\text{La}_2\text{CuRhO}_6$ (Fig. 3.11, Table 3.3) relative to other La_2MRhO_6 (Fig. 3.10, Table 3.3) compounds suggests a strong contribution of both Cu and Rh states at the top of the valence band. Thus, integer values for the oxidation states of Cu and Rh may not be meaningful. This is likely valid for Ni and may be valid for Mn and Co. The high electrical conductivity of $\text{La}_2\text{CuRhO}_6$ combined with its high Seebeck coefficient has a positive impact on its thermoelectric power factor, especially at higher temperatures (Fig. 3.12).

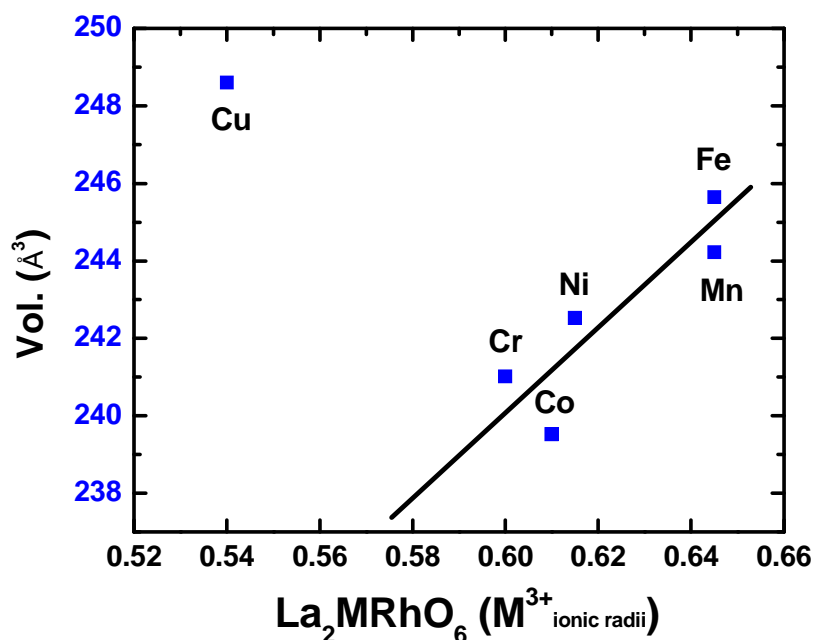


Figure 3.16 La_2MRhO_6 unit cell volumes vs. M^{3+} radii

The disorder of the M and Rh cations complicates interpretation of the magnetic properties. The interaction of the M cations with each other through M-O-M linkages of approximately 180° is expected to be the dominant consideration, and this would be antiferromagnetic in nature explaining the negative value of Θ_w for Cr, Co, Ni and Cu. Rather simple antiferromagnetic behavior is found for M = Ni and Co as has been previously reported [48, 60-62]. No indication of magnetic ordering is found in the case of $\text{La}_2\text{CuRhO}_6$ (Fig. 3.13). However, the magnetic data for $\text{La}_2\text{FeRhO}_6$ and $\text{La}_2\text{CrRhO}_6$ (Fig. 3.14 and 3.15) show evidence of weak ferromagnetism and is reinforced by the observation of a hysteresis loop at 5 K (Fig. 3.17 and 3.18). The observed magnetic behavior for $\text{La}_2\text{FeRhO}_6$ is probably due to disorder of Fe and Rh in octahedral sites resulting in short-range Fe-O-Fe and Fe-O-Rh interactions which could give rise to antiferromagnetism coupled with short range weak ferromagnetism.

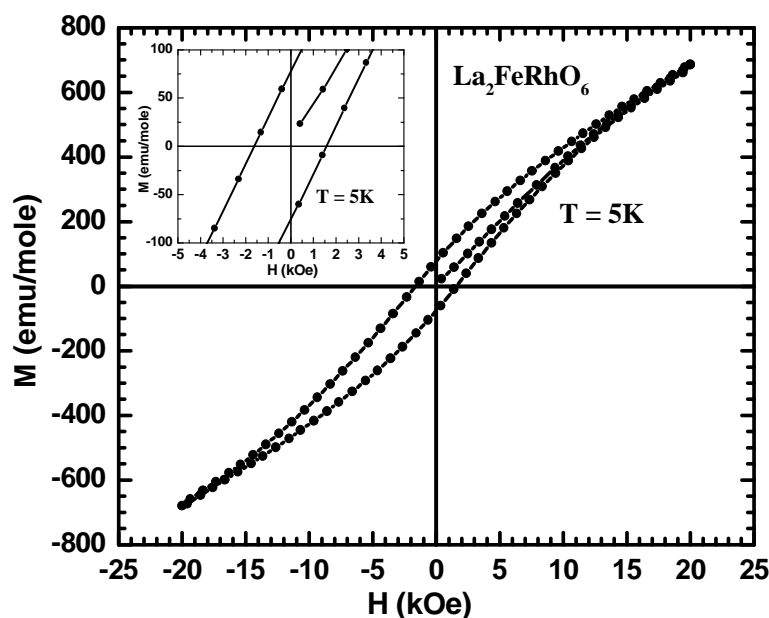


Figure 3.17 Hysteresis loop for $\text{La}_2\text{FeRhO}_6$ obtained at 5 K.

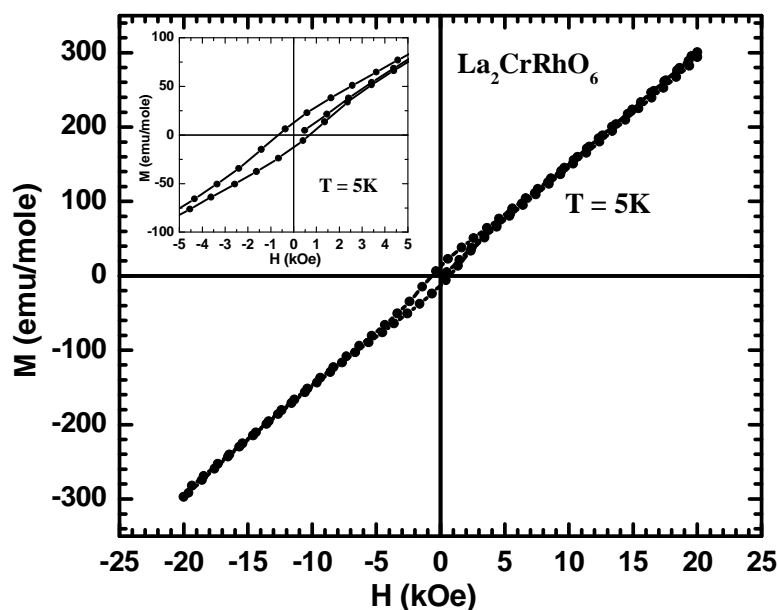


Figure 3.18 Hysteresis loop for $\text{La}_2\text{CrRhO}_6$ obtained at 5 K.

Two values of Θ_w are proposed in Table 3.4. Further assessment is necessary to fully understand the magnetic interactions in these compounds.

3.4.4 Conclusion

The compositions $\text{La}_2\text{FeRhO}_6$, $\text{La}_2\text{CrRhO}_6$, $\text{La}_2\text{CuRhO}_6$ were prepared for the first time, and their electrical and magnetic properties were determined. Known $\text{La}_2\text{MnRhO}_6$, $\text{La}_2\text{CoRhO}_6$, and $\text{La}_2\text{NiRhO}_6$ were also prepared and their properties determined for comparison. All six phases have the orthorhombic perovskite structure. Electrical resistivity measurements as a function of temperature indicate that all phases are semiconducting. Seebeck measurements show that all are p-type conductors. Magnetic measurements indicate generally antiferromagnetic interactions

for all compositions, although evidence for weak ferromagnetism is found in the case of $\text{La}_2\text{CrRhO}_6$ and $\text{La}_2\text{FeRhO}_6$. The oxidation state of M appears to be close to 3+ for Fe and Cr, and a mixture of 2+/3+ for Cu. A favorable combination of electrical conductivity and Seebeck coefficient results in a relatively high thermoelectric power (1.11 W/m-K^2 at $\sim 575\text{K}$) factor for $\text{La}_2\text{CuRhO}_6$.

3.4.5. Experimental

Polycrystalline samples of La_2MRhO_6 with $\text{M} = \text{Cr, Mn, Fe, Co, Ni, and Cu}$ were synthesized by traditional solid state methods. Starting materials of La_2O_3 (Aldrich 99.9%), Co_3O_4 (Alfa Aesar 99.7%), NiO (Alfa Aesar 99.998%), CuO (Aldrich 99.99%), Fe_2O_3 (JMC 99.99%), Cr_2O_3 (Aldrich 99%), Mn_2O_3 (JMC 98%+) and Rh_2O_3 were mixed thoroughly in appropriate ratios. Rh_2O_3 was obtained by the oxidation of RhI_3 (JMC 98%+) in an oxygen gas flow at 700°C for 12 hours. La_2O_3 was dried at 850°C overnight before weighing. The mixed powders of starting materials were calcined at 1000°C for 12 hours in air with ramp rates of 300°C/hr . The samples were reground and sintered in air from $1100\text{-}1400^\circ\text{C}$ for another 36-80 hours with intermediate grinding. $\text{M} = \text{Cu and Ni}$ were reacted under a steady oxygen flow. The reacted powders were cold pressed into pellets before sintering. Table 1 lists the compounds made, final heating temperature, total heating time, and color of the powder. Powder X-ray diffraction data were collected with a Rigaku MiniFlex II powder diffractometer using $\text{Cu K}\alpha$ radiation and a graphite monochromator on the diffracted beam. The low temperature electrical resistivities were measured from ~ 100

- 200 to 320 K by a standard four-probe technique with a PPMS (Physical Property Measurement System). The electrical resistivities and Seebeck coefficients at $T \geq 320$ K were measured by a standard four-probe technique with a ULVAC-ZEM themoanalyzer in a He(g) atmosphere. The Seebeck coefficient of constantan was measured as a reference. The absolute uncertainties in both parameters are estimated to be below 5%. Magnetism was also measured with a PPMS from 5 to 320 K. A field of 0.5 Tesla was applied for measurements after zero field cooling (ZFC) and field cooling (FC). Magnetic moments were calculated from the higher temperature regions ($\sim 200 - 320$ K) of $1/\chi$ vs. T plots.

3.5 Lattice crossover and mixed valency in the $\text{LaCo}_{1-x}\text{Rh}_x\text{O}_3$ solid solution

3.5.1 Introduction

A constraint in the ideal cubic AMO_3 perovskite structure is that the A-O bond distance must equal the M-O bond distance times $\sqrt{2}$. Thus, Goldschmidt defined a tolerance factor, t , as $t = (r_A + r_O) / [\sqrt{2} (r_M + r_O)]$, where r_A , r_M and r_O are the radii of the A cation, M cation, and O anion, respectively [10]. The relative sizes of the A and M cations are such in most compounds with the perovskite structure that t is less than 1.0. Temperature impacts t because the A cations have higher thermal expansion than the M cations; thus, increasing temperature increases t . Reducing t from 1.0 results in distortions of the perovskite structure, which decrease the coordination number of the A cation. These distortions may be described as a tilting of the octahedra in the MO_3 network [66, 67]. The most common tilt structure has orthorhombic symmetry, and this structure is found for many RMO_3 perovskites where R is a rare earth cation and t is less than about 0.985 [68, 69]. As the size of R increases t increases, and a change occurs to a tilt structure with rhombohedral symmetry, and with increasing temperature the further increase in t results in a transformation to the ideal cubic structure [69]. However before the change from orthorhombic to rhombohedral occurs for the RMO_3 perovskites, there is a crossover of all three orthorhombic cell edges such that powder diffraction patterns appear to be cubic at the crossover point. This sequence observed for the RMO_3 perovskites is not universal for all AMX_3

compounds with the perovskite structure. For example, in the $\text{Na}_{1-x}\text{K}_x\text{MgF}_3$ solid solution with increasing x and t , there is no crossover of the orthorhombic cell edges, which ultimately convert to tetragonal and then cubic [70]. Increasing temperature for low x phases results in a smooth transition to the ideal cubic structure with no crossover and no structure of intermediate symmetry [71]. We have now observed dramatic crossover behavior with a change of the M cation as x is varied in the $\text{LaCo}_{1-x}\text{Rh}_x\text{O}_3$ solid solution.

Transition metal oxides with perovskite-type structures have been of interest for many years due to their great variety of observed properties, including very high dielectric constants, high T_c superconductivity, ferromagnetism, and useful catalytic behavior [72]. Little attention was given to oxides as potentially efficient thermoelectrics until good thermoelectric properties were found for some Co based oxides [47, 73-76]. Subsequently, there has been an increased interest in the thermoelectric properties of perovskite oxides [77, 78]. In general, oxides have an advantage over other thermoelectric materials, like bismuth chalcogenides, in that they are stable to far higher temperatures. Solid solutions of LaCoO_3 and LaRhO_3 have been studied for their electrical, magnetic and catalytic properties [48, 49, 59, 79-83]. However, the crystallographic, electrical and magnetic properties of the entire solid solution in $\text{LaCo}_{1-x}\text{Rh}_x\text{O}_3$ have not been reported. Our goal was to investigate the structural variation and physical properties of the complete solid solution between LaCoO_3 and LaRhO_3 .

3.5.2 Results and Discussion

3.5.2.1 Structural Behavior

X-ray powder diffraction patterns of the compositions $\text{LaCo}_{1-x}\text{Rh}_x\text{O}_3$ ($x = 0$ to 1) are shown in Fig. 3.19. With the increasing amount of Rh, a rhombohedral-to-orthorhombic transition occurs between x values of 0.1 and 0.2. This transition is evident from the change in the splittings of the pseudocubic peaks of the ideal perovskite structure and from the appearance and rise of new peaks such as the (111) reflection near $25.5^\circ 2\theta$. The diffraction data were fitted by Rietveld

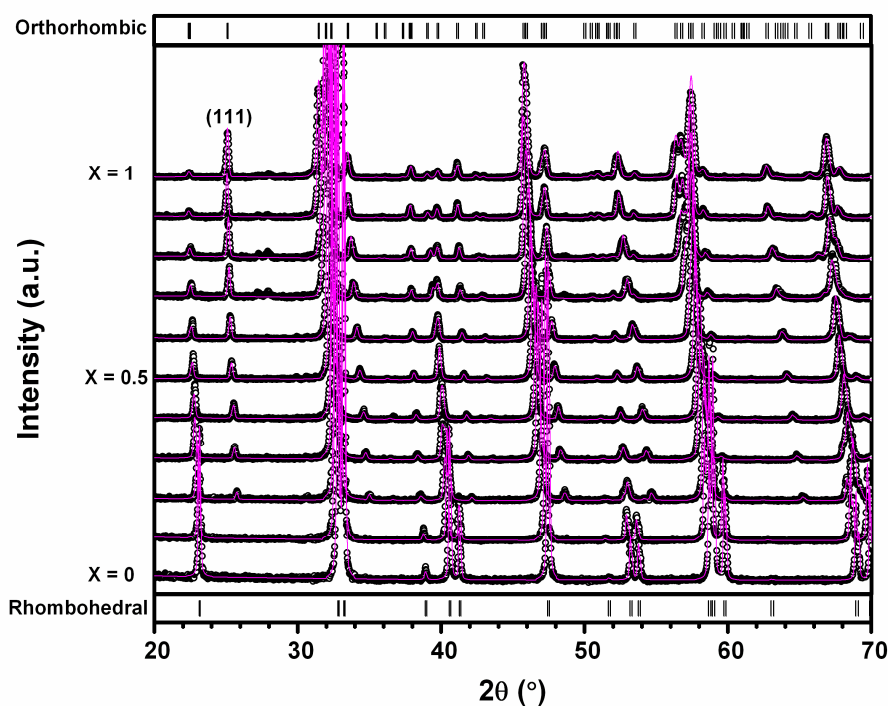


Figure 3.19 XRD patterns of $\text{LaCo}_{1-x}\text{Rh}_x\text{O}_3$ (open circles) and calculated data (solid line) by Rietveld refinement. Allowed Bragg reflections are shown as vertical lines for both structural variations.

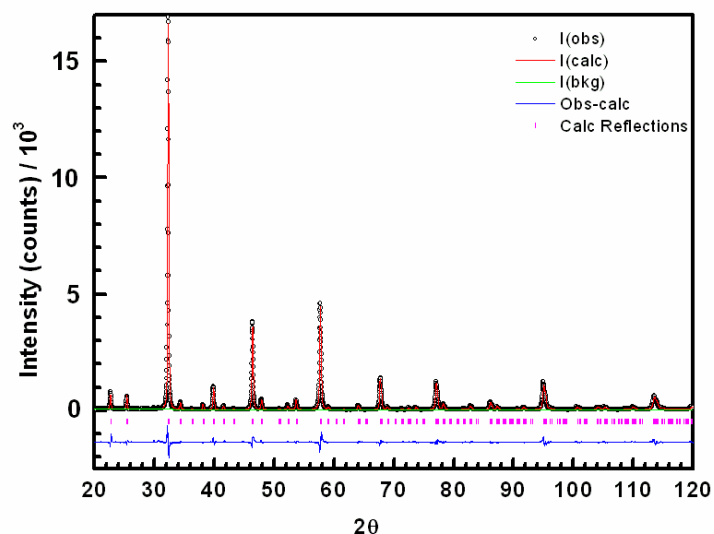


Figure 3.20 Rietveld refinement of $\text{LaCo}_{1-x}\text{Rh}_x\text{O}_3$ ($x = 0.5$) with orthorhombic structure. Observed data are shown as open circles, calculated data as the solid line, allowed Bragg reflections as vertical lines, and difference curve ($I_o - I_c$) at the bottom.

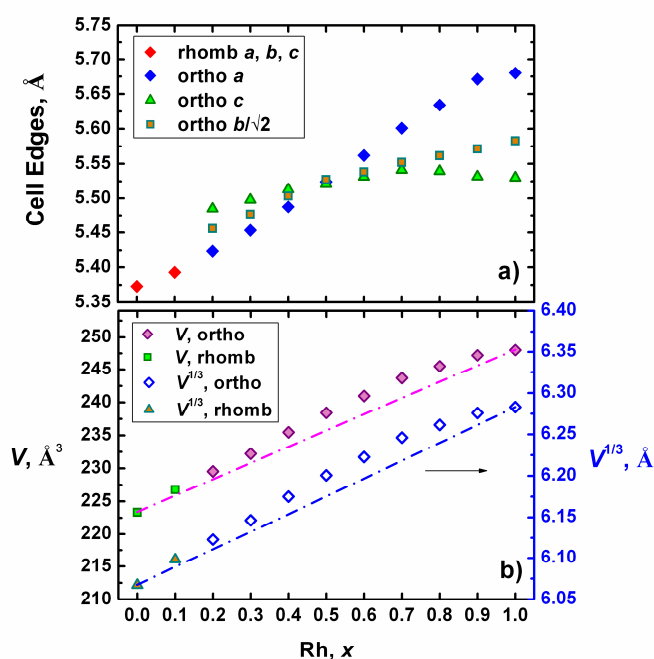


Figure 3.21 Cell parameters as a function of Rh concentration for solid solutions $\text{LaCo}_{1-x}\text{Rh}_x\text{O}_3$. Straight lines are drawn to guide the eyes. (a) Cell edge b of the orthorhombic phase was divided by $\sqrt{2}$; (b) Cell volume V of the rhombohedral phase was normalized ($\times 2$), based on Z , to match the orthorhombic cell volume.

refinements using the GSAS software suite [84, 85]. A typical calculated profile is given for $\text{LaCo}_{1-x}\text{Rh}_x\text{O}_3$ ($x = 0.5$) in Figure 3.20. Unit cell parameters vs. composition are shown in Fig. 3.21. The b cell edge has been divided by $\sqrt{2}$ because this would then have the same value as a and c , if the structure were the ideal cubic perovskite structure (Fig. 3.21(a)). The unit cell volume (V) vs. composition and $V^{1/3}$ vs. composition are shown in Fig. 3.21(b). Végard's Law would have a linear relationship for $V^{1/3}$ vs. composition, but it is generally found that V vs. composition is more likely to be linear [86]. Either way the volume plot shows a positive deviation. The α angle for rhombohedral phases increases from 60.8° for $x = 0$ to 61.0° for $x = 0.1$ showing a slightly increased rhombohedral distortion with increasing Rh concentration. The possibility of ordering of Co and Rh on the octahedral sites was considered and was found not to occur for any value of x .

The continuous solid solution of $\text{LaCo}_{1-x}\text{Rh}_x\text{O}_3$ ($x = 0.2$ to 0.9) is found to be isostructural with perovskite LaRhO_3 [87]. The structure for this very common orthorhombic distortion of the cubic perovskite is described in space group #62. There are six different settings for this space group, each with its unique space group designation. The two most commonly used designations are Pnma and Pbnm . We have chosen to use the Pnma setting for the orthorhombic $\text{LaCo}_{1-x}\text{Rh}_x\text{O}_3$ phases. The cell volume increases as expected when replacing Co with larger Rh ions in the LaCoO_3 structure (Fig. 3.21(b)), mainly a result of the lattice expansion of the a cell edge. The c cell edge remains almost unchanged. The refined site occupancies for

Table 3.5 Structural parameters for $\text{LaCo}_{1-x}\text{Rh}_x\text{O}_3$ ($0.0 \leq x \leq 1.0$) system. The atomic positions of Co/Rh are at (0,0,0) and (0,0,1/2) in rhombohedral and orthorhombic structures, respectively.

Rh, x	Space Group	a , Å	b , Å	c , Å	V , Å ³	α , °	Rh, Occupancy		
0.0	R-3cR	5.3730(1)	5.3730(1)	5.3730(1)	111.67(1)	60.8(1)	0		
0.1	R-3cR	5.3928(1)	5.3928(1)	5.3928(1)	113.39(1)	61.0(1)	0.12(1)		
0.2	Pnma	5.4238(2)	7.7157(3)	5.4849(1)	229.53(1)	90	0.23(1)		
0.3	Pnma	5.4532(2)	7.7454(3)	5.4979(2)	232.22(1)	90	0.31(1)		
0.4	Pnma	5.4875(3)	7.7830(5)	5.5131(2)	235.46(1)	90	0.42(1)		
0.5	Pnma	5.5243(2)	7.8169(3)	5.5209(3)	238.41(1)	90	0.52(1)		
0.6	Pnma	5.5618(2)	7.8326(3)	5.5315(2)	240.97(1)	90	0.63(1)		
0.7	Pnma	5.6011(2)	7.8518(3)	5.5412(2)	243.69(1)	90	0.71(1)		
0.8	Pnma	5.6342(2)	7.8654(3)	5.5396(2)	245.49(1)	90	0.81(1)		
0.9	Pnma	5.6711(1)	7.8792(1)	5.5317(1)	247.18(1)	90	0.91(1)		
1.0	Pnma	5.6800(2)	7.8956(3)	5.5302(2)	248.01(1)	90	1		

Rh, x	La			O1			O2		
	x	y	z	x	y	z	x	y	z
0.0	1/4	1/4	1/4	0.205(2)	0.295(2)	3/4	—	—	—
0.1	1/4	1/4	1/4	0.1975(9)	0.3025(9)	3/4	—	—	—
0.2	0.4789(2)	1/4	0.4940(4)	0.229(2)	0.043(2)	0.771(2)	0.998(2)	1/4	0.506(5)
0.3	0.4733(2)	1/4	0.5035(6)	0.224(2)	0.043(2)	0.776(2)	0.002(2)	1/4	0.450(2)
0.4	0.4687(2)	1/4	0.5052(6)	0.217(2)	0.039(2)	0.783(2)	0.007(2)	1/4	0.439(3)
0.5	0.4637(2)	1/4	0.5058(4)	0.215(1)	0.039(1)	0.786(1)	0.008(2)	1/4	0.411(3)
0.6	0.4591(2)	1/4	0.5058(6)	0.207(1)	0.037(2)	0.792(2)	0.012(2)	1/4	0.404(2)
0.7	0.4548(3)	1/4	0.5060(6)	0.206(2)	0.041(2)	0.794(2)	0.010(2)	1/4	0.403(2)
0.8	0.4501(2)	1/4	0.5077(5)	0.209(1)	0.044(1)	0.791(1)	0.006(2)	1/4	0.397(2)
0.9	0.4463(1)	1/4	0.5118(2)	0.2037(9)	0.047(1)	0.796(1)	0.010(1)	1/4	0.393(2)
1.0	0.4446(2)	1/4	0.5132(3)	0.203(1)	0.048(1)	0.797(1)	0.013(2)	1/4	0.396(2)

Table 3.6 Bond distances (Å) and angles (°) for orthorhombic $\text{LaCo}_{1-x}\text{Rh}_x\text{O}_3$ ($0.2 \leq x \leq 1.0$).

	$x = 0.2$	$x = 0.3$	$x = 0.4$	$x = 0.5$	$x = 0.6$	$x = 0.7$	$x = 0.8$	$x = 0.9$	$x = 1.0$
M-O1, 2×	1.965(4)	1.978(3)	1.985(3)	1.995(4)	2.007(4)	2.021(4)	2.027(4)	2.036(4)	2.044(4)
M-O1, 2×	1.961(4)	1.973(3)	1.985(3)	1.994(4)	2.012(4)	2.031(4)	2.036(4)	2.059(4)	2.059(4)
M-O2	1.929(1)	1.956(2)	1.975(3)	2.015(4)	2.030(3)	2.036(3)	2.048(3)	2.058(3)	2.058(3)
La-O1, 2×	2.59(2)	2.58(2)	2.64(2)	2.65(1)	2.70(2)	2.68(2)	2.63(1)	2.63(1)	2.63(1)
La-O1, 2×	2.80(2)	2.81(2)	2.76(2)	2.75(1)	2.70(2)	2.73(2)	2.75(1)	2.76(1)	2.77(1)
La-O1, 2×	2.46(1)	2.428(9)	2.432(9)	2.445(8)	2.438(8)	2.428(8)	2.448(8)	2.414(6)	2.411(8)
La-O1, 2×	3.12(1)	3.203(9)	3.250(8)	3.291(8)	3.347(8)	3.406(8)	3.432(8)	3.508(6)	3.531(8)
La-O2	2.61(1)	2.59(1)	2.56(1)	2.57(1)	2.547(9)	2.55(1)	2.58(1)	2.56(1)	2.54(1)
La-O2	2.74(3)	2.50(1)	2.46(2)	2.32(2)	2.29(1)	2.29(1)	2.26(1)	2.27(1)	2.30(1)
La-O2	2.82(1)	2.90(1)	2.97(1)	3.05(1)	3.11(1)	3.16(1)	3.19(1)	3.26(1)	3.29(1)
La-O2	2.75(3)	3.01(1)	3.07(2)	3.23(2)	3.28(1)	3.29(1)	3.31(1)	3.32(1)	3.29(1)
O1-M-O1	92.2(1)	92.1(1)	91.6(1)	91.3(1)	90.9(1)	90.9(1)	90.8(1)	90.6(1)	90.5(1)
O1-M-O2	100.1(7)	93.6(6)	91.7(7)	91.9(7)	93.0(6)	92.3(6)	92.8(5)	92.5(4)	91.7(5)
O1-M-O2	100.5(6)	94.4(5)	92.0(6)	90.9(6)	92.2(5)	91.0(5)	90.5(4)	90.5(3)	90.4(4)
M-O1-M	158.5(6)	157.1(5)	156.8(5)	156.3(4)	154.7(5)	152.9(4)	153.0(4)	150.7(3)	150.1(4)
M-O2-M	177.9(5)	163.8(8)	160.4(5)	151.7(5)	149.5(7)	149.3(7)	147.5(6)	146.3(5)	147.2(6)

Rh are in good agreement with the intended substitution levels. Detailed crystallographic results for $\text{LaCo}_{1-x}\text{Rh}_x\text{O}_3$ are available in Tables 3.5 and 3.6. The correctness of our assignments of the a and c axes was verified by comparison with refinements where a and c were interchanged.

The most common perovskite tilt structure is the orthorhombic structure that we describe in the Pnma space group [68]. However, this tilt structure normally converts to a tilt structure of higher symmetry with increasing t before finally converting to the ideal cubic structure with no tilting. For RMO_3 phases where R is a trivalent rare earth cation, the Pnma orthorhombic structure transforms to a rhombohedral tilt structure with increasing t [69, 88]. Such behavior occurs for $\text{M} = \text{Co}, \text{Ni}, \text{ and Al}$ as the size of the rare earth cation increases [69]. However before the transformation to rhombohedral, there is a crossover of the cell edges of the orthorhombic phase such that $a = c = b/\sqrt{2}$ at the crossover point. The diffraction pattern at this point can be indexed as cubic even though the true symmetry remains orthorhombic. Tilting of ideal octahedra in Pnma necessarily results in $a > b/\sqrt{2} > c$. This is the order observed for the lower values of t , but after the crossover with increasing t the order becomes $a < b/\sqrt{2} < c$. This order can only be achieved through a distortion of the MO_6 octahedra, and a deviation of O-M-O angles of only 1° from 90° can account for the crossover [89].

The behavior that we observe for $\text{LaCo}_{1-x}\text{Rh}_x\text{O}_3$ phases with changing x is thus analogous to that reported for RMO_3 phases. As x for $\text{LaCo}_{1-x}\text{Rh}_x\text{O}_3$ phases decreases t increases, and there is first a crossover of the orthorhombic cell edges

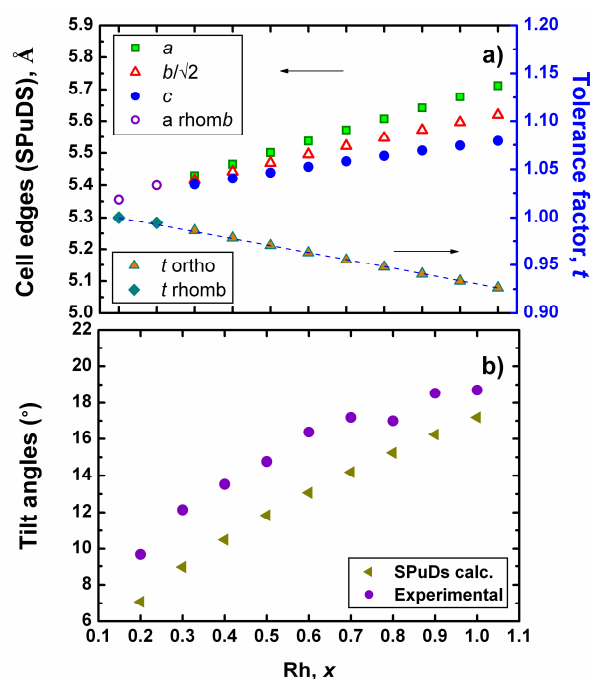


Figure 3.22 Cell edges and tolerance factor t calculated by SPuDS (a), and observed and predicted tilt angles calculated by Tubers and SPuDS, respectively (b).

and then a transformation to a rhombohedral structure. SPuDS software calculates t , cell dimensions and tilt angles based on cation sizes and an assumed tilt structure with ideal octahedra [90]. These values calculated with SPuDS for the $\text{LaCo}_{1-x}\text{Rh}_x\text{O}_3$ solid solution are shown in Fig. 3.22. As expected, SPuDS predicts a monotonic decrease of cell edges with decreasing x and a smooth transition to cubic symmetry. It cannot predict the crossover because the crossover cannot occur for the ideal octahedra assumed by SPuDS. The observed crossover point for $\text{LaCo}_{1-x}\text{Rh}_x\text{O}_3$ occurs at $x = 0.5$ where there are equal amounts of Rh and Co. The lattice strain caused by the orthorhombic distortion has become zero at the crossover point (Fig. 3.23). When the

octahedra become distorted, there is no longer a precise definition of the tilt angle.

However, using the equations of O’Keeffe and Hyde [91]

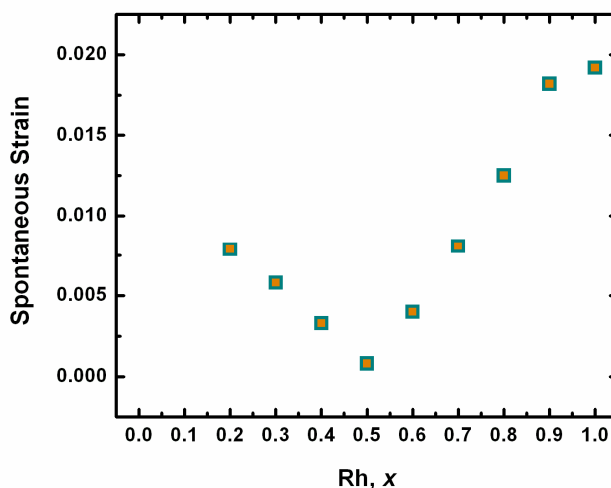


Figure 3.23 Compositional dependence of lattice strain $[2(a^2 + b^2 + c^2 - ab - bc - ca)/3a_0^2]^{1/2}$ caused by orthorhombic distortion.

the tilt angles (Fig. 3.22) were calculated from our refined O positions using Tubers software [90]. The slopes of the tilt angle vs. x curves are essentially the same from SPuDS and Tubers, but the values calculated from our refined structures are always somewhat higher.

An x value for the crossover of 0.5 might seem a mere coincidence, except that such behavior has been previously observed in the $\text{La}_{1-x}\text{Sr}_x\text{RuO}_3$ system [92]. The orthorhombic Pnma structure exists for all values of x in this system, but there is a crossover at $x = 0.5$ where there are equal amounts of La and Sr and of Ru^{3+} and Ru^{4+} . This suggests the possibility that the crossover point of $x = 0.5$ in both systems is not accidental and merits a more intensive study. The value of t is the same at the crossover point for both $\text{LaCo}_{1-x}\text{Rh}_x\text{O}_3$ and $\text{La}_{1-x}\text{Sr}_x\text{RuO}_3$, 0.96 as calculated by

SPuDS. However, the crossover point for the RNiO_3 series is found for NdNiO_3 where the value of t is 0.92 as calculated by SPuDS [69].

Bond distances and bond angles vs. composition for $\text{LaCo}_{1-x}\text{Rh}_x\text{O}_3$ phases are shown in Fig. 3.24 and 3.25. We know that the MO_6 octahedra must be

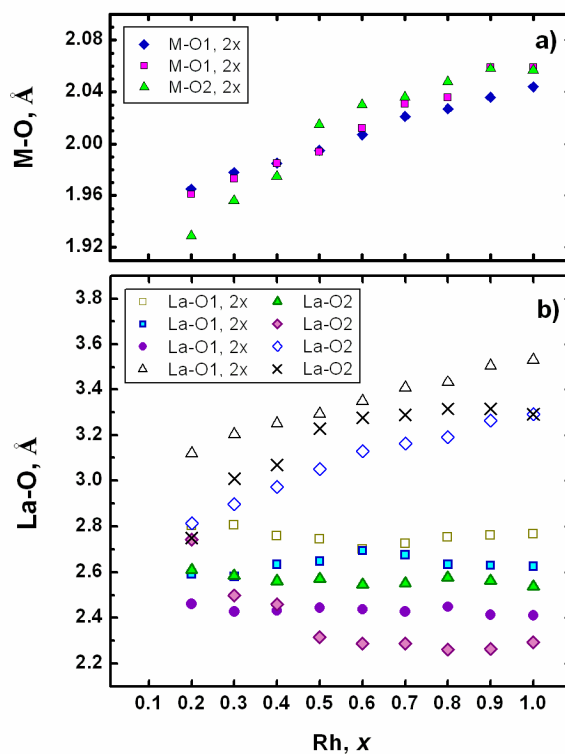


Figure 3.24 Bond distances vs. x in $\text{LaCo}_{1-x}\text{Rh}_x\text{O}_3$.

distorted on the Co rich side of the crossover, but some distortion is also expected on the Rh rich side because such distortion has been reported for LaRhO_3 [87]. We observe an increase in octahedral distortion with decreasing x and increasing t , and the distortion becomes more pronounced with regard to both bond angles and M-O distances on the Co rich side of the crossover. The shorter M-O distance along the b

axis at $x = 0.2$ is suggestive of orbital ordering for Co^{2+} , but further studies would be required to establish this. We cannot assume that the oxidation states of Co and

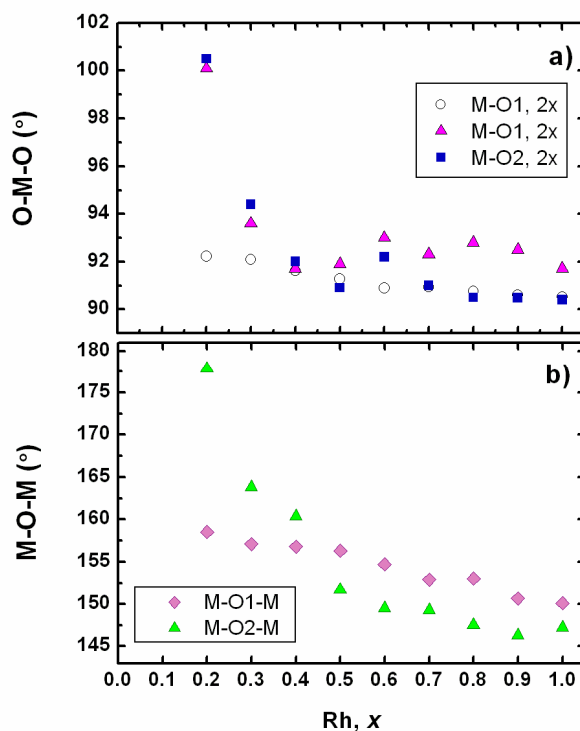


Figure 3.25 Bond angles vs. x in $\text{LaCo}_{1-x}\text{Rh}_x\text{O}_3$.

Rh are +3 in the solid solution. In the case of the $\text{LaCo}^{3+}\text{O}_3 - \text{CaRu}^{4+}\text{O}_3$ solid solution, the oxidation states are Co^{2+} and Ru^{5+} for the composition LaCaCoRuO_6 [93]. Furthermore, evidence is found at this composition for orbital ordering for Co^{2+} . The electronic configuration of $t_{2g}^5 e_g^2$ for high spin Co^{2+} favors a tetragonal distortion of an octahedron to produce 4 long and 2 short M-O distances, as observed in LaCaCoRuO_6 and apparently also at low x values in orthorhombic $\text{LaCo}_{1-x}\text{Rh}_x\text{O}_3$ phases. No configuration of Co^{3+} is expected to give such a distortion. This distortion of the

octahedra is facilitated in the low x orthorhombic $\text{LaCo}_{1-x}\text{Rh}_x\text{O}_3$ phases because the octahedron must be distorted on that side of the crossover.

3.5.2.2 Electrical Properties

Both Rh^{3+} and Co^{3+} are d^6 cations. For Rh^{3+} oxides the low spin state always pertains due to the gap of about 2.2 eV between the t_{2g} and e_g bands. Thus, Rh^{3+} oxides are insulating with room temperature resistivities higher than $10^6 \Omega\text{cm}$ unless they are doped, which may be inadvertent [44]. Doping or nonstoichiometry can lead to holes in the t_{2g} band or electrons in the e_g band, thus giving either p-type or n-type conductivity. The gap between the t_{2g} and e_g bands in Co^{3+} oxides is much less than for Rh^{3+} oxides. At the lowest temperatures all of the 3d electrons for LaCoO_3 are in the t_{2g} levels, which are filled giving low spin Co^{3+} . The gap to the e_g levels is so small that electrons from the t_{2g} levels are excited into these levels with increasing temperature [94]. On reaching 640 K there are equal amounts of low spin and high spin Co^{3+} . The excitations of electrons from t_{2g} to e_g levels do not necessarily occur on the same Co atom. Thus, this excitation creates some Co^{2+} and Co^{4+} , and this is believed to be an important aspect of the conduction process in LaCoO_3 [94]. As Rh is substituted for Co we see an increase in resistivity due to the dilution of the 3d electrons (Fig. 3.26).

The situation is much simpler on the Rh rich end of the $\text{LaCo}_{1-x}\text{Rh}_x\text{O}_3$ solid solution. The observed electrical conductivity for $x = 1.0$ (Fig. 3.26) is due to holes in

the Rh $4d$ t_{2g} band. The drop in both resistivity and Seebeck coefficient is most pronounced for the first 10% replacement of Co for Rh, especially noticeable at higher temperatures (Fig. 3.26). The increase in conductivity with the 10% Co substitution indicates that Co is an effective p-type dopant for LaRhO_3 . This is equivalent to the

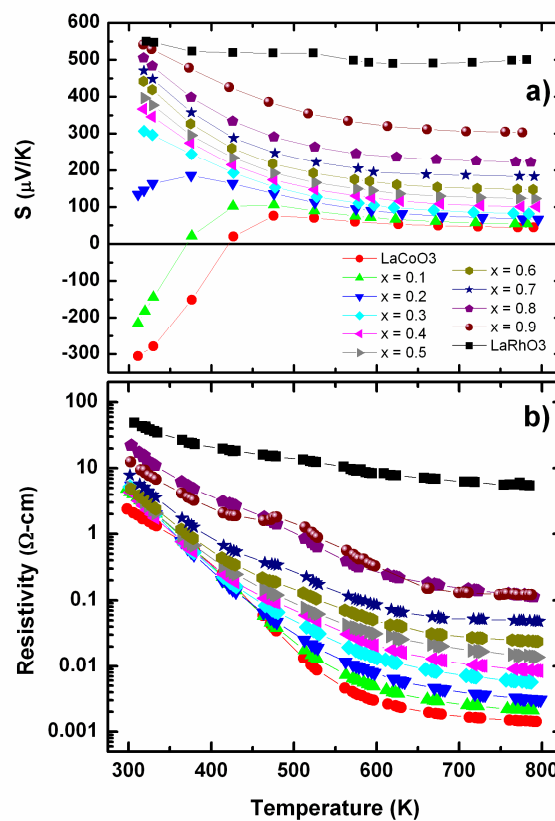


Figure 3.26 Temperature dependence of the Seebeck coefficient (a) and electrical resistivity (b) for $\text{LaCo}_{1-x}\text{Rh}_x\text{O}_3$.

conversion of $\text{Rh}^{3+}/\text{Co}^{3+}$ to $\text{Rh}^{4+}/\text{Co}^{2+}$. The positive deviation from linearity of the unit cell volume vs. composition plot (Fig. 2(b)) can now be explained because a $\text{Rh}^{4+}/\text{Co}^{2+}$ combination occupies more space than a $\text{Rh}^{3+}/\text{Co}^{3+}$ combination. The radius sum for $\text{Rh}^{4+}/\text{Co}^{2+}$ is 1.35 \AA compared to a radius sum for $\text{Rh}^{3+}/\text{Co}^{3+}$ of 1.21 or

1.27 Å, depending on whether Co^{3+} is low spin or high spin [65]. The positive deviation in Fig. 3.21(b) suggests that some conversion of $\text{Rh}^{3+}/\text{Co}^{3+}$ to $\text{Rh}^{4+}/\text{Co}^{2+}$ occurs over the entire range where both Co and Rh are present. This is thus a very complicated region where Rh^{3+} , Rh^{4+} , Co^{2+} , Co^{3+} (low-spin), and Co^{3+} (high-spin) are all present, and their relative amounts are likely changing with temperature.

The Seebeck coefficient behavior we find for LaCoO_3 with a crossover from negative to positive values at about 450 K is similar to that reported by He, et al. [79]. With increasing Rh substitution and increasing resistivity, the Seebeck coefficient (Fig. 3.26) also increases.

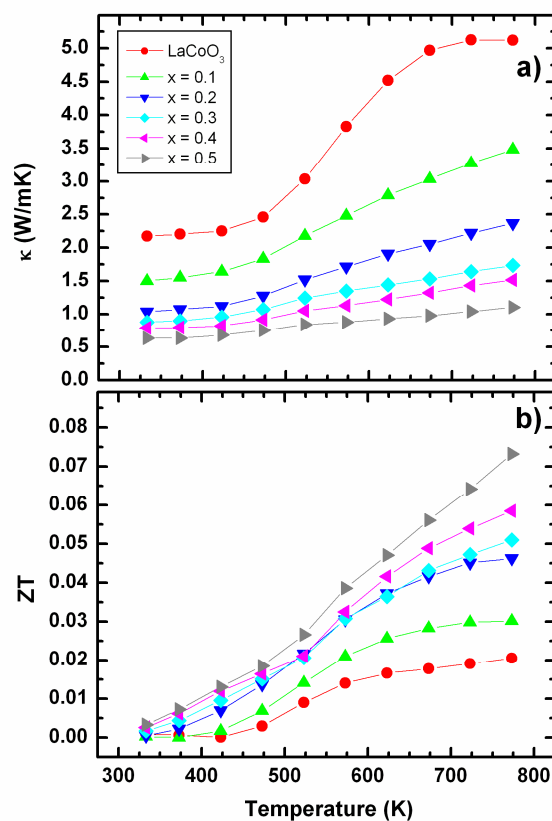


Figure 3.27 Temperature dependence of the thermal conductivity (a) and dimensionless figure-of-merit ZT (b) for $\text{LaCo}_{1-x}\text{Rh}_x\text{O}_3$.

The temperature dependence of thermal conductivity and ZT for $\text{LaCo}_{1-x}\text{Rh}_x\text{O}_3$ ($x = 0$ to 0.5) phases are shown in Fig. 3.27. The thermal conductivity of LaCoO_3 reported here is consistent with previous reports [79, 95, 96]. Substitution of Rh for Co decreases the thermal conductivity dramatically. Using the Wiedmann-Franz law, $\kappa = L_0 T / \rho$ (where $L_0 = 2.44 \times 10^{-8} \text{ V}^2/\text{K}^2$) and our experimental results, the electronic contribution to the thermal conductivity was calculated for LaCoO_3 ($\sim 13\%$ at $\sim 520 \text{ K}$) and $\text{LaCo}_{1-x}\text{Rh}_x\text{O}_3$ where $x = 0.1$ to 0.5 (9.5%, 6.5%, 4%, 2.5%, 2% respectively at 520 K). The electronic contribution to the thermal conductivity increases with increasing temperature. Thus, the lattice thermal conductivity is important and the introduction of Rh suppresses the electronic contribution to the total thermal conductivity. This reduction may be attributed to increased phonon scattering due to the lattice disruption caused by having Rh^{3+} , Rh^{4+} , Co^{2+} , Co^{3+} (low-spin), and Co^{3+} (high-spin) all occupying the octahedral sites. The large changes in the thermopower, resistivity, and thermal conductivity occur consistently in the same temperature range. An increase in the ZT occurs in $\text{LaCo}_{1-x}\text{Rh}_x\text{O}_3$ phases as x increases to 0.5 (Fig. 3.27). In all cases ZT increases with increasing temperature. A ZT of ~ 0.075 is obtained for $\text{LaCo}_{0.5}\text{Rh}_{0.5}\text{O}_3$ at 775 K . It is expected that the ZT of this sample may reach as high as 0.15 at $T = 1000 \text{ K}$ based on best fit approximations.

3.5.2.3 Magnetic Properties

The magnetic properties of LaCoO_3 have been previously investigated by many

groups. The $1/\chi$ vs. T plot (Fig. 3.28) for LaCoO_3 might suggest Curie-Weiss behavior above ~ 150 K. However, we know that there is actually no temperature

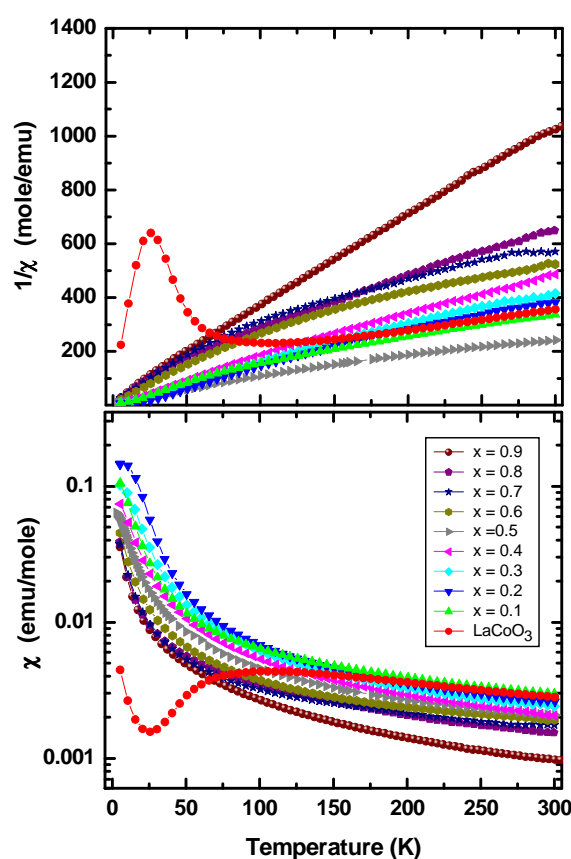


Figure 3.28 Magnetic susceptibility (a) and inverse susceptibility (b) for $\text{LaCo}_{1-x}\text{Rh}_x\text{O}_3$ measured at 0.5 Tesla.

region of Curie-Weiss behavior for LaCoO_3 . This is because the relative amount of high spin Co^{3+} is steadily increasing with increasing temperature. The situation becomes even more complex in the $\text{LaCo}_{1-x}\text{Rh}_x\text{O}_3$ solid solution because Rh^{3+} , Rh^{4+} , Co^{2+} , Co^{3+} (low-spin), and Co^{3+} (high-spin) are all present, and the relative amounts of these species are likely temperature dependent at each composition. Thus, an interpretation of the plots as Curie-Weiss behavior is not possible.

3.5.3 Effect of Sr on the thermoelectric performance of $\text{LaCo}_{1-x}\text{Rh}_x\text{O}_3$

In an effort to improve the thermoelectric properties of Rh substituted LaCoO_3 , samples were also prepared with Sr substitution for La. All Sr substituted samples were indexed with an orthorhombic structure. A previous report by Androulakis, 2004, showed that slight Sr substitution of the A site in LaCoO_3 significantly improved the ZT from negligible to $ZT \sim 0.18$ at room temperature [73]. A later report by Iwasaki, 2008, was unable to reproduce the high ZT at room temperature and observed a value of $ZT = \sim 0.045$ instead [95]. It should be noted however, that these reports are different by the processing method and may provide a key to the importance of grain size on the thermoelectric properties.

The Seebeck coefficient (Figure 3.29) is large and positive for all samples indicating again holes as the conduction means. As expected, when Sr is present in the structure, there is no transition from negative to positive Seebeck coefficient for $x = 0.1$ due to the increased number of holes in the conduction band. A gradual decrease in the Seebeck coefficient over the temperature range can be seen for all samples, but is higher than that reported, again showing that the Rh substitution increases the overall Seebeck character. Increases in the Seebeck coefficient have also been reported elsewhere [59]. These values are reasonable considering the observed values by Iwasaki for $\text{La}_{0.95}\text{Sr}_{0.05}\text{CoO}_3$. Sr substitution decreases the resistivity (Figure 3.29) considerably in all samples compared to LaCoO_3 , and are semiconducting similar to Rh substituted samples. Samples containing Sr are better

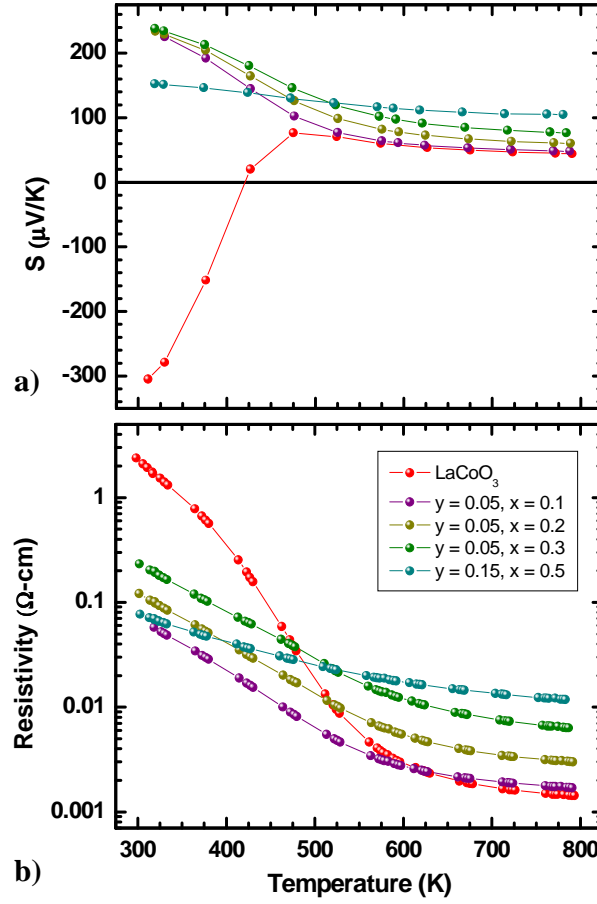


Figure 3.29 Temperature dependence of the Seebeck coefficient (a) and electrical resistivity (b) for $\text{La}_{1-y}\text{Sr}_y\text{Co}_{1-x}\text{Rh}_x\text{O}_3$ samples from 300 to 800 K.

conductors at lower temperatures, but do not show such substantial differences at high temperatures. The commonly low values of thermopower in highly conducting samples tend to yield lower power factors. Sr and Rh co-doping may provide a route around this trend. Thermal conductivity and figure-of-merit of $\text{La}_{1-y}\text{Sr}_y\text{Co}_{1-x}\text{Rh}_x\text{O}_3$ are shown in Figure 3.30. Sr substitution decreases the total thermal conductivity of all samples in $\text{LaCo}_{1-x}\text{Rh}_x\text{O}_3$ compared to samples without Sr. From experimental values, the calculated electronic contribution to the total

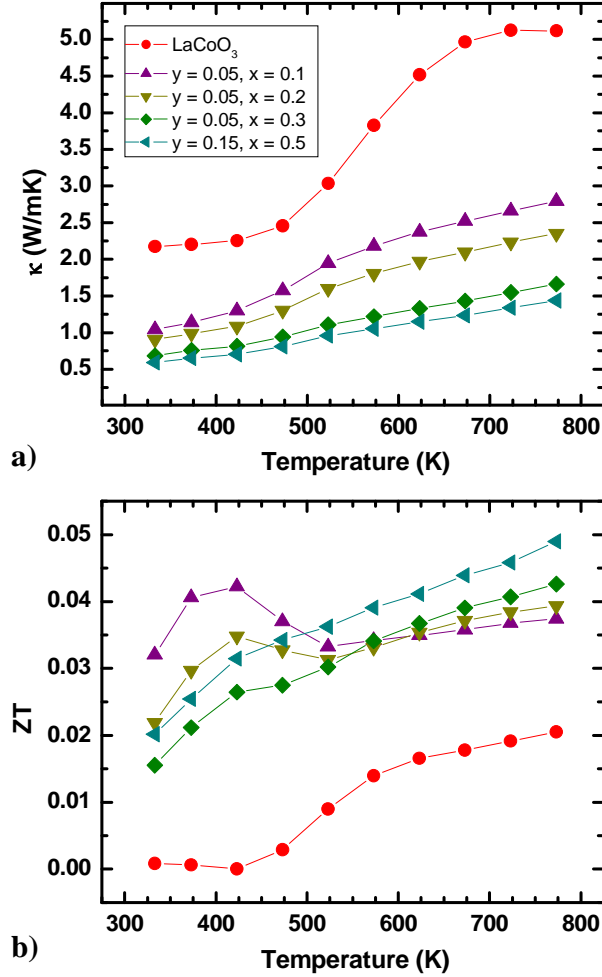


Figure 3.30 Temperature dependence of the thermal conductivity (a) and dimensionless figure-of-merit, ZT , for $\text{La}_{1-y}\text{Sr}_y\text{Co}_{1-x}\text{Rh}_x\text{CrO}_3$ from 300 to 800 K

thermal conductivity was 26.75%, 12.75%, 5.75% and 5.70% for $\text{La}_{1-y}\text{Sr}_y\text{Co}_{1-x}\text{Rh}_x\text{CrO}_3$ where $y = 0.05$ and $x = 0.1, 0.2, 0.3$ and $y = 0.15$ and $x = 0.5$ respectively. The values represent increases in the electronic contribution and are similarly observed in other A-site to substituted samples [79]. This contribution would correspondingly be attributed the reduction of the lattice thermal conductivity through lattice strain from A-site disorder in addition to B-site disorder and the combination of several oxidation

states and spin states for Co and Rh. As can be seen, the ZT is improved for all Sr substituted samples in the full temperature range compared to LaCoO_3 . A peak in the ZT is observed at ~ 425 K for all Sr substituted samples before decreasing and again increasing. For $\text{La}_{0.95}\text{Sr}_{0.05}\text{Co}_{0.9}\text{Rh}_{0.1}\text{O}_3$, a $ZT = 0.045$ is observed at 425 K representing an improvement as the absence of Sr in the same Rh compositions are all well below $ZT \sim 0.02$.

3.5.4 Conclusions

We have no explanation as to why crossover of lattice parameters occurs in both the $\text{LaCo}_{1-x}\text{Rh}_x\text{O}_3$ and $\text{La}_{1-x}\text{Sr}_x\text{RuO}_3$ systems at $x = 0.5$, and perhaps this is accidental. It is, however, the value of x where charge ordering is most likely to occur. Charge ordering of Ru^{3+} and Ru^{4+} might seem a possibility in the $\text{La}_{1-x}\text{Sr}_x\text{RuO}_3$ system, but this will be impeded by the disorder of La and Sr on the A sites and by the delocalized nature of the $4d$ electrons of Ru. Likewise, charge order would be very difficult in the $\text{LaCo}_{1-x}\text{Rh}_x\text{O}_3$ system considering the likely simultaneous presence of Rh^{3+} , Rh^{4+} , Co^{2+} , Co^{3+} (low-spin), and Co^{3+} (high-spin) species. Furthermore, it is not obvious how charge ordering might relate to the crossover. There are no reported structure refinements near the crossover for the $\text{La}_{1-x}\text{Sr}_x\text{RuO}_3$ system, and our structure refinements in the $\text{LaCo}_{1-x}\text{Rh}_x\text{O}_3$ system are not very accurate. We plan to refine structures close to the crossover point in both systems using neutron diffraction data. This should also help define whether there is a good basis for orbital ordering

for Co^{2+} . Although there is reason to believe that some conversion of $\text{Rh}^{3+}/\text{Co}^{3+}$ to $\text{Rh}^{4+}/\text{Co}^{2+}$ occurs in the $\text{LaCo}_{1-x}\text{Rh}_x\text{O}_3$ system, the degree to which this occurs is uncertain. Resolving this would be a very challenging spectroscopic study. Our transport measurements indicate that increasing rhodium in the $\text{LaCo}_{1-x}\text{Rh}_x\text{O}_3$ system improves thermoelectric properties, and Sr substitution in this system improve the thermoelectric properties at lower temperatures.

3.5.5 Experimental

Polycrystalline samples of $\text{LaCo}_{1-x}\text{Rh}_x\text{O}_3$ ($x = 0 - 1$) were synthesized using traditional solid state methods. Starting materials of La_2O_3 (Aldrich 99.9%), SrCO_3 (Aldrich 99.9+%), Co_3O_4 (Alfa Aesar 99%), and Rh_2O_3 were mixed thoroughly in appropriate ratios. Rh_2O_3 was obtained by the oxidation of RhI_3 (JMC 98%) in an oxygen gas flow at 700°C for 12 hours. La_2O_3 was dried at 850°C overnight and SrCO_3 was dried at 80°C 3-5 hours before weighing. The mixed powders of starting materials were calcined at 1200°C for 12 hours in air with ramp rates of 300°C/hr . The samples were reground and sintered twice in air at 1250°C for 12 hours with a ramp up rate of 150°C/hr and a ramp down rate of 100°C/hr . LaRhO_3 was prepared by heating at 1200°C in an oxygen gas flow. The reacted powders were cold pressed before sintering. Powder X-ray diffraction data were collected with a Rigaku MiniFlex II powder diffractometer using $\text{Cu K}\alpha$ radiation and a graphite monochromator on the diffracted beam. The electrical resistivities and Seebeck coefficients were measured

from 300 to 800 K by a standard four-probe technique with a ULVAC-ZEM themoanalyzer in a He atmosphere. The Seebeck coefficient was measured with constantan as a reference. The absolute uncertainty in both parameters is estimated to be below 5%. The thermal conductivity was determined using a Netzsch Laser Microflash with reference material of graphite-coated Pyroceram for diffusivity and the heat capacity was assumed to be that of LaCoO_3 . The samples were measured without graphite coatings. Magnetism was measured with a PPMS Physical Property Measurement System from 5 to 300 K under an applied field of 0.5 Tesla.

3.6 References

1. A. Navrotsky, D.J. Wiedner, *Perovskite: A Structure of Great Interest to Geophysics and Materials Science*, American Geophysical Union, Washington, D.C., 1989; vol 45, pp xi.
2. P.M. Woodward. *Structural Distortions, Phase Transitions, and Cation Ordering in the Perovskite and Tungsten Trioxide Structures*, Ph.D. Thesis, Oregon State University, Corvallis, OR, 1996
3. R. H. Mitchell. *Perovskites-Modern and Ancient*, Alamaz Press Inc.: Ontario, Canada, 2002
4. W. D. Kingery, H. K. Bowen, D. R. Uhlmann. *Introduction to Ceramics*, 2nd ed.; John Wiley & Sons: New York, 1976
5. M. A. Subramanian, D. Li, N. Duan, B.A. Reisner, A.W. Sleight. *J. Sol. State Chem.*, 151 (2000) 323
6. A.R. West. *Basic Solid State Chemistry*, 2nd ed.; John Wiley & Sons: New York, 1999
7. B. Raveau, A. Maignan, C. Martin, M. Hervieu, *Chem. Mater.*, 10 (1998) 2641
8. N.S. Rogado, J. Li, A.W. Sleight, M.A. Subramanian, *Adv. Mater.* 2005, 17, 2225-2227

9. A.W. Sleight, J.L. Gillson, P.E. Bierdstedt, *Solid State Comm.*, 17 (1975) 27
10. V.M. Goldschmidt, *Naturwissenschaften* 14 (1926) 477
11. H. Guo, J. Burgess, S. Street, A. Gupta, T. G. Calvarese, and M. A. Subramanian, *Appl. Phys. Lett.*, 89 (2006) 022509
12. H. Guo, A. Gupta, T. G. Calvarese, and M. A. Subramanian, *Appl. Phys. Lett.*, 89 (2006) 262503
13. M. Hashisaka, D. Kan, A. Masuno, M. Takano, and Y. Shimakawa, *Appl. Phys. Lett.*, 89 (2006) 032504
14. S. Zhou, L. Shi, H. Yang, and J. Zhao, *Appl. Phys. Lett.*, 91 (2007) 172505
15. K. D. Truong, J. Laverdiere, M. P. Singh, S. Jandl, and P. Fournier, *Phys. Rev. B*, 76 (2007) 132413
16. M. P. Singh, K. D. Truong, and P. Fournier, *Appl. Phys. Lett.*, 91 (2007) 042504
17. M. P. Singh, C. Grygiel, W. C. Sheets, P. Boullay, M. Hervieu, W. Prellier, B. Mercey, C. Simon, and B. Raveau, *Appl. Phys. Lett.*, 91 (2007) 012503
18. M. P. Singh, S. Charpentier, K. D. Truong, and P. Fournier, *Appl. Phys. Lett.*, 90 (2007) 211915
19. S. F. Matar, M. A. Subramanian, A. Villesuzanne, V. Eyert, and M. H. Whangbo, *J. Mag. Magn. Mater.*, 308 (2007) 116
20. M. N. Iliev, H. Guo, and A. Gupta, *Appl. Phys. Lett.*, 90 (2007) 151914
21. M. N. Iliev, M. V. Abrashev, A. P. Litvinchuk, V. G. Hadjiev, H. Guo, and A. Gupta, *Phys. Rev. B*, 75 (2007) 104118
22. H. Z. Guo, A. Gupta, J. Zhang, M. Varela, and S. J. Pennycook, *Appl. Phys. Lett.*, 91 (2007) 202509
23. P. Padhan, H. Z. Guo, P. LeClair, and A. Gupta, *Appl. Phys. Lett.*, 92 (2008) 022909
24. H. Z. Guo, J. Burgess, E. Ada, S. Street, A. Gupta, M. N. Iliev, A. J. Kellock, C. Magen, M. Varela, and S. J. Pennycook, *Phys. Rev. B*, 77 (2008) 174423

25. H. Das, U. V. Waghmare, T. Saha-Dasgupta, and D. D. Sarma, *Phys. Rev. Lett.*, 100 (2008) 186402
26. N. S. Rogado, J. Li, A. W. Sleight, and M. A. Subramanian, *Adv. Mater.*, 17 (2005) 2225
27. R. I. Dass, J.-Q. Yan, and J. B. Goodenough, *Phys. Rev. B*, 68 (2003) 064415
28. W. Eerenstein, N. D. Mathur, and J. F. Scott, *Nature*, 442 (2006) 759
29. M. T. Haque, H. Satoh, and N. Kamegashira, *J. Alloys Compd.*, 390 (2005) 115
30. M. T. Haque and N. Kamegashira, *J. Alloys Compd.*, 395 (2005) 220
31. M. T. Haque, H. Satoh, and N. Kamegashira, *Mater. Res. Bull.*, 39 (2004) 375
32. M. T. Haque, H. Satoh, and N. Kamegashira, *Mater. Lett.*, 58 (2004) 1571
33. C. Schinzer, *J. Phys. Chem. Solids*, 61 (2000) 1543
34. R. C. Currie, J. F. Vente, E. Frikkee, and D. J. W. Ijdo, *J. Solid State Chem.*, 116 (1995) 199
35. A. V. Powell, J. G. Gore, and P. D. Battle, *J. Alloys Compd.*, 201 (1993) 73
36. J. Blasco, M. C. Sanchez, J. Perez-Cacho, J. Garcia, G. Subias, and J. Campo, *J. Phys. Chem. Solids*, 63 (2002) 781
37. C. L. Bull, D. Gleeson, and K. S. Knight, *J. Phys.: Condens. Matter*, 15 (2003) 4927
38. J. B. Goodenough, *J. Phys. Chem. Solids*, 6 (1958) 287
39. J. Kanamori, *J. Phys. Chem. Solids*, 10 (1959) 87
40. R. I. Dass and J. B. Goodenough, *Phys. Rev. B*, 67 (2003) 014401
41. M. Filippi, B. Kundys, R. Ranjith, A. K. Kundu, and W. Prellier, *Appl. Phys. Lett.*, 92 (2008) 212905
42. G. Catalan, *Appl. Phys. Lett.*, 88 (2006) 102902
43. J. F. Scott, *J. Mater. Res.*, 22 (2007) 2053

44. H.S. Jarrett, A.W. Sleight, H.H. Kung, J.L. Gilson, *J. Appl. Phys.*, 51 (1980) 3916
45. L. Giebeler, D. Kiebling, G. Wendt, *Chem. Eng. Tech.*, 30 (2007) 889
46. H. Mizoguchi, M. Hirano, S. Fujitsu, T. Takeuchi, K. Ueda, H. Hosono, *Appl. Phys. Lett.*, 80 (2002) 1207
47. I. Terasaki, N. Murayama (Eds.), *Oxide Thermoelectrics*, Research Signpost, Trivandrum, India, (2002)
48. T. Kyomen, Y. Asaka, M. Itoh. *Phys. Rev. B*, 67 (2003) 144424
49. M.A. Senaris-Rodriguez, J.B. Goodenough, *J. Solid State Chem.*, 118 (1995) 323
50. K. Kurosaki, H. Muta, M. Uno, S. Yamanaka, *J. Alloys Comp.*, 315 (2001) 234
51. T. Seetawan, V. Amornkitbamrung, T. Burinprakhon, S. Maensiri, K. Kurosaki, H. Mutab, M. Uno, and S. Yamanaka, *J. Alloys Comp.*, 407 (2006) 314
52. H. Kuriyama, M. Nohara, T. Sasagawa, K. Takubo, T. Mizokawa, K. Kimura, H. Takagi, *International Conference on Thermoelectrics* (2006), 25th(Pt. 1), 97-98
53. H. Mizoguchi, W. J. Marshall, A.P. Ramirez, A.W. Sleight, and M.A. Subramanian, *J. Solid State Chem.*, 180 (2007) 3463
54. H. Mizoguchi, A.P. Ramirez, L. N. Zakharov, A.W. Sleight, M.A. Subramanian, *J. Solid State Chem.*, 181 (2008) 56
55. H. Mizoguchi, L. N. Zakharov, A. P. Ramirez, A. W. Sleight, M. A. Subramanian, *Inorg. Chem.*, 48 (2009) 204
56. H. Mizoguchi, L. N. Zakharov, W. J. Marshall, A. W. Sleight, M. A. Subramanian, *Chem. Mater.*, 21 (2009) 994
57. K. Hayashi, T. Nozaki, T. Kajitani, *Jap. J. Appl. Phys.*, 46 (2007) 5226
58. S. Shibusaki, W. Kobayashi, I. Terasaki, *Phys. Rev. B*, 74 (2006) 235110
59. S Shibusaki, Y Takahashi and I Terasaki, *J. Phys.: Condens. Matter*, 21 (2009) 115501

60. K.-S. Kwong, Andrew E. Smith, M.A. Subramanian, *Mat. Res. Soc. Symp. DD: Thermoelectric Materials*, (In press: vol. 1267) (2010)
61. C. Schinzer, *J. Alloys Comp.*, 288 (1999) 65
62. P.D. Battle, J.F. Vente, *J. Solid State Chem.*, 146 (1999) 163
63. C. Schinzer, and G. Demazeau, *J. Mater. Sci.*, 34 (1999) 251
64. C. Zobel, M. Kriener, D. Bruns, J. Baier, M. Gruninger, T. Lorenz, *Phys. Rev. B*, 66 (2002) 020402
65. R.D. Shannon. *Acta Cryst. A*, 32 (1976) 751
66. A.M. Glaser, *Acta Cryst. B*, 28 (1972) 3384
67. P.M. Woodward, *Acta Cryst. B* 53 (1997) 32
68. P.M. Woodward, *Acta Cryst. B*, 53 (1997) 44
69. P. Lacorre, J.B. Torrance, J. Pannetier, A.I. Nazzari, P.W. Wang, Y.C. Huang, *J. Solid State Chem.*, 91 (1991) 225
70. Y. Zhao, *J. Solid State Chem.*, 141 (1998) 121
71. A. Yoshiasa, D. Sakamoto, H. Okudera, M. Ohkawa, K. Ota, *Mat. Res. Bull.*, 38 (2003) 421
72. F. C. Galasso, *Perovskites and High Tc Superconductors*, Gordon and Breach Science Publishers, New York, 1990
73. J. Androulakis, P. Migiakis, J. Giapintzakis, *Appl. Phys. Lett.*, 84 (2004) 1099
74. Y. Wang, Y. Suia, J. Cheng, X. Wang, W. Su., *J. Alloys Compd.*, 477 (2009) 817
75. K. Kurosaki, H. Muta, M. Uno, S. Yamanaka, *J. Alloys Compd.*, 315 (2001) 234
76. T. Seetawan, V. Amornkitbamrung, T. Burinprakhon, S. Maensiri, K. Kurosaki, H. Mutab, M. Uno, and S. Yamanaka, *J. Alloys Compd.*, 407 (2006) 314
77. T. M. Tritt, M. A. Subramanian, *Mat. Res. Soc. Bull.*, 31 (2006) 188
78. A. E. Smith, A. W. Sleight, M. A. Subramanian, *Mat. Res. Bull.*, 45 (2010) 460

79. T. He, J. Chen, T.G. Calvarese, M.A. Subramanian, *Solid State Sci.*, 8 (2006) 467
80. S. Shibasaki, Y Takahashi and I. Terasaki, *J. Electronic Mat.*, 38 (2009) 1013
81. M. Kriener, C. Zobel, A. Reichl, J. Baier, M. Cwik, K. Berggold, H. Kierspel, O. Zabara, A. Freimuth, and T. Lorenz, *Phys. Rev. B*, 69 (2004) 094417
82. P.R. Watson, G.A. Somorjai, *J. Catal.*, 74 (1982) 282
83. N.N. Lubinskii, L.A. Bashkirov, G.S. Petro, S.V. Schevchenko, I.N. Kandidatova, M.V. Bushinskii, *Glass and Ceramics*, 66 (2009) 59
84. A.C. Larson, R.B. Von Dreele, "General Structure Analysis System (GSAS)," Los Alamos National Laboratory Report LAUR 86-784 (2004)
85. B.H. Toby, EXPGUI, a graphical user interface for GSAS, *J. Appl. Cryst.*, 34 (2001) 210
86. K.A.Gschneiderner, G.H. Vineyard, *J Appl. Phys.*, 33 (1962) 3444.
87. R.B. Macquart, M.D. Smith, H.C. zur Loye, *Cryst. Growth Design*, 6 (2006) 1361
88. J.-S. Zhou, J.B. Goodenough, *Phys. Rev. Lett.* 94 (2005) 065501
89. P.M. Woodward, T. Vogt, D.E. Cox, A. Arulraj, C.N.R. Rao, P. Karen, A.K. Cheetham, *Chem. Mater.*, 10 (1998) 3652
90. M.W. Lufaso, P.M. Woodward, *Acta Cryst. B*, 57 (2001) 725
91. M. O'Keeffe, B.G. Hyde, *Acta Cryst. B.*, 33 (1977) 3802
92. R.J. Bouchard, J.F. Weiher, *J. Solid State Chem.*, 3 (1972) 80
93. J.W.G. Bos, J.P. Attfield, L.-Y. Jang, *Phys. Rev. B*, 72 (2005) 014101
94. M.A. Senaris-Rodriguez, J.B. Goodenough, *J. Solid State Chem.*, 116 (1995) 224
95. K. Iwasaki, T. Ito, T. Nagasaki, Y. Arita, M. Yoshino, T. Matsui, *J. Solid State Chem.*, 181 (2008) 3145
96. C. G. S. Pillai, A. M. George, *Int. J. Thermophys.*, 4 (1983) 183

Chapter 4

Effect of Cation Substitution on the Structure, Magnetic, Electrical and Optical Properties of Hexagonal YMnO₃ Based Oxides

4.1 Abstract

In this chapter we discuss the synthesis and physical properties of some new hexagonal oxides based on YMnO₃. For the first time, we have prepared complete solid solutions in YInO₃ – YMnO₃, YAlO₃ – YMnO₃ and YCu_{0.5}Ti_{0.5}O₃ – YMnO₃ systems. The YInO₃ – YMnO₃ solid solution was found to exhibit an interesting change in the structure and thus corresponding properties. We have discovered that a surprisingly intense bright-blue color is obtained when Mn³⁺ is introduced into the trigonal bipyramidal sites of metal oxides. We observe a blue color over much of the YIn_{1-x}Mn_xO₃ solid-solution range, in spite of the fact that YInO₃ and YMnO₃ are white and black, respectively. We conclude that the blue color is a consequence of both the crystal field splitting associated with the trigonal bipyramidal coordination and the short apical Mn-O bonds. In addition, the magnetic, dielectric, and thermodynamic properties of In substituted YMnO₃ were investigated to elucidate the suppression of the multiferroic phase developing below T_N. We find that the magnetodielectric coupling associated with the multiferroic phase persists in the In substituted samples, but that T_N decreases approximately linearly with increasing In fraction. We have found that there is a significant enhancement in the magnitude magnetocapacitive coupling with In substitution, although the sign of this coupling varies with x through some mechanism that is not at all clear at this time.

The co-substitution of Cu^{2+} and Ti^{4+} (in equal quantities) into the hexagonal YMnO_3 compound at the Mn site yielded the hexagonal structure. All Mn compositions were black. Suppression of magnetic transitions are observed upon co-doping of Cu/Ti into YMnO_3 , and this is comparable to previous reports of Ga, In, and Cu/Mo substitutions. The Neel temperatures determined from magnetic susceptibility and capacitance measurements agree well for values dropping from 73.1 K to 45.5 K to 10.5 K for $x = 0, 0.2$ and 0.4 respectively. Field dependent capacitance is needed to properly asses these materials as magneto-electric multiferroics. Al substitution into pale green $\text{YCu}_{0.5}\text{Ti}_{0.5}\text{O}_3$ enhanced the color resulting in an intense green. Optical measurements agree well with the observed color and are consistent with optical properties observed for $\text{YIn}_{1-x}\text{Mn}_x\text{O}_3$.

In light of our discoveries in $\text{YIn}_{1-x}\text{Mn}_x\text{O}_3$ as a blue chromophore, it was determined that the cost of such materials as pigments is hampered mainly by the expense of indium. Our initial interest in YAlO_3 , also having the hexagonal structure, was for use as a platform for cheaper blue inorganic pigments, as the cost of Al much less compared to In. The structure of YAlO_3 , however, has not been recently addressed, and a close investigation of the last and only structural description revealed improper bond valence values. Our investigations of IR-spectroscopy, acid tests, and TGA concluded that a CO_3 group is likely present in the basal plane, and that for YAlO_3 and Mn substituted compositions, the formulas may be more properly written as $\text{YAlO}_{3-x}(\text{CO}_3)_x$ and $\text{YAl}_{1-x}\text{Mn}_x\text{O}_{3-y}(\text{CO}_3)_y$.

Publications based on this chapter:

- 1) Smith, Andrew E., Mizoguchi, Hiroshi, Delaney, Kris, Spaldin, Nicola A., Sleight, Arthur W., Subramanian, M. A., Mn^{3+} in Trigonal Bipyramidal Coordination: a New Blue Chromophore. *Journal of the American Chemical Society*, 191 (2009) 17084-17086
- 2) Dixit, A., Smith, Andrew E., Subramanian, M. A., Lawes, G., Suppression of multiferroic order in hexagonal $\text{YMn}_{1-x}\text{In}_x\text{O}_3$ ceramics. *Solid State Communications*, 150 (15-16) (2010) 746-750
- 3) Smith, Andrew E., Sleight, A. W., Subramanian, M. A. Synthesis and magnetism of YMnO_3 - $\text{Y}(\text{Cu}_{0.5}\text{Ti}_{0.5})\text{O}_3$ ceramics. (To submit to *Materials Research Bulletin* 2010).
- 4) Smith, Andrew E., Li, J., Sleight, A. W., Subramanian, M. A. Structural investigation of YMnO_3 - YAlO_3 solid solution (In preparation).

4.2 Introduction

In recent years, there has been a renewed interest in multiferroic materials based on perovskites and hexagonal structures. This interest stems from the potential applications ranging from multiple state memory elements, transformers, transducers and spintronics, to current controlled magnetic valves, GMR reed heads and magnetic field sensors [1, 2]. Multiferroism is a general term for a class of materials having more than one of the ‘ferroic’ properties; ferromagnetism (including antiferromagnetism or ferrimagnetism), ferroelectricity, and ferroelasticity. In multiferroics, these properties generally have a strong coupling where the magnetization (M), electric polarization (P), and strain (ϵ) can be manipulated by a magnetic field (H), electric field (E), and stress (σ) respectively (Fig. 4.1).

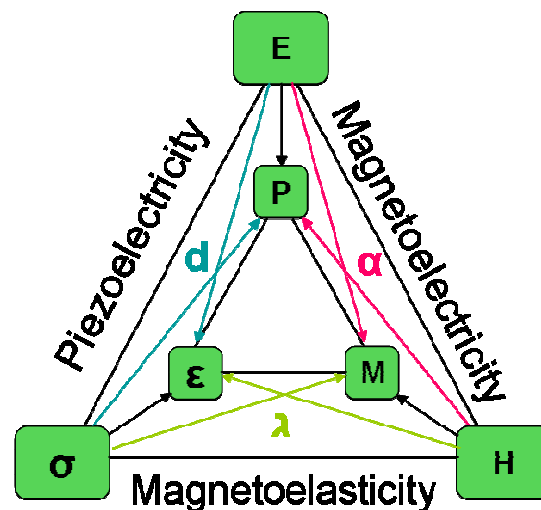


Figure 4.1 Interrelationships of the properties of multiferroics; ferromagnetism, ferroelectricity, and ferroelasticity. Adapted from N.A. Spaldin et al [2].

In a ferroic material, M , P , or ε occur spontaneously resulting in ferromagnetism, ferroelectricity, or ferroelasticity, respectively. Those materials possessing ferromagnetism (a linear change in the magnetization as a result of an applied electric field) and ferroelectricity (a linear change in the polarization as a result of an applied magnetic field) are known as magnet-oelectric multiferroics. Multiferroics are exceedingly rare materials with few existing in nature and few synthesized in the laboratory. The difficulty in preparation is due to the contradicting properties where magnetism arises from partially filled atomic orbitals (d^n where $n = 1 - 9$) and electric dipoles arise from either empty or filled atomic orbitals (d^n where $n = 0, 10$) and/or where electron lone pairs are present. These properties are thus considered chemically incompatible.

Nickel Iodine boracite, ($\text{Ni}_3\text{B}_2\text{O}_{13}\text{I}$) was the first material to show multiferroism with ferroelectric and ferromagnetic behavior coexisting below 64 K [1]. There has since been a heightened interest in discovering novel materials with such magnetoelectric coupling. Some of the better known materials include BiMnO_3 [3], BiFeO_3 [4], Pb_2CoWO_6 [5], RMn_2O_5 [6], and RMnO_3 [7] ($R = \text{Y}$ and $\text{Dy} - \text{Lu}$) [8], all of which have the perovskite or hexagonal structure. BiFeO_3 , a perovskite, is currently the only material to exhibit coupling between the magnetic and electric order parameters above room temperature (AFM 643 K, FE 1100 K).

Rare-earth manganites of the RMnO_3 formula, where R is trivalent, crystallize in two structures depending on the ionic radius of the rare earth. For those rare earths with large ionic radii, $\text{La} - \text{Dy}$, the orthorhombic (Pnma) perovskite structure is

prevails, and for those rare earths with small ionic radii, Y and Ho – Lu, the hexagonal ($P6_3cm$) structure is prevails. When $R = \text{La} - \text{Dy}$, RMnO_3 has the orthorhombically distorted perovskite structure, Figure 4.2, with Mn^{3+} occupying an octahedral coordination with oxygen. The octahedral coordination, however, is not ideal due to the Jahn-Teller effect of Mn^{3+} which causes orbital ordering. A cooperative rotational distortion of the polyhedra is due to the size mismatch between the bond lengths of Mn-O and R-O. These octahedra are corner connected and share a Mn-O-Mn bond

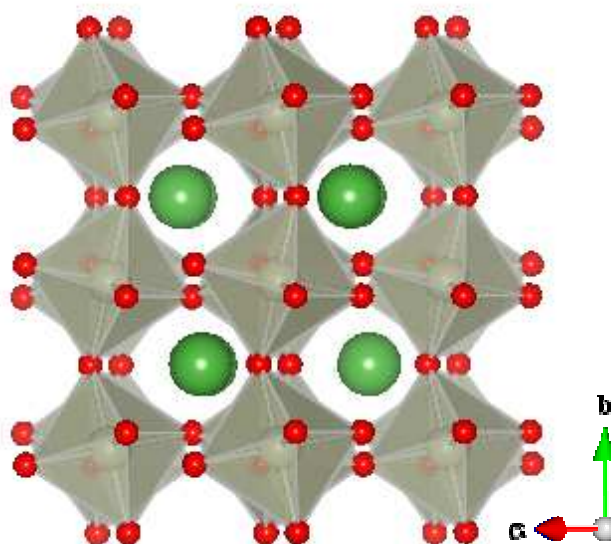


Figure 4.2 Orthorhombic structure for RMnO_3 oxides where $R = \text{La} - \text{Dy}$. Green spheres are R^{3+} cations, Red spheres are oxygen cations, and Mn occupies the center of the octahedra, light grey.

angle generally less than 180° . This supports an indirect magnetic exchange interaction that results in antiferromagnetic ordering. In addition, paraelectric and antiferroelectric ordering temperatures are also observed and occur from 40-140 K [9, 10].

Despite the similar formula to perovskites, RMnO_3 , where $\text{R} = \text{Y, Dy} - \text{Lu}$, have the hexagonal ($\text{P6}_3\text{cm}$) YAlO_3 structure [8]. This structure has distinct differences in comparison to the AMO_3 perovskites and can be described as corner shared MO_5 trigonal bipyramids sheets with unique apical oxygen ions connected to RO_7 polyhedra Figure 4.3.

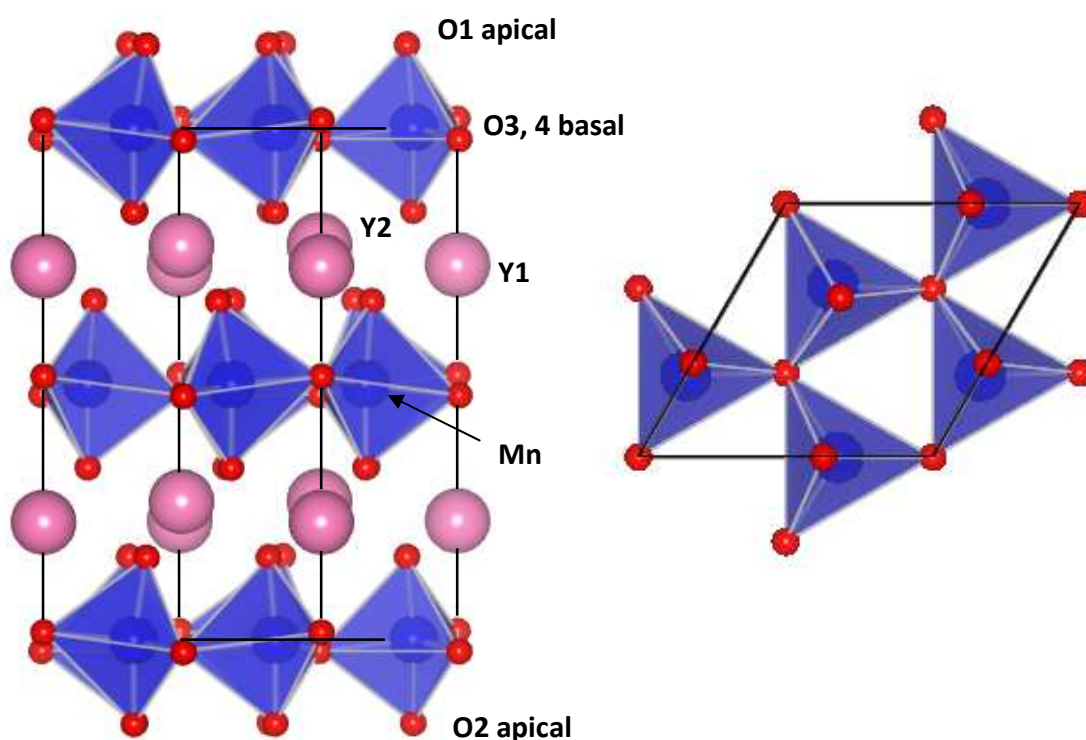


Figure 4.3 Representation of the asymmetric hexagonal YMnO_3 structure with unique atoms labeled. Note the displaced Y1 and Y2 atoms and the unique coordination of Mn^{3+} in rotationally distorted MnO_5 polyhedra.

The Mn^{3+} ions occupy the barycenter of trigonal bipyramids, and form a triangular network separated from adjacent layers by apical oxygen ions and intervening yttrium ions. Below the ferroelectric ordering temperature the MnO_5 polyhedra cooperatively rotate displacing R^{3+} ions along the c-axis. The existence of ferroelectricity, generally

requiring empty d-orbitals, is inconsistent with Mn^{3+} (d^4) in which the d-orbitals are partially filled. The displacement of R^{3+} is considered to be the root of the ferroelectric observation. The hexagonal RMnO_3 ($\text{R} = \text{Y}$ and $\text{Dy} - \text{Lu}$) show a ferroelectric polarization generally between ~ 550 K and 1000 K, and an antiferromagnetic ordering below ~ 100 K [7, 11, 12]. A wide range for the FE ordering temperature is suggested because of the difficulties in measurements due to increased conductivity at higher temperatures.

Due to the large magnetoelectric effect present in manganate materials like RMnO_3 and TbMn_2O_5 there have been extensive studies to realize the magnetic and electric behavior. YMnO_3 in particular has received a great deal of attention due to the initial interest as a promising ferroelectric. However, the coexistence of ferroelectricity and antiferromagnetism, in addition to the coupling between these parameters, has made it a fundamentally important material for the study of multiferroic systems. In YMnO_3 the antiferromagnetic Néel temperature is ~ 80 K and the ferroelectric Curie temperature is ~ 914 K.

The fact that both YInO_3 and YGaO_3 are isostructural with YMnO_3 and are also ferroelectric [13, 14], demonstrates again that the origin of ferroelectricity is not related to d orbitals, a characteristic unlike most oxide ferroelectrics. Instead, the origin of the spontaneous polarization parallel to the c -axis (perpendicular to the a - b basal plane) has been attributed to the displacement of R^{3+} ions relative to the basal plane due to canting or buckling of the MO_5 trigonal bipyramids. In YMnO_3 , the Mn^{3+} ions in the MnO_5 polyhedra are located near the barycenter and would not contribute

to the polarization. In contrast, the polarization found in BaTiO_3 is due to Ti^{4+} offset from the barycenter in the TiO_6 polyhedra, whereas in BiMnO_3 and BiFeO_3 , the polarization is caused by Bi lone pairs and Bi-O hybridization [3, 4, 13]. It is also interesting that the dielectric constant for YMnO_3 in the a - b plane decreases significantly near the Néel temperature, $T_N \sim 80$ K and not in the polar c -axis where it would be expected. The magnetism observed in YMnO_3 at ~ 80 K arises from a canting of the MnO_5 polyhedra along the basal plane and antiferromagnetic ordering of Mn^{3+} spins [9, 15]. In magnetoelectric multiferroics, the magnetic ordering is generally driven by super exchange interactions. The strength depends primarily on the overlap of orbitals and is generally determined by M – O – M bond angles and bond lengths. Local distortions are induced by the application of an electric field which affects the ligand field and therefore the orbital contribution to the magnetic moment of the metal ions [16].

In view of the interest in the hexagonal RMnO_3 phases as potential room temperature multiferroic materials, there have been many attempts to substitute various cations on the A site. However, substitutions on the Mn site have only been mildly considered. Substitutions include Fe, Co, Ni, Cr, Ti, Ga, Cu, Cu/Mo, and Al (Fig. 4.4). The amount of substitution is always very limited before the structure converts from hexagonal to the rhombic or orthorhombic perovskite structure. Interestingly enough, attempts to synthesize full solid solutions between YGaO_3 , YFeO_3 and YAlO_3 with YMnO_3 have all failed despite being isostructural [8, 17, 18]. Figure 4.4 shows the substitutions allowed and the respective structure for those

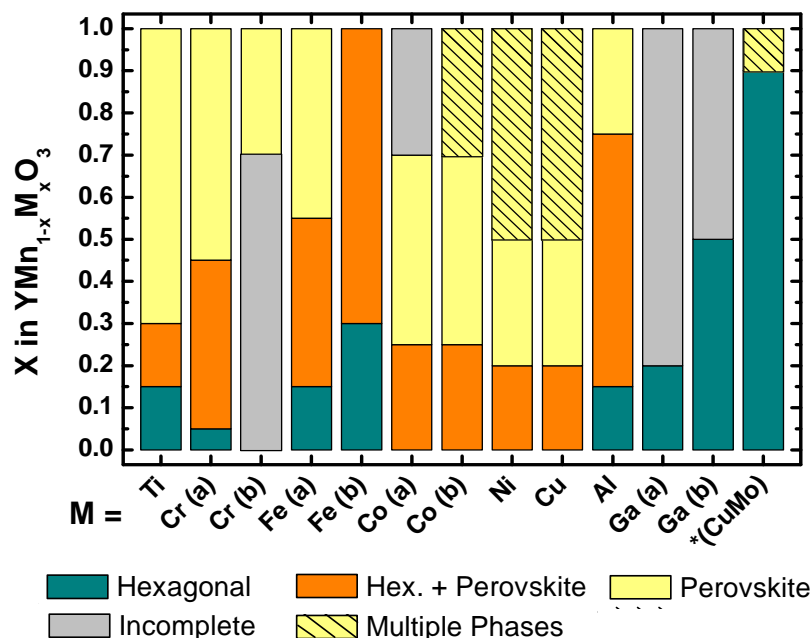


Figure 4.4 M-site substitutional effects on YMnO₃ structure. Dark cyan is observed hexagonal structure, orange is coexisting hexagonal and perovskite structures, yellow is perovskite structure, and yellow/hash marks are perovskite and impurities. Gray bars are unreported compositions or incomplete analysis. *Cu-Mo co substitution is a 3:1 ratio [8,17-26]

substitutions. It is interesting to note that there are no full solid solutions formed upon substitution in YMnO₃. The importance of substitutions with various cations is that it allows for structural tuning (i.e. bond angles, bond lengths, and covalency) and property specific tuning (orbital overlap, magnetism, and electrical behavior). For example, Ga doping in RMnO₃ (R = Y and Ho) increased the ferroelectric Curie temperature and decreased the Néel temperature [21], and Fe doping increased the Néel temperature [17]. It is thus necessary to understand in detail the structural effects of substitutions in order to fabricate materials in this structure with specific and enhanced properties.

4.3 Effects of Indium Substitution in YMnO_3 Ceramics

We have investigated the effects of substituting In for Mn on the antiferromagnetic phase transition in YMnO_3 using magnetic, dielectric, and specific heat measurements. We prepared a set of isostructural phase pure hexagonal $\text{YMn}_{1-x}\text{In}_x\text{O}_3$ samples having $x=0$ to $x=0.9$, which exhibit a systematic decrease of the antiferromagnetic ordering temperature with increasing In content. The multiferroic phase, which develops below T_N , appears to be completely suppressed for $x \geq 0.5$ in the temperature range investigated, which can be attributed solely to the dilution of magnetic interactions as the crystal structure remains hexagonal. Similar to previous reports, we find an enhancement of the magnetocapacitive coupling on dilution with non-magnetic ions. In addition, we have discovered that a surprisingly intense and bright blue color is obtained when Mn^{3+} is introduced into the trigonal bipyramidal sites of metal oxides. We demonstrate this behavior by substituting Mn for In in hexagonal YInO_3 and obtain a blue color over much of the $\text{YIn}_{1-x}\text{Mn}_x\text{O}_3$ solid solution range, in spite of the fact that YInO_3 and YMnO_3 are white and black, respectively. We show that a blue color is obtained when Mn^{3+} is introduced into trigonal bipyramidal sites in other layered oxides. We conclude that the blue color is a consequence of both the crystal field splitting associated with the trigonal bipyramidal coordination and the short apical Mn-O bonds. We expect that our results will lead to routes for the development of inexpensive, earth-abundant, environmentally benign, highly stable blue inorganic pigments.

4.3.1 Suppression of Multiferroic Order in Hexagonal $\text{YMn}_{1-x}\text{In}_x\text{O}_3$ Ceramics

4.3.1.1 Introduction

The hexagonal rare earth manganites, RMnO_3 with $\text{R}=\text{Ho}$, Er , Tm , Yb , Lu , or Y , have been widely studied because of their magnetoelectric properties [27-32]. YMnO_3 , which develops ferroelectric order at $T_C \sim 900$ K and antiferromagnetic order below $T_N \sim 80$ K, and is therefore multiferroic below T_N , has been the subject of numerous investigations exploring the nature of the magnetoelectric coupling in this class of materials. Early measurements on the temperature dependent dielectric constant of YMnO_3 found clear anomalies associated with the antiferromagnetic transition, pointing to coupling between the ferroelectric and magnetic orders [27]. Optical studies on YMnO_3 also find clear evidence for coupling between the ferroelectric and antiferromagnetic domain walls [29], with measurements on the related compound HoMnO_3 demonstrating control of the magnetic phase using a static electric field [33]. The microscopic origins of the spin-charge coupling in YMnO_3 has also been investigated in detail using Raman scattering [34, 35] and magnetoelastic measurements [32]. Raman studies on YMnO_3 thin films provide evidence for spin-phonon coupling below T_N [35], while neutron measurements of spin excitations highlight the importance of magnetoelastic coupling in this system [32]. Theoretical studies on YMnO_3 point to the importance of the displacement of the Y^{3+} ions [36],

which is facilitated by hybridization of the Y 4d orbitals with the O 2p orbitals and the buckling of the MnO_5 bipyramids [37].

Because the multiferroic properties of YMnO_3 are relatively well understood, it is illuminating to determine how the magnetic and ferroelectric characteristics change on substituting on the both the Y and Mn sites. The ferroelectric distortion and magnetic ordering are found to be suppressed when Zr replaces Y [7], which also decreases the carrier concentration [38]. The carrier concentration can be increased by replacing Y with Mg or Li, the latter of which also produces weak ferromagnetic behavior [38]. The magnetocapacitive coupling in YMnO_3 is found to increase when Mn is replaced by modest amounts of Ti [39] or Ga [20], although increasing the Ti content above approximately 20% is found to suppress the ferroelectric $P6_3cm$ structure in favor of a centrosymmetric $R\bar{3}c$ structure [39]. Previous studies have shown that Ga doping, which does not produce any change in crystal structure, significantly affects the magnetocapacitive coupling along the c-axis, while producing much more modest changes for the dielectric constant measured perpendicular to the c-axis [20]. Substituting non-magnetic Ga on the Mn^{3+} sites slightly increases the Curie temperature while systematically reducing the antiferromagnetic ordering temperature [21]. However, the reduction of the spin-lattice interactions in the Ga doped system increases the thermal conductivity, despite the introduction of additional impurity scattering [8]. The central focus of this investigation was to determine how the magnetic, thermodynamic, and dielectric properties of $\text{YIn}_{1-x}\text{Mn}_x\text{O}_3$ at the antiferromagnetic phase transition depend on x over a wide range of compositions.

4.3.1.2 Results and Discussion

In order to more fully investigate the magnetoelectric properties of YMnO_3 at the antiferromagnetic phase transition with substitution on the Mn site we investigated solid solutions of YMnO_3 and YInO_3 . Both of these compounds can be stabilized in the hexagonal structure, having similar M-O bond lengths in the basal plane but with the Mn-O apical bond length being considerably shorter than the In-O apical bond length [19]. Because both end members of the $\text{YMn}_{1-x}\text{In}_x\text{O}_3$ series can be prepared in

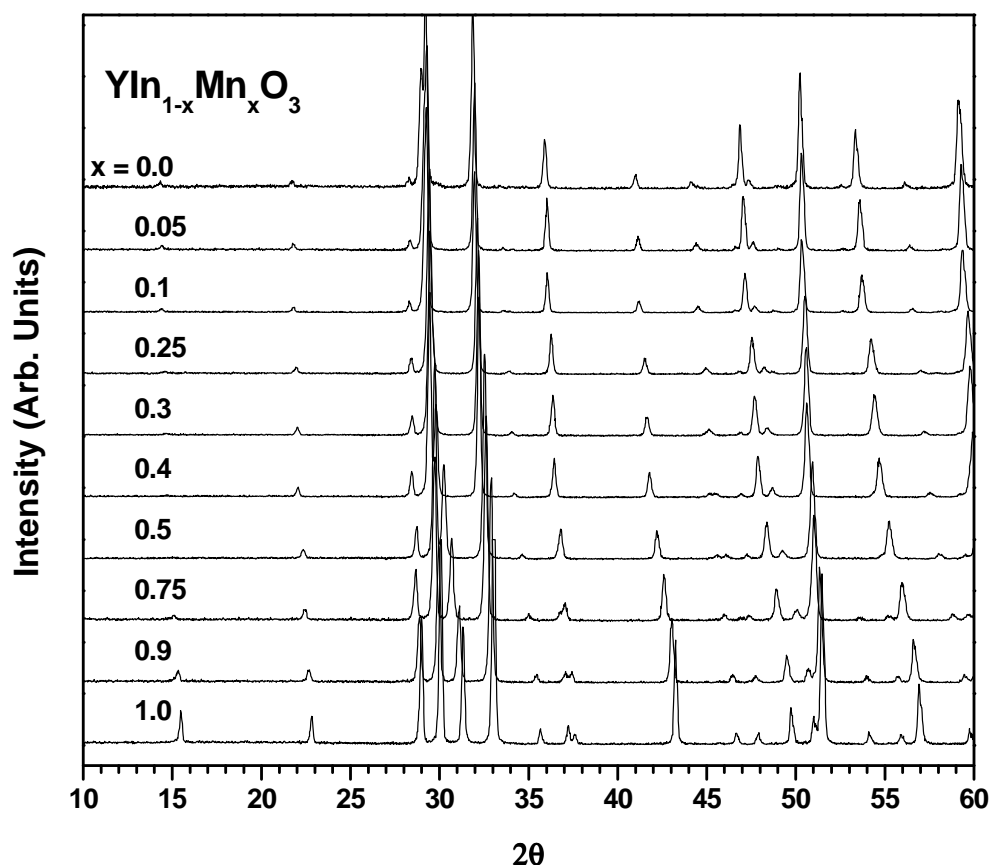


Figure 4.5 Normalized powder x-ray diffraction patterns for the full solid solution in $\text{YIn}_{1-x}\text{Mn}_x\text{O}_3$. YMnO_3 and YInO_3 parent compounds are on bottom and top respectively.

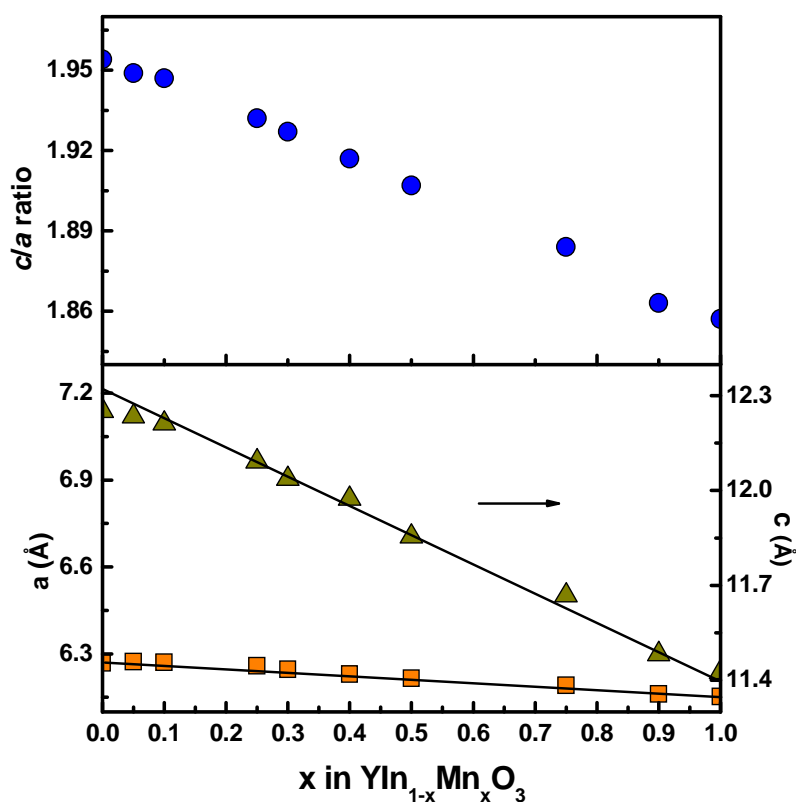


Figure 4.6 Unit cell dimensions and c/a ratio for the $\text{YIn}_{1-x}\text{Mn}_x\text{O}_3$ solid solution. It is clear that the similar basal-plane bond lengths in end members lead to a weak variation of across the solid solution series. The c/a ratio varies strongly due to the large apical bond-length difference for In-O and Mn-O.

the hexagonal structure, we presume that the structural instabilities that affect other systems, such as $\text{YMn}_{1-x}\text{Ti}_x\text{O}_3$, can be avoided over the entire range of compositions $0 \leq x \leq 1$. The XRD powder patterns are shown in Figure 4.5. All peaks can be fully indexed to the hexagonal $\text{P6}_3\text{cm}$ structure, with no evidence for the formation of any secondary phases. A number of peak positions change systematically with the Mn:In ratio and the variation is illustrated in a Végard's law plots in Figure 4.6.

The linear variations in a and c lattice parameter are consistent with the length of the apical M-O bond increasing as the In fraction of the compound increases. Because

it is possible to stabilize high concentrations of In in this structure, the antiferromagnetic transition can be suppressed completely for large x , which allows us to probe the properties of the paramagnetic system down to low temperatures.

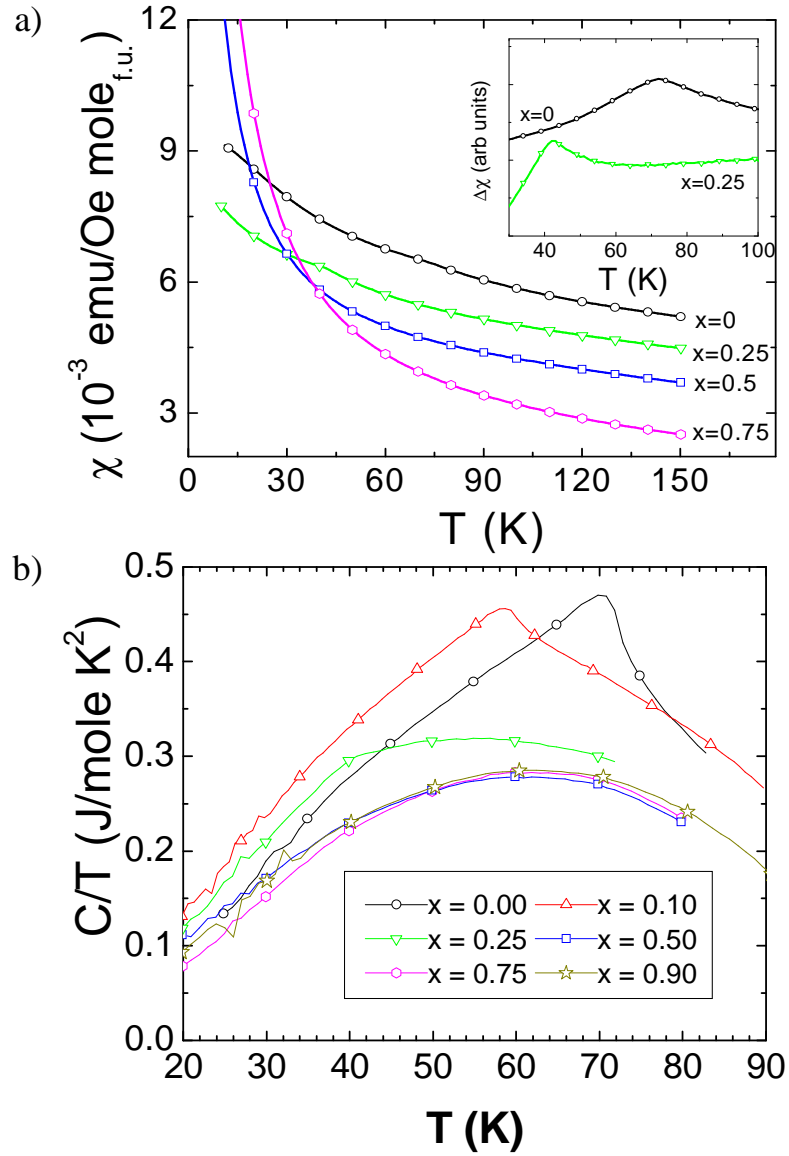


Figure 4.7 (a) Temperature dependence of the magnetic susceptibility measured at $\mu_0 H = 0.5 \text{ T}$ for different $\text{YIn}_{1-x}\text{Mn}_x\text{O}_3$ samples, as indicated. The inset plots the susceptibility less a background correction to more clearly emphasize the magnetic anomalies in the $x=1$ and $x=0.25$ samples. (b) Specific heat, plotted as C/T versus T , for the $\text{YIn}_{1-x}\text{Mn}_x\text{O}_3$ samples, as indicated.

The temperature dependent magnetic susceptibilities for the $x=1$, $x=0.75$, $x=0.5$, and $x=0.25$ samples measured at $\mu_0 H=0.5$ T are plotted in Figure 4.7a. There is a systematic decrease in the high temperature susceptibility with increasing x , consistent with replacing Mn^{3+} with non-magnetic In^{3+} ions. The Curie-Weiss temperature, Θ_{CW} , estimated from the high temperature susceptibility varies systematically from $\Theta_{\text{CW}}=-337$ K for $x=1$ to -325 K, -240 K, and -83 K for $x=0.75$, $x=0.5$, and $x=0.25$ respectively. The effective moment per Mn estimated from the high temperature susceptibility is $4.2 \pm 0.5 \mu_B$ for all samples. At low temperatures, the paramagnetic Curie-Weiss behaviour for the $x=0.5$ and $x=0.25$ samples leads to a larger susceptibility than in the magnetically ordered $x=1$ and $x=0.75$ samples. The magnetic anomalies associated with the development of antiferromagnetic order for the $x=1$ and $x=0.75$ samples can be seen more clearly in the inset to Figure 4.7a, which plots the susceptibility corrected for the background paramagnetic behavior. The magnetic transition occurs at $T_N=72$ K for YMnO_3 , consistent with previously observed values [27]. The transition temperature is suppressed as Mn is replaced by non-magnetic In, falling to $T_N=42$ K for the $\text{YMn}_{0.75}\text{In}_{0.25}\text{O}_3$ sample. The magnitude of this suppression is what has been observed previously in Ga substituted YMnO_3 having a similar fraction of non-magnetic Ga replacing the Mn^{3+} ions [20]. We do not observe any clear anomalies in the magnetization curves for samples having $x \leq 0.5$, suggesting that the antiferromagnetic transition temperature is pushed to below $T=20$ K, where the paramagnetic Curie tail obscures the magnetization data.

We plot the temperature dependent specific heat for different $\text{YIn}_{1-x}\text{Mn}_x\text{O}_3$

samples in Fig. 4.7b, all measured at zero applied field. This plot shows only the contribution from the magnanite samples; the background silver contributed was measured separately and removed. The samples having smaller In fractions exhibit a clear peak in heat capacity at the antiferromagnetic phase transition, while the In-rich samples do not show any clear anomalies. For $x=0.5$ and above, the heat capacity is roughly the same for all compositions, confirming that the differences in specific heat arise solely from the magnetic order of the Mn ions and not from any significant difference in lattice contributions. Estimating the lattice contribution to the YMnO_3 heat capacity from the $\text{YMn}_{0.5}\text{In}_{0.5}\text{O}_3$ data, and neglecting the slight difference in mass between Mn and In, we find that the magnetic entropy between 25 K and 85 K associated with Mn spin ordering is approximately 5.3 J/mole K. This is considerably smaller than the $R\ln 5 = 13.4$ J/mole K expected for the full ordering of $S=2$ Mn^{3+} ions, which has been observed in previous studies of YMnO_3 samples [30]. We attribute this discrepancy to the considerable entropy developing above $T=85$ K, which is excluded from our estimate, as well as errors associated with correcting for the silver background contributions.

One of the signatures of the coupling between the magnetic and ferroelectric order parameters in YMnO_3 is the presence of a dielectric anomaly at the antiferromagnetic transition temperature. The relative temperature dependent dielectric constants for selected $\text{YIn}_{1-x}\text{Mn}_x\text{O}_3$ samples, scaled to the value at $T=80$ K just above the transition temperature for YMnO_3 , are plotted in Figure 4.8.

The slight anomalies in the dielectric constant coincident with antiferromagnetic

ordering, visible mainly as a small change in slope, are indicated by arrows. The value of T_N is slightly reduced for $\text{YMn}_{0.9}\text{In}_{0.1}\text{O}_3$ as compared to YMnO_3 , and still further reduced in $\text{YMn}_{0.75}\text{In}_{0.25}\text{O}_3$. There is no dielectric anomaly in the temperature range investigated for $x \leq 0.5$, consistent with our magnetic and specific heat measurements, neither of which show any phase transition. The dielectric constant for the $x=0.75$ sample varies more with temperature than the other samples. We tentatively attribute this to the fact that the dielectric loss (not shown) for this particular sample is slightly larger than the loss for other compositions, rather than reflecting any intrinsic response to In substitution.

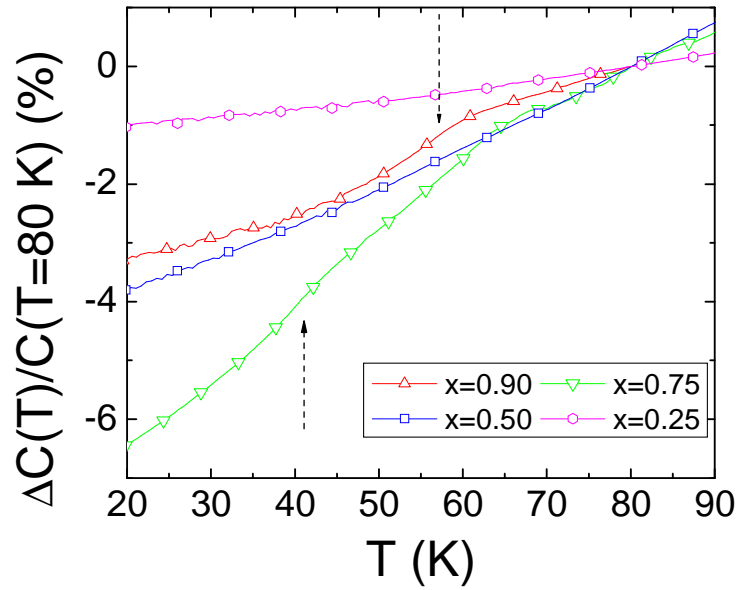


Figure 4.8 Relative change in capacitance for $\text{YIn}_{1-x}\text{Mn}_x\text{O}_3$ samples as labeled. The dielectric anomalies associated with the magnetic ordering transitions are indicated by the dashed arrow.

Previous studies on YMnO_3 doped with Ga found evidence for a significant enhancement of the magnetocapacitance, which was attributed, at least in part, to the

non-magnetic ions relieving the frustration leading to larger magnetoelectric coupling along the c axis [20]. To explore whether similar behavior would develop in In doped YMnO_3 and whether the enhancement in the coupling would persist to larger fractions of non-magnetic ions, we measured the temperature and magnetic field dependence of the capacitance for the different samples. The field dependence of the relative change in capacitance measured at $T=10$ K is shown for the different samples in Figure 4.9. This temperature is below the magnetic ordering temperature for the $x=1$, $x=0.9$, and $x=0.75$ samples, and above any possible ordering temperature for the $x=0.25$ sample. Because of the very capacitive signal in these samples, the data were rather noisy, so the results shown in Figure 4.9 plot the results after smoothing. The solid bars on the $x=0$, $x=0.5$, $x=0.25$ curves provide a visual estimate of the spread in the data before

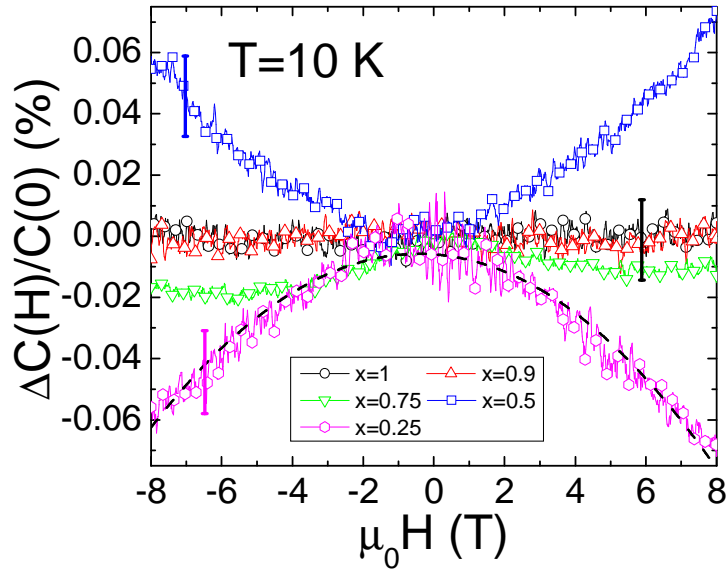


Figure 4.9 Magnetic field dependence of the capacitive response for different samples, as indicated. The solid bars on the $x=1$, $x=0.5$, and $x=0.25$ curves provide a visual estimate of the scatter in the data before smoothing. The dashed line on the $x=0.25$ curve shows the fit described in the text.

magnetocapacitive coupling, with some small shift in the capacitance observed for the $x=0.75$ sample. The $x=0.5$ and $x=0.25$ samples show significant larger field-induced shifts in capacitance, with the change in capacitance reaching over 0.05% in an applied field of $\mu_0 H=8$ T. These changes may be consistent with those observed for single crystal $\text{YMn}_{0.7}\text{Ga}_{0.3}\text{O}_3$ samples, where the shift reached approximately -0.25% for $E \parallel c$ and 0.025% for $E \perp c$ at similar magnetic fields [20]. As the magnetocapacitive shift in Fig. 9 represents a powder average of the response for $E \parallel c$ and $E \perp c$, we would expect the magnitude of the shift to be intermediate between the values for the single crystal Ga:YMnO_3 sample.

One of the most striking features of the magnetocapacitive shift shown in Figure 4.9 is the change in sign between different samples. At a mean field level, the relative magnetocapacitive shift is expected to be proportional to the square of the applied magnetic field, $\Delta C/C \approx \gamma H^2$, arising from the lowest order term coupling P and H allowed by symmetry in the free energy [40]. A fit to this functional form for the $x=0.75$ sample (allowing a small offset) is indicated by the dashed line in Fig. 9. We fit the temperature dependence of the coupling parameter γ for the $x=0.5$ and $x=0.25$ samples, selected as these show the largest magnetocapacitive shifts, having roughly similar magnitudes, and remain paramagnetic over the entire temperature range, and plot the results in Fig. 9.

We find that $\gamma(T)$ decreases systematically with increasing temperature for the $x=0.5$ sample, which we attribute to first approximation to the reduction in the magnetic susceptibility. The response for the $x=0.25$ sample however shows a rather

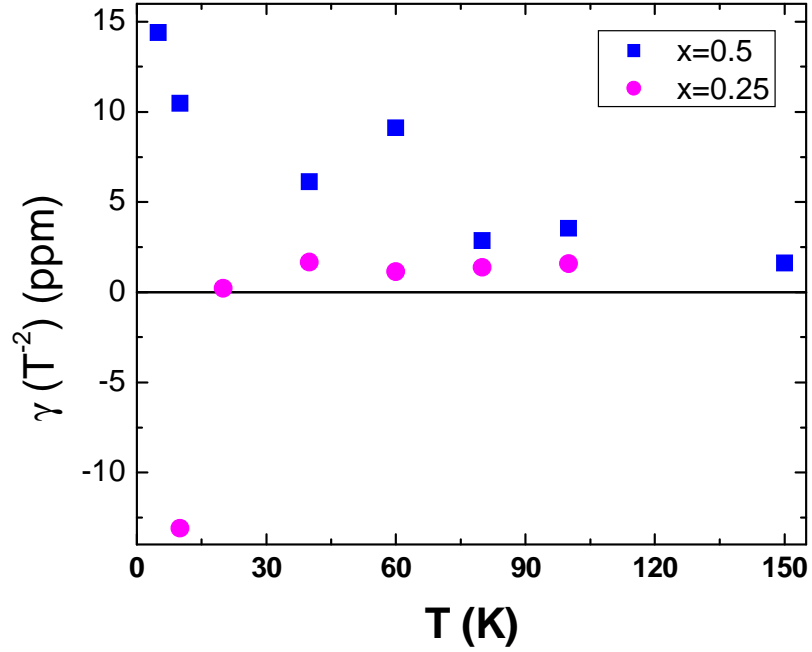


Figure 4.10 Temperature dependence of the magnetocapacitive coupling constant (as described in the text) for the $x=0.5$ and $x=0.25$ $\text{YIn}_{1-x}\text{Mn}_x\text{O}_3$ samples.

different temperature dependence, with a negative magnetocapacitive shift at low temperatures crossing over to a positive shift at higher temperatures. Repeated measurements show qualitatively similar behaviour for the temperature dependence of the coupling, although the magnitude of $\gamma(T)$ shows some small changes.

It has been suggested that since both the dielectric response of layered YMnO_3 is highly anisotropic, the magnetocapacitive coupling may be different parallel to and perpendicular to the c axis, leading to magnetocapacitive shifts as $\Delta C_{\parallel}/C_{\parallel} \approx \gamma_{\parallel} H^2$ and $\Delta C_{\perp}/C_{\perp} \approx \gamma_{\perp} H^2$ (neglecting contributions from the sublattice magnetization, which are expected to be absent for our paramagnetic $x=0.5$ and $x=0.25$ samples) [20]. Studies on $\text{YMn}_{1-y}\text{Ga}_y\text{O}_3$ find that the γ_{\parallel} component measured at $T=5$ K changes sign

as y changes from 0 to 0.3, leading to both positive and negative magnetocapacitive shifts in the compound series [20]. As the capacitance plotted in Fig. 10 represents the powder average of the anisotropic response, a change in the sign of $\gamma(T)$ could be produced by a change of sign in $\gamma_{||}(T)$. However, since both the $x=0.5$ and $x=0.25$ samples are expected to be paramagnetic over the entire temperature range considered, it is unclear why there would be any change in sign, either as a function of In fraction or as a function of temperature. Understanding the mechanisms responsible for the change in sign of the low temperature magnetocapacitive coupling between the $x=0.5$ and $x=0.25$ samples may help to clarify the nature of the spin-charge coupling in the parent YMnO_3 compound.

We summarize the results of our magnetic, dielectric, and specific heat studies in Fig. 11, which plots the antiferromagnetic ordering temperature estimated from these different measurements against the In content of the sample. The transition temperatures extracted using these different measurement techniques all agree, confirming that there is a single magnetic transition giving rise to the dielectric anomalies even in the In substituted samples. The magnitude of the suppression of T_N in YMnO_3 with In substitution is very similar to what was observed previously with Ga substitution, where the antiferromagnetic order temperature is suppressed to $T_N=35$ K with 30% Ga substitution [20]. This scaling of T_N with x can be understood in terms of simple site dilution by non-magnetic ions. The initial slope of the suppression of T_N with In substitution, $p = -(dT_N/dx)/T_N$, is approximately 1.6. This reduction in T_N on substituting non-magnetic ions is larger than one would typically

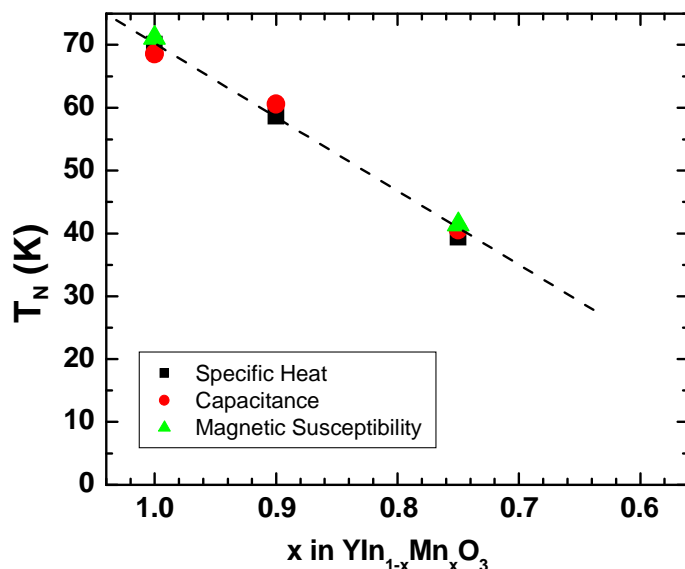


Figure 4.11 Temperature dependence of the antiferromagnetic ordering transition on x in $\text{YIn}_{1-x}\text{Mn}_x\text{O}_3$. The different symbols represent the transition temperature extracted from different measurements, as indicated. The dashed line shows the curve used to estimate the initial suppression of T_N , as described in the text.

expect for a three dimensional system, where $p \approx 1.2$ [28], and is more consistent with that expected for Ising spins in two dimensions, where p normally ranges from 1.6 to 1.9 [41]. This confirms the importance of the in-plane interactions among Mn^{3+} ions in developing long range antiferromagnetic order.

4.3.2 Mn^{3+} in Trigonal Bipyramidal Coordination: A New Blue Chromophore

4.3.2.1 Introduction

Development of the first known synthetic blue pigment, Egyptian blue, ($\text{CaCuSi}_4\text{O}_{10}$), is believed to have been patronized by the Egyptian pharaohs who

promoted the advancement of pigment technologies for use in the arts [42]. The subsequent quest for blue pigments has a rich history linked with powerful civilizations, such as the Han Chinese (Han blue – $\text{BaCuSi}_4\text{O}_{10}$.) and the Maya (Maya blue – indigo intercalated in magnesium aluminosilicate clays). Currently used blue inorganic pigments are cobalt-blue (CoAl_2O_4) [43], ultramarine ($\text{Na}_7\text{Al}_6\text{Si}_6\text{O}_{24}\text{S}_3$) [44], Prussian Blue ($\text{Fe}_4[\text{Fe}(\text{CN})_6]_3$) [45] and azurite ($\text{Cu}_3(\text{CO}_3)_2(\text{OH})_2$.) [46]. All suffer from environmental and/or durability issues (cobalt is considered highly toxic, ultramarine and azurite are not stable to heat and acidic conditions. In addition, the manufacture of ultramarine involves a large amount SO_2 emission. Prussian blue liberates HCN under mild acidic conditions). Hence the identification of intense blue inorganic pigments that are environmentally benign, earth-abundant, and durable is important but remains a challenge today.

4.3.2.2 Results and Discussion

Both YInO_3 and YMnO_3 are known in the common orthorhombic and centric form of the perovskite structure [47, 48], but they are also readily prepared in an acentric hexagonal structure (Fig. 12) that is not perovskite related [14, 49]. This hexagonal structure consists of layers of Y^{3+} ions separating layers of corner-shared MO_5 trigonal bipyramids ($\text{M} = \text{In}$ or Mn). This structure has been of considerable recent interest because it exhibits an unusual form of improper geometric ferroelectricity accompanied by tilting of the MO_5 polyhedra [37, 50, 51]. Such ferroelectricity is

compatible with M-site magnetism and therefore allows multiferroic behavior. Two detailed features of isostructural hexagonal YInO_3 and YMnO_3 are important for this work. First, their basal-plane M-O bond lengths are almost equal (2.05 Å for YMnO_3 and 2.1 Å for YInO_3). Second, in YMnO_3 the apical Mn-O distances are considerably shorter (1.86 Å) than those in the basal plane, while in YInO_3 , all In-O bonds are roughly the same length. The crystal field splitting of the d orbital energies in trigonal bipyramidal coordination is shown in Figure 4.12. Notice that the e' to a' energy splitting, which is the lowest energy excitation for a d^4 cation in the cluster limit, depends sensitively on the apical M-O bond length through its influence on the energy

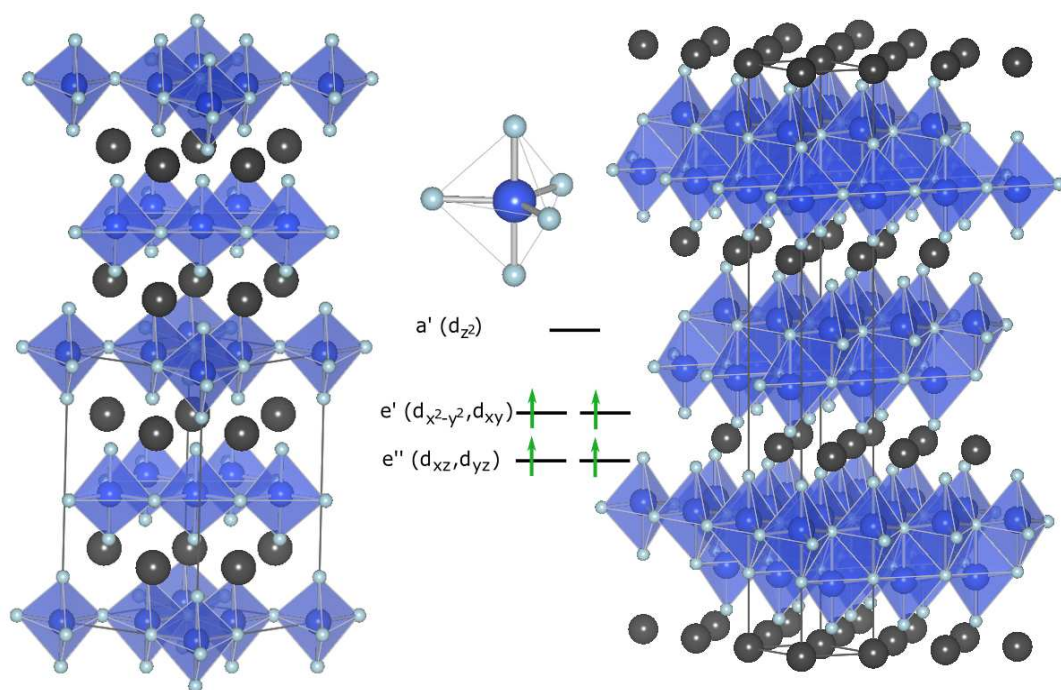


Figure 4.12 The structures of YMnO_3 (left) and YbFe_2O_4 (right) as blue trigonal bipyramids (Mn or Fe), grey Y or Yb and cyan O atoms. The YMnO_3 structure consists of layers of corner-shared MnO_5 trigonal bipyramids. The YbFe_2O_4 structure is similar, but has a double-layer of corner-shared trigonal bipyramids that edge share between the layers. Schematic energy levels for the spin up Mn^{3+} 3d orbitals in trigonal bipyramidal coordination are shown. We note that transitions from e' to a' are formally dipole allowed in this symmetry.

of the d_{z^2} orbital. While the crystal field stabilization associated with a d^4 cation in trigonal bipyramidal coordination has been invoked to explain the stability of hexagonal YMnO_3 relative to the competing perovskite structure, trigonal bipyramidal is not a common coordination for Mn^{3+} , and we are not aware of its occurrence in compounds other than the hexagonal RMnO_3 compounds where R is a small rare earth cation [35].

In view of the interest in the hexagonal RMnO_3 phases as multiferroic materials, there have been many attempts to substitute Mn for various cations, such as Fe, Co, Ni, Cr, Ti, Ga, and Al [17, 20-25]. The amount of substitution is always very limited before the structure converts to the perovskite structure even in those solid-solution compositions where the end-point compound is stable in the hexagonal phase. It is thus surprising that we have been able to prepare a complete single phase $\text{YIn}_{1-x}\text{Mn}_x\text{O}_3$ solid solution (synthesis details are given in the supporting information), despite the fact that the size mismatch between In^{3+} and Mn^{3+} is greater than in the cases where the solid solution is more limited. We attribute this complete miscibility to the similar In-O and Mn-O basal plane distances in hexagonal YInO_3 and YMnO_3 . The large size difference between In^{3+} and Mn^{3+} only manifests in apical distances. A plot of unit cell edges for the $\text{YIn}_{1-x}\text{Mn}_x\text{O}_3$ solid solution is shown in Figure 4.13. Both the c lattice parameter and the c/a ratio decrease dramatically with x due to the short apical Mn-O distances.

The blue color of the $\text{YIn}_{1-x}\text{Mn}_x\text{O}_3$ powders is evident in Figure 4.14 for even very low values of x. To understand the origin of this blue color we perform diffuse

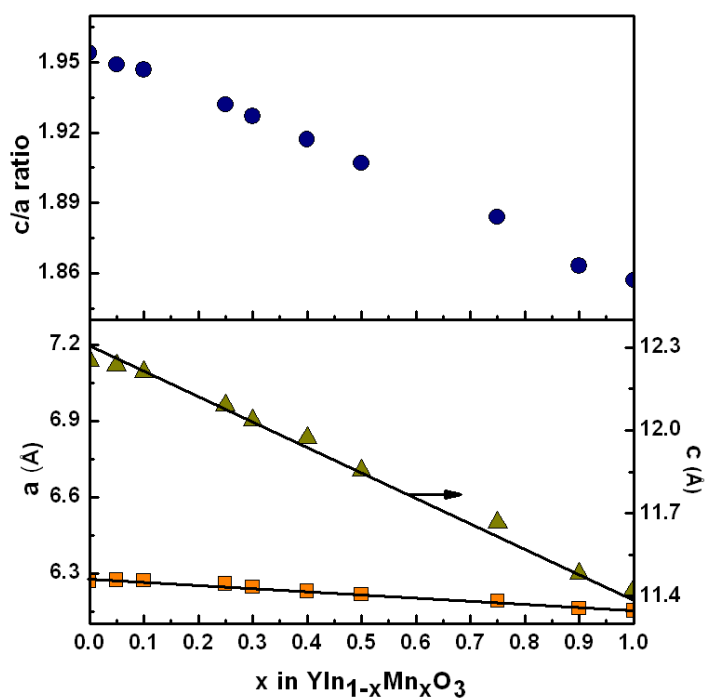


Figure 4.13 Unit cell dimensions and c/a ratio for the $\text{YIn}_{1-x}\text{Mn}_x\text{O}_3$ solid solution. It is clear that the similar basal-plane bond lengths in end members lead to a weak variation of a across the solid solution series. The c/a ratio varies strongly due to the large apical bond-length difference for In-O and Mn-O.

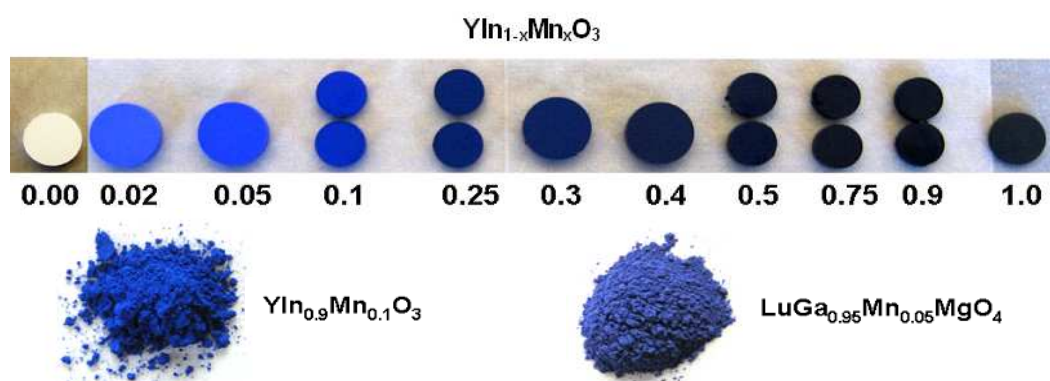


Figure 4.14 Colors of pellets and powders at selected compositions. The intense blue color appears at our lowest concentration of Mn doping in YMnO_3 . With increasing Mn composition, the color darkens until eventually YMnO_3 is found to be black.

reflectance spectra and first-principles density functional calculations within the LSDA+U method, which has been previously shown to give reliable results for YMnO_3 [50]. Results of our diffuse reflectance measurements are shown in Figure 4.15. We see that, at low doping concentrations, there is a strong, narrow (~ 1 eV width) absorption centered at around 2 eV, which absorbs in the red-green region of the visible spectrum. Absorption then drops between 2.5 – 3 eV before a second onset near 3 eV. The absence of absorption in the 2.5 – 3 eV (blue) region of the spectrum results in the blue color. As the concentration of Mn is increased, the lower energy absorption peak broadens and the higher energy onset shifts to lower energy consistent

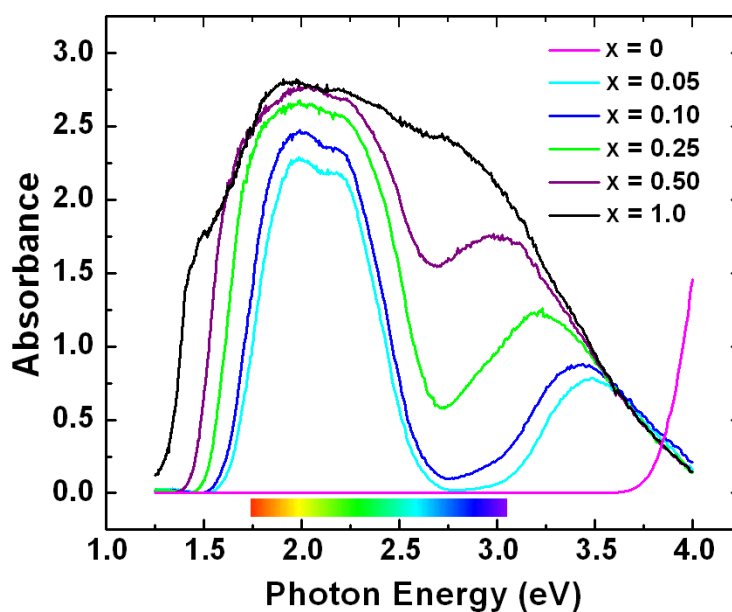


Figure 4.15 Diffuse reflectance spectra for the $\text{YIn}_{1-x}\text{Mn}_x\text{O}_3$ solid solution. Strong absorption in the red-green spectral region, combined with a relatively weak absorption in the blue region, is responsible for the observed intense blue color. With increasing Mn composition, the first absorption peak broadens and the second onset lowers in energy, such that YMnO_3 absorbs almost equally throughout the visible region (see text).

with the gradual darkening of the samples towards navy blue. In pure YMnO_3 absorption occurs through the entire visible region resulting in the black color. Although we know of no precedent for a blue color arising from Mn^{3+} in trigonal bipyramidal coordination, a blue color is observed for the d^4 cation Cr^{2+} in trigonal bipyramidal coordination in $[\text{Cr}(\text{Me,tren})\text{Br}]\text{Br}$ [52]. To our knowledge, divalent chromium is not known in oxides.

Our density functional calculations of the densities of states and optical properties of the fully relaxed end-point compounds and selected intermediates (for details see Supplementary Online Material) indicate that the peak at ~ 2 eV arises from the transition between the valence band maximum, consisting of $\text{Mn } 3d_{x^2-y^2, xy}$ states strongly hybridized with $\text{O } 2p_{x,y}$ states, and the lowest unoccupied energy level, which in lightly Mn-doped YInO_3 is a narrow band formed from the $\text{Mn } 3d_z$ state that lies in the band gap of YInO_3 . (The absence of mid-gap $\text{Mn } 3d_z$ states in pure YInO_3 leaves it colorless). Note that in the local D_{3h} symmetry of the trigonal bipyramids, the d-d component of this transition – between symmetry labels a' and e' in Figure 4.12 – is formally symmetry allowed according to the Laporte selection rule. This results in a high transition probability and intense absorption. The strong d-d absorption here is in striking contrast to the behavior in the approximate O_h crystal field environment of perovskites, where it is formally symmetry forbidden. In O_h symmetry, hybridization with ligands or structural distortions are required to circumvent the dipole selection rules, and d-d transitions are usually weak. Indeed, we find no blue color on substitution of Mn^{3+} into YGaO_3 or YAlO_3 with the perovskite structure where the

Mn^{3+} would be in approximate O_h symmetry.

We assign the higher energy peak to the onset of the transition from the O 2*p* band to the Mn 3*d*_{z²} band. Note that our assignments are consistent with earlier optical studies of YMnO_3 using second-harmonic generation [53], but that the topic has been controversial [54]. With increasing Mn concentration, our calculations indicate that the Mn 3*d* levels – particularly the lowest unoccupied state corresponding to the 3*d*_{z²} band – broaden substantially, causing the absorption peaks to become broader.

Next we investigate the structural properties of some intermediate compositions in order to determine which structural features correlate with the blue color, and in turn to develop guidelines for a general search for blue compounds. Interestingly, our density functional calculations of the relaxed structures for both $\text{Y}_8\text{Mn}_2\text{In}_6\text{O}_{24}$ and $\text{Y}_8\text{Mn}_6\text{In}_2\text{O}_{24}$ units show that, while the basal plane Mn-O and In-O distances in these

Table 4.1 Bond lengths (Å) for $\text{YIn}_{0.37}\text{Mn}_{0.63}\text{O}_3$

Y1-O1	×3	2.44(3)
Y1-O1'	×3	2.18(3)
Y1-O2	×3	2.36(2)
Y1-O2'	×3	2.17(3)
Y1-O3		2.38(2)/3.51(2)
Y2-O1	×3	2.32(2)
Y2-O1'	×3	2.36(2)
Y2-O2	×3	2.28(1)
Y2-O2'	×3	2.18(1)
Y2-O4	×3	2.53(1)/3.35(1)
Mn/In-O1		1.86(3)
Mn/In-O1'		2.05(3)
Mn/In-O2		1.89(2)
Mn/In-O2'		2.20(3)
Mn/In-O3		2.074(3)
Mn/In-O4	×2	2.080(3)

Table 4.2 Atomic coordinates and equivalent isotropic displacement parameters ($\text{\AA}^2 \times 10^3$). $U(\text{eq})$ is defined as one third of the trace of the orthogonalized U_{ij} tensor.

	x	y	z	$U(\text{eq})$
Y1	0	0	0	3(1)
Y2	1/3	2/3	0.9636(1)	13(1)
Mn/In ^a	0.3342(4)	0	0.7211(4)	6(1)
O1	0.322(4)	0	0.879(3)	21(6)
O1'	0.289(5)	0	0.893(2)	0(6)
O2	0.635(3)	0	0.061(2)	0(3)
O2'	0.655(5)	0	0.034(2)	7(6)
O3	0	0	0.202(2)	24(4)
O4	1/3	2/3	0.749(1)	13(3)

^aRefining occupation parameters gave an Mn/In ratio of 1.70 for this site. The O1/O1' and O2/O2' occupancy ratios are fixed at the Mn/In ratio.

Table 4.3 Crystal data and structure refinement for $\text{YIn}_{0.37}\text{Mn}_{0.63}\text{O}_3$ at 173 K

Formula weight	214.00
Wavelength	0.71073 \AA
Crystal system	Hexagonal
Space group	$P6_3\text{cm}$
Unit cell dimensions	$a = 6.1709(6) \text{\AA}$; $c = 11.770(2) \text{\AA}$
Volume, Z	$388.17(9) \text{\AA}^3$, 6
Density (calculated)	5.437 mg/m^3
Absorption coefficient	28.267 mm^{-1}
$F(000)$	576
Crystal size	$0.05 \times 0.03 \times 0.01 \text{ mm}^3$
Theta range for data collection	3.46 to 28.31°
Index ranges	$-7 \leq h \leq 8$, $-7 \leq k \leq 7$, $-15 \leq l \leq 15$
Reflections collected	3766
Independent reflections	363 [$R(\text{int}) = 0.0263$]
Completeness to $\theta = 28.31^\circ$	98.0 %
Absorption correction	Semi-empirical from equivalents
Max. and min. transmission	0.7653 and 0.3322
Refinement method	Full-matrix least-squares on F^2
Data / restraints / parameters	363 / 0 / 31
Goodness-of-fit on F^2	1.178
Final R indices [$I > 2\sigma(I)$]	$R1 = 0.0219$, $wR2 = 0.0407$
R indices (all data)	$R1 = 0.0288$, $wR2 = 0.0438$
Largest diff. peak and hole	0.934 and -0.629 e/\AA^3

intermediates are similar to each other and to those of the end members, the apical Mn-O and In-O distances are very different from each other, maintaining values close to those of the respective end members (Table 1-3).

Because the energy of the d_{z^2} state relative to the valence band maximum is determined primarily by the Mn-O apical bond length, this explains the lack of shift in the energy of the 2 eV absorption peak as a function of Mn concentration. If we artificially insert Mn into the YInO_3 structure without allowing the structure to relax to its energy minimum, the d_{z^2} peak shifts to considerably lower energy and the calculated absorption spectrum changes markedly.

For our single crystal X-ray diffraction study, we focus specifically on the $\text{YMn}_{0.63}\text{In}_{0.37}\text{O}_3$ compound and refine the structure using the $\text{P6}_3\text{cm}$ space group of hexagonal YMnO_3 and YInO_3 . The structure refined normally except for the displacement parameters for one of the apical O atoms, suggesting the presence of static disorder arising from the different In-O and Mn-O distances. Indeed, refinement of the $\text{YMn}_{0.63}\text{In}_{0.37}\text{O}_3$ structure with two O atoms at each apical site, with occupation values fixed based on the Mn/In ratio, converges with shorter distances for the sites with the higher occupation. We extract apical Mn-O distances of 1.86 and 1.89 Å and apical In-O distances of 2.05 and 2.20 Å, in excellent agreement with the results of our first-principles calculations Tables 1-3. Violations of Friedel's law in our diffraction data confirm a polar space group. Relative to the paraelectric structure, displacements of atoms along the c axis, which is the polar axis, are found to be of the same magnitude as in YMnO_3 . However, our first-principles calculations suggest that the

polarization might be substantially suppressed from the values in the end-member compounds due to frustration of the cooperative tiltings by the different sizes of the MO_5 polyhedra, which may be the reason for the intriguing dielectric properties observed.

Finally, motivated by our findings in the $\text{YIn}_{1-x}\text{Mn}_x\text{O}_3$ system, we substituted Mn^{3+} into another structure with trigonal-bipyramidal sites, the YbFe_2O_4 structure [55]. This structure (Figure 4.12) consists of layers of rare earth cations alternating with double layers of MO_5 trigonal bipyramids. As in YMnO_3 , the polyhedra in each MO_3 plane corner-share through their basal-plane oxygen atoms; here the second plane shares edges between an apical and a basal oxygen with the first. As in YMnO_3 , the topology of the layering should allow the apical bond lengths to adopt different values for the different M-site cations without introducing large strain energies into the lattice. Although YbFe_2O_4 is not a suitable host due to its black color related to $\text{Fe}^{2+}/\text{Fe}^{3+}$ mixed valency, there are a selection of oxides with this structure that are transparent throughout the visible spectrum [56]. Again we find that an intense blue color is produced with 5% doping of Mn^{3+} into these compounds, which include ScAlMgO_4 , ScGaMgO_4 , LuGaMgO_4 , ScGaZnO_4 , and InGaMgO_4 . Thus, we conclude that the blue color is a general characteristic of Mn^{3+} in a trigonal-bipyramidal site in oxides, provided that structural features such as layering allow for the appropriate apical Mn-O bond length.

4.3.3 Conclusion

In summary, we have characterized the magnetic, dielectric, and thermodynamic properties of In substituted YMnO_3 to investigate the suppression of the multiferroic phase developing below T_N . We find that the magnetodielectric coupling associated with the multiferroic phase persists in the In substituted samples, but that T_N decreases approximately linearly with increasing In fraction. The antiferromagnetically ordered state in $\text{YIn}_{1-x}\text{Mn}_x\text{O}_3$ appears to vanish for $x \leq 0.5$ and the behaviour of the initial suppression is consistent with two dimensional spin systems. There is a significant enhancement in the magnitude magnetocapacitive coupling with In substitution, although the sign of this coupling varies with x through some mechanism that is not at all clear at this time. Taken collectively, these measurements confirm that replacing Mn by non-magnetic In simply suppresses magnetic ordering without introducing any new phase transitions while simultaneously enhancing the magnetocapacitive coupling. Since it is possible to form a complete solid solution series of $\text{YIn}_{1-x}\text{Mn}_x\text{O}_3$ compounds, more detailed measurements on the microscopic properties of this system may help to clarify the mechanisms giving rise to the multiferroic behaviour in the parent compound.

In addition, we have shown for the first time that an intense and bright blue color occurs through most of the $\text{YIn}_{1-x}\text{Mn}_x\text{O}_3$ solid solution, in spite of the fact that the YInO_3 and YMnO_3 end members are colorless and black, respectively. The compositions as well as color are quite stable to acidic and basic conditions. We have

explained the origin of the color through a detailed structural investigation and by first-principles density functional calculations. It is shown that this color is a general feature of Mn^{3+} in trigonal bipyramidal coordination where the structure can accommodate the required short Mn-O apical bond; this should be particularly favorable in layered structures. Our results suggest a route to the development of inexpensive, earth-abundant, environmentally benign blue pigments that are based on manganese [57].

4.3.4 Experimental

Ceramic samples of $\text{YMn}_{1-x}\text{In}_x\text{O}_3$ for compositions ranging from $x=0$ to 1 were prepared by heating the appropriate ratio of metal oxides at elevated temperatures with intermediate grindings. Reactants were Y_2O_3 (Nucor: Research Chemicals, 99.99 %), Mn_2O_3 (JMC, 99%+), and In_2O_3 (Aldrich, 99.99%). Powders of Y_2O_3 were dried at 850°C before weighing. Appropriate quantities of reactants were mixed thoroughly under ethanol in an agate mortar. Intimately mixed powders were pressed into pellets under a pressure of approximately 500 psi. The pellets were calcined for twelve hours once in air at 1200°C, and twice in air at 1300°C with intermediate grinding. Ramp rates were 300°C/hr. Single crystals were grown in a PbF_2 flux using a 10-fold excess by weight of flux. The mixture was placed in a platinum crucible, which was inserted into an alumina crucible and capped. The mixture was rapidly heated in air to 840°C (melting point of PbF_2) and held for 3 hours. The sample was then heated slowly (5°C/hr) to the 950°C at which point PbF_2 evaporates, and held for 6 hours before cooling to room

temperature at 300°C/hr. The flux was dissolved in nitric acid. The product consisted of thin black hexagonal plates.

X-ray powder diffraction data (XRD) was collected at room temperature with a RIGAKU MINIFLEX II diffractometer using Cu K α and a graphite monochromator. Single crystal X-ray diffraction data were collected on a Bruker SMART APEXII CCD system at 173 K. A standard focus tube was used with an anode power of 50 kV at 30 mA, a crystal to plate distance of 5.0 cm, 512_512 pixels/frame, beam center (256.52, 253.16), total frames of 6602, oscillation/frame of 0.501, exposure/frame of 10.0 s/frame and SAINT integration. A subsequent SADABS correction was applied. The crystal structure was solved with the direct method program SHELXS and refined with full-matrix least-squares program SHELXTL (1). Results are given in Tables 1S-4S. The crystal was found to be twinned with an up/down polarization ratio of 0.35(3).

A Quantum Design MPMS SQUID magnetometer and a Quantum Design Physical Property Measurement System (PPMS) were used to measure the magnetic properties of ~30 mg of the powder samples. For the specific heat measurements, we thoroughly mixed approximately 50 mg of each sample with the same mass of Ag powder then pressed this composite into small disks to ensure good thermal contact throughout the entire sample. The heat capacity was then measured using the standard option on the Quantum Design PPMS. This system was also used to provide temperature and magnetic field control for the capacitance measurements, which were done on cold-pressed pellets prepared from the YMn_{1-x}In_xO₃ powders having electrodes fashioned from silver epoxy. The dielectric measurements were done at a measuring frequency

of 30 kHz. Separate measurements (not shown) indicated that the frequency response of these samples was flat in the region between 1 kHz and 100 kHz.

The diffuse reflectance spectra of powdered samples in the range of 250 – 900 nm were obtained using Xe lamp and a grating double monochromator as the source. The spectrometer is calibrated from a He-Ne laser and known Xe source emission lines and position. The diffuse light reflected by the powders was collected with an integrating sphere and detected using a Si diode detector. The data were normalized to the signal obtained from MgO powder under the same conditions. The data were transformed into absorbance using Kubelka-Munk function.

4.4 Synthesis and Magnetic Properties of YMnO_3 - $\text{YCu}_{0.5}\text{Ti}_{0.5}\text{O}_3$ Solid Solution

4.4.1 Introduction

Strong coupling of magnetic and electric parameters is a behavior unique to few systems. This is due to the fundamental understanding that ferroelectrics inherently lack unpaired electrons, and ferromagnetic materials do not. Where this coupling does exist, the induced electric polarization or magnetization is generally too weak for proposed applications such as a magneto-electric switch [58]. It is thus easy to recognize that the understanding and coexistence of these properties is not only necessary, but also of great importance to the development of next generation devices.

One of the few classes of materials that exhibit magneto-electric coupling is the RMnO_3 system ($\text{R} = \text{Ho-Lu}$, and Y). This class has the unique hexagonal structure where Mn occupies layers of corner shared trigonal bipyramids (TBP), Figure 4.3. R^{3+} cations sit in an off-center position due to the crystal field splitting of (d^4) Mn^{3+} in TBP coordination where the unoccupied d_{z^2} orbital is hybridized with O 2p along the c-axis [7, 9, 49, 59]. The result of the off-centering is a polar structure where ferroelectricity is observed. In YMnO_3 , ferroelectric and antiferromagnetic ordering temperatures have been identified at $T_C \sim 900$ K and $T_N \sim 80$ K respectively [27, 30, 59, 60]. Capacitance measurements show there is a clear anomaly at T_N , an observation indicative of coupling between electric and magnetic order parameters [27].

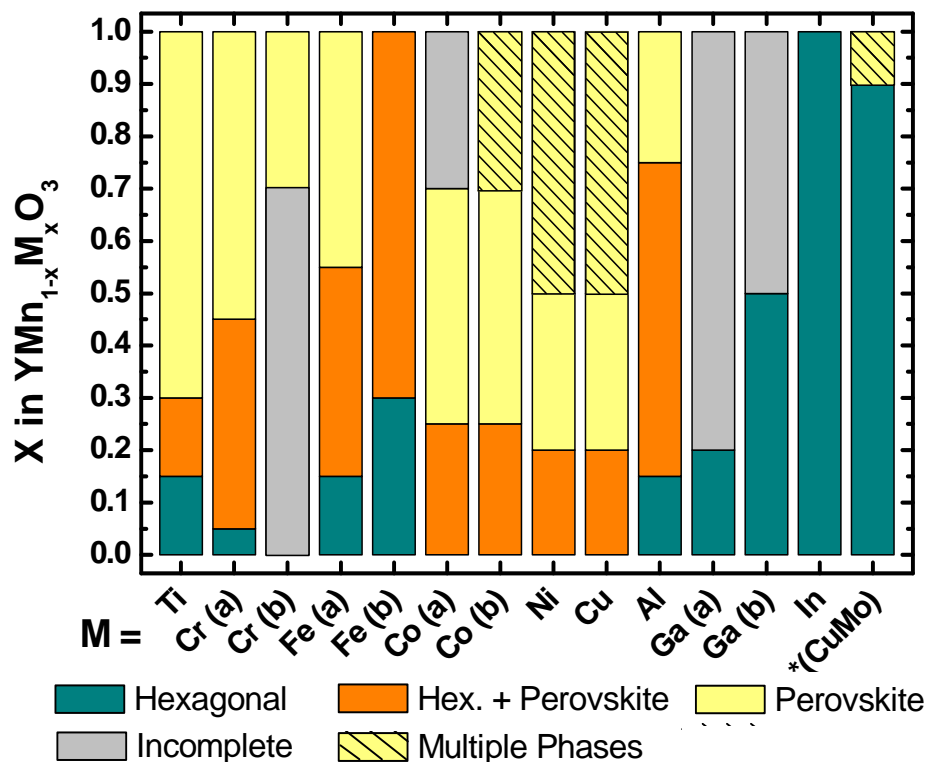


Figure 4.16 Structural variation for substitutions in $\text{YMn}_{1-x}\text{M}_x\text{O}_3$.

In recent years, investigations have attempted to elucidate the magnetoelectric coupling in YMnO_3 by doping on the Mn sites [17 19-26] Figure 4.16. For example low doping of gallium onto the Mn site retained the hexagonal structure and resulted in a slight increase of the ferroelectric ordering temperature and an enhancement of the magnetocapacitive coupling [20, 21]. Despite the several accounts of substitutions on the Mn site for materials where the end compound is hexagonal (YGaO_3 , YAlO_3 , YFeO_3), the recently reported solid solution of YMnO_3 and hexagonal YInO_3 is the only full solid solution to maintain the hexagonal structure [17, 19-21, 61, 62]. This was a unique discovery as the structural instability observed with other dopants was

eliminated, thus allowing for magnetoelectric coupling to be assessed as the magnetic transition was suppressed. In addition, it was found that a brilliant blue color was present over much of the substitution range despite YMnO_3 and YInO_3 being black and white respectively. This presents the foundation for hexagonal oxides containing Mn^{3+} as potentially inexpensive, environmentally benign inorganic pigments in addition to the interest as potential multiferroic materials. As such, continued exploration of miscibility in YMnO_3 based phases is warranted due to the potential for novel properties.

There also exists a family of copper containing materials related to the RMnO_3 phases including $\text{RCu}_{0.5}\text{Ti}_{0.5}\text{O}_3$ ($\text{R} = \text{Tb-Lu, Y}$) and $\text{LaCu}_{2/3}\text{V}_{1/3}\text{O}_3$ with the hexagonal structure [63, 64]. In addition, Mn doped $\text{YCu}_{3/4}\text{Mo}_{1/4}\text{O}_3$ also has the hexagonal structure for Mn compositions above 0.1 [65]. As doping of a single cation onto the Mn site in YMnO_3 is limited, it is perplexing to consider co-doping on the Mn site may yield new compositions of hexagonal YMnO_3 based materials. To date, there are currently no investigations on the stability of Cu/Ti co-doping onto the Mn site to enhance the magneto-electric properties in YMnO_3 . We present here on the magnetic and dielectric properties of a new full solid solution between YMnO_3 and $\text{YCu}_{0.5}\text{Ti}_{0.5}\text{O}_3$.

4.4.2 Results and Discussion

Up until the recent report on In doped YMnO_3 , there had been no reports of a full,

single phase solid solution with YMnO_3 that retained the hexagonal structure. Interestingly, we have been able to form a full solid solution between YMnO_3 and $\text{YCu}_{0.5}\text{Ti}_{0.5}\text{O}_3$ (Cu:Ti ratio is kept at 1:1) which also has the hexagonal structure and could be indexed to $\text{P6}_3\text{cm}$ space group. The powder diffraction patterns for polycrystalline $\text{YMn}_{1-x}(\text{Cu}_{0.5}\text{Ti}_{0.5})_x\text{O}_3$ ($0 \leq x \leq 1$) are shown in Figure 4.17.

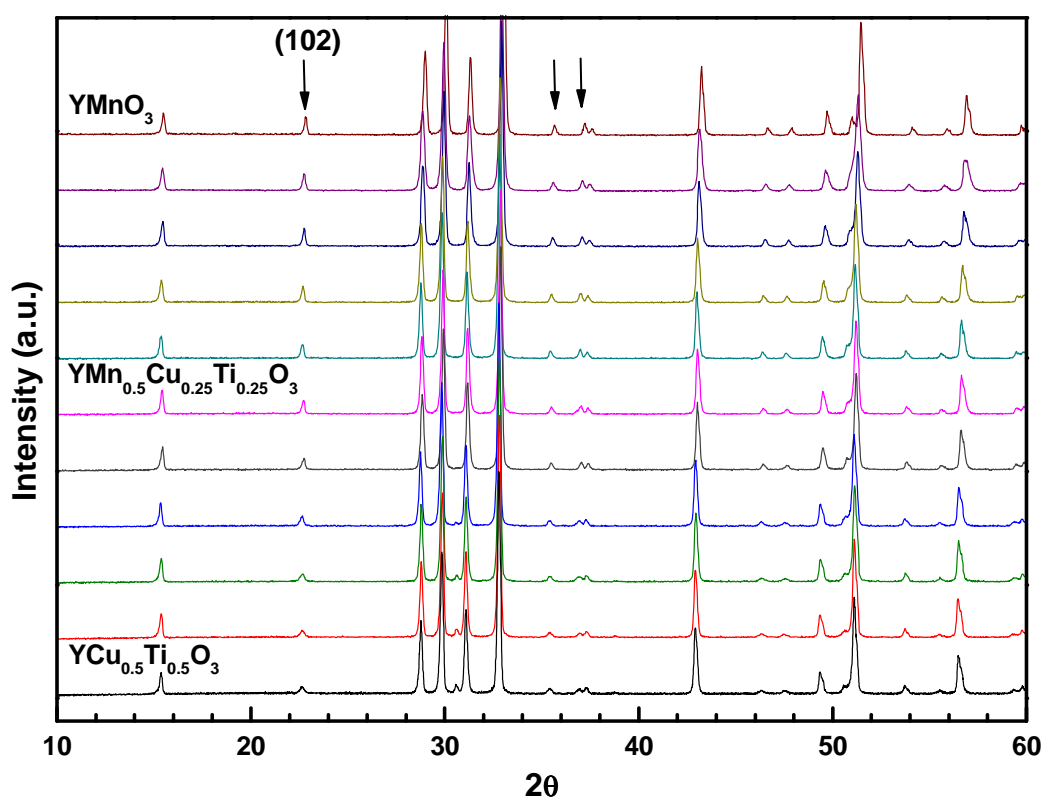


Figure 4.17 X-ray diffraction patterns for $\text{YMn}_{1-x}(\text{Cu}_{0.5}\text{Ti}_{0.5})_x\text{O}_3$. End members are at the bottom ($\text{YCu}_{0.5}\text{Ti}_{0.5}\text{O}_3$) and top (YMnO_3).

Aside from the similarities in the powder patterns, the variation of relative intensities can be seen for several crystallographic reflections such as the (102) reflection at $22\text{--}23^\circ$ 2θ , and others marked with arrows in Figure 4.17. In YMnO_3 ,

these reflections are representative of the $\sqrt{3} \times \sqrt{3}$ distortion of Mn^{3+} trimers [7]. As seen elsewhere for substitutions, Cu/Ti co-substitutions in YMnO_3 also results in a decrease of these reflections [65].

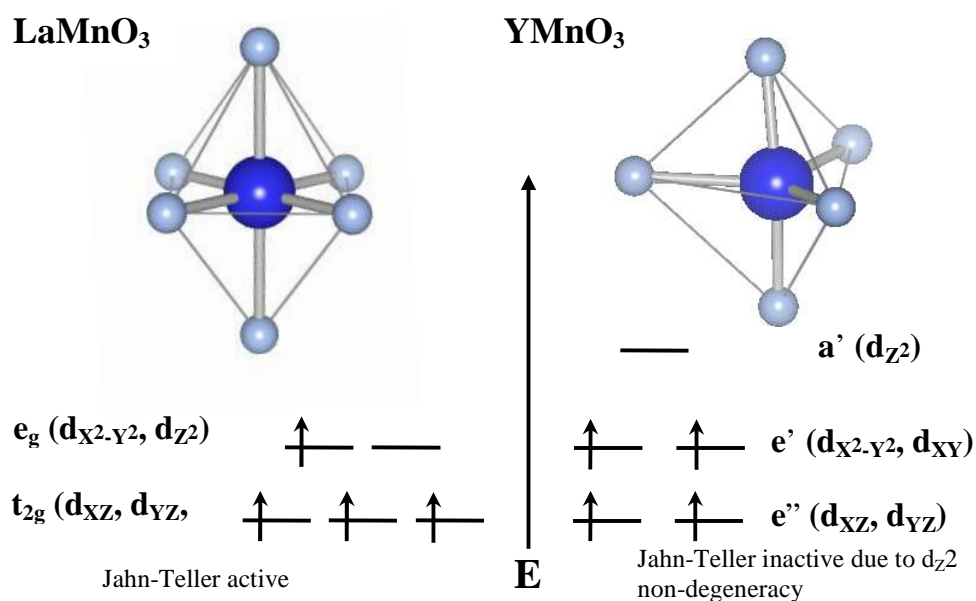


Figure 4.18 Local coordination environment and energy level diagrams from Mn^{3+} in the perovskite (LaMnO_3 - left) and hexagonal (YMnO_3 - right) structures.

We expect the substitution of Cu^{2+} and Ti^{4+} for Mn^{3+} to result in two effects on the TBP site. First, a change of the orbital occupations due to the substitution of (d^9) Cu^{2+} and (d^0) Ti^{4+} is expected. A (d^9) Cu^{2+} atom would have an electron occupying the d_z^2 orbital and would cause an elongation of the c-axis and a decrease of the TBP tilt (it should be noted that (d^4) Mn^{3+} is not Jahn-Teller active, and has no electron occupation of the non-degenerate d_z^2 orbital, Figure 4.18). However, (d^0) Ti^{4+} has no electron occupation of 3d orbitals and would not contribute to c-axis changes. The second effect of substitutions to be expected is due to the size differences of Cu^{2+} and

Ti^{4+} compared to Mn^{3+} in TBP coordination. The average ionic radius of Cu^{2+} and Ti^{4+} , 0.58 Å, is the same as Mn^{3+} for a 5 coordinated polyhedra [66]. Thus, we expect there to be little change in the a parameter due to ionic radii. However, as the tilt angle should slightly decrease with an elongation of the apical Mn-O bond distance, we would expect a slight change in the a parameter. Indeed, we observe an increase in the a and c lattice parameters calculated from powder x-ray diffraction (Figure 4.19). The

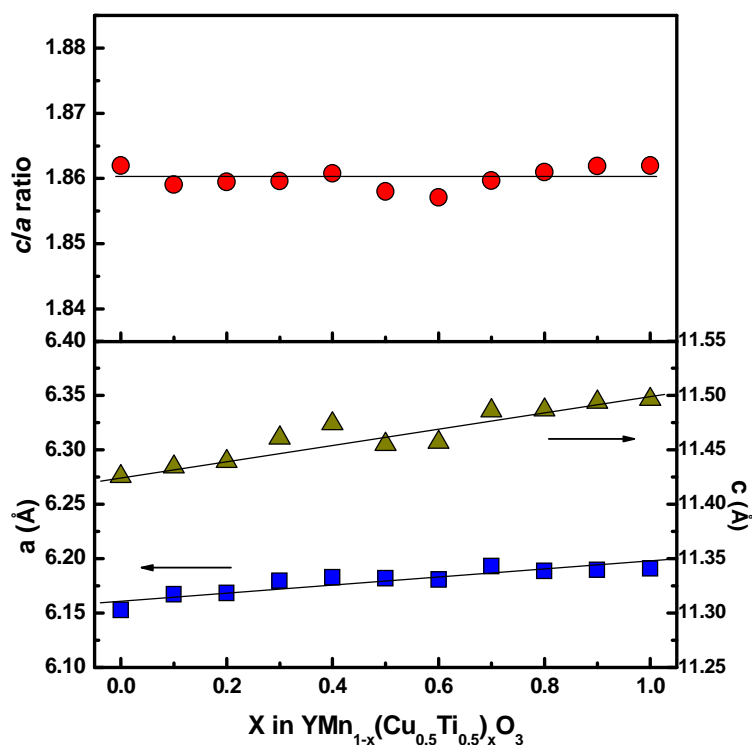


Figure 4.19 Unit cell dimensions (bottom) and c/a ratio (top) for $\text{YMn}_{1-x}(\text{Cu}_{0.5}\text{Ti}_{0.5})_x\text{O}_3$.

c/a ratio stays relatively flat indicating that for varying compositions, the apical and basal M-O bond distances change consistently with each other ($\Delta c \sim 2\Delta a$). In order to address this further, single crystal analysis is necessary and will be the subject of

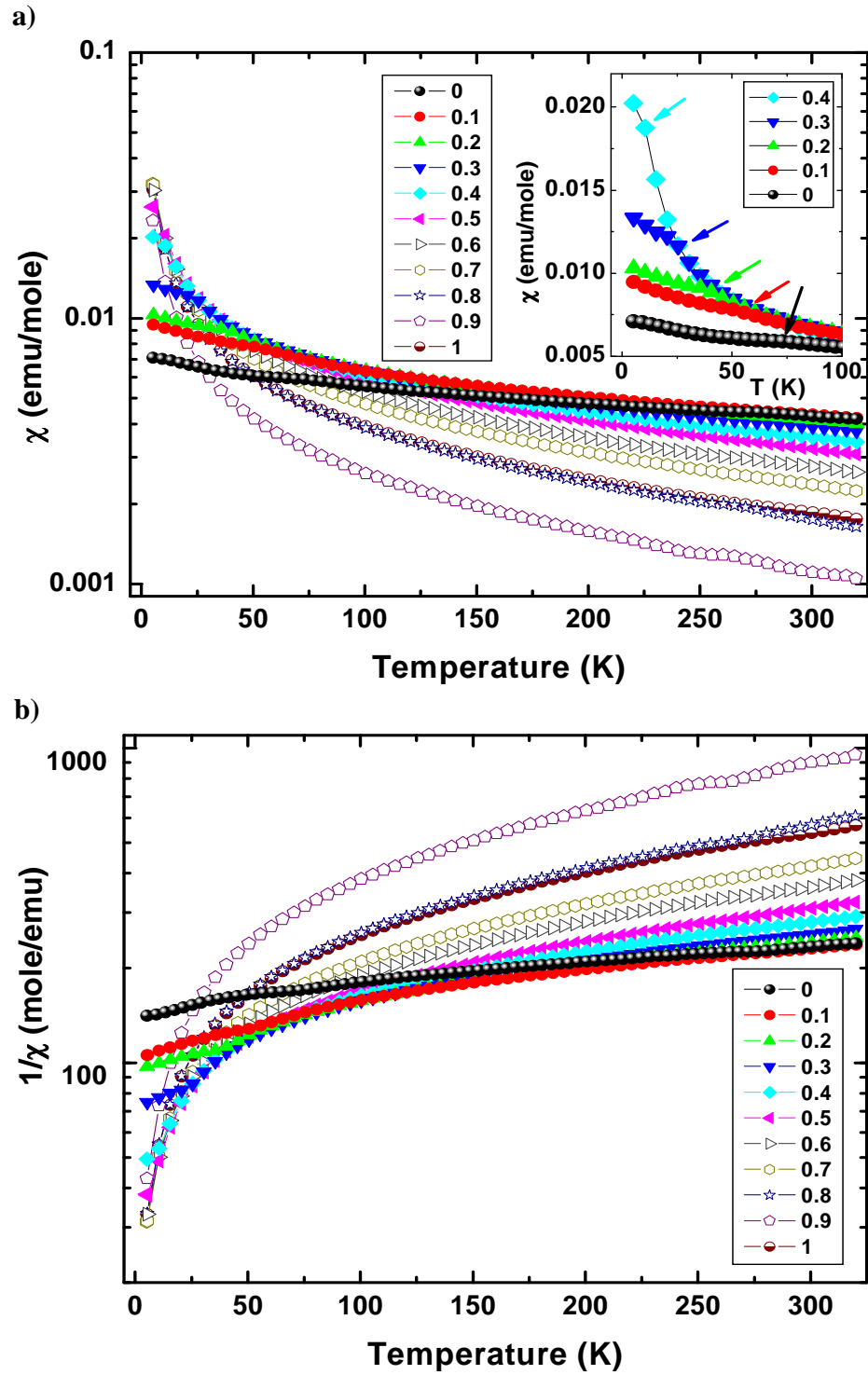


Figure 4.20 Inverse magnetic susceptibility (a) and magnetic susceptibility (b) for $\text{YMn}_{1-x}(\text{Cu}_{0.5}\text{Ti}_{0.5})_x\text{O}_3$. Magnetic anomalies are labeled by arrows (a-inset).

future work.

The temperature dependence of the magnetic susceptibility (χ) and inverse magnetic susceptibility ($1/\chi$) for all compositions of $\text{YMn}_{1-x}(\text{Cu}_{0.5}\text{Ti}_{0.5})_x\text{O}_3$ measured at $H = 0.5\text{T}$ are illustrated in Figures 4.20 (a) and (b) respectively. All samples can be fitted reasonably to the Curie-Weiss law for temperatures greater than 175 K, however, fitting to temperatures above the measurements made here would be more accurate. Therefore, some deviation from theoretical values is expected. A systematic decrease in the high temperature $\chi(T)$ is observed with increasing x which is to be expected for diluting a magnetic lattice with a combination of non-magnetic (d^0) Ti^{4+} and less magnetic (d^9) Cu^{2+} cations. A pronounced anomaly in the slope of $1/\chi(T)$ can be seen for values of $x \leq 0.4$ indicating an antiferromagnetic ordering transition. Upon dilution in YMnO_3 ($T_N \sim 73\text{ K}$) by $\text{Cu}^{2+}(S=1/2)$ / $\text{Ti}^{4+}(S=0)$, the antiferromagnetic transition is suppressed until no ordering anomaly in $1/\chi(T)$ is observed for $x = 0.5$

Table 4.4 Results for Curie-Weiss analysis of magnetic susceptibility.

x	$\Theta_{\text{CW}} (\text{K})$	C (mole/emu*K)	calculated $\mu_{\text{eff}} \mu_B$	Observed $*\mu_{\text{eff}} \mu_B$	$T_N (\text{K})$	Frustration $ \Theta_W / T_N$
1	-75.09	0.686	1.223	2.338	-	-
0.9	-50.92	0.389	1.936	1.764	-	-
0.8	-65.78	0.644	2.449	2.271	-	-
0.7	-100.48	0.949	2.872	2.757	-	-
0.6	-113.08	1.124	3.241	3.001	-	-
0.5	-157.64	1.480	3.571	3.442	-	-
0.4	-173.39	1.668	3.874	3.654	10.5	16.51
0.3	-226.98	2.027	4.154	4.029	25.6	8.86
0.2	-298.01	2.456	4.417	4.435	45.5	6.55
0.1	-357.90	2.831	4.665	4.761	55.6	6.44
0	-415.49	3.065	4.900	4.954	73.1	5.68

(Figure 4.20 (a) and inset). This indicates that $\text{Cu}^{2+}/\text{Ti}^{4+}$ doping disrupts the magnetic array, weakening the $\text{Mn}^{3+} - \text{O} - \text{Mn}^{3+}$ interactions until they are completely quenched. Theoretical and experimental values calculated from the Curie-Weiss analysis are listed in Table 4.4, and indicate a very steady change in the effective magnetic moment, Neel temperature (for $x \leq 0.4$), and Curie-Weiss temperature.

Negative Curie-Weiss temperatures are observed for all compositions revealing antiferromagnetic interactions are dominant. In addition, there is a consistent broadening of $1/\chi(T)$ as the Mn content is decreased. We attribute this to the disorder caused from a random distribution of $\text{Mn}^{3+}/\text{Cu}^{2+}/\text{Ti}^{4+}$ on the same site. The magnetic properties of $\text{YCu}_{0.5}\text{Ti}_{0.5}\text{O}_3$ have not been previously assessed, but indicate that there is no long range magnetic ordering.

Due to the triangular geometric array of Mn^{3+} ions, a spin frustration is present. Ramirez [67] determined that the frustration in antiferromagnetic geometric systems could be quantified as a ratio of the Curie-Weiss temperature to the ordering temperature, $f = |\theta_{\text{CW}}| / T_{\text{N}}$. For slight doping of $\text{Cu}^{2+}/\text{Ti}^{4+}$ there is an increase in the frustration from $f = 5.68$ to 6.44 and up to 16.51 for $x = 0, 0.1$ and 0.4 respectively. The value of 5.68 is comparable to previous reports of moderate frustration ($f > 10$ is a highly frustrated system) in YMnO_3 [30]. We attribute the decrease in the magnetic ordering temperature to the increase in the magnetic frustration from disorder of the Mn site.

Previous studies have revealed that magneto-electric coupling in YMnO_3 can be observed by the presence of a magnetic anomaly at the antiferromagnetic ordering

temperature. As the intent of this work was to address the impact of cation substitution on the magnetic properties, the dielectric behavior at the magnetic ordering temperature was also measured. Figure 4.21 illustrates the temperature dependence of the relative capacitance for various compositions. Slight anomalies are observed at the magnetic ordering temperatures which is indicative of magneto-electric coupling. Only compositions $0 < x \leq 0.4$ are plotted with ordering temperatures indicated by arrows. The inset ($\text{YCu}_{0.5}\text{Ti}_{0.5}\text{O}_3$) is plotted for comparison as no magnetic ordering temperature is observed in the magnetic susceptibility data. The results of the

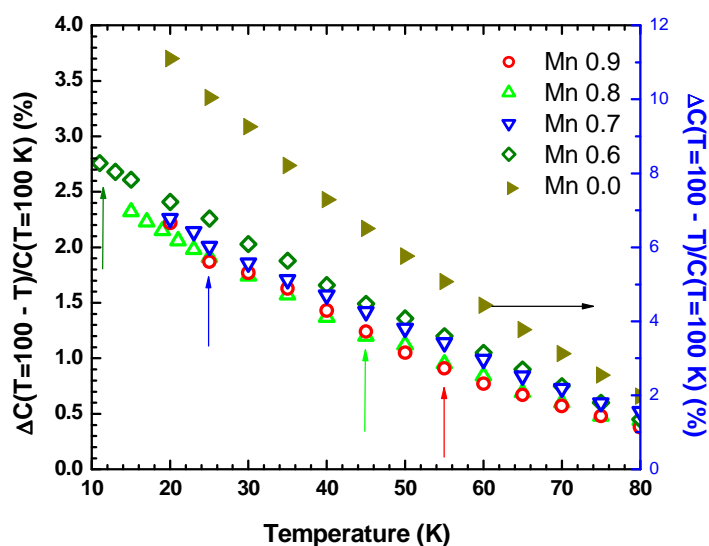


Figure 4.21 Temperature dependence of the relative capacitance for $\text{YMn}_{1-x}(\text{Cu}_{0.5}\text{Ti}_{0.5})_x\text{O}_3$ with arrows indicating the magnetic ordering temperature.

magnetic analysis (Neel temperature from magnetism and capacitance, Curie-Weiss temperature, and effective magnetic moments) are summarized in Figure 4.22.

Due to the interest in inorganic oxide pigments, such as that found in $\text{YIn}_{1-x}\text{Mn}_x\text{O}_3$, we also considered the potential for color in this work. $\text{YCu}_{0.5}\text{Ti}_{0.5}\text{O}_3$ has a unique

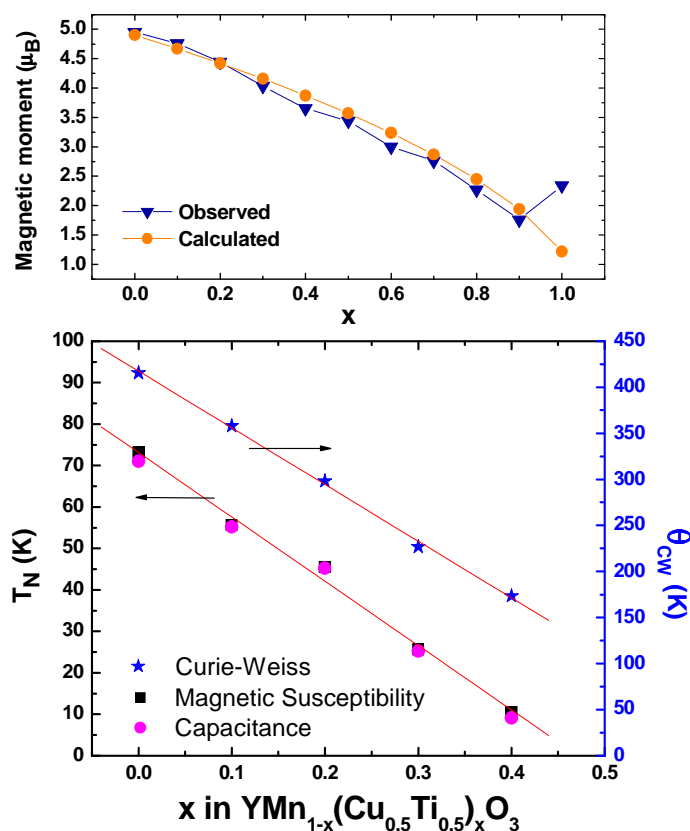


Figure 4.22 Compositional dependence of the antiferromagnetic ordering temperature and Curie-Weiss temperature (bottom) and calculated and observed magnetic moments (top) for $\text{YMn}_{1-x}(\text{Cu}_{0.5}\text{Ti}_{0.5})_x\text{O}_3$.

light green color. However, upon Mn substitution into the lattice, there was an immediate change to black which persisted for all compositions. Additional compositions were also considered to address the miscibility limits of the structure and the potential for enhancing the color. Compositions included Cr, Fe, Al, Ga, and In for values up to $x = 0.5$. It was found that regardless of cation, all substitutions formed impurity phases for $x > 0.2$, Figure 4.23.

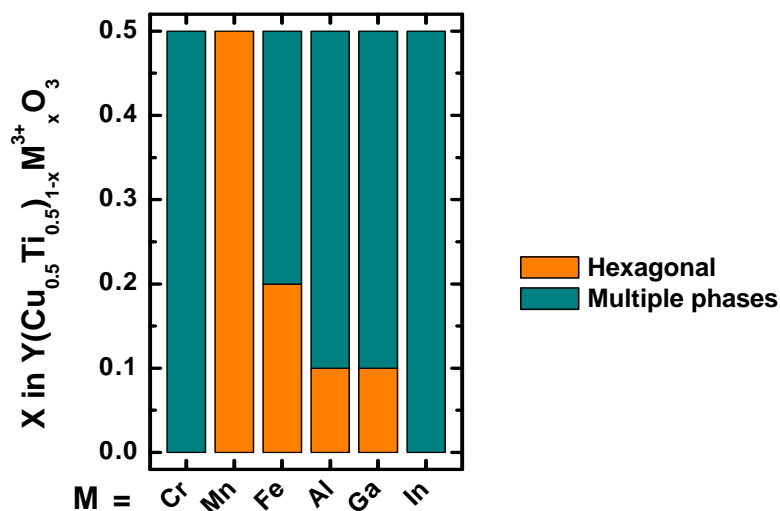


Figure 4.23 Substitutional allowance in hexagonal $\text{YCu}_{0.5}\text{Ti}_{0.5}\text{O}_3$.

Because Al, Ga, and In lack unpaired electrons we expected to observed a more diluted green color. However, a more intense green color is evident for all at $x = 0.1$. Al substitution was found to be most efficient as an intensifier and is evident in diffuse reflectance spectra. Results of the optical measurements are illustrated in Figure 4.24.

We see that, at low doping concentrations, there is a strong and narrow (~ 1 eV width) absorption centered at around 1.6 eV, which absorbs in the red region of the visible spectrum. Absorption then drops between 1.75 – 2.5 eV before a second onset near 3 eV. Strong absorption in the red and blue spectral region, and the absence of absorption in the 1.75 – 2.5 eV (yellow-green) region is responsible for the observed intense green color. As the concentration of Al increases, the lower energy absorption peak is slowly quenched, and the higher energy onset is slowly diminished and

broadened, consistent with the gradual lightening of the samples towards pale green and then white. In pure YAlO_3 absorption is absent through the entire visible region

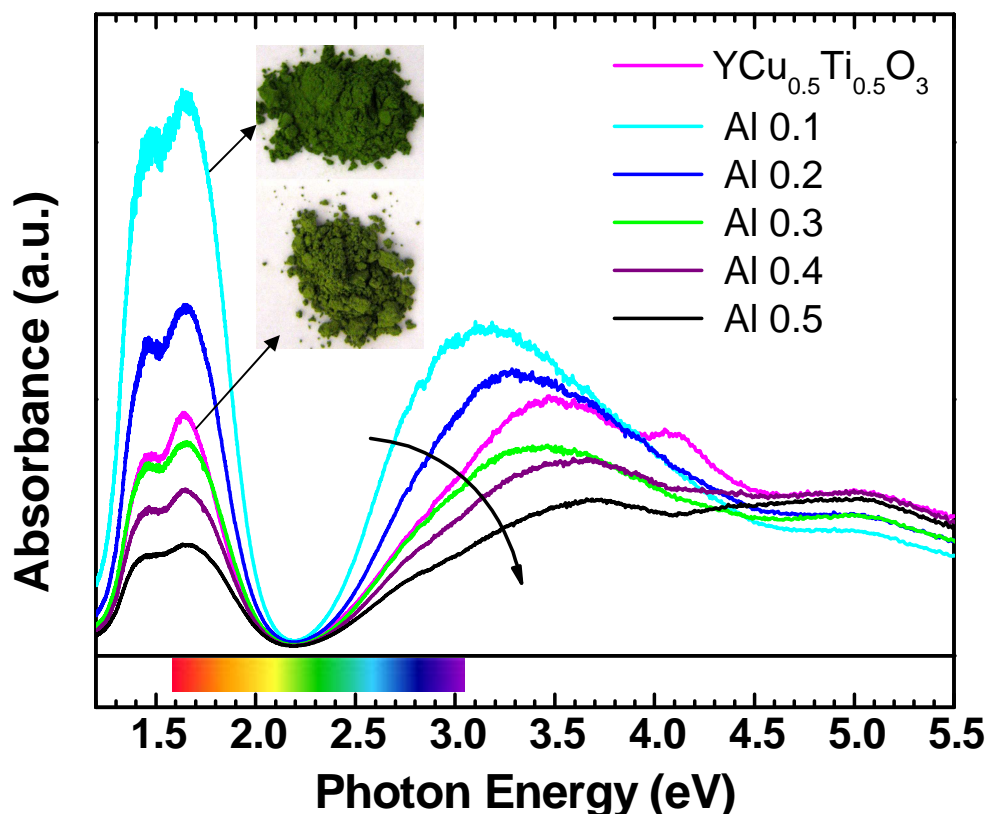


Figure 4.24 Diffuse reflectance spectra for the $\text{Y}(\text{Cu}_{0.5}\text{Ti}_{0.5})_{1-x}\text{Al}_x\text{O}_3$ for $x \leq 0.5$.

resulting in the white color. It should be noted that from $x = 0$ ($\text{YCu}_{0.5}\text{Ti}_{0.5}\text{O}_3$) to $x = 0.1$ the sharpness and intensity of the 1.6 eV peak dramatically increases. In addition, the peak sharpness of the second onset also increases. The result of this is a brighter and more intense green color as opposed to the more pale color of $\text{YCu}_{0.5}\text{Ti}_{0.5}\text{O}_3$. The same scenario is also observed in hexagonal $\text{YIn}_{1-x}\text{Mn}_x\text{O}_3$ as discussed earlier.

4.4.3 Conclusions

The co-substitution of Cu^{2+} and Ti^{4+} (in equal quantities) into the hexagonal YMnO_3 compound yields only the hexagonal structure for all compositions. Some slight formation of the pyrochlore $\text{Y}_2\text{Ti}_2\text{O}_7$ phase exists for the parent $\text{YCu}_{0.5}\text{Ti}_{0.5}\text{O}_3$, as reported, and for $x \leq 0.3$, however the quantities are quite small. No additional impurities could be identified by x-ray powder diffraction. The structural trends from a and c parameter changes are consistent with expectations based on orbital occupancy and ionic radii differences. There is a clear and consistent trend of magnetic suppression upon doping of Cu/Ti into YMnO_3 , and this is comparable to previous reports on the effect of Ga, In, and Cu/Mo substitutions on the magnetic properties [21, 61, 65]. The Néel temperatures determined from magnetic susceptibility and capacitance measurements agree well with values dropping from 73.1 K to 45.5 K to 10.5 K for $x = 0, 0.2$ and 0.4 respectively. Strong interactions between neighboring Cu atoms in $\text{YCu}_{0.5}\text{Ti}_{0.5}\text{O}_3$ are also suppressed upon Mn introduction as is evident in the magnetic moment calculations. Field dependent capacitance is needed to properly assess these materials as magneto-electric multiferroics. As reinforced here, there remains compositions to be found where co-substitution on the Mn site can stabilize the hexagonal structure.

4.4.4 Experimental

Polycrystalline samples of $\text{YMn}_x(\text{Cu}_{0.5}\text{Ti}_{0.5})_{1-x}\text{O}_3$ ($x = 0 - 1$) used in this investigation were prepared by conventional solid state synthesis by powder-sintering samples with precursors of 98.0% or higher. Reactants of Y_2O_3 (Nucor Research Chemicals 99.9%), Mn_2O_3 (JMC 98%+), CuO (Aldrich 99.99%), and TiO_2 (JMC 99.99%), were mixed thoroughly in stoichiometric ratio in ethanol. Y_2O_3 was first heated to 850°C for 6-8 hours to remove any moisture. The mixed powders of starting materials were calcined at 900°C for 12 hours and then at 1050°C for an additional 24 hours with intermediate grinding. The intimately mixed powder was cold pressed into pellets under a pressure of ~ 1000 psi. The pellets were sintered in air at 1050°C for 12 hours. Ramping rates were 300°C/hr . X-ray powder diffraction (XRD) patterns were obtained after each heating with a Rigaku MiniFlex II diffractometer using $\text{Cu K}\alpha$ radiation and a graphite monochromator. Pattern processing and phase identification were determined using JADE Materials Data software utilizing several diffraction databases. Lattice parameter refinements were calculated using WinCell, and were done so with ~ 12 -18 reflections in the range of 10 - $80^\circ 2\theta$. Magnetism was measured using a Physical Property Measurement System from 5K to 300K. A field of 0.5 Tesla was applied after zero field cooling. For capacitance measurements, pellets of samples were polished, electroded with silver paint (Haerus high temp Ag-paste in n-butyl acetate) and then dried for 3–5h at 100°C . Measurements on the pellets utilized an HP-4275A LCR meter in the temperature range of 5–100 K at frequencies up to 13 MHz.

4.5 Structural Investigation of Hexagonal YAlO_3 and Related Compositions

4.5.1 Introduction

The hexagonal structure has been reported for several RMO_3 compounds where M is Mn, Ga, In, Fe, or Al as mentioned previously [9, 28, 62, 68-70]. The R cation is generally In, Y, or a heavier rare earth. Within this hexagonal group, there are two common symmetries observed, the simpler, centric and paraelectric $\text{P6}_3/\text{mmc}$ ($Z = 2$) and the more complicated, non-centric and ferroelectric $\text{P6}_3/\text{cm}$

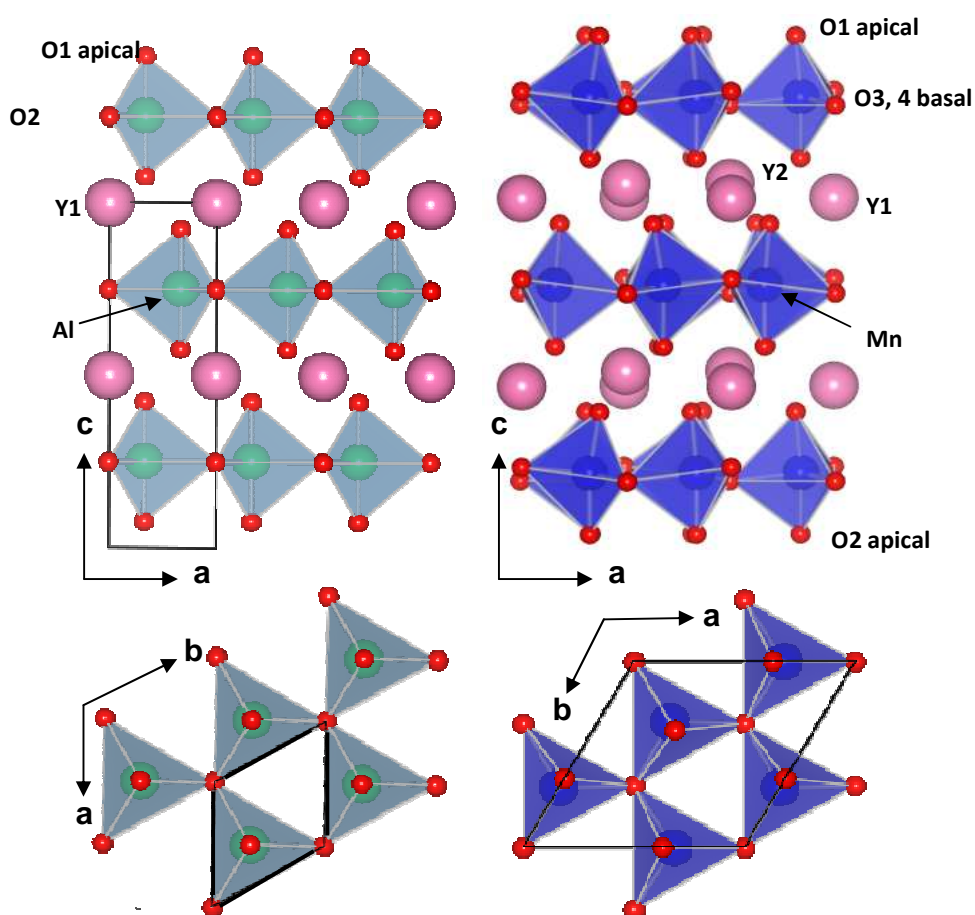


Figure 4.25 Centric YAlO_3 (left) and non-centric YMnO_3 (right) ($Z = 6$), Figure 4.25.

The non-centric form is distorted thus causing an increase in the cell edges, compared to the non- centric form, by a factor of $\sqrt{3}$, thus changing Z from 2 to 6. These two structural variations are illustrated in Figure X. The centric paraelectric structure has been observed from InMO_3 where $\text{M} = \text{Ga}, \text{Fe}$ and Mn , and also for RMO_3 where R is a heavier rare earth, and M is Fe or Al. The structural reports on these materials are far from few, and are quite reliable. The only exception is for the RAIO_3 compositions which were originally reported in 1963 based on powder diffraction data acquired from films [62]. This series is the only one in which the lattice parameters are dramatically different from all other observations. Based on simple bond valence calculations and an understanding of the structure, we feel this structure hasn't been properly reported. The focus of this work is to address the structural inconsistencies reported for YAlO_3 and to report on structure and synthesis of the solid solution $\text{YAl}_{1-x}\text{Mn}_x\text{O}_3$ with the hexagonal structure.

4.5.2 Results and Discussion

The formation of hexagonal phases is generally a high temperature synthesis when RMnO_3 is considered ($\text{R} = \text{heavier rare earth}$). However for YAlO_3 and YFeO_3 the synthetic methods for preparation are quite different, distinguished mainly by a low temperature solutions route due to the ease of impurity formation. If one considers the $\text{Y}_2\text{O}_3\text{-Al}_2\text{O}_3$ phase diagram, they will find several materials of considerable interest, specifically $\text{Y}_4\text{Al}_2\text{O}_9$ and Y_2O_3 as a phosphor host matrix, $\text{Y}_3\text{Al}_5\text{O}_{12}$ as a

component of phosphors in cathode ray tubes, and perovskite YAlO_3 and $\text{Y}_3\text{Al}_5\text{O}_{12}$ (YAG) as potential host matrices for solid state lasers [71]. It is also interesting to note that the formations of many of these phases are present, including hexagonal YAlO_3 , in the synthesis of any individual phase. Therefore, a great deal of consideration must be put into synthetic methods when preparing a material in this phase diagram. As such, it was found that h- YAlO_3 can be synthesized in single phase by a low temperature solution based method [62]. Our attempts to repeat this failed. We used a modified citrate-gel precursor method to prepare nearly single phase YAlO_3 . The citrate-gel route is important because it can lower synthesis temperatures, and increase

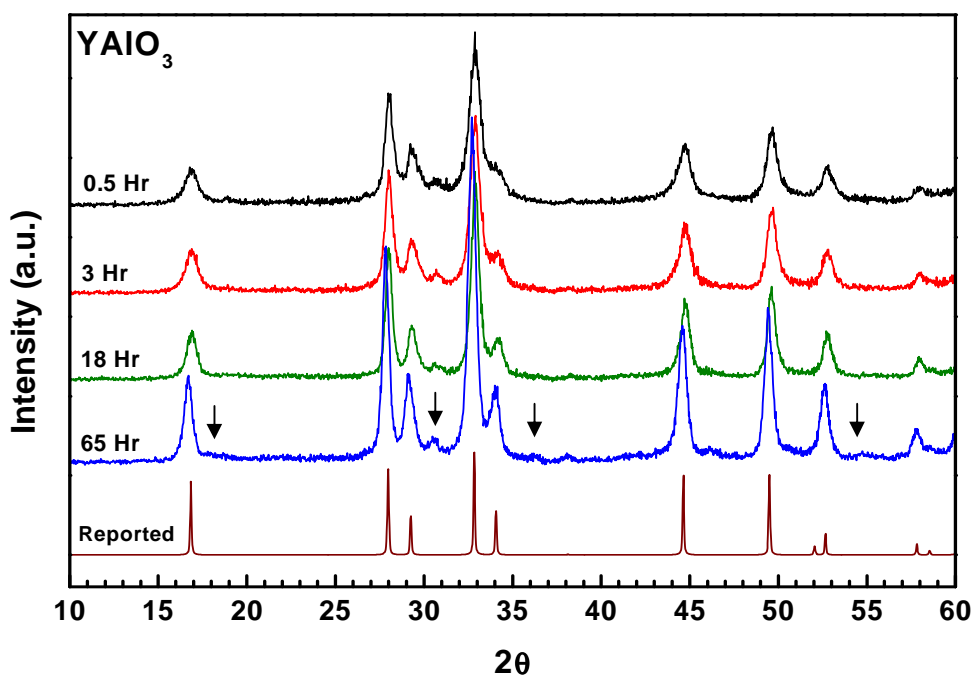


Figure 4.26 Powder x-ray diffraction patterns for YAlO_3 . Arrows indicate the impurity phase $\text{Y}_4\text{Al}_2\text{O}_9$.

surface area leading to increased reactivity, and stabilize meta-stable phases which are

otherwise impossible to stabilize in high temperature bulk reactions. Figure 4.26 illustrates the x-ray powder diffraction data collected for h-YAlO₃ synthesis. The formation of h-YAlO₃ was found to occur in a very narrow temperature range. Despite previous reports on the formation at 900°C - 1000°C, we found the formation to only occur at 875°C [62] through thermal gravimetric analysis, Figure 4.27. Powder x-ray diffraction was collected on samples after TGA on the dried gel and on samples heated to 750°C prior to TGA. It is clear that there is a weight loss onset at about 825°C which ends approximately at 875°C and then again continues to drop. Impurity formations at 900°C are listed in Figure 4.27. Increased dwell times resulted in more phase pure compositions, however, the presence of Y₄Al₂O₉ was always observed

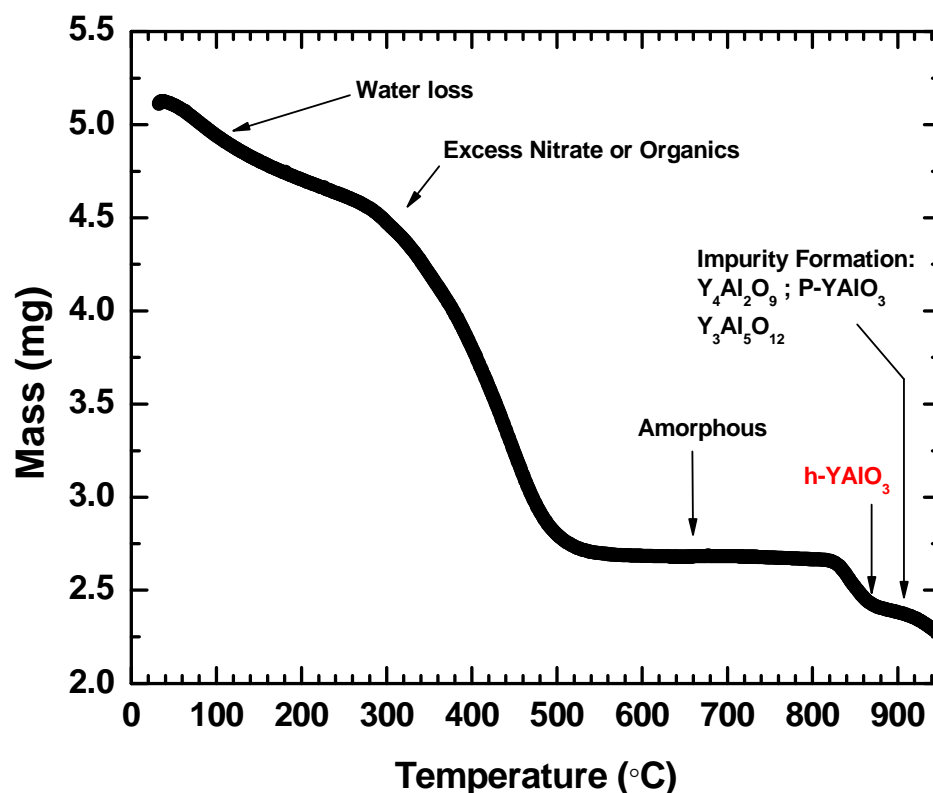


Figure 4.27 Thermal Gravimetric Analysis of YAlO₃ from a dehydrated citrate gel.

(marked as arrows in Figure 4.26). Further attempts to improve this were unsuccessful.

A closer examination YAlO_3 and other hexagonal compositions reveals that the unit cell reported, $a = 3.68 \text{ \AA}$ and $b = 10.52 \text{ \AA}$, is strikingly large compared to YMnO_3 which has unit cell parameters of $a = 6.14 \text{ \AA}$ and $b = 11.44 \text{ \AA}$ [28]. This occurs despite the fact that Al^{3+} is smaller than Mn^{3+} in trigonal bipyramidal coordination. Based on ionic radii alone, the average Al-O bond distance should be $\sim 1.86 \text{ \AA}$, and this is similar to the reported value of 1.82 \AA . The values for the three basal plane oxygen is $\sim 2.125 \text{ \AA}$ meaning that the average Al-O bond distance is 2.01 \AA , or about 0.2 \AA larger than expectations based on ionic radii. This is a convincing argument that the reported structure may be incorrect. In addition, the bond valence sums for Y (3.35) and Al (2.39) are unacceptable. Simple modification of the structure by moving the apical oxygen away from Y and toward Al also resulted in BVS that were unacceptable for Al, although an improvement was seen for Y. If we adjust the unit cell to $a = 3.2 \text{ \AA}$ and $b = 12.8 \text{ \AA}$, reasonable BVS values are observed for Y, Al, and Oa, but not Ob. We conclude that this must mean that Ob atoms are weakly bound no matter where they lay in the Al plane. Moving the Ob atoms from a 2b position to a 6h position means that O is moving from a completely occupied site to a 1/3 occupied site. In order to keep the Al coordination at 3, half of the sites need to be filled. This suggests a ratio for Y:Al:O of 1:1:3.5 which could be achieved by hydration such as $\text{YAlO}_{2.5}(\text{OH})$. Figure 4.28 shows the IR spectra for BaCO_3 standard and for two samples of YAlO_3 . BaCO_3 was used as a reference as it has been well characterized, and also would provide insight to whether samples were carbon containing as in that

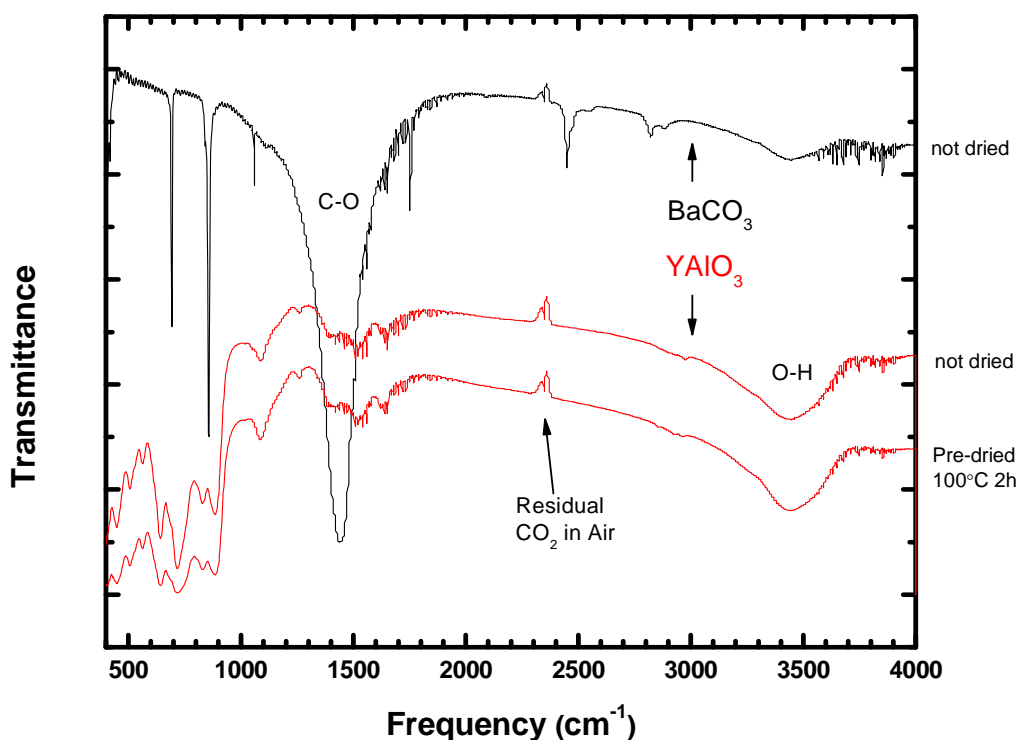


Figure 4.28 IR-spectra of YAlO_3 and BaCO_3 as reference.

of carbonate groups. The peaks observed below $\sim 1000 \text{ cm}^{-1}$ generally represent a finger print region which, for YAlO_3 , is unique to Al-O and Y-O interactions. It is interesting to note the O-H stretch at about 3500 cm^{-1} . We believe this may in fact be due to a hydroxyl group present in our samples, and work done by J. Mareschal suggests this may likely be from physisorbed water [72]. This would then be consistent of our conclusion that the Ob atoms are weakly bound, and would potentially allow weakly bound hydroxyl groups by van der Waals forces which is the main mechanism for physisorption [73]. The results here are still relatively inconclusive. A further investigation of the potential for a carbonate group was

perhaps more convincing. The TGA pattern in Figure 4.27 shows a distinct loss above 900°C. This is potentially due to the decomposition of a carbonate group as many carbonates are known to be stable up to high temperatures, some as high 1200°C. A simple acid test on YAlO_3 resulted in dramatic bubbling which is indicative of CO_2 release. A test of some YAlO_3 powder in water resulted in no bubbling.

As our initial interest in YAlO_3 was to provide a host for cheaper inexpensive pigments from our work on $\text{YIn}_{1-x}\text{Mn}_x\text{O}_3$, we addressed the influence of Mn

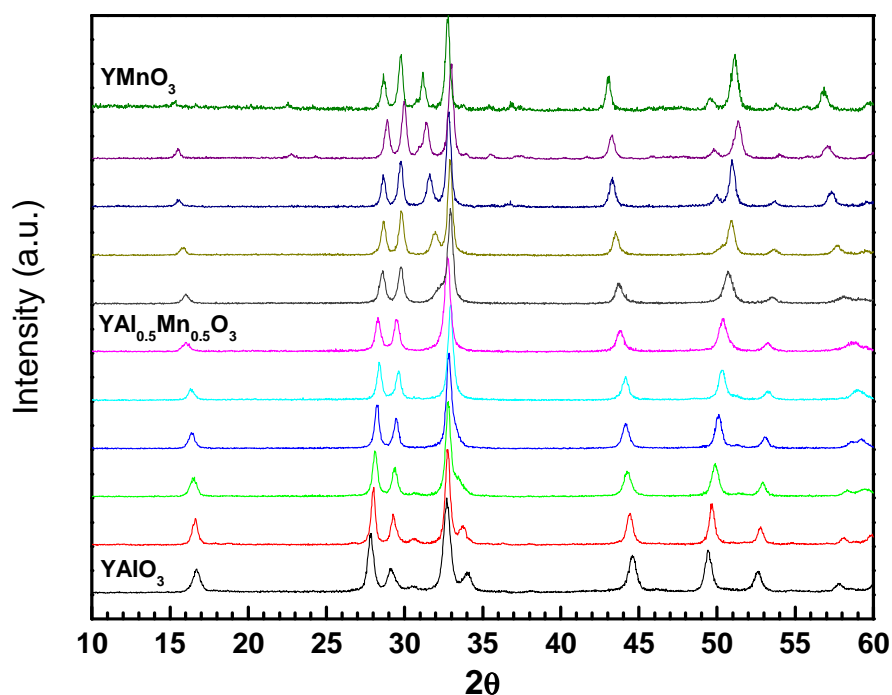
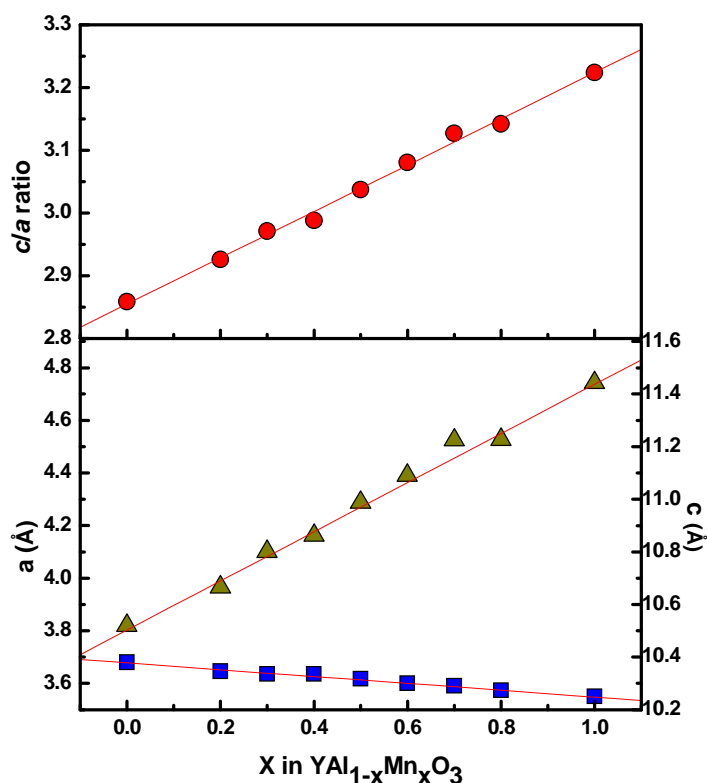


Figure 4.29 Powder x-ray diffraction patterns for $\text{YAl}_{1-x}\text{Mn}_x\text{O}_3$ in $x = 0.1$ intervals.

substitution on not only the structure, but also the color. Figure 4.29 illustrates the powder diffraction patterns for Mn substituted YAlO_3 prepared at 900°C, and Figure 4.30 shows the unit cell parameter variation. Compositions of $\text{YAl}_{1-x}\text{Mn}_x\text{O}_3$, where



4.30 Unit cell dimensions (bottom) and c/a ratio (top) for YAl_{1-x}Mn_xO₃

$0.3 \leq x \leq 0.8$, were found to be single phase. Initial refinements on $x = 0.2$ proved difficult, similar to YAlO₃. A deep navy blue was observed for compositions of $0.4 \leq x \leq 0.6$, however there was no range in which an intense blue was present such as that in YIn_{1-x}Mn_xO₃. This may be due to the size differences of Al compared to In and the resulting effect on the apical bond distance. As it was determined that YAlO₃ may contain a carbonate group, an acid test was also performed on YAl_{0.5}Mn_{0.5}O₃ and YAl_{0.7}Mn_{0.3}O₃ compositions. It was found that both compositions resulted in bubbling upon the addition of acid, however, there did not appear to be a large difference in the amount of bubbling between the compositions. This indicates that a carbonate group is

present. Metallic Mn or Cu may also result in bubbling upon acid addition, however, this can be excluded as all compositions are made in air at high temperatures. The presence of the carbonate group may not be dependent on composition and is likely to have an allowed range such as $\text{YAl}_{1-x}\text{Mn}_x\text{O}_{3-y}(\text{CO}_3)_y$. This was reinforced by sporadic unit cell volumes for the $\text{YAl}_{1-x}\text{Mn}_x\text{O}_3$ compositions. A more detailed structural investigation will provide a better understanding of the YAlO_3 structure and the effect of Mn substitution. Neutron diffraction is currently underway.

4.5.3 Conclusion

Our investigation into YAlO_3 and Mn substituted YAlO_3 leads us to believe that the initial structural report is incorrect. We base this on an assessment of the hexagonal structure family and on bond valence sums from the report on YAlO_3 . Although $\text{YMn}_{0.9}\text{Al}_{0.1}\text{O}_3$ has been previously prepared, there has been no report of low temperature synthesis compositions within this solid solution [18]. We realize that an in-depth structural investigation is warranted and currently have beam time assigned on the BT1 High Resolution Neutron Powder Diffractometer at NIST for YAlO_3 and several Mn substituted compositions. We expect that the resolution in these measurements will give us unique details in atomic positions and structural variation for various compositions and will lead to a better understanding of the structural variations in this family of materials. We also plan to address the magnetic and magneto-dielectric properties of Mn substituted compositions.

4.5.4 Experimental

Analytical grade metal nitrates can also be used in the preparation of hexagonal $\text{YAl}_{1-x}\text{Mn}_x\text{O}_3$. $\text{Y}(\text{NO}_3)_3 \cdot 6\text{H}_2\text{O}$ (Alfa Aesar, 99.9%), $\text{Al}(\text{NO}_3)_3 \cdot 9\text{H}_2\text{O}$ (Alfa Aesar, 99.99%) and $\text{Mn}(\text{NO}_3)_2 \cdot 4\text{H}_2\text{O}$ (Aldrich, 99%) were dissolved in approximately 20 ml of deionized water under stirring. The solution was heated to 60°C and allowed to sit under stirring for about 15 minutes to ensure all precursors are dissolved into solution. Citric acid (Mallinckrodt) was then added in a molar ratio of 2:1 metal nitrate. The solution was then neutralized with ammonium hydroxide and then evaporated at ~90°C for several hours until a viscous gel was formed. The dried gel was then combusted at 250°C for 2 hours to decompose the nitrates. The resulting black product was then ground and heated at 700°C for 10 hours to eliminate the organic components. Initial powder x-ray diffraction measurements of samples heated at 700°C indicated the materials were completely amorphous. An additional heating at 900°C in air as pellets for a total of about 12 hours resulted in a phase pure hexagonal phase for most compositions. YAlO_3 was prepared in an alternate method due the metastability and ease of impurity formation. The dried gel of was ground and spread out in an alumina tray as a shallow bed. The sample was inserted into a preheated furnace at 875°C for 65 hours, and quenched to room temperature. X-ray powder diffraction (XRD) patterns were obtained after each heating with a Rigaku MiniFlex II diffractometer using $\text{Cu K}\alpha$ radiation and a graphite monochromator. Pattern processing and phase identification were determined using JADE Materials Data software utilizing several diffraction databases.

4.6 References

1. E. Ascher, H. Rieder, H. Schmid and H. Stössel, *J. Appl. Phys.*, 37 (1966) 1404
2. N. A. Spaldin and M. Fiebig, *Science*, 309 (2005) 391
3. T. Kimura, G. Lawes and A. P. Ramirez, *Phys. Rev. Lett.*, 94 (2005) 137201
4. Wang, J. B. Neaton, H. Zheng, V. Nagarajan, S. B. Ogale, B. Liu, D. Viehland, V. Vaithyanathan, D. G. Schlom, U. V. Waghmare, N. A. Spaldin, K. M. Rabe, M. Wutting and R. Ramesh, *Science*, 299 (2003) 1719
5. W. Brixel, I. P. Rivera, A. Steiner and H. Schmid, *Ferroelectrics*, 79 (1988)201
6. N. Hur, S. Park, P. A. Sharma, J. S. Ahn, S. Guha and S-W. Cheong, *Nature*, 429 (2004) 392
7. T. Katsufuji, S. Mori, M. Masaki, Y. Moritomo, N. Yamamoto and H. Takagi, *Phys. Rev. B*, 64 (2001) 104419.
8. J.-S. Zhou, J. B. Goodenough, J. M. Gallardo-Amores, E. Morán, M. A. Alario Franco, and R. Caudillo, *Phys. Rev. B*, 74 (2006) 014422
9. H. Yakel, W. Koehler, E. Bertaut, F. Forrat, *Acta Cryst.*, 16 (1963) 957
10. J. B. Goodenough, J. M. Longo, Magnetic and Other Properties of Oxides and Related Compounds, Landolt-Börnstein, Numerical data and Functional Relations in Science and Technology, New Series Vol. III. 4 (Springer, Berlin, 1970)
11. T. Lonkai, D. G. Tomuta, U. Amann, I. Ihringer, R. W. A. Hendrikx, D. M. Tobbens, A. Mydosh, *Phys. Rev. B*, 69 (2004) 134108(1).
12. A. Munoz, J. A. Alonso, M. Martinez-Lope, M. T. Casais, L. Martinez, M. T. Fernandez-Daiz, *Phys. Rev. B*, 62 (2000) 9498
13. W. J. Merz, *Phys. Rev.*, 76 (1949) 1221
14. C. W. F. T. Pistorius, and J.G. Kruger, *J. Inorg. Nucl. Chem.*, 38 (1976) 1471
15. A. Munoz, J. A. Alonso, M. Martinez-Lope, M. T. Casais, L. Martinez, M. T. Fernandez-Daiz, *Phys. Rev. B*, 62 (2000) 9498

16. G. H. Gehring, *Ferroelectrics*, 161 (1994) 275
17. S. L. Samal, W. Green, S. E. Lofland, K. V. Ramanujachary, D. Das, A. K. Ganguli, *J. Solid State Chem.*, 61 (2008) 181
18. J. Park, M. Kang, J. Kim, K.H. Jang, A. Pirogov, J.G. Park, *Phys. Rev. B*, 79 (2009) 064417
19. A.E. Smith, H. Mizoguchi, K. Delaney, N.A. Spaldin, A.W. Sleight, M.A. Subramanian, *J. Am. Chem. Soc.*, 131 (2009) 17084
20. A. A. Nugroho, N. Bellido, U. Adem, G. Nénert, Ch. Simon, M. O. Tjia, M. Mostovoy, and T. T. M. Palstra, *Phys. Rev. B*, 75 (2007) 174435
21. H. D. Zhou, J. C. Denyszyn, and J. B. Goodenough, *Phys. Rev. B*, 72 (2005) 224401
22. H. I. Ismailzade, G. A. Smolenskii, V. I. Nesterenko, F. A. Agaev, *Phys. Stat. Sol. (a)*, 5 (1971) 83
23. D. Gutiérrez, O. Peña, K. Ghanimi, P. Durán, C. Moure, *J. Phys. Chem. Sol.*, 63 (2002) 1975
24. O. Peña, M. Bahout, D. Gutiérrez, J. F. Fernández, P. Durán, C. Moure, *J. Phys. Chem. Sol.*, 61 (2000) 2019
25. T. Asaka, K. Nemoto, K. Kimoto, T. Arima, Y. Matsui, *Phys. Rev. B*, 71 (2005) 014114
26. O. Peña, M. Bahout, D. Gutiérrez, J.F. Fernández, P. Durán, C. Moure, *J. Phys. Chem. Sol.*, 61 (2000) 2019
27. Z. J. Huang, Y. Cao, Y. Y. Sun, Y. Y. Xue, and C. W. Chu, *Phys. Rev. B*, 56 (1997) 2623
28. T. Katsufuji, S. Mori, M. Masaki, Y. Moritomo, N. Yamamoto, and H. Takagi, *Phys. Rev. B*, 64 (2001) 104419
29. M. Fiebig, Th. Lottermoser, D. Frohlich, A. V. Goltsev, and R. V. Pisarev, *Nature*, 419 (2002) 818
30. D G Tomuta, S Ramakrishnan, G J Nieuwenhuys and J A Mydosh, *J. Phys.: Condens. Matter*, 13 (2001) 4543

31. M. Tachibana, J. Yamazaki, H. Kawaji, T. Atake, *Phys. Rev. B*, 72 (2005) 064434
32. X. Fabreges, S. Petit, I. Mirebeau, S. Pailhes, L. Pinsard, A. Forget, M. T. Fernandez-Diaz, and F. Porcher, *Phys. Rev. Lett.*, 103 (2009) 067204
33. T. Lottermoser, T. Lonkai, U. Amann, D. Hohlwein, J. Ihringer, M. Fiebig, *Nature*, 430 (2004) 541
34. M. N. Iliev, H.-G. Lee, V. N. Popov, M. V. Abrashev, A. Hamed, R. L. Meng, and C. W. Chu, *Phys. Rev. B*, 56 (1997) 2488
35. H. Fukumura, N. Hasuike, H. Harima, K. Kisoda, K. Fukae, T. Takahashi, T. Yoshimura and N. Fujimura, *J. Phys.: Conf. Series*, 92 (2007) 012126
36. D.-Y. Cho et al, *Phys. Rev. Lett.*, 98 (2007) 217601
37. B.B. Van Aken, T.T.M. Palstra, A. Filippetti, N. Spaldin, *Nature Materials*, 3 (2004) 164
38. N. Fujimura, H. Sakata, D. Ito, T. Yoshimura, T. Yokota, and T. Ito, *J. Appl. Phys.*, 93 (2003) 6990
39. S. Mori, J. Tokunaga, Y. Horibe, Y. Aikawa, T. Katsufuji, *Phys. Rev. B*, 72 (2005) 224434
40. G. Lawes, A. P. Ramirez, C.M. Varma, and M. A. Subramanian, *Phys. Rev. Lett.*, 91 (2003) 257208
41. T. Idogaki, Y. Miyoshi and J.W. Tucker, *J. Magn. Magn. Mater.*, 154 (1996) 221
42. H. Jaksch, W. Seipel, K.L. Weiner, A. El Goresy, *Naturwissenschaften.*, 70 (1983) 525
43. http://en.wikipedia.org/wiki/Cobalt_blue. Accessed May 2009.
44. <http://en.wikipedia.org/wiki/Ultramarine>. Accessed May 2009.
45. http://en.wikipedia.org/wiki/Prussian_blue. Accessed May 2009
46. <http://en.wikipedia.org/wiki/Azurite>. Accessed May 2009
47. R.D. Shannon, *Inorg. Chem.*, 6 (1967) 1474

48. A. Waintal, J. Chenavas, *CR Acad.Sci. Paris.*, (1967) 264
49. B. B. Van Aken, A. Meetsma, T. M. Palstra, *Acta Cryst.* 2001, C57, 230
50. C. J. Fennie, K. M. Rabe, *Phys. Rev. B*, 72 (2005) 100103
51. A. Filippetti, N. A. Hill, *Phys. Rev. B*, 65 (2002) 195120
52. M. Ciampolini, *Chem. Commun.*, 2 (1966) 47
53. C. Degenhardt, M. Fiebig, D. Fröhlich, Th. Lottermoser, R. V. Pisarev, *Appl. Phys. B*, 73 (2003) 139
54. A. M. Kalashnikova, R. V. Pisarev, *JETP Lett.*, 78 (2003) 143
55. K. Kato, I. Kawada, N. Kimizuka, *Z. Kristallogr.*, 141 (1975) 314
56. N. Kimizuka, T. Mohri, *J. Solid State Chem.*, 60 (1985) 382
57. There was once in use a blue pigment called Mn-blue. This pigment was prepared from permanganate solutions and has been shown to be BaSO_4 containing Mn^{5+} and Mn^{6+} . The blue chromophore was identified as Mn^{5+} in tetrahedral coordination to oxygen. This pigment is no longer in use due to toxicity issues relating to the Ba. The term “Mn-blue” is still used to describe the hue of this Mn containing pigment [D. Reinen, T. C. Brunold, H. O. Guedel, N. D. Yordanov, *Zeit. Anorg. Allg. Chem.*, 624 (1998) 438]
58. W. Eerenstein, N.D. Mathur, J.F. Scott, *Nature*, 442 (2006) 759
59. I.G. Ismailzade, S.A. Kizhaev, *Sov. Phys. Solid State.*, 7 (1965) 236
60. G.A. Smolenskii, V.A. Vokov, *J. Appl. Phys.*, 35 (1964) 915
61. A. Dixit, A.E. Smith, M.A. Subramanian, G. Lawes, *Solid State Comm.*, 150 (2010) 746
62. E.F. Bertaut, J. Mareschal, *Compt. Rend.*, 257 (1963) 867
63. N. Floros, J.T. Rijssenbeek, A.B. Martinson, K.R. Poeppelmeier, *Solid State Sciences* 4 (2002) 1495
64. D.A. Vander Griend, S. Malo, K.T. Wang, K.R. Poeppelmeier, *J. Am. Chem. Soc.*, 122 (2000) 7308

- 65. S. Malo, A. Maignan, S. Marinl, M. Hervieu, K.R. Poeppelmeier, B. Raveau, *Solid State Sci.*, 7 (2005) 1492
- 66. R.D. Shannon, *Acta Cryst. A*, 32 (1976) 751
- 67. A.P. Ramirez, *Geometric Frustration: Handbook of Magnetic Materials*, Ed K.H.J. Buschow (Amsterdam: North-Holland/Elsevier) (2001)
- 68. D.M. Giaquinta, H.C. Zur Loye, *J. Am. Chem. Soc.*, 114 (1992) 10952
- 69. D.M. Gianquinta, H.C. Zur Loye, *Chem. Mater.*, 6 (1994) 365
- 70. J. Li, U.G. Singh, T.D. Schladt, J.K. Stalick, S.L. Scott, R. Seshadri, *Chem. Mater.*, 20 (2008) 6567
- 71. P. Florian, M. Gervais, A. Douy, D. Massiot, J.P. Coutures, *J. Phys. Chem. B*, 105 (2001) 379
- 72. J.C. Marchal. *Synthesis, analysis and processing of novel materials in the Y_2O_3 - Al_2O_3 system*. Ph.D. Thesis, The University of Michigan, Ann Arbor, MI, 2008
- 73. E.M. McCash. *Surface Chemistry*; Oxford University Press: New York, 2001

Chapter 5

Tuning the Dielectric Properties of $\text{CaCu}_3\text{Ti}_4\text{O}_{12}$ Through Compositional Control

5.1 Abstract

In this chapter we discuss the compositional variation of the parent compound $\text{CaCu}_3\text{Ti}_4\text{O}_{12}$ and its effect on the dielectric properties. For the first time, we have shown that single phases of fluorine substitution on the oxygen site can be prepared at compositions as high as $x = 1.3$ in $\text{CaCu}_3\text{Ti}_4\text{O}_{12-x}\text{F}_x$. The variation in the dielectric behavior for lower fluorine compositions resulted in improved loss values and a high dielectric constant. We attribute the lower loss and retained high dielectric constant to the difficulty of electron movement through fluorine as compared to oxygen, and that fluorine may be occupying important planar defects in $\text{CaCu}_3\text{Ti}_4\text{O}_{12}$.

The co-substitution of Mn and Fe for Cu and Ti, respectively, in $\text{CaCu}_3\text{Ti}_4\text{O}_{12}$ resulted in single phase materials from $x = 0 - 0.5$ and 1. Mossbauer analysis confirmed Fe occupies both the Ti octahedral site, and Cu square planar site. Other known samples such as $\text{LaCu}_3\text{Ti}_3\text{FeO}_{12}$ are similar. We attribute the drop in the dielectric constant to the disorder of 3 cations in both the Cu and Ti sites and the quenching of magnetic order to weakened superexchange interactions.

Publications based on this chapter:

- 1) Smith, Andrew E., Sleight, Arthur W., Subramanian, M. A., An anion substitution route to low loss colossal dielectric $\text{CaCu}_3\text{Ti}_4\text{O}_{12}$. *Journal of Solid State Chemistry*, 182 (2009) 409-411

5.2 Introduction

Many oxides with the perovskite or closely related structure have unique and intriguing properties which include superconductivity, multiferroism, high-K dielectricity, thermoelectricity, piezoelectricity, and distinct magnetic behavior [1]. The variety of properties has made the perovskite structure one of the most studied and most used in industrial technologies. Interestingly, they continue to raise many questions regarding the fundamentals of structure-property relationships [2]. Current applications are largely focused in integrated circuit technologies, which are not only evolving quickly, but are also tending towards the miniaturization of most components. Generally, this miniaturization requires novel materials with enhanced properties. As in capacitive components for dynamic and static memory, the degree of enhancement will likely be determined by the magnitude of the dielectric constant and loss. Thus, the study of materials with high dielectric constants and low losses are of great importance.

Several simple and complex perovskite oxides have been reported to show relatively high dielectric constants and are currently integrated as components in modern devices. This includes the simple perovskites SrTiO_3 and BaTiO_3 [3-5]. Generally, high dielectric constants are associated with ferroelectric or relaxor behavior where the dielectric constant shows a peak as a function of temperature. The behavior is dictated by a spontaneous polarization related to a structural transition from higher to lower symmetry. This limits the functionality of the material and therefore limits its practical use in devices. BaTiO_3 is a perfect case study of a

ferroelectric material due to the systematic structural phase transitions and thus changes in the spontaneous polarization resulting in high dielectric constants. The Ti^{4+} displace from its barycenter toward an oxygen anion upon lowering temperature, Figure 5.1, thus resulting in a structural transition from cubic to tetragonal which occurs at 120°C . Upon further cooling, the Ti^{4+} displace toward yet another oxygen anion, resulting in a structural transition from tetragonal to orthorhombic. A third distortion of Ti^{4+} toward a 3rd oxygen anion results in a structural transition from orthorhombic to rhombohedral. Each of these distortions, and thus structural or ferroelectric transitions coincides and a peak in the dielectric constant (in relaxors, a broad hill is observed at the transition temperature) versus temperature, Figure 5.2 [3, 5]. Small substitutions in the lattice can be made to stabilize some features of the dielectric properties, including the temperature dependence. For example, due to the large change in the dielectric constant in BaTiO_3 at the ferroelectric ordering

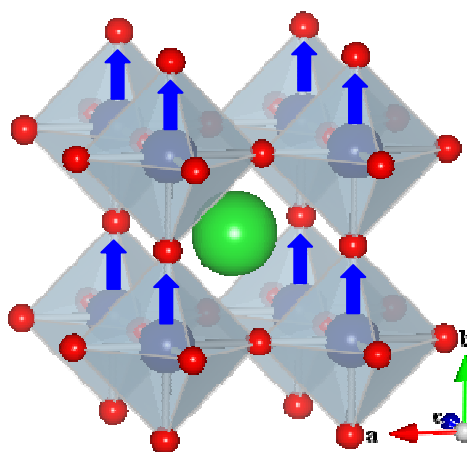


Figure 5.1 Structural illustration of cubic perovskite BaTiO_3 with arrows indicating Ti^{4+} offset within corner shared octahedra upon decreasing temperature from cubic to tetragonal structure. Red spheres are oxygen, and the Green central sphere is barium.

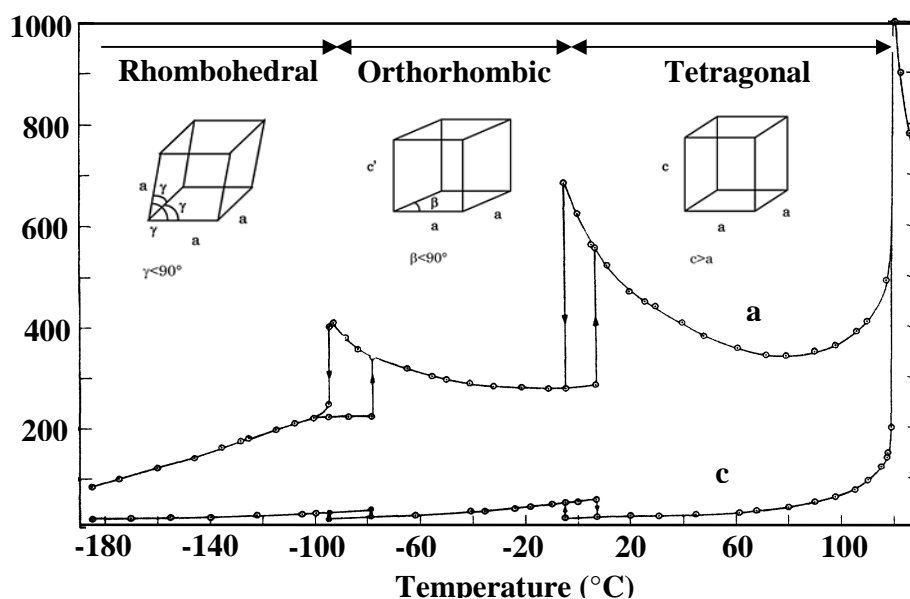


Figure 5.2 Dielectric constant of BaTiO_3 as a function of temperature. Structures are inset at the proper temperature ranges. Adapted from W.J. Merz [5].

temperature, it is often doped with Sr. This suppresses the dielectric anomalies associated with the ferroelectric transition temperatures.

When ionic radii and coordination environments are considered, the majority of the periodic table can be accommodated into the perovskite structure. When substitutions are made into the simple perovskite formula ABX_3 , ordering of the substituted site can occur such as $\text{A}_{1-x}\text{A}'_x\text{BO}_3$ and $\text{AB}_{1-x}\text{B}'_x\text{O}_3$. Here, A or A' generally represent a lanthanide, alkali metal or alkali earth metal, and B or B' represents a transition metal. In 1967 Deschanvres *et al* reported on a unique new structure of the materials $\text{CaCu}_3\text{Ti}_4\text{O}_{12}$ and $\text{CdCu}_3\text{Ti}_4\text{O}_{12}$, Figure 5.3 [6]. Between 1967 and 1988 there were a handful of reports that included detailed structural investigations by neutron diffraction [7], magnetic measurements, and the effect of

high pressures on the synthesis of new and similar materials. It was then shown that when A' is Cu or Mn, A site ordering generally occurs at a 1:3 ratio, $A_{0.25}A'_{0.75}BO_3$ (more commonly reported as $AA'_3B_4O_{12}$) where A = Ca, Sr, Na, Bi, Ln or a vacancy, and B = Ge, Ti, Cr, Mn, or Ru.

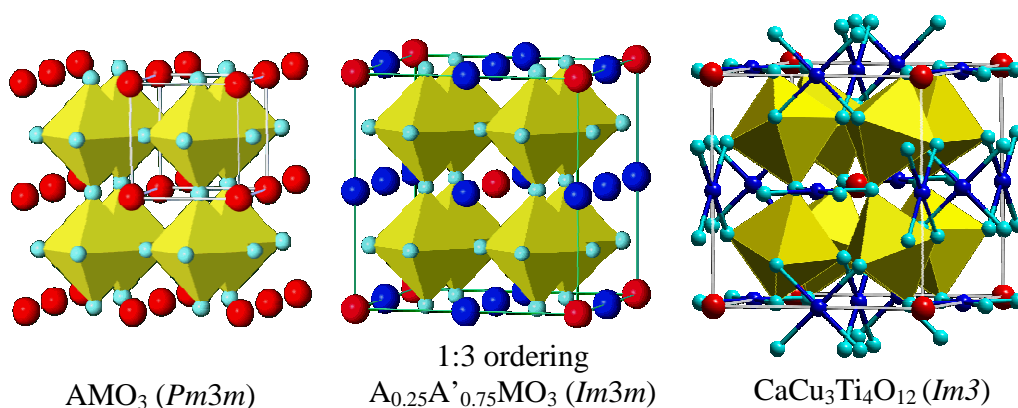


Figure 5.3 Transformation of AMO_3 cubic perovskite (left) to the A-site ordered perovskite (center), and the distorted pseudo-cubic perovskite $CaCu_3Ti_4O_{12}$ (right). Yellow TiO_6 octahedra, calcium at the body center (12 CN), red, and copper square planar coordination, dark blue. Oxygen anions are turquoise.

The ideal perovskite has a unit cell parameter of 4 Å, Figure 5.3. However, by ordering of either the a-site or b-site, the unit cell doubles and thus expands to ~ 8 Å. The ordering of the A-site, specifically for Copper, occurs due to a size difference between Cu and Ca, and the rotational distortion of the B-site octahedra (along four different [111] directions). The rotational distortion also occurs to accommodate a Cu^{2+} square planar coordination. These factors together cause a decrease in the unit cell to ~7.4 Å. This rotation also decreases the coordination of the or A-site cation from 12 to 8, and removes a mirror plane. The result is the rigid pseudo-cubic $CaCu_3Ti_4O_{12}$ structure [6].

In 2000, Subramanian *et al* reported a colossal dielectric constant of $\kappa \sim 10,000$, and a loss of $\tan \delta \sim 0.15$ in polycrystalline pellets. Even more interesting was the observation of little change in the dielectric properties from 100-500K and the absence of a structural phase transition throughout the full temperature range [8]. Studies in the last two decades have determined that this behavior can not be related to a ferroelectric transition, but there is still disagreement as to a proper explanation for the unique behavior [9]. A general consensus is that the behavior is not intrinsic as the high κ has been correlated to semiconducting grains and insulating grain boundaries. This is often referred to as an internal barrier layer mechanism and models the behavior in $\text{CaCu}_3\text{Ti}_4\text{O}_{12}$ to a reasonable degree [10-12]. The observation of an extremely high κ in single crystals [13] points toward insulating barriers within the crystals as opposed to the grain boundaries in polycrystalline samples. Twinning, in high concentrations, was observed in single crystals and is suggested to be the source of insulating barriers resulting in the high dielectric constant. It should be noted, however, that other lattice imperfections may also act as insulating barriers.

Great success has been made in furthering our understanding the unique properties of $\text{CaCu}_3\text{Ti}_4\text{O}_{12}$, but there is still disagreement as to the source of the colossal dielectric constant. It is thus necessary to continue researching the effect of substitutions on the dielectric properties in order to further understand the anomalies present. In the recent past, there has been a great deal of work concerning substitutional effects in $\text{CaCu}_3\text{Ti}_4\text{O}_{12}$ and related materials. Much of this has revolved around substitutions on the A or B sites to lower the dielectric loss or increase the dielectric constant.

5.3 Substitutional Variations in the High κ Dielectric $\text{CaCu}_3\text{Ti}_4\text{O}_{12}$

5.3.1 An Anion Substitution Route to Low Loss Colossal Dielectric $\text{CaCu}_3\text{Ti}_4\text{O}_{12}$

5.3.1.1 Introduction

Perovskite type oxides (ABO_3) have long been an important focus for development of new materials with high dielectric constants. With the discovery of the colossal dielectric constant in the body-centered cubic pseudo-perovskite $\text{CaCu}_3\text{Ti}_4\text{O}_{12}$, Figure 5.4, there has been much interest in the an unusually high dielectric constant, $\kappa = \sim 10,000$, over a broad range of temperatures (300-600K) without a phase transition.

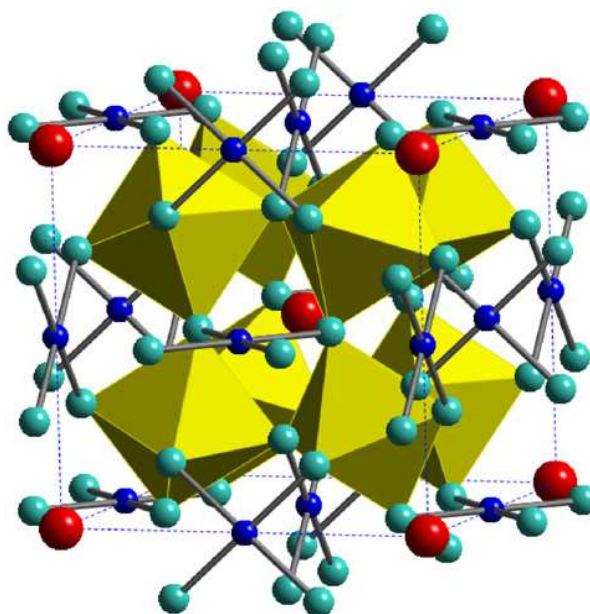


Figure 5.4 Structure of the cubic pseudo-perovskite ($\text{Im}\bar{3}$) $\text{CaCu}_3\text{Ti}_4\text{O}_{12}$ with TiO_6 octahedra, Cu in square planar coordination (small black spheres) about O (small light grey spheres) and Ca at the origin and cube center (medium size grey spheres). Unfortunately, the $\text{CaCu}_3\text{Ti}_4\text{O}_{12}$ loss tangent of ~ 0.15 is high for present ceramic

application requirements [8]. The best known high- κ dielectric material is barium titanate, BaTiO_3 , which has a dielectric constant and loss favorable for application, $\kappa = \sim 1,500$ and $\tan \delta = \sim 0.01$. There are several reports of cation substitution in $\text{CaCu}_3\text{Ti}_4\text{O}_{12}$. Substitution has included Co, Fe, Ni, Zr, Sc and Nb on the Ti site, and La or Na on the Ca site [14-18]. Some reports indicate success in lowering the dielectric loss. For example, a loss of 0.015 was reported for $\text{Ca}_{0.8}\text{La}_{0.2}\text{Cu}_3\text{Ti}_4\text{O}_{12}$; however, the dielectric constant was also suppressed to 3,000 [18]. Some compounds with the $\text{CaCu}_3\text{Ti}_4\text{O}_{12}$ structure show a low loss tangent but not a giant dielectric constant [19]. In this communication, we present a novel route for decreasing the $\tan \delta$ of $\text{CaCu}_3\text{Ti}_4\text{O}_{12}$ by anion substitution.

5.3.1.2 Results and Discussion

Analysis of powder XRD patterns indicated that the substitution of fluorine for oxygen was successful for doping levels of $x = 0.05 - 1.3$. Attempted doping levels above $x = 1.3$ resulted in secondary phases, mainly CaF_2 and TiO_2 . Figure 5.5 shows XRD patterns for pure $\text{CaCu}_3\text{Ti}_4\text{O}_{12}$ and doping levels of $x = 0.2, 0.4, 0.6$, and 0.8 . The shift of peaks to lower 2θ values with increasing F content indicates an increase in the lattice constant of the cubic phase (Figure 5.5 inset). With the addition of F, increased grain (crystallite) size could be expected. This would account for the initial sharpening of the peaks upon F addition. The broadening that occurs with further F addition is most likely due to inhomogeneity of the F (and Cu^{1+}) distribution, which

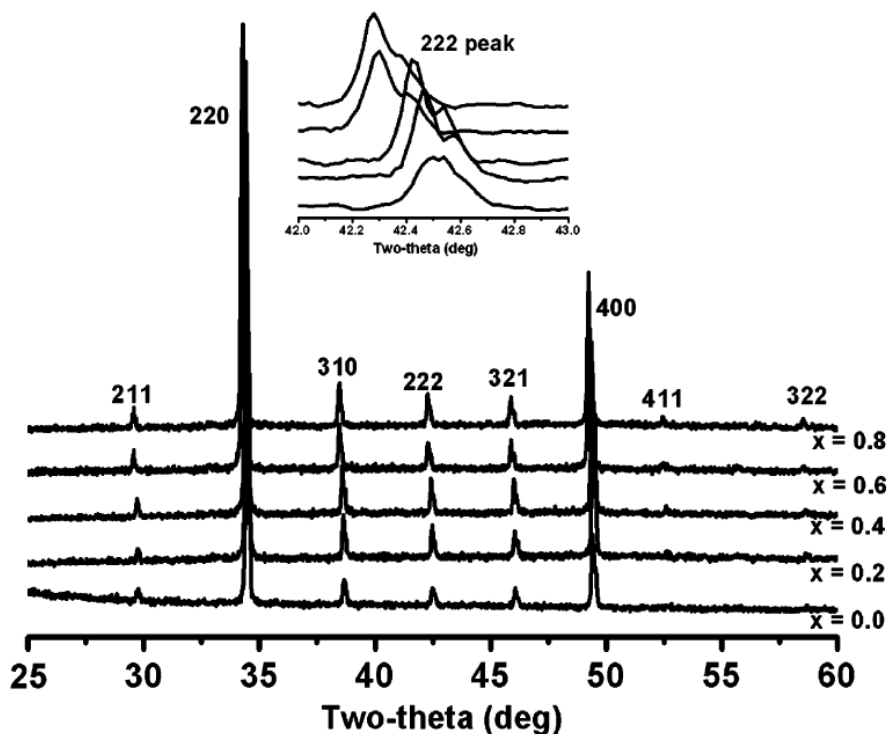


Figure 5.5 Room temperature XRD powder patterns for $\text{CaCu}_3\text{Ti}_4\text{O}_{12-x}\text{F}_x$ samples where $x = 0\text{--}0.8$. The inset in the upper left corner is an expanded view of the shift in (222) peak around $2\theta\ 42.5^\circ$. Shoulders in the peaks are due to $\text{CuK}\alpha_2$ radiation.

Table 5.1 Fluorine content of selected samples

Sample	Calculated (Wt.%)	Measured (Wt.%)
$\text{CaCu}_3\text{Ti}_4\text{O}_{11.6}\text{F}_{0.4}$	1.23	1.1 ± 0.1
$\text{CaCu}_3\text{Ti}_4\text{O}_{11.4}\text{F}_{0.6}$	1.85	1.7 ± 0.2
$\text{CaCu}_3\text{Ti}_4\text{O}_{11.2}\text{F}_{0.8}$	2.46	2.3 ± 0.2
$\text{CaCu}_3\text{Ti}_4\text{O}_{11}\text{F}$	3.08	3.1 ± 0.1
$\text{CaCu}_3\text{Ti}_4\text{O}_{10.8}\text{F}_{1.2}$	3.67	3.6 ± 0.1
$\text{K}_2\text{NbO}_3\text{F}^*$	7.99	8.1 ± 0.1

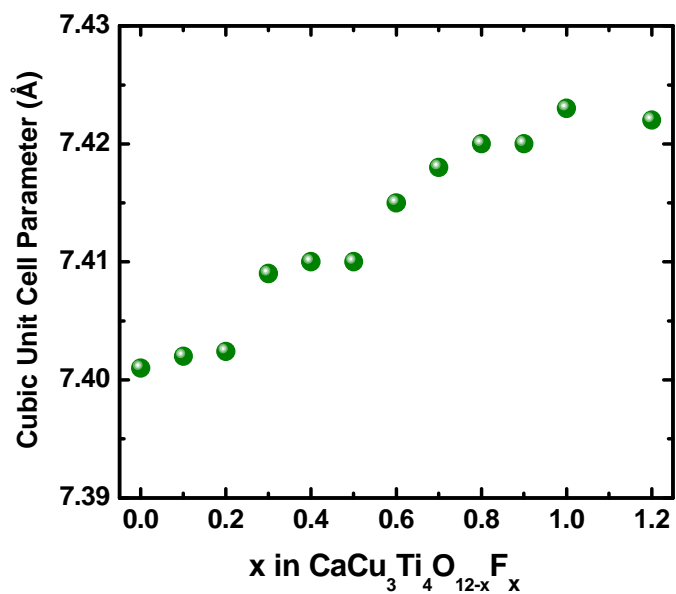


Figure 5.6 Lattice parameter expansion as a result of fluorine substitution for oxygen, and the valence reduction of $\text{Cu}^{2+} \rightarrow \text{Cu}^{1+}$.

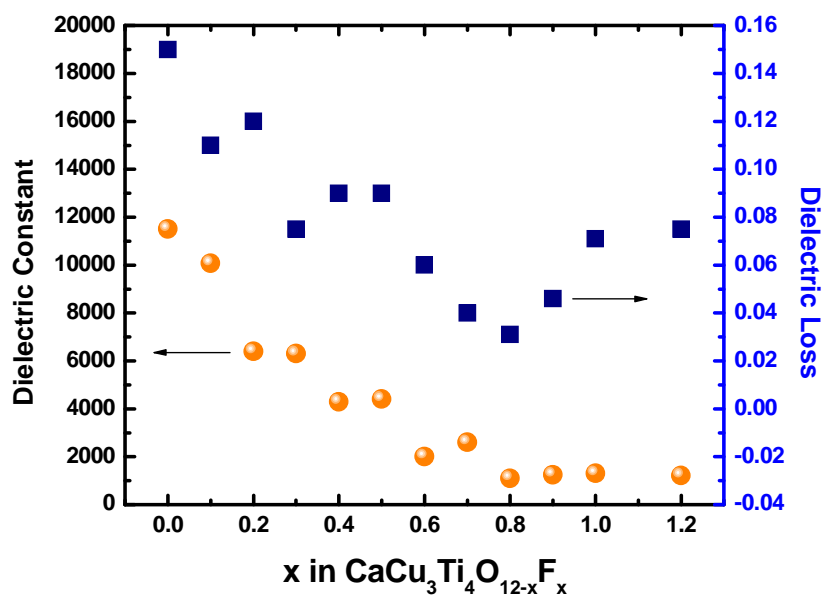


Figure 5.7 Result of fluorine substitution on the dielectric constant (κ) and dielectric loss (loss tangent, $\tan \delta$) for pure and F-doped $\text{CaCu}_3\text{Ti}_4\text{O}_{12-x}\text{F}_x$ where $x = 0-1.2$ at 25°C at a frequency of 100 kHz.

apparently causes lattice strain [20]. The ionic radius difference between fluorine and oxygen is negligible [21]. The observed increase in the lattice constant (Figure 5.6) is attributed to the conversion of Cu^{2+} to Cu^{1+} as F^{1-} is substituted for O^{2-} . Thus, the formula for these phases is represented as $\text{CaCu}_{3-x}^{2+}\text{Cu}_x^{1+}\text{Ti}_4\text{O}_{12-x}^{2-}\text{F}_x^{1-}$. The F substitution was verified by chemical analysis (Table 5.1). The F content was always as expected within the error of the analysis. Any F loss that occurs during the calcination in air is negligible.

Figure 5.7 shows the dielectric constant and the dielectric loss as a function of fluorine content in $\text{CaCu}_3\text{Ti}_4\text{O}_{12}$ at 25°C and 100 kHz. As fluorine doping increases, the dielectric constant and loss tangent decrease. As the fluorine doping increases from $x = 0.1$ to 0.5, a large dielectric constant is still observed but is decreased from $\kappa = 10,080$ to 4,404, and $\tan \delta$ is decreased from 0.11 to 0.075. Taking into consideration both the constant and loss, an optimal fluorine content is $x = 0.3$ where the dielectric constant is $\kappa = 6,310$ and $\tan \delta$ is 0.075

The temperature dependence of the dielectric constant and loss tangent relationships for select fluorine doped levels in $\text{CaCu}_3\text{Ti}_4\text{O}_{12-x}\text{F}_x$ is presented in Figure 5.8 and 5.9 respectively. The dielectric constants remain essentially temperature independent for the various doping levels from 25° to 175°C. This is an improvement over pure $\text{CaCu}_3\text{Ti}_4\text{O}_{12}$ at 100 kHz where the dielectric constant increases steadily with $\tan \delta$ throughout the full temperature range.

There is a consensus that the giant dielectric constant in $\text{CaCu}_3\text{Ti}_4\text{O}_{12}$ is due to an internal barrier layer mechanism (IBLM). This mechanism normally applies to

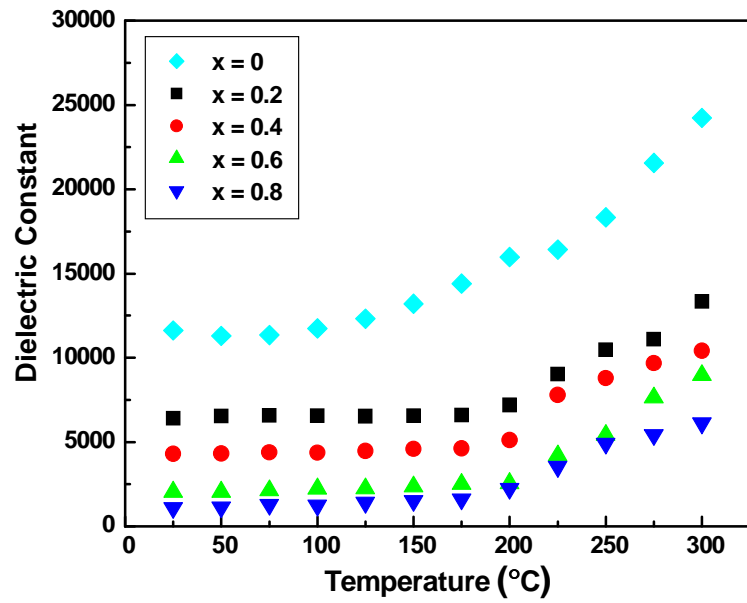


Figure 5.8 Temperature dependence of the dielectric constant (κ) for pure and F-doped $\text{CaCu}_3\text{Ti}_4\text{O}_{12-x}\text{F}_x$ at a frequency of 100 kHz.

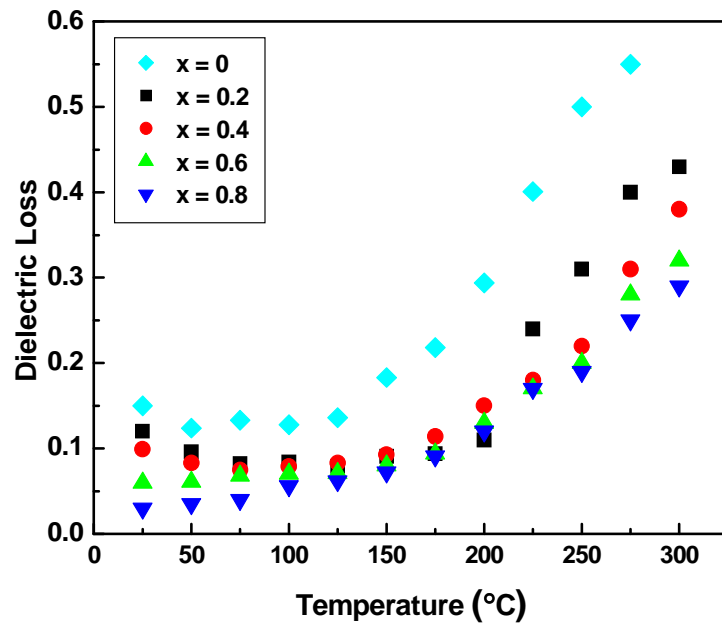


Figure 5.9 Temperature dependence of the dielectric loss (loss tangent, $\tan \delta$) for pure and F-doped $\text{CaCu}_3\text{Ti}_4\text{O}_{12-x}\text{F}_x$ at a frequency of 100 kHz.

materials with conducting grains and insulating grain boundaries. However, in $\text{CaCu}_3\text{Ti}_4\text{O}_{12}$ it has been shown that the giant dielectric constant is obtained within grains [8, 11, 18, 22]. Thus, there must be insulating planar defects in these grains. Despite much effort, there is still no good definition of these defects. Dopants frequently concentrate at lattice defects. Thus, the F may be concentrating on the important planar defects in $\text{CaCu}_3\text{Ti}_4\text{O}_{12}$. This could increase the electrical resistivity of the internal barrier and decrease the dielectric loss. Movement of electrons from cation to cation through F is much more difficult than through O.

5.3.1.3 Conclusion

It has been shown in this study that anion substitution by fluorine in $\text{CaCu}_3\text{Ti}_4\text{O}_{12-x}\text{F}_x$ was successful, and that single phase samples were prepared for fluorine doping levels of $x < 1.3$. A lower dielectric loss tangent, $\tan \delta = 0.075$, and a giant dielectric constant, $\kappa = 6310$, was obtained for a fluorine doped level of $x = 0.3$.

5.3.1.4 Experimental

The samples in this investigation were prepared by conventional solid state synthesis. Reactants were CaCO_3 (99%+, Spectrum), CuO (99.9%+, Aldrich), CuF_2 (99.5%+, Alfa Aesar), and TiO_2 (99.9%+, Aldrich). Appropriate quantities were thoroughly mixed by grinding in an agate mortar. The mixed powder was first

calcined in air at 900°C for about 12 hours, and then reground, pressed into pellets, and sintered in air at 1025°C for 12 hours. In both heating cycles, the ramping and cooling rate were 300°C/hr. X-ray powder diffraction (XRD) patterns were recorded with a Rigaku MiniFlex II diffractometer (Cu K α radiation) in the range of 10-60° 2 θ . In order to analyze the F content of the sample, the fluorine was first leached from the sample by means of sodium hydroxide fusion in a platinum crucible. This process was carried out in a closed Inconel vessel to avoid the fluorine loss. The percentage of fluorine was determined using a fluoride ion selective electrode. A sample of K₂NbO₃F was used as a reference and to check the accuracy of the measurements. Accuracy depends on F content and size of sample used. For dielectric constant and loss tangent measurements pellets of samples were polished, electroded with silver paint and then dried for 3-5 hours at 100°C. Measurements on the pellets utilized an HP-4275A LCR meter in the temperature range of 25°C to 300°C at a frequency of 100 kHz.

5.3.2 Colossal Drop in the Colossal Dielectric $\text{CaCu}_3\text{Ti}_4\text{O}_{12}$

5.3.2.1 Introduction

As mentioned previously, the perovskite structure is accommodating of most cations when charge and ionic radii are taken into consideration. However, the perovskite structure of $\text{CaCu}_3\text{Ti}_4\text{O}_{12}$ is quite rigid due to the rotational distortions of the TiO_6 polyhedra, Figure 5.4 [8]. The rotations are due to the preferential square planar coordination of a Jahn-Teller copper ion and to the size of the A-site cation Ca in a site somewhat too small. Because of this rigidity, the dielectric constant of $\text{CaCu}_3\text{Ti}_4\text{O}_{12}$ is actually enhanced [8, 19]. The enhancement, however, comes at a cost to the allowance of substitution on any of the sites. We've shown in the last chapter that for small fluorine substitutions, there is a reasonable change in the dielectric constant and loss values that prove beneficial. Here, we will show that substitutional variations of the Cu and Ti site are much more susceptible to quenching the dielectric properties.

5.3.2.2 Results and Discussion

Figure 5.10 shows the powder x-ray diffraction patterns for pure $\text{CaCu}_3\text{Ti}_4\text{O}_{12}$ and substituent levels of $x = 0.05 - 0.5$ and 1. Charge neutrality was preserved by keeping the ratio of substituent Mn^{3+} to Fe^{3+} the same as Cu^{2+} to Ti^{4+} . Analysis of the diffraction patterns indicated that the co-substitution of manganese and iron for copper and titanium was successful for doping levels of $x = 0.05 - 0.5$ and 1 in

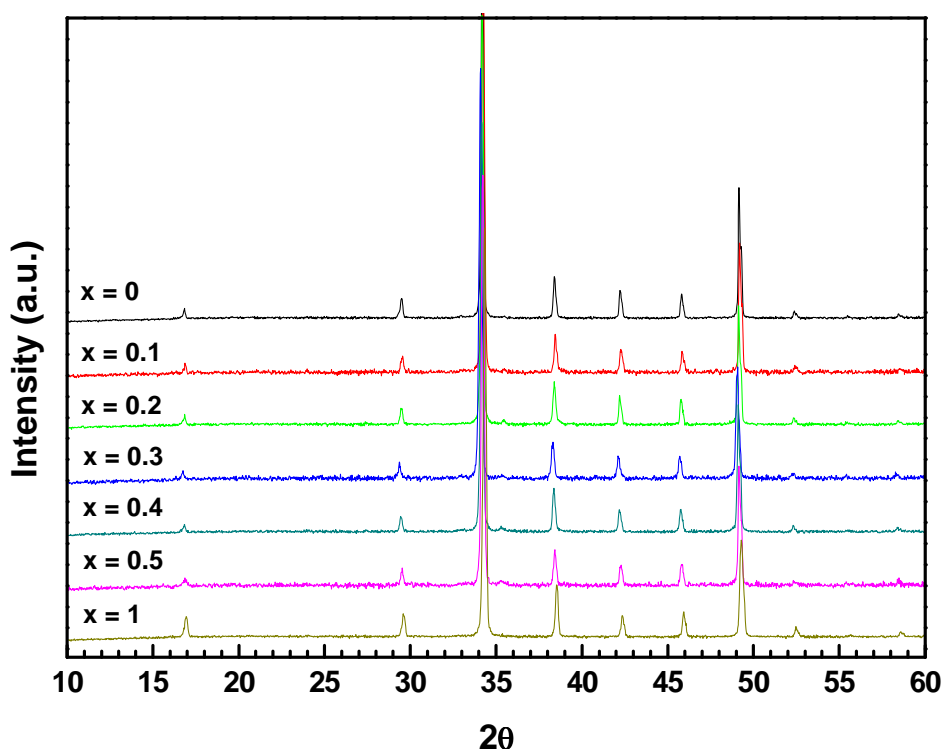


Figure 5.10 Room temperature powder x-ray diffraction patterns for $\text{CaCu}_3\text{Ti}_4\text{O}_{12-x}\text{F}_x$ samples where $x = 0-0.5, 1$.

$\text{Ca}^{2+}\text{Cu}_{3-x}^{2+}\text{Mn}_x^{3+}\text{Ti}_{4-x}^{4+}\text{Fe}_x^{3+}\text{O}_{12}^{2-}$, and all samples could be indexed to a cubic Im3 space group. It should be noted that there was great difficulty in repeated attempts to synthesize $0.5 < x \leq 1$, and as such, they are not reported here. Observed secondary phases for $x > 1$ were found to be primarily Fe_2O_3 and CaTiO_3 . The narrowness of the diffraction lines is comparable in all the samples, which confirms reasonable sintering and similar values of the crystallite size. A rough estimation of crystallite size by Williamson Hall plots utilizing a profile analysis of peaks for full width at half maximum (FWHM) and suggests values greater than ~ 300 nm.

The inconsistent shift of peaks with increasing Mn/Fe content, and the monotonic variation in the Vegard's law plot (Figure 5.11) indicates the possibility of site swapping for various compositions, meaning that although we intend for Fe to occupy the Ti site, there is a possibility it may also occupy the Cu site. If the site compositions are allowed to intermix with some kind of randomness, this would explain the variation in the powder diffraction patterns, and thus the Vegard's law plots. Mössbauer analysis was utilized to address the possibility of Fe site swapping. Figure 5.12 illustrates the Mössbauer data collected. The isomer shift and quadrupole splitting (bottom of Figure 5.12) indicate that Fe occupies two different coordination environments, namely the D_{4h} (square planar) and O_h (octahedral) at percentages of ~17% and 83% respectively. This makes the situation much more complicated, but now confirms our suspicion that the lattice variation may be due to site swapping. The true composition may thus be regarded as $\text{Ca}(\text{Cu}_{2.5}\text{Mn}_{0.415}\text{Fe}_{0.085})(\text{Ti}_{3.5}\text{Fe}_{0.415}\text{Mn}_{0.085})\text{O}_{12}$.

Several reports have shown the substitutional allowances of $\text{CaCu}_3\text{Ti}_4\text{O}_{12}$ including Mn on the copper site and Fe on the Ti site [8, 19, 23-25]. These reports have also shown that dramatic changes can occur in the dielectric values for small compositional variations, especially for the copper site. For a copper deficiency of 0.05, the dielectric constant was halved from 10,000 to ~5,500, illustrating the sensitivity of the site to manipulations [8]. However, this is not to say that the copper site is the sole factor in the large dielectric constant of $\text{CaCu}_3\text{Ti}_4\text{O}_{12}$ as many other

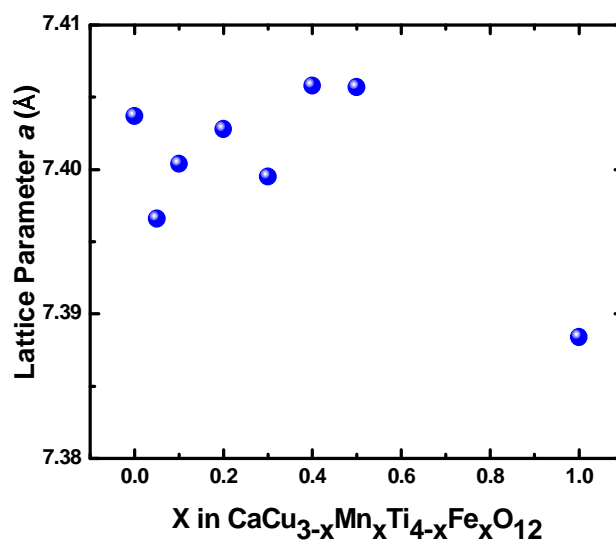
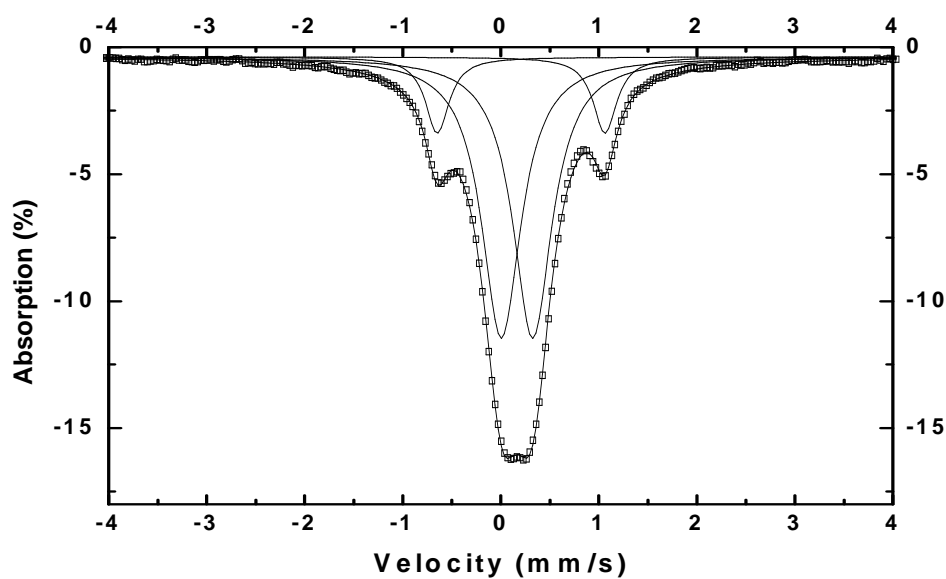


Figure 5.11 Lattice parameter expansion as a result of Mn and Fe co-substitution for Cu and Ti respectively.



Site	Isomer Shift δ (mm/s)	Quadrupole Splitting (Avg.) (mm/s)	FWHM Γ (mm/s)	%	Site
1	0.411(8)	1.708(8)	0.290(5)	17	$\text{Fe}^{3+} [\text{D}_{4h}]$
2	0.369(3)	0.318(3)	0.485(3)	83	$\text{Fe}^{3+} [\text{O}_h]$

Figure 5.12 Mossbauer analysis of the nominal composition $\text{CaCu}_{2.5}\text{Mn}_{0.5}\text{Ti}_{3.5}\text{Fe}_{0.5}\text{O}_{12}$.

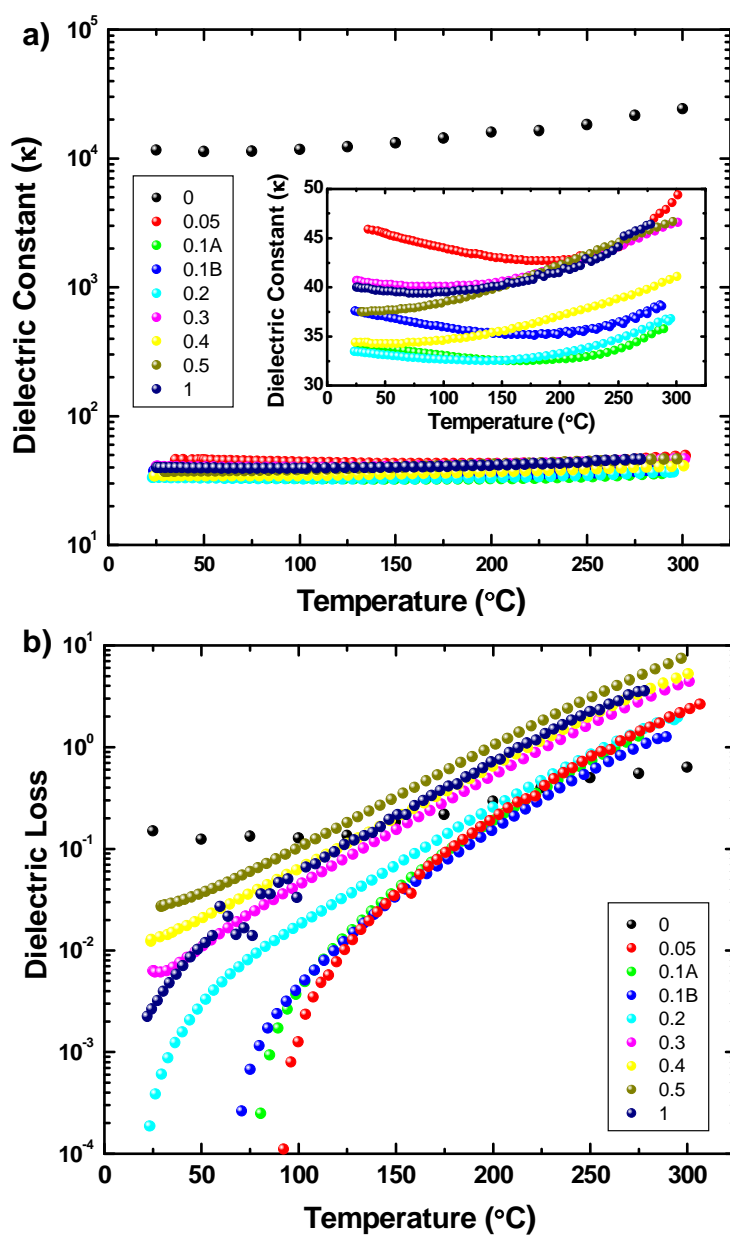


Figure 5.13 Temperature dependence of (a) the dielectric constant, and (b) the dielectric loss for $\text{CaCu}_{3-x}\text{Mn}_x\text{Ti}_{4-x}\text{Fe}_x\text{O}_{12}$ at a frequency of 1 MHz.

compositions containing stoichiometric copper do not show a large dielectric constant.

The $\text{ACu}_3\text{Ti}_3\text{FeO}_{12}$ series for which $A = \text{Y, La, Nd, Sm-Tm, Y, Bi}$ all show a dielectric constant below 1,000 [8].

Figure 5.13 shows the dielectric constant and dielectric loss as a function of temperature. A colossal drop can be observed for all substitutions regardless of the amount of substitution. The inset of figure 5.13 shows the variation in the dielectric constant for all values of x . The substitutions show a dramatic effect much like that reported by Li *et al.* for $\text{CaCu}_{2.94}\text{Mn}_{0.06}\text{Ti}_4\text{O}_{12}$ where the dielectric constant was suppressed to ~ 45 at 1 k Hz [26]. Our measurements indicate a similar effect as expected. However, if we now assume that all compositions have site swapping to some extent, we find it is not extremely difficult to rationalize the drop in the dielectric constant specifically to Mn or Fe occupation as Cai *et al.* also showed that for $\text{CaCu}_3\text{Ti}_{4-x}\text{Mn}_x\text{O}_{12}$ ($x \leq 0.2$) a colossal drop in the dielectric constant was also observed [23]. The expected dielectric constants based on the polarizabilities of the present elements are less than 100 based on calculations using the Clausius-Mosotti equation [27].

The magnetic molar susceptibilities χ_m of Mn and Fe co-substituted samples were measured in an applied magnetic field of 10000 Oe (1 Tesla) from 5 K to 300 K. $\text{CaCu}_3\text{Ti}_4\text{O}_{12}$ shows a classic antiferromagnetic ordering transition at $T_N \sim 25$ K here and as reported elsewhere, Figure 3.14 [17, 28]. Paramagnetic behavior of the inverse susceptibility well above T_N (150 - 300 K) was fitted by the Curie-Weiss law. Data calculated from these fits, namely T_N , θ_{CW} , and the μ_{eff} , are listed in Table 5.2. In $\text{CaCu}_3\text{Ti}_4\text{O}_{12}$, the Cu^{2+} (d^9) spins order in ferromagnetic planes with adjacent planes ordering antiferromagnetically along the body diagonal [111]. The superexchange interaction occurs through nonmagnetic Ti rather than O as would be expected for

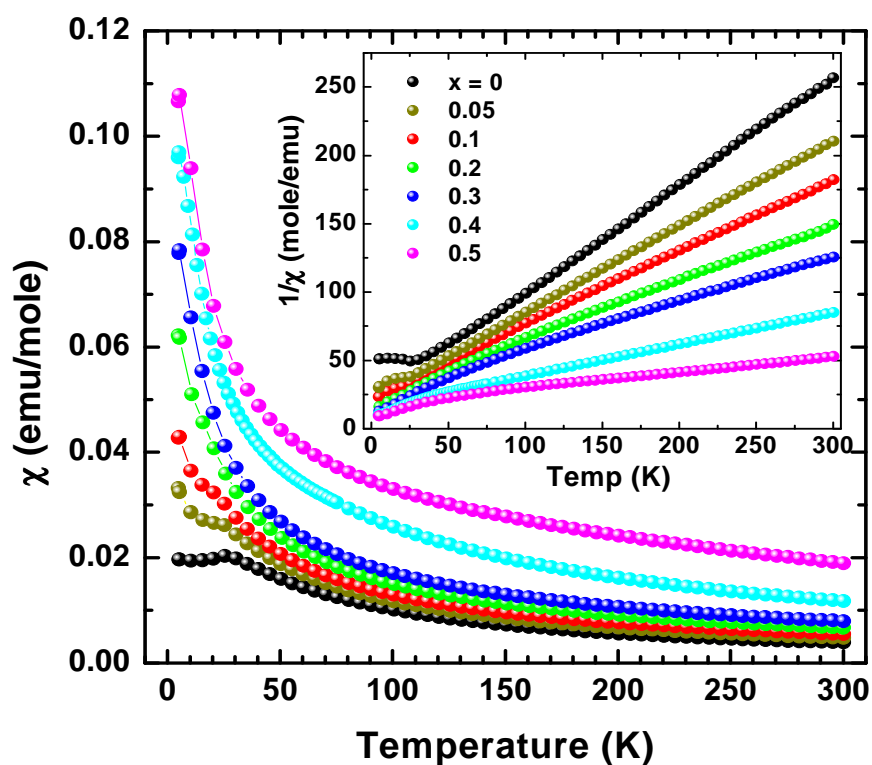
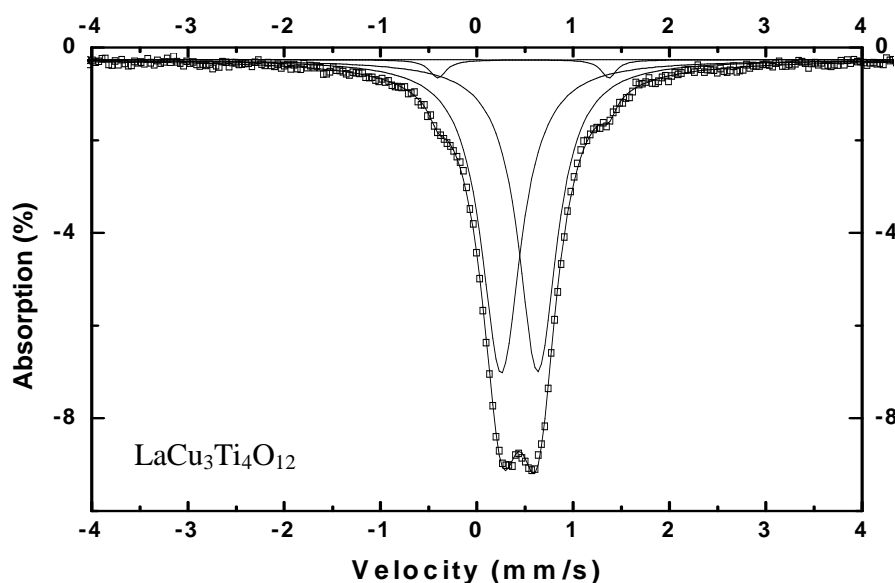


Figure 5.14 Magnetic susceptibility versus temperature of $\text{CaCu}_{3-x}\text{Mn}_x\text{Ti}_{4-x}\text{Fe}_x\text{O}_{12}$ for $x = 0$, and 0.1-0.5 measured at 1 Tesla. Inset: inverse susceptibility of the aforementioned compositions.

Table 5.2 Magnetic data calculated from paramagnetic region, $T > 150\text{K}$				
x	C (emu-K/mole)	P_{eff} (μ_B)	θ_{CW} (K)	T_N (K)
0	1.261	3.18	-24.6	~ 25
0.05	1.590	3.57	-36.0	~ 25
0.1	1.941	3.94	-52.8	~ 20
0.2	2.503	4.48	-72.5	~ 15
0.3	3.070	4.96	-87.6	-
0.4	4.307	5.87	-90.4	-
0.5	9.058	8.52	-175.1	-



Site	Isomer Shift δ (mm/s)	Quadrupole Splitting (Avg.) (mm/s)	FWHM Γ (mm/s)	%	Site
1	0.42(8)	1.71(8)	0.30(5)	4	$\text{Fe}^{3+} [\text{D}_{4h}]$
2	0.38(3)	0.36(3)	0.48(3)	96	$\text{Fe}^{3+} [\text{O}_h]$

Figure 5.15 Mössbauer analysis of the nominal composition $\text{LaCu}_3\text{Ti}_3\text{FeO}_{12}$.

cubic perovskites [17]. Thus, the effect of Mn and Fe co-substitution on the magnetic character is two-fold. First, the substitution on the Ti site perturbs the Cu superexchange resulting in a weakening of the overall interactions. This results in a gradual quench of the antiferromagnetic ordering temperature from $T_N \sim 25$ K to ~ 15 K for $x = 0.2$. The second effect is the onset of a greater ferromagnetic component which can be observed in the susceptibility data by a bowing near 50 K. $\text{ACu}_3\text{Ti}_3\text{FeO}_{12}$ where A = Bi and La were also found to exhibit a ferromagnetic-like onset. Due to the number of magnetic cations and the dual site occupations, it is extremely difficult to suggest specific interactions.

Due to our observation of Fe site swapping, we considered that the drop in the dielectric constant of Cu stoichiometric compounds containing Fe on the Ti site may in fact be due to the occupation of Fe on the Cu site. $\text{LnCu}_3\text{Ti}_3\text{FeO}_{12}$ compositions where $\text{Ln} = \text{Y, La, Nd, Sm-Tm, Y, Bi}$ have all been previously reported [8, 19]. There have since been no reports of Mössbauer analysis to determine the coordination environment of Fe in these materials. Figure 5.15 illustrates Mössbauer analysis for $\text{LaCu}_3\text{Ti}_3\text{FeO}_{12}$. Again, we see that Fe does in fact occupy the Cu site and may thus be a large contributing factor in the suppression of the dielectric constant observed, $\kappa \sim 60$ at room temperature and 1 M Hz. A more complete analysis of Fe containing materials with the $\text{CaCu}_3\text{Ti}_4\text{O}_{12}$ type structure is warranted.

5.3.2.3 Conclusion

We have shown that single phase samples with nominal compositions of $\text{CaCu}_{3-x}\text{Mn}_x\text{Ti}_{4-x}\text{Fe}_x\text{O}_{12}$, $x = 0.05-0.5$ and 1 were prepared. Mössbauer analysis confirmed that Fe occupies both the Ti octahedral site and the Cu square planar site. Previous reports have shown that Mn suppresses the dielectric constant whether substituted on the Cu or Ti site. As Fe occupies both sites, Mn must also, and as such it is not surprising we also observe a colossal drop in the dielectric constant. In addition we also observed that other known compositions reported with Fe on the Ti site also have minor amounts of Fe on the Cu site. Substitutions and deficiencies of the Cu site normally result in suppressed dielectric properties, especially when substituent cations

are Fe. This work may prove useful in understanding why $\text{CaCu}_3\text{Ti}_4\text{O}_{12}$ is the only of its family to have a dielectric constant above 4,000 at room temperature.

5.3.2.4 Experimental

The samples in this investigation were prepared by conventional solid state synthesis. Reactants were CaCO_3 (99%+, Spectrum), CuO (99.9%+, Aldrich), Mn_2O_3 (JMC 98%+), Fe_2O_3 (99.99%, Alfa Aesar), TiO_2 (99.9%+, Aldrich), La_2O_3 (99.99%, Alfa Aesar), Bi_2O_3 (99.99%, Aldrich). Appropriate quantities were thoroughly mixed by grinding in an agate mortar. The mixed powder was first calcined in air at 900°C for about 12 hours, and then reground, pressed into pellets, and sintered in air at 1025°C for 12 hours. In both heating cycles, the ramping and cooling rate were 300°C/hr . Powder x-ray diffraction patterns were recorded using a Rigaku MiniFlex II diffractometer ($\text{Cu K}\alpha$ radiation) in the range of 10 - $60^\circ 2\theta$. Mössbauer analysis was performed in order to analyze the Fe coordination environment in the samples. However, due to the low Fe content and potential issues with resolution of Mössbauer peaks, we prepared several compositions with ^{57}Fe in Fe_2O_3 (Isotec Inc., 95.27 atom% ^{57}Fe Lot# PV1324) at 3 mole % in our compositions. Mössbauer was measured by Dr. Alain Wattiaux at ICMCB-CNRS, France. For dielectric constant and loss tangent measurements, pellets of samples were polished, electroded with silver paint and then dried for 3-5 hours at 100°C . Measurements on the pellets utilized an HP-4275A LCR meter in the temperature range of 25°C to 300°C at a frequencies from 1 kHz to 1

MHz, and cole-cole plots were prepared using an HP-4284A LCR meter. Magnetism was measured using a PPMS Physical Property Measurement System with He(l) recycling system from 5K to 300K. A field of 0.5Tesla was applied after zero field cooling

5.4 References

1. J.B. Goodenough, *Prog. Solid State Chem.*, 5 (1971) 145
2. F.S. Galasso. *Perovskites and High T_C Superconductors.*; Gordon and Breach Science Publishers: New York, 1990
3. W.D. Kingery, H.K. Bowen, D.R. Uhlmann. *Introduction to Ceramics*, 2nd ed.; John Wiley & Sons: New York, 1976
4. R.H. Mitchell. *Perovskites-Modern and Ancient*, Alamaz Press Inc.: Ontario, Canada, 2002
5. W.J. Merz, *Phys. Rev.*, 76 (1949) 1221
6. A. Deschanvres, B. Reveau, F. Tollemmer, *Bull. Soc. Chim. Fr.*, (1967) 4077
7. B. Bochu, M.N. Deschizeaux, J.C. Joubert, *J. Solid State Chem.*, 29 (1979) 291
8. M. A. Subramanian, D. Li, N. Duan, B. A. Reisner, and A. W. Sleight. *J. Solid State Chem.: Rapid Comm.*, 151 (2000) 323
9. P.R. Bueno, R. Tararan, R. Parra, E. Joanni, M.A. Ramirez, W.C. Ribeiro, E. Longo, J.A. Varela. *J. Phys. D: Appl. Phys.*, 42 (2009) 055404
10. D.C. Sinclair, T.B. Adams, F.D. Morrison, A.R. West. *Appl. Phys. Lett.*, 80(12) (2002) 2153
11. T.B. Adams, D.C. Sinclair, A.R. West. *Adv. Mater.*, 14 (2002) 1321
12. A.R. West, T.B. Adams, F.D. Morrison, D.C. Sinclair. *J. Eur. Ceram. Soc.*, 24 (2004) 1439

13. C.C. Homes, T. Vogt, S.M. Shapiro, S. Wakimoto, A.P. Ramirez. *Science*, 293 (2001) 673
14. G. Chiodelli, V. Massarotti, D. Capsoni, M. Bini, C. B. Azzoni, M. C. Mozzati and P. Lupotto. *J. Solid State Comm.*, 132, 241-246 (2004)
15. O. Parkash, D. Kumar, A. Goyal, A. Agrawal, A. Mukherjee, S. Singh and P. Singh. *J. Phys. D: Appl. Phys.*, 41 (2008) 1
16. S.Y. Chung, S. I. Lee, J. H. Choi, and S. Y. Choi. *Appl. Phys. Lett.* 89 (2006) 1
17. R. K. Grubbs, E. L. Venturini, P. G. Clem, J. J. Richardson, B. A. Tuttle, and G. A. Samara. *Phys Rev. B.*, 72 (2005) 1
18. L. Feng, X. Tang, Y. Yan, X. Chen, Z. Jiao, and G. Cao. *Phys. Stat. Sol.: Rap. Res. Lett.*, 203(4) (2006) 22
19. M. A. Subramanian, A. W. Sleight. *J. Solid State Sci.*, 4 (2002) 347
20. P. Karen, P. M. Woodward. *J. Solid State Chem.*, 141 (1998) 78
21. R. D. Shannon. *Acta Cryst. A*, 32 (1976) 751
22. S. W. Choi, S. H. Hong, and Y. M. Kim. *J. Am. Ceram. Soc.* 90 (2007) 4009
23. J. Cai, Y.-H. Lin, C.-W. Nan, J. He, Y. Wu, X. Chen, *Appl. Phys. Lett.*, 91 (2007) 252905
24. C. Mu, H. Zhang, Y. He, P. Liu, J. Shen, *Mat. Sci. Eng. B*, 162 (2009) 195
25. W. Kobayashi, I. Terasaki, *Physica B*, 329 (2003) 771
26. M. Li, A. Feteira, D.C. Sinclair, A.R. West, *Appl. Phys. Lett.*, 88 (2006) 232903
27. R.D. Shannon, *J. Appl. Phys.* 73, (1993) 348
28. S. Krohns, J. Lu, P. Lunkenheimer, V. Brizé, C. Autret-Lambert, M. Gervais F. Gervais, F. Bourée, F. Porcher, and A. Loidl, *Eur. Phys. J. B*, 72 (2009) 173

Chapter 6

Miscellaneous Oxide Systems

6.1 Introduction

During the course of this thesis, there were several attempts to investigate different systems that were related to the compositions discussed in the bulk of chapters 3, 4, and 5. In order to investigate the other works in detail, these compositions were set aside. Due to the amount of work already completed in these systems, TiO_2 based bronzes and perovskite iridates it is worth discussing. This work should be considered preliminary, and the conclusions made merely suggestions rather than concrete. Further work in these systems is certainly necessary.

6.2 Transition metal bronzes based on $\beta\text{-TiO}_2$

Our work on $\text{CaCu}_3\text{Ti}_4\text{O}_{12}$ had partially focused on the design and characterization of novel compositions containing Na on the A-site (some Na containing CCTO-based compositions are known [1]). During this investigation, a sample was prepared which melted in the furnace and resulted in single crystals. Those crystals were analyzed using single crystal diffraction. The work in this section is largely the result of this single crystal analysis and the compositional formula determined.

In 1962, Anderson and Wadsley reported a new compound of structural interest, Na_xTiO_2 , the alkali metal titanium dioxide bronze [2]. The alkali metal bronze drew

attention for the possibility of conduction by the free electron in the framework from the alkali metal, but also due to the odd structural stabilization by sodium. Later work found the Na_xTiO_2 composition to show a metal-insulator transition [3]. Na can also be washed away thus resulting in the pure $\beta\text{-TiO}_2$ structure. The beta form of TiO_2 , also referred to as a bronze structure, is one of seven known TiO_2 structures (Columbite, Rutile, Brookite, Anatase, Ramsdellite, Bronze and Hollandite). It is a monoclinic system with space group C2/m [2,4]. The related phases, anatase, ramsdellite and hollandite, share octahedral units averaging 4 corners and 4 edges each. The bronze TiO_2 form also shares 4 corners, but is different from the other TiO_2 phases in that it averages 4.5 octahedral edges shared [4]. This non-integer value represents the two distinct octahedral sites in which one shares 4 edges and the other shares 5 edges. The distinct octahedral sites can be seen in Figure 6.1a. The structure contains a ‘zig-zag ribbon’ of double octahedron along the a-axis and closely related edge and corner shared alternating distorted perovskite-like units, Figure 6.1b. In the case of alkali metal TiO_2 bronze [3], sodium is situated in the 2(a) point position in a disordered fashion within channels formed by titanium octahedral linkages. These channels lie along the b-axis and can also be seen in Figure 6.1b. A detailed structural analysis of Na_xTiO_2 is given in reference 2.

Our single crystal analysis on crystals formed from a melt in the preparation of $\text{NaCu}_3\text{Ti}_4\text{O}_{12}$ is presented in Table 6.1. The formula was refined to $\text{Na}_{0.8}\text{Cu}_{0.4}\text{Ti}_{3.6}\text{O}_8$. The formula and unit cell parameters agree quite well with the report by Avdeev in 2001 by ICDD grant-in-aid, which reported x-ray diffraction data on the sodium

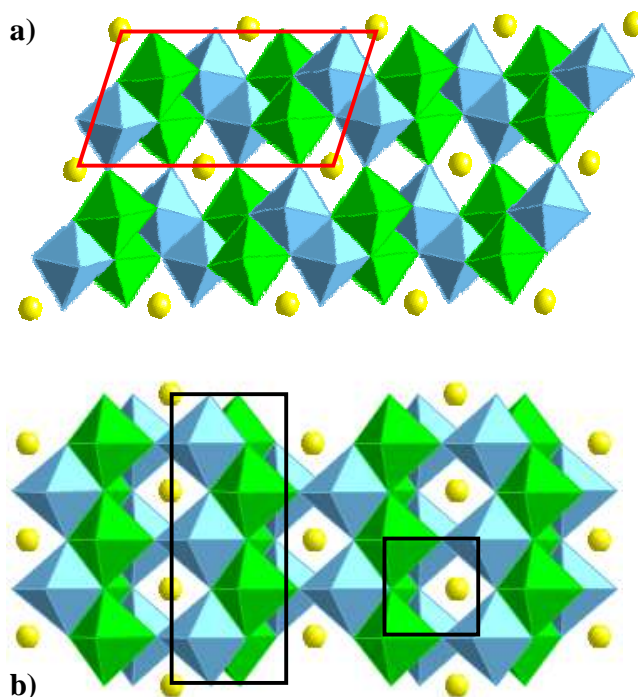


Figure 6.1 Monoclinic C2/m bronze structure of Na_xTiO_2 . The structure contains a zig-zag row of double octahedra (black lined rectangle), two distinct octahedral sites (one with 4 edges shared, blue, and 5 edges shared, green), and a closely related perovskite unit (black lined square). This representation shows a full occupation of the Na site. In reality, there would be a disordered partial occupation.

copper titanium bronze system ($\text{Na}_{0.86}\text{Cu}_{0.43}\text{Ti}_{3.57}\text{O}_8$) [5].

Our analysis of the Cu analogue led us to believe that additional compositions may also be possible for Mn, Fe, Co, Ni, Zn and Mg in place of copper. A more in depth literature search concluded that the mineral Freudenbergitte, $\text{NaFeTi}_3\text{O}_8$, and various derivatives were known [6-7]. Despite previous reports, little work had been performed on the physical properties. Our goal was to address some of the physical properties. The compositions prepared were based on the formula $\text{Na}_{0.86}\text{M}_{0.43}\text{Ti}_{3.57}\text{O}_8$

Table 6.1 Crystallographic data and unit cell parameters from single crystal analysis of $\text{NaCu}_3\text{Ti}_4\text{O}_{12}$ melt. The refined values yielded a formula of $\text{Na}_{0.8}\text{Cu}_{0.4}\text{Ti}_{3.6}\text{O}_{12}$

	x	y	z	U(eq)
Ti(1)	3978(1)	0	7992(2)	7(1)
Ti(2)	2013(1)	-5000	7901(1)	9(1)
Cu(2)	2013(1)	-5000	7901(1)	9(1)
O(1)	2355(4)	0	8441(7)	9(1)
O(2)	4417(4)	0	1329(7)	8(1)
O(3)	3713(4)	0	4961(6)	10(1)
O(4)	3642(4)	-5000	7913(7)	8(1)
Na(1)	5000	-5000	5000	27(1)
<u>Unit cell dimensions</u>				FW 344.25 g/mol
a = 12.2278(14) Å	$\alpha = 90^\circ$			Temp 173(2) K
b = 3.7970(4) Å	$\beta = 107.268(2)^\circ$			Wavelength MoK α 0.71073 Å
c = 6.4920(7) Å	$\gamma = 90^\circ$			Crystal system Monoclinic
Volume 287.83(5) Å ³				Space group C2/m
Z = 2				

Table 6.2 Cell dimensions based on monoclinic C2/m space group, dielectric properties and color $\text{Na}_{0.86}\text{M}_{0.43}\text{Ti}_{3.57}\text{O}_8$

M =	Mg	Zn	Mn	Fe*	Co	Ni	Cu	Cu (0.4)
a (Å)	12.253	12.279	12.272	12.302	12.333	12.259	12.242	12.228
b (Å)	3.771	3.767	3.784	3.812	3.846	3.8093	3.8039	3.797
c (Å)	6.423	6.438	6.524	6.547	6.521	6.468	6.506	6.492
Beta, β (°)	106.96	107.25	106.86	107.16	107.21	107.01	107.20	107.27
Vol (Å ³)	283.98	284.35	289.93	293.34	295.46	288.84	289.42	287.84
Calc. κ	17.77	18.46	17.28	15.68	16.14	15.65	16.67	-
Obs. κ (1MHz)	15.81	11.69	19.74	18.36	19.19	16.46	22.83	-
Obs. Tan δ	0.0168	0.0051	0.0346	0.0803	0.0183	0.0136	0.0065	-
Color	White	White	Black	Orange	Grey	Green	Green	-

in which case the M cation is in M^{2+} . For Fe^{3+} , the formula was adjusted to accommodate the charge difference, $NaFeTi_3O_8$, such as in Freudenbergite [6]. Oxide precursors were mixed in stoichiometric ratios and heated from 900-1000°C for ~24-36 hours with intermittent grinding. Pure phases were obtained for Mg, Co, Ni, Cu, and Zn. The impurity phases found in Mn and Fe were primarily rutile TiO_2 and $Na_2Ti_6O_{13}$ indicating that composition stoichiometry was out of single phased limits. In some cases repeated synthesis of Co and Mg also resulted in the aforementioned impurities. It is well known that the Na and M content can vary, and several compositions have been reported previously [7]. Refined unit cell parameters from powder XRD are reported, Table 6.2, and includes those compositions found with impurities as a comparison. The values calculated agree with reported values.

Table 6.3 Summary of magnetic measurements for $Na_{0.86}M_{0.43}Ti_{3.57}O_8$ measured at 1.0 Tesla from 5 – 300 K

M =	Mn	Fe*	Co	Ni	Cu
Θ_w (K)	-0.50	-27.09	-5.40	0.35	1.65
C (emu K/mole)	1.3829	1.4302	1.1963	0.5179	0.1126
$\mu_{calc}(\mu_B) M^{2+}$	3.882	3.207	2.538	1.856	1.134
$\mu_{calc}(\mu_B) M^{3+}$	3.207	3.882	3.207	1.134	-
$\mu_{obs} (\mu_B)$	3.348	3.384	3.095	2.037	0.9496

Curie –Weiss relationship is based off $1/\chi$ vs. T plots (100 - 300 K)

Preliminary magnetic measurements indicate that all compositions are paramagnetic with Curie-Weiss temperatures close to 0 Kelvin, Table 6.3. The observed and calculate magnetic moments for Cu and Ni agree, but the moments for

Mn, Fe and Co do not. This is likely due to paramagnetic impurities such as $\text{Na}_2\text{Ti}_6\text{O}_{13}$ and deviation from calculated stoichiometry. Preliminary optical measurements indicate band gaps ranging from 1.65eV to 2.70eV.

6.3 Perovskite Lanthanide Iridates

The ternary and quaternary oxides of Ru, Rh, and Ir have a rich history as complex magnetic materials; $\text{La}_2\text{RhMnO}_6$ is a well known ferromagnet, the $\text{La}_{2-x}\text{Sr}_x\text{CoRuO}_6$ series shows antiferromagnetic, ferromagnetic and spin-glass regions, and $\text{La}_2\text{NiIrO}_6$ exhibits an antiferromagnetic order with a ferromagnetic component [8-10]. Most of the chemistry involving Ir is that of Ir^{4+} which has a $5d^5$ (LS) electron configuration (although Ir^{5+} is also known) [11]. This electron occupation results in empty eg orbitals, and for Ir^{4+} -O-M interactions where the M is cation has half filled or filled eg orbitals, Goodenough-Kanamori rules dictate strong ferromagnetic exchange interactions. The 3d-O-3d interactions are relatively well known, however, that of the 4d/5d-O-3d are sparse. In addition, it is not particularly clear whether the Goodenough-Kanamori rules are followed for 4d and 5d cations. Thus, the study of oxides containing 4d/5d cations and a 3d cation are important.

As mentioned previously, $\text{La}_2\text{NiIrO}_6$ has been shown to exhibit complex magnetism, however, the other lanthanides in this series have not been reported. In this study, we synthesized $\text{Ln}_2\text{NiIrO}_6$ where $\text{Ln} = \text{La, Pr, Nd, Sm}$ by solid state methods. Figure 6.2 shows the powder diffraction patterns. A very systematic peak

evolution can be seen upon going from La to Pr to Nd to Sm as evidenced by the central 100% intensity peak comprised of the (020), (112), and (200) reflections which tend to separate. In addition, it was originally reported that $\text{La}_2\text{NiIrO}_6$ could potentially be orthorhombic with space group pbnm due to the lattice parameters of $a \approx b \approx 5.6 \text{ \AA}$, and $\beta \approx 90^\circ$. However, the first peak at $\sim 19^\circ 2\theta$ was quite wide indicating two peaks are likely present, the (011) and

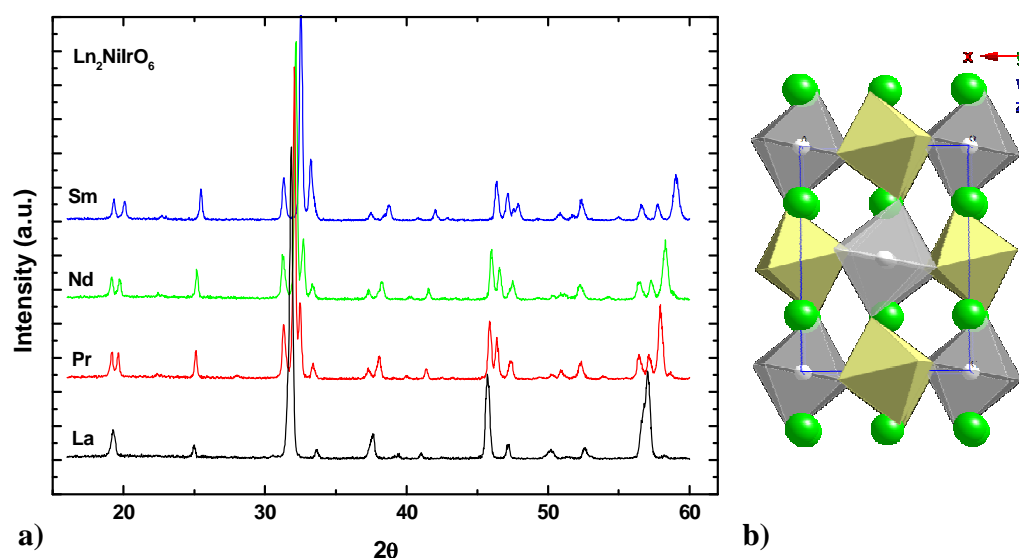


Figure 6.2 Powder diffraction patterns for $\text{Ln}_2\text{NiIrO}_6$ where $\text{Ln} = \text{La}, \text{Pr}, \text{Nd}, \text{Sm}$ (a) and monoclinic structure along the y -axis with Ni and Ir ordered in octahedral centers, and Ln as green spheres.

(101). The (011) reflection is forbidden for an orthorhombic space group pbnm . Thus, Blasse and Currie determined the system to be monoclinic with space group $\text{P2}_1/\text{n}$ [12, 13]. Moreover, the Pr, Nd, and Sm powder patterns reported here all show this obvious splitting at $\sim 19^\circ 2\theta$. As such, all compositions here could also be indexed to the monoclinic structure with $\text{P2}_1/\text{n}$ space group, Table 6.4.

Table 6.4 Unit Cell dimensions

$\text{Ln}_2\text{NiIrO}_6$	La	Pr	Nd	Sm
a (Å)	5.552	5.555	5.572	5.529
b (Å)	5.565	5.599	5.599	5.538
c (Å)	7.851	7.852	7.874	7.822
Vol (Å ³)	242.52	244.22	245.64	239.52
t (tolerance factor)	0.8682	0.8567	0.8509	0.8407
Color	Black	Black	Black	Black

The magnetic properties of potential combinations of cation interaction between the d orbitals of $\text{Ni}^{2+}(3d^8)$ and low-spin $\text{Ir}^{4+}(4d^5)$ cations, through oxygen $2p$ orbitals are summarized in Table 6.5. These interactions can be understood on the basis of rules for spin-spin super-exchange interactions by Goodenough and Kanamori [14, 15]. Spin interactions between empty orbitals to half-filled, $\text{Ir}^{4+}(e_g)\text{--O--Ni}^{2+}(e_g)$, along

Table 6.5 Expected super-exchange interactions for ordered $\text{Ln}_2\text{NiIrO}_6$

<i>M</i>-Cation		<i>M'</i>-Cation		Interaction	Result
$\text{Ir}^{4+}, 4d^5$	(LS)	$\text{Ni}^{2+}, 3d^5$	(HS)		
2 e_g	Empty	2 e_g	Half	σ	FM
1 t_{2g}	Half	1 t_{2g}	Full	π	FM
2 t_{2g}	Full	2 t_{2g}	Full	π	AFM
$\text{Ir}^{4+}, 4d^5$	(LS)	$\text{Ir}^{4+}, 4d^5$	(LS)		
1 t_{2g}	Half	1 t_{2g}	Half	π	AFM
1 t_{2g}	Half	2 t_{2g}	Full	π	FM
$\text{Ni}^{2+}, 3d^5$	(HS)	$\text{Ni}^{2+}, 3d^5$	(HS)		
2 e_g	Half	2 e_g	Half	σ	AFM

with half-filled to full orbitals, $\text{Ni}^{2+}(t_{2g})\text{--O--Ir}^{4+}(t_{2g})$, yield ferromagnetic coupling. In contrast, antiferromagnetic coupling results from spin transfer between half-filled to half-filled orbitals, for example, $\text{Ni}^{2+}(t_{2g})\text{--O--Ir}^{4+}(t_{2g})$, $\text{Ir}^{4+}(t_{2g})\text{--O--Ir}^{4+}(t_{2g})$, and $\text{Ni}^{2+}(e_g)\text{--O--Ni}^{2+}(e_g)$. Due to the greater overlap of e_g vs. t_{2g} orbitals, previously discussed in Chapter one, ferromagnetic interactions are stronger, and a ferromagnetic coupling is expected. It should be noted that any disorder in the system would produce additional antiferromagnetic interactions within the sample, and would be especially strong for $\text{Ni}^{2+}(e_g)\text{--O--Ni}^{2+}(e_g)$.

Magnetic measurements are presented in Figure 6.3 and 6.4. All samples show an obvious ferromagnetic component as expected for an ordered system. However, each sample also shows the complex magnetic components of competing AFM and FM interactions. Although we expect an ordered system based on the monoclinic structure, oxidation state differences, cationic size differences, and the observation of FM in magnetic susceptibility data, it is apparent that point defects or phase transitions may play a role at low temperatures. We conclude this due to the additional ordering anomalies at low temperature, and the negative Weiss temperature which would indicate AFM. Table 6.6 summarizes the magnetic data calculated from the Curie-Weiss relationship. The calculated and observed magnetic moments agree well with spin-orbit approximations. One may notice that the calculated magnetic moments are larger for Pr, Nd, and Sm, and this is due to the contribution of unpaired $4f^n$ electrons ($0 \leq n \leq 14$) from the lanthanide. In calculating the magnetic moments for the lanthanide contribution, it is often necessary to include a spin-orbit coupling term.

This accounts for the angular momentum which can drastically affect the calculated and often the observed magnetic moment. The calculated values in Table 6.6 have the spin-orbit coupling terms applied. An interesting point to note is the extremely

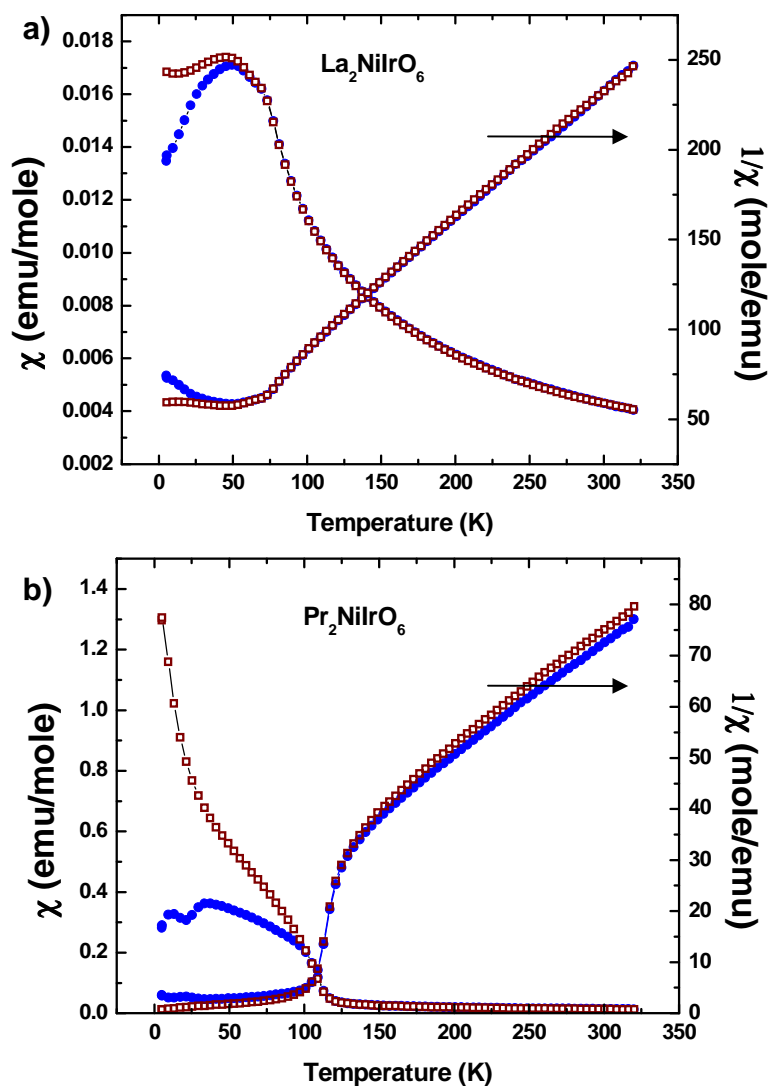


Figure 6.3 Magnetic susceptibility and inverse magnetic susceptibility for ZFC (blue) and FC (red) measurements on (a) $\text{La}_2\text{NiIrO}_6$, and (b) $\text{Pr}_2\text{NiIrO}_6$.

complex magnetic behavior of the Sm analogue. The susceptibility data shows a diamagnetic phase at temperatures up to 50 K at which time there are two distinct AFM peaks before a FM type onset. This is extremely perplexing and warrants the

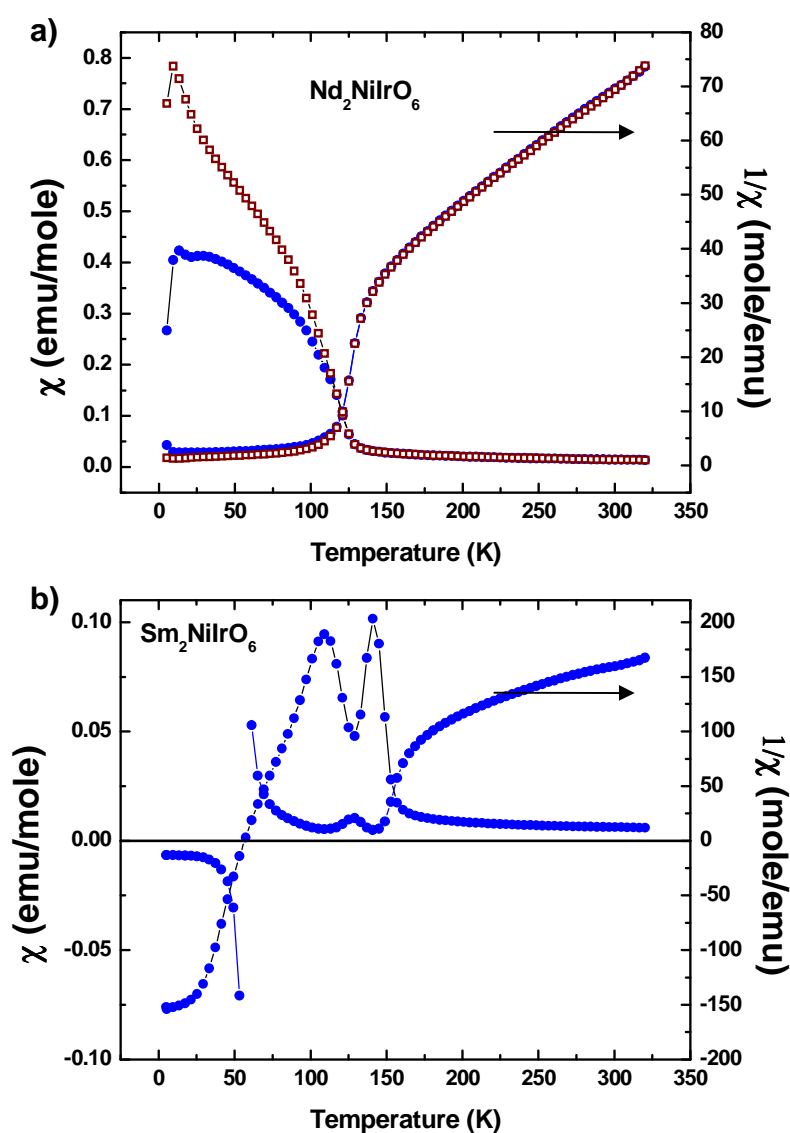


Figure 6.4 Magnetic susceptibility and inverse magnetic susceptibility for ZFC (blue) and FC (red) measurements on (a) $\text{Nd}_2\text{NiIrO}_6$, and (b) $\text{Sm}_2\text{NiIrO}_6$.

Table 6.6 Summary of ZFC and FC magnetic measurements at 0.5 Tesla at 5 – 320 K

$\text{Ln}_2\text{NiIrO}_6$	La ZFC	La FC	Pr ZFC	Pr FC	Nd ZFC	Nd FC	Sm ZFC	Sm FC
Θ_w (K)	-32.4	-36.3	-34.4	-39.0	-38.4	-37.1	-45.2	n/a
C (emu-K/mole)	1.429	1.445	4.591	4.510	4.869	4.841	2.084	n/a
μ_{calc} (so)	3.317		6.053		6.100		4.09	
μ_{obs}	3.383	3.402	6.064	6.010	6.245	6.227	4.085	n/a
T_{fo} (K)	70		105		110		145	

Data for $\text{Ln} = \text{La}$ was reproduced and is relatively consistent with reported values [10, 12]. The paramagnetic region of $1/\chi$ vs. T plots (~200 - 300 K) was used for calculations.

consideration of potential impurities. No impurities were found after another analysis of the powder x-ray diffraction data. Due to the sensitivity of magnetic susceptibility to magnetic impurities, SmNiO_3 , Sm_2O_3 , IrO_2 , and NiO were investigated. SmNiO_3 is AFM at ~220 K, Sm_2O_3 does not show an ordering temperature down to 2 K, IrO_2 is paramagnetic, and NiO is AFM at ~520K, well above the anomalies seen here [16]. Thus, the multiple anomalies in the magnetic susceptibility for these compositions cannot be fully explained. It would be interesting to acquire neutron diffraction data over a range of temperatures to gain more insight into the magnetic structure. Additional magnetic measurements including field dependence and AC susceptibility may also provide insight into the ordering behavior observed.

The results shown here reinforce the observations that Ir based materials are rich and diverse in magnetic behavior. The observation of separate, distinct ordering regimes is unique and intriguing, and a better understanding of the spin interactions and magnetic contributions may prove useful in the design of novel materials.

6.4 References

1. M.A. Subramanian, A.W. Sleight, *Solid State Sci.*, 4 (2002) 347
2. S. Anderson and A. D. Wadsley, *Acta Cryst.*, 15 (1962) 201
3. H. Sakurai, M. Kato, K. Yoshimura, N. Tsujii, K. Kosuge, *Phys. Rev. B*, 75 (2007) 115128
4. X. Rocquefelte, F. Goubin, H-J. Koo, M-H. Whangbo, S. Jobic, *J. Inorg. Chem.*, 43(7) (2004) 2246
5. M. Avdeev, Dept. of Ceramics and Glass Engineering, Univ. of Aviero, Portugal. Taken from ICSD: PDF#00-053-0081 (2001)
6. T. Ishiguro, K. Tanaka, F. Marumo, M.G.M.U. Ismail, S. Hirano, S. Somiya, *Acta Cryst. B*, 34 (1978) 255
7. G. Bayer, W. Hoffmann, *Z. Krist.*, 121 (1965) 9
8. P. Tomeš, J. Hejtmánek, K. Knížek, *Solid State Sci.*, 10 (2008) 486
9. C. Schinzer, *J. Phys. Chem. Sol.*, 61 (2000) 1543
10. A.V. Powell, J.G. Gore, and P.D. Battle, *J. Alloys Compd.*, 201 (1993) 73
11. D. Harada, M. Wakeshima, Y. Hinatsu. *J. Solid State Chem.*, 145 (1999) 356
12. R.C. Currie, J. F. Vente, E. Frikkee, D.J.W.Ijdo, *J. Solid State Chem.*, 116 (1995) 199
13. G. Blasse, *J. Inorg. Nucl. Chem.*, 27 (1965) 993
14. J. B. Goodenough, *J. Phys. Chem. Sol.*, 6 (1958) 287
15. J. Kanamori, *J. Phys. Chem. Sol.*, 10 (1959) 87
16. M.M. Schieber, *Experimental Magnetochemistry: Nonmetallic Magnetic Materials*; Interscience Publishers, John Wiley & Sons: New York, 1967

General Conclusions and Future Work

The nature of transition metal oxides, and their often strongly interacting electron systems, offer a wide range of electronic properties (insulators, ferroelectrics, semiconductors, metals, and superconductors), magnetic properties (paramagnetism, ferro/ferrimagnetism, antiferromagnetism, and diamagnetism), and cross coupling of electric and magnetic properties (magneto capacitance, magnetoresistance, and multiferroics in general). Nearly each of these physical property examples was discussed in this thesis on the basis of 3 main ‘parent’ compositions, $\text{CaCu}_3\text{Ti}_4\text{O}_{12}$, $\text{La}_2\text{RhMnO}_6$, and YMnO_3 . This indicates the importance of material exploration as the future of electronic devices is dependent on the development of novel materials with improved or novel properties.

We discussed the design, synthesis, structure, and physical property characterization of novel materials. We showed that in a well known family of materials, La_2MRhO_6 , that unique magnetic and electric properties could still be discovered. The $\text{La}_2\text{MnRhO}_6$ thin films were found to exhibit a change in the defect structure, surface morphology, and magnetic properties for films grown at different oxygen pressures revealing the importance of deposition methods. Bulk ceramics of La_2MRhO_6 ($\text{M} = \text{Cr}, \text{Mn}, \text{Fe}, \text{Co}, \text{Ni}$ and Cu) were found to be orthorhombic p-type semiconductors. Complex magnetism was found for $\text{M} = \text{Fe}$ and Cr with both showing magnetic hysteresis at 5K. The Cu analogue is likely to be in a $2+/3+$ oxidation state, and showed a favorable power factor up to ~ 575 K. $\text{LaCo}_{1-x}\text{Rh}_x\text{O}_3$ compositions were found to exhibit an interesting lattice crossover $x = 0.5$. Strong evidence for at least

some conversion of $\text{Rh}^{3+}/\text{Co}^{3+}$ to $\text{Rh}^{4+}/\text{Co}^{2+}$ is found in both structural and electrical transport data. A thermoelectric figure-of-merit (ZT) of about 0.075 has been achieved for $\text{LaCo}_{0.5}\text{Rh}_{0.5}\text{O}_3$ at 775 K

The well known magnetoelectric, YMnO_3 , was found to form complete or nearly complete solid solutions with YInO_3 , YAlO_3 , and $\text{YCu}_{0.5}\text{Ti}_{0.5}\text{O}_3$ systems. Our results indicate exciting optical properties as a wide range of blue was observed in the YInO_3 solid solution, the intensity of which was critically dependent on the apical bond distances and the crystal field splitting. The YInO_3 and $\text{YCu}_{0.5}\text{Ti}_{0.5}\text{O}_3$ systems showed magnetic and magnetoelectric suppression for increasing values as expected, but the field dependent capacitance for the YInO_3 showed a unique improvement and sign swap indicating a magneto-electric coupling. We determined the YAlO_3 structure to have been improperly reported based on bond valence calculations. Our investigation into the YAlO_3 - YMnO_3 system is likely to help in this structural clarification.

For the high-k dielectric $\text{CaCu}_3\text{Ti}_4\text{O}_{12}$, the limits of x, y were determined for $\text{CaCu}_{3-x}\text{Mn}_x\text{Ti}_{4-y}\text{Fe}_y\text{O}_{12}$ and $\text{CaCu}_3\text{Ti}_4\text{O}_{12-x}\text{F}_x$. With small compositional variations, we showed an improvement and a colossal suppression of the dielectric properties. The results here show the unique rigidity of the structure and its effect on the physical properties for small substitutions. This may provide into the future design of improved dielectrics based on $\text{CaCu}_3\text{Ti}_4\text{O}_{12}$.

If there is one lesson I've learned in this thesis work, it is that the work is never over. Our desire to learn as researchers is insatiable, and as such, there is much more I would like to investigate within these families of materials. For example, the YMnO_3

solid solutions provide several pathways for continuation. For such a well known material, it is perplexing to consider such discoveries as intense blues and greens are possible. We have only touched the surface of what I think is possible in this class. Therefore, a continuation of compositional exploration is warranted. In addition, it is necessary to clarify the original structure that many use to classify these types of materials. Neutron diffraction on $\text{YMnO}_3\text{-YAlO}_3$ can help determine the exact structure and likely shed light on the variation of unit cell dimensions compared to other materials in this class. As the miniaturizations of electronic devices continue, the components are shifting towards thin films. For this reason, and investigation of thin film YMnO_3 solid solutions may yield unique properties and interactions.

Bibliography

- T.B. Adams, D.C. Sinclair, A.R. West, *Adv. Mater.* 14 (18) (2002) 1321–1323
- B.B. Van Aken, T.T.M. Palstra, A. Filippetti, N. Spaldin, *Nature Materials*, 3 (2004) 164
- B.B. Van Aken, A. Meetsma, T.M. Palstra, *Acta Cryst. C*, 57 (2001) 230
- P.W. Anderson. *Phys. Rev.*, 79 (1950) 350
- S. Anderson and A. D. Wadsley. *Acta Cryst.*, 15 (1962) 201-206
- J. Androulakis, P. Migiakis, J. Giapintzakis, *Appl. Phys. Lett.*, 84 (2004) 1099
- T. Asaka, K. Nemoto, K. Kimoto, T. Arima, Y. Matsui, *Phys. Rev. B*, 71 (2005) 014114
- E. Ascher, H. Rieder, H. Schmid and H. Stössel, *J. Appl. Phys.*, 37 (1966) 1404
- M. Avdeev, Dept. of Ceramics and Glass Engineering, Univ. of Aviero, Portugal.
Taken from ICSD: PDF#00-053-0081 (2001)
- G.E. Bacon. *Neutron Scattering in Chemistry*; Butterworths Inc.: Boston, 1977
- M.N. Baibich, J.M. Broto, A. Fert, F. Nguyen Van Dau, F. Petroff, P. Eitenne, G. Creuzet, A. Friederich, J. Chazelas. *Phys. Rev. Lett.*, 61 (1988) 2472
- P.D. Battle, J.F. Vente, *J. Solid State Chem.*, 146 (1999) 163
- G. Bayer, W. Hoffmann. *Z. Krist.*, 121 (1965) 9-13
- E.F. Bertaut, J. Mareschal, *Compt. Rend.*, 257 (1963) 867
- G. Binasch, P. Grunberg, F. Saurenbach, W. Zinn. *Phys. Rev. B*, 39 (1989) 4828
- J. Blasco, M. C. Sanchez, J. Perez-Cacho, J. Garcia, G. Subias, J. Campo, *J. Phys. Chem. Solids*, 63 (2002) 781
- G. Blasse, *J. Inorg. Nucl. Chem.*, 27 (1965) 993
- B. Bochu, M.N. Deschizeaux, J.C. Joubert, *J. Solid State Chem.*, 29 (1979) 291

- J.W.G. Bos, J.P. Attfield, L.-Y. Jang, *Phys. Rev. B*, 72 (2005) 014101
- R.J. Bouchard, J.F. Weiher, *J. Solid State Chem.* 3 (1972) 80
- W. Brixel, P. Rivera, A. Steiner, H. Schmid, *Ferroelectrics*, 79 (1988) 201
- R.C. Buchanan. *Ceramic Materials for Electronics: Processing, Properties, and Applications*, Marcel Dekker, Inc.: New York, 1986
- P.R. Bueno, R. Tararan, R. Parra, E. Joanni, M.A. Ramirez, W.C. Ribeiro, E. Longo, J.A. Varela. *J. Phys. D: Appl. Phys.*, 42 (2009) 055404
- C. L. Bull, D. Gleeson, and K. S. Knight, *J. Phys.: Condens. Matter.*, 15 (2003) 4927
- G. Catalan, *Appl. Phys. Lett.*, 88 (2006) 102902
- J. Cai, Y.-H. Lin, C.-W. Nan, J. He, Y. Wu, X. Chen, *Appl. Phys. Lett.*, 91 (2007) 252905
- G. Chiodelli, V. Massarotti, D. Capsoni, M. Bini, C. B. Azzoni, M. C. Mozzati and P. Lupotto. *J. Solid State Comm.*, 132 (2004) 241-246
- D.-Y. Cho, *Phys. Rev. Lett.*, 98 (2007) 217601
- S.W. Choi, S.H. Hong, Y.M. Kim. *J. Am. Ceram. Soc.*, 90 (2007) 4009-4011
- S.Y. Chung, S.I. Lee, J.H. Choi, S.Y. Choi. *Appl. Phys. Lett.*, 89 (2006) 1-3
- M. Ciampolini, *Chem. Commun.*, 2 (1966) 47
- B.D. Cullity, S.R. Stock. *Elements of X-Ray Diffraction*, 3rd ed.; Prentice Hall; New Jersey, 2001.
- R.C. Currie, J.F. Vente, E. Frikkee, D.J.W. Ijdo, *J. Solid State Chem.*, 116 (1995) 199-204
- H. Das, U. V. Waghmare, T. Saha-Dasgupta, and D. D. Sarma, *Phys. Rev. Lett.*, 100 (2008) 186402
- R. I. Dass, J. B. Goodenough, *Phys. Rev. B*, 67 (2003) 014401
- R.I. Dass, J.-Q. Yan, J.B. Goodenough, *Phys. Rev. B*, 68 (2003) 064415

- C. Degenhardt, M. Fiebig, D. Fröhlich, Th. Lottermoser, R.V. Pisarev, *Appl. Phys. B*, 73 (2001) 139
- G. Demazeau, B. Siberchicot, S.F. Matar, C. Gayet, A. Largeteau, *J. Appl. Phys.*, 75 (1994) 4617.
- A. Deschanvres, B. Reveau, F. Tollemer, *Bull. Soc. Chim. Fr.*, (1967) 4077
- A. Dixit, A.E. Smith, M.A. Subramanian, G. Lawes *Solid State Comm.*, 150 (2010) 746
- W. Eerenstein, N.D. Mathur, J.F. Scott, *Nature*, 442 (2006) 759
- G. Ellert. *The Physics Hypertextbook: Dielectrics*. N.p., Jan. 2010. Web. 23 Mar. 2010
- X. Fabreges, S. Petit, I. Mirebeau, S. Pailhes, L. Pinsard, A. Forget, M.T. Fernandez-Diaz, and F. Porcher, *Phys. Rev. Lett.*, 103 (2009) 067204
- L. Feng, X. Tang, Y. Yan, X. Chen, Z. Jiao, and G. Cao. *Phys. Stat. Sol.: Rap. Res. Lett.*, 203(4) (2006) 22-24
- C.J. Fennie, K.M. Rabe, *Phys. Rev. B*, 72 (2005) 100103
- M. Fiebig, Th. Lottermoser, D. Frohlich, A. V. Goltsev, and R. V. Pisarev, *Nature*, 419 (2002) 818
- A. Filippetti, N.A. Hill, *Phys. Rev. B*, 65 (2002) 195120
- M. Filippi, B. Kundys, R. Ranjith, A. K. Kundu, and W. Prellier, *Appl. Phys. Lett.* 92 (2008) 212905
- P. Florian, M. Gervais, A. Douy, D. Massiot, J.P. Coutures, *J. Phys. Chem. B*, 105 (2001) 379
- N. Floros, J.T. Rijssenbeek, A.B. Martinson, K.R. Poeppelmeier, *Solid State Sci.*, 4 (2002) 1495
- N. Fujimura, H. Sakata, D. Ito, T. Yoshimura, T. Yokota, and T. Ito, *J. Appl. Phys.*, 93 6990 (2003).
- H Fukumura, N Hasuike, H Harima, K Kisoda, K Fukae, T Takahashi, T Yoshimura and N Fujimura, *J. Phys.: Conf. Series* 92 (2007) 012126

- F.S. Galasso. *Perovskites and High T_C Superconductors.*; Gordon and Breach Science Publishers: New York, 1990
- G.H. Gehring, *Ferroelectrics*, 161 (1994) 275
- D.M. Giaquinta, H.C. Zur Loye, *J. Am. Chem. Soc.*, 114 (1992) 10952
- D.M. Gianquinta, H.C. Zur Loye, *Chem. Mater.*, 6 (1994) 365
- L. Giebeler, D. Kiebling, G. Wendt, *Chem. Eng. Tech.*, 30 (2007) 889
- A.M. Glaser, *Acta Cryst. B*, 28 (1972) 3384
- V.M. Goldschmidt, *Naturwissenschaften*, 14 (1926) 477
- J.B. Goodenough, *J. Phys. Chem. Solids*, 6 (1958) 287
- J.B. Goodenough. *Magnetism and the Chemical Bond*; John Wiley & Sons: New York, 1963
- J.B. Goodenough. *Prog. Solid State Chem.*, 5 (1971) 145
- J.B. Goodenough, A.L. Loeb. *Phys. Rev.*, 98 (1955) 391; J.B. Goodenough. *ibid.* 100, 564 (1955)
- J.B. Goodenough and J. M. Longo *Landolt-Bornstein, Group III, Vol. 4: Magnetic and Other Properties of Oxides and Related Compounds*, Springer-Verlag, New York (1970) p. 126
- J.B. Goodenough, A. Wold, R.J. Arnott, N. Menyuk. *Phys. Rev.*, 124 (1961) 373
- R. K. Grubbs, E. L. Venturini, P. G. Clem, J. J. Richardson, B. A. Tuttle, and G. A. Samara. *Phys Rev. B*, 72 (2005) 1-11
- K.A.Gschneiderner, G.H. Vineyard, *J Appl. Phys.* 33 (1962) 3444
- H. Guo, J. Burgess, S. Street, A. Gupta, T. G. Calvarese, and M. A. Subramanian, *Appl. Phys. Lett.*, 89 (2006) 022509
- H. Z. Guo, J. Burgess, E. Ada, S. Street, A. Gupta, M. N. Iliev, A. J. Kellock, C. Magen, M. Varela, and S. J. Pennycook, *Phys. Rev. B*, 77, 174423 (2008)
- H. Guo, A. Gupta, T. G. Calvarese, and M. A. Subramanian, *Appl. Phys. Lett.*, 89 (2006) 262503

- H. Z. Guo, A. Gupta, J. Zhang, M. Varela, and S. J. Pennycook, *Appl. Phys. Lett.*, 91 (2007) 202509
- D. Gutiérrez, O. Peña, K. Ghanimi, P. Durán, C. Moure, *J. Phys. Chem. Sol.*, 63 (2002) 1975
- D. Harada, M. Wakeshima, Y. Hinatsu. *J. Solid State Chem.*, 145 (1999) 356-360
- M. Hashisaka, D. Kan, A. Masuno, M. Takano, and Y. Shimakawa, *Appl. Phys. Lett.*, 89 (2006) 032504
- M.T. Haque and N. Kamegashira, *J. Alloys Compd.*, 395 (2005) 220
- M.T. Haque, H. Satoh, and N. Kamegashira, *Mater. Res. Bull.*, 39 (2004) 375
- M.T. Haque, H. Satoh, and N. Kamegashira, *Mater. Lett.*, 58 (2004) 1571
- M.T. Haque, H. Satoh, and N. Kamegashira, *J. Alloys Compd.*, 390 (2005) 115
- K. Hayashi, T. Nozaki, T. Kajitani, *Jap. J. Appl. Phys.*, 46 (2007) 5226
- T. He, J. Chen, T.G. Calvarese, M.A. Subramanian, *Solid State Sci.* 8 (2006) 467-469
- C.C. Homes, T. Vogt, S.M. Shapiro, S. Wakimoto, A.P. Ramirez. *Science*, 293 (2001) 673
- Z.J. Huang, Y. Cao, Y.Y. Sun, Y.Y. Xue, and C.W. Chu, *Phys. Rev. B* 56, (1997) 2623
- N. Hur, S. Park, P.A. Sharma, J.S. Ahn, S. Guha and S-W. Cheong, *Nature*, 429 (2004) 392
- T. Ishiguro, K. Tanaka, F. Marumo, M.G.M.U. Ismail, S. Hirano, S. Somiya. *Acta Cryst. B* 34 (1978) 255-256
- T. Idogaki, Y. Miyoshi and J.W. Tucker, *J. Magn. Magn. Mater.*, 154 (1996) 221
- M. N. Iliev, M. V. Abrashev, A. P. Litvinchuk, V. G. Hadjiev, H. Guo, and A. Gupta, *Phys. Rev. B* 75 (2007) 104118
- M. N. Iliev, H. Guo, and A. Gupta, *Appl. Phys. Lett.*, 90 (2007) 151914
- M. N. Iliev, H.-G. Lee, V. N. Popov, M. V. Abrashev, A. Hamed, R. L. Meng, and C. W. Chu, *Phys. Rev. B* 56 (1997) 2488

- I.G. Ismailzade, S.A. Kizhaev, *Sov. Phys. Solid State*. 7 (1965) 236
- H. I. Ismailzade, G. A. Smolenskii, V. I. Nesterenko, F. A. Agaev, , *Phys. Stat. Sol. (a)*, 5 (1971) 83
- K. Iwasaki, T. Ito, T. Nagasaki, Y. Arita, M. Yoshino, T. Matsui, *J. Solid State Chem.*, 181 (2008) 3145.
- B. Jaffe, W.R. Cook, Jr., H. Jaffe. *Piezoelectric Ceramics*. Academic Press: New York, 1971
- H. Jaksch, W. Seipel, K.L. Weiner, A. El Goresy, *Naturwissenschaften.*, 70 (1983) 525
- J.P Jakubovics. *Magnetism and Magnetic Materials*, Institute of Metals: London, 1987
- H.S. Jarrett, A.W. Sleight, H.H. Kung, J.L. Gilson, *J. Appl. Phys.*, 51 (1980) 3916
- A.M. Kalashnikova, R.V. Pisarev, *JETP Lett.*, 78 (2003) 143
- J. Kanamori, *J. Phys. Chem. Solids* 10 (1959) 87
- P. Karen, P. M. Woodward. *J. Solid State Chem.*, 141 (1998) 78-88
- S.O. Kasap, *Thermoelectric Effects in Metals: Thermocouples*. An e-booklet (1997-2001)
- K. Kato, I. Kawada, N. Kimizuka, *Z. Kristallogr.*, 141 (1975) 314
- T. Katsufuji, S. Mori, M. Masaki, Y. Moritomo, N. Yamamoto, and H. Takagi, *Phys. Rev. B* 64 (2001) 104419
- W. D. Kingery, H. K. Bowen, D. R. Uhlmann. *Introduction to Ceramics*, 2nd ed.; John Wiley & Sons: New York, 1976
- N. Kimizuka, T. Mohri, *J. Solid State Chem.* 60 (1985) 382
- T. Kimura, G. Lawes and A. P. Ramirez, *Phys. Rev. Lett.*, 94 (2005) 137201
- W. Kobayashi, I. Terasaki, *Physica B* 329-222 (2003) 771-772
- M. Kriener, C. Zobel, A. Reichl, J. Baier, M. Cwik, K. Berggold, H. Kierspel, O. Zabara, A. Freimuth, and T. Lorenz, *Phys. Rev. B*, 69 (2004) 094417

- S. Krohns, J. Lu, P. Lunkenheimer, V. Brizé, C. Autret-Lambert, M. Gervais F. Gervais, F. Bourée, F. Porcher, and A. Loidl, *Eur. Phys. J. B*, 72 (2009) 173-182
- H. Kuriyama, M. Nohara, T. Sasagawa, K. Takubo, T. Mizokawa, K. Kimura, H. Takagi, *International Conference on Thermoelectrics* (2006), 25th(Pt. 1), 97-98
- K. Kurosaki, H. Muta, M. Uno, S. Yamanaka, *J. Alloys Comp.* 315 (2001) 234
- R. Kykyneshi. M.S. Thesis, Oregon State University, Corvallis, OR, 2004
- T. Kyomen, Y. Asaka, M. Itoh. *Phys. Rev. B* 67 (2003) 144424
- P. Lacorre, J.B. Torrance, J. Pannetier, A.I. Nazzal, P.W. Wang, Y.C. Huang, *J. Solid State Chem.*, 91 (1991) 225
- B. Lamp. "Instrumental Analysis." Truman State University.
http://www2.truman.edu/~blamp/chem322/pdf/chapter%201%20_9-3%20corrections_.pdf. Accessed May 2010.
- A.C. Larson, R.B. Von Dreele, "General Structure Analysis System (GSAS)," Los Alamos National Laboratory Report LAUR 86-784 (2004)
- G. Lawes, A. P. Ramirez, C.M. Varma, and M. A. Subramanian, *Phys. Rev. Lett.*, 91 (2003) 25720
- M. Li, A. Feteira, D.C. Sinclair, A.R. West, *Appl. Phys. Lett.* 88 (2006) 232903
- J. Li, U.G. Singh, T.D. Schladt, J.K. Stalick, S.L. Scott, R. Seshadri, *Chem. Mater.* 20 (2008) 6567
- T. Lonkai, D. G. Tomuta, U. Amann, I. Ihringer, R. W. A. Hendrikx, D. M. Tobbens and I. A. Mydosh, *Phys. Rev. B*, 69 (2004) 134108(l).
- T. Lottermoser, T. Lonkai, U. Amann, D. Hohlwein, J. Ihringer, M. Fiebig, *Nature*, 430 (2004) 541
- N.N. Lubinskii, L.A. Bashkirov, G.S. Petro, S.V. Schevchenko, I.N. Kandidatova, M.V. Bushinskii, *Glass and Ceramics*, 66 (2009) 59
- M.W. Lufaso, P.M. Woodward, *Acta Cryst. B*, 57 (2001) 725
- R.B. Macquart, M.D. Smith, H.C. zur Loye, *Cryst. Growth Design* 6 (2006) 1361.
- G.D. Mahan, J.O. Sofo, *Proc. Natl. Acad. Sci.*, 19 (1996) 7436

- S. Malo, A. Maignan, S. Marin, M. Hervieu, K.R. Poeppelmeier, B. Raveau, *Solid State Sci.*, 7 (2005) 1492
- J.C. Marchal. Synthesis, analysis and processing of novel materials in the Y_2O_3 - Al_2O_3 system. Ph.D. Thesis, The University of Michigan, Ann Arbor, MI, 2008
- S. F. Matar, M. A. Subramanian, A. Villesuzanne, V. Eyert, and M. H. Whangbo, J. *Magn. Magn. Mater.*, 308 (2007) 116
- D.C. Mattis. The Theory of Magnetism Made Simple. World Scientific Publishing Co.: New York, 2006
- E.M. McCash. *Surface Chemistry*; Oxford University Press: New York, 2001
- W. J. Merz, *Phys. Rev.*, 76 (1949) 1221
- R. H. Mitchell. Perovskites-Modern and Ancient, Alamaz Press Inc.: Ontario, Canada, 2002
- H. Mizoguchi, W. J. Marshall, A.P. Ramirez, A.W. Sleight, and M.A. Subramanian, *J. Solid State Chem.*, 180 (2007) 3463
- H. Mizoguchi, A.P. Ramirez, L. N. Zakharov, A.W. Sleight, M.A. Subramanian, *J. Solid State Chem.*, 181 (2008) 56
- H. Mizoguchi, M. Hirano, S. Fujitsu, T. Takeuchi, K. Ueda, H. Hosono, *Appl. Phys. Lett.*, 80 (2002) 1207
- H. Mizoguchi, L.N. Zakharov, A.P. Ramirez, A.W. Sleight, M.A. Subramanian, *Inorg. Chem.*, 48 (2009) 204
- H. Mizoguchi, L.N. Zakharov, W.J. Marshall, A.W. Sleight, M.A. Subramanian, *Chem. Mater.*, 21 (2009) 994
- S. Mori, J. Tokunaga, Y. Horibe, Y. Aikawa, T. Katsufuji, *Phys. Rev. B*, 72 (2005) 224434
- C. Mu, H. Zhang, Y. He, P. Liu, J. Shen, *Mat. Sci. Eng. B*, 162 (2009) 195-199
- A. Munoz, J.A. Alonso, M.L. Martinez-Lope, M.T. Casais, L. Martinez, M.T. Fernandez-Daiz, *Phys. Rev. B*, 62 (2000) 9498

- A. Navrotsky, D.J. Wiedner, *Perovskite: A Structure of Great Interest to Geophysics and Materials Science*, American Geophysical Union, Washington, D.C., 1989; vol 45, pp xi.
- A.A. Nugroho, N. Bellido, U. Adem, G. Nénert, Ch. Simon, M.O. Tjia, M. Mostovoy, T.T.M. Palstra, *Phys. Rev. B*, 75 (2007) 174435
- Ocean Optics, Inc. “*We Make A Fiber For That!*” Ocean Optics, Inc.
<http://www.oceanoptics.com/Products/opticalfibers.asp>. Accessed May 2010
- M. O’Keeffe, B.G. Hyde, *Acta Cryst. B*, 33 (1977) 3802
- P. Padhan, H.Z. Guo, P. LeClair, A. Gupta, *Appl. Phys. Lett.*, 92 (2008) 022909
- J. Park, M. Kang, J. Kim, K.H. Jang, A. Pirogov, J.G. Park, *Phys. Rev. B*, 79 (2009) 064417
- O. Parkash, D. Kumar, A. Goyal, A. Agrawal, A. Mukherjee, S. Singh and P. Singh. *J. Phys. D: Appl. Phys.*, 41 (2008) 1-8
- O. Peña, M. Bahout, D. Gutiérrez, J.F. Fernández, P. Durán, C. Moure, *J. Phys. Chem. Solids*, 61 (2000) 2019
- C.G.S. Pillai, A.M. George, *Int. J. Thermophys.*, 4 (1983) 183
- C.W.F.T. Pistorius, and J.G. Kruger, *J. Inorg. Nucl. Chem.*, 38 (1976) 1471
- A.V. Powell, J.G. Gore, and P.D. Battle, *J. Alloys Compd.*, 201 (1993) 73
- Quantum Design. *Physical Property Measurement System Hardware and Operations Manual*, 2nd Ed.; Quantum Design, 1999
- A.P. Ramirez, *Geometric Frustration: Handbook of Magnetic Materials* ed K.H.J. Buschow (Amsterdam: North-Holland/Elsevier) (2001)
- A.P. Ramirez, M.A. Subramanian, M. Gardel, G. Blumberg, D. Li, T. Vogt, S.M. Shapiro. *Solid State Commun.*, 115 (2000) 217
- C.N.R. Rao, B. Reveau. *Transition Metal Oxides: Structure, Properties, and synthesis of Ceramic Oxides*, 2nd ed.; John Wiley & Sons: New York, 1998
- B. Raveau, A. Maignan, C. Martin, M. Hervieu, *Chem. Mater.*, 10 (1998) 2641-2652

- D. Reinen, T. C. Brunold, H. O. Gudel, N. D. Yordanov, *Zeit. Anorg. Allg. Chem.* 1998, 624, 438 There was once in use a blue pigment called Mn-blue. This pigment was prepared from permanganate solutions and has been shown to be BaSO_4 containing Mn^{5+} and Mn^{6+} . The blue chromophore was identified as Mn^{5+} in tetrahedral coordination to oxygen. This pigment is no longer in use due to toxicity issues relating to the Ba. The term “Mn-blue” is still used to describe the hue of this Mn containing pigment.
- Rigaku Corporation. *X-Ray Diffractometer MiniFlexx II Instruction Manual*, 2nd ed.; Rigaku Corporation, 2006
- X. Rocquefelte, F. Goubin, H-J. Koo, M-H. Whangbo, S. Jobic. *J. Inorg. Chem.*, 43(7) (2004) 2246-2251
- N.S. Rogado, J. Li, A.W. Sleight, M.A. Subramanian, *Adv. Mater.* 17 (2005) 2225-2227
- H. Sakurai, M. Kato, K. Yoshimura, N. Tsujii, K. Kosuge. *Phys. Rev. B.* 75 (2007) 115128
- S.L. Samal, W. Green, S.E. Lofland, K.V. Ramanujachary, D. Das, A.K. Ganguli, *J. Solid State Chem.* 181 (2008) 61
- R. Schad, C.D. Potter, P. Belien, G. Verbanck, V.V. Moschchalkov, Y. Bruynseraede. *Appl. Phys. Lett.*, 64, 3500 (1994)
- M.M. Schieber, *Experimental magnetochemistry: Nonmetallic magnetic materials*, Vol. 8; John Wiley & Sons: New York, 1967
- C. Schinzer, *J. Alloys Comp.*, 288 (1999) 65
- C. Schinzer, *J. Phys. Chem. Solids*, 61 (2000) 1543
- C. Schinzer, G. Demazeau, *J. Mater. Sci.*, 34 (1999) 251
- SciFinder: Scholar. *Am. Chem. Soc. Web.* 23 Mar. 2010
- J.F. Scott, *J. Mater. Res.*, 22 (2007) 2053
- T. Seetawan, V. Amornkitbamrung, T. Burinprakhon, S. Maensiri, K. Kurosaki, H. Mutab, M. Uno, and S. Yamanaka, *J. Alloys Comp.*, 407 (2006) 314
- M.A. Senaris-Rodriguez, J.B. Goodenough, *J. Solid State Chem.*, 116 (1995) 224

- M.A. Senaris-Rodriguez, J.B. Goodenough, *J. Solid State Chem.*, 118 (1995) 323
- P.W. Selwood. *Magnetochemistry*; Interscience Publishers, Inc.: New York, 1943
- R.D. Shannon, *J. Appl. Phys.* 73, (1993) 348
- R.D. Shannon. *Acta Cryst. A.*, 32 (1976) 751-767
- R.D. Shannon, *Inorg. Chem.*, 6 (1967) 1474
- S. Shibusaki, W. Kobayashi, I. Terasaki, *Phys. Rev. B*, 74 (2006) 235110
- S. Shibusaki, Y. Takahashi, I. Terasaki, *J. Phys.: Condens. Matter.*, 21 (2009) 115501
- S. Shibusaki, Y. Takahashi, I. Terasaki, *J. Electronic Mat.*, 38 (2009) 1013
- D.C. Sinclair, T.B. Adams, F.D. Morrison, A.R. West. *Appl. Phys. Lett.*, 80(12) (2002) 2153
- M.P. Singh, S. Charpentier, K.D. Truong, P. Fournier, *Appl. Phys. Lett.*, 90 (2007) 211915
- M.P. Singh, C. Grygiel, W. C. Sheets, P. Boullay, M. Hervieu, W. Prellier, B. Mercey, C. Simon, B. Raveau, *Appl. Phys. Lett.*, 91 (2007) 012503
- M.P. Singh, K.D. Truong, P. Fournier, *Appl. Phys. Lett.*, 91 (2007) 042504
- A.W. Sleight, J.L. Gillson, P.E. Bierdstedt, *Solid State Comm.* 17 (1975) 27
- A.E. Smith, H. Mizoguchi, K. Delaney, N.A. Spaldin, A.W. Sleight, M.A. Subramanian, *J. Am. Chem. Soc.*, 131 (2009) 17084
- A.E. Smith, J. Li, K.S. Kwong, C. Powell, M.A. Subramanian, to be published
- A.E. Smith, A.W. Sleight, M.A. Subramanian, *Mat. Res. Bull.*, 45 (2010) 460
- G.A. Smolenskii, V.A. Vokov, *J. Appl. Phys.*, 35 (1964) 915
- N.A. Spaldin and M. Fiebig, *Science*, 309 (2005) 391.
- M.A. Subramanian, D. Li, N. Duan, B.A. Reisner, A.W. Sleight. *J. Solid State Chem.*, 151 (2000) 323-325
- M.A. Subramanian, A.W. Sleight. *Solid State Sciences* 4 (2002) 347–351

- M.A. Subramanian, personal communication, November 2009
- M. Tachibana, J. Yamazaki, H. Kawaji, T. Atake, *Phys. Rev. B*, 72 (2005) 064434
- I. Terasaki, N. Murayama (Eds.), *Oxide Thermoelectrics*, Research Signpost, Trivandrum, India, (2002)
- B.H. Toby, EXPGUI, a graphical user interface for GSAS, *J. Appl. Cryst.* 34 (2001) 210
- P. Tomeš, J. Hejtmánek, K. Knížek, *Solid State Sci.* 10 (2008) 486-490
- T.M. Tritt. *Thermoelectric Materials: Principles, Structure, Properties, and Applications*. Encyclopedia of Materials: Science and Technology (2002) 1-11
- T.M. Tritt, M.A. Subramanian, *Mat. Res. Soc. Bul.* 31 (2006) 188-194
- K.D. Truong, J. Laverdiere, M.P. Singh, S. Jandl, and P. Fournier, *Phys. Rev. B*, 76 (2007) 132413
- D.G. Tomuta, S. Ramakrishnan, G.J. Nieuwenhuys, J.A. Mydosh, *J. Phys.: Condens. Matter*, 13 (2001) 4543
- ULVAC-RIKO, Inc. *Model ZEM-3 Thermoanalyzer: Power Conversion Efficiency Measuring Instrument Instruction Manual*.
- D.A. Vander Griend, S. Malo, K.T. Wang, K.R. Poeppelmeier, *J. Am. Chem. Soc.*, 122 (2000) 7308
- N.Y. Vasanthacharya, P. Ganguly, J.B. Goodenough, C.N.R. Rao. *J. Phys. C: Solid State Phys.*, 17 (1984) 2745
- A. Waintal, J. Chenavas, *CR Acad.Sci. Paris.*, (1967) 264
- J.B. Wang, H. Neaton, V. Zheng, V. Nagarajan, S.B. Ogale, B. Liu, D. Viehland, V. Vaithyanathan, D.G. Schlom, U.V. Waghmare, N.A. Spaldin, K.M. Rabe, M. Wutting and R. Ramesh, *Science*, 299 (2003) 1719
- Y. Wang, Y. Suia, J. Cheng, X. Wang, W. Su., *J. Alloys Compd.*, 477 (2009) 817
- A.R. West. *Basic Solid State Chemistry*, 2nd ed.; John Wiley & Sons: New York, 1999
- A.R. West, T.B. Adams, F.D. Morrison, D.C. Sinclair. *J. Eur. Ceram. Soc.*, 24 (2004) 1439

- Wikipedia, <http://en.wikipedia.org/wiki/Azurite>. Accessed May 2009
- Wikipedia, http://en.wikipedia.org/wiki/Cobalt_blue. Accessed May 2009
- Wikipedia, http://en.wikipedia.org/wiki/Prussian_blue. Accessed May 2009
- Wikipedia, <http://en.wikipedia.org/wiki/Ultramarine>. Accessed May 2009
- A. Wold, R.J. Arnott, J. B. Goodenough, *J. Appl. Phys.*, 29 (1958) 387
- P.M. Woodward, *Structural Distortions, Phase Transitions, and Cation Ordering in the Perovskite and Tungsten Trioxide Structures*, Ph.D. Thesis, Oregon State University, Corvallis, OR, 1996
- P.M. Woodward, *Acta Cryst. B*, 53 (1997) 32.
- P.M. Woodward, *Acta Cryst. B*, 53 (1997) 44.
- P.R. Watson, G.A. Somorjai, *J. Catal.*, 74 (1982) 282.
- P.M. Woodward, T. Vogt, D.E. Cox, A. Arulraj, C.N.R. Rao, P. Karen, A.K. Cheetham, *Chem. Mater.* 10 (1998) 3652
- H. Yakel, W. Koehler, E. Bertaut, F. Forrat, *Acta Cryst.*, 16 (1963) 957
- A. Yoshiasa, D. Sakamoto, H. Okudera, M. Ohkawa, K. Ota, *Mat. Res. Bull.* 38 (2003) 421
- Y. Zhao, *J. Solid State Chem.*, 141 (1998) 121
- H.D. Zhou, J.C. Denyszyn, J.B. Goodenough, *Phys. Rev. B*, 72 (2005) 224401
- J.-S. Zhou, J.B. Goodenough, *Phys. Rev. Lett.*, 94 (2005) 065501
- J.-S. Zhou, J.B. Goodenough, J.M. Gallardo-Amores, E. Morán, M.A. Alario-Franco, R. Caudillo, *Phys. Rev. B*, 74 (2006) 014422
- S. Zhou, L. Shi, H. Yang, and J. Zhao, *Appl. Phys. Lett.*, 91 (2007) 172505
- C. Zobel, M. Kriener, D. Bruns, J. Baier, M. Gruninger, T. Lorenz, *Phys. Rev. B*, 66 (2002) 020402